Author:
Palumbo, Rita

Title:
A multi-scale reinforced natural composite sandwich panel concept for vibroacoustic applications

A Multi-Scale Reinforced Natural Composite Sandwich Panel Concept for Vibroacoustic Applications

By

RITA PALUMBO

Department of Aerospace Engineering
UNIVERSITY OF BRISTOL

A dissertation submitted to the University of Bristol in accordance with the requirements of the degree of DOCTOR OF PHILOSOPHY.

OCTOBER 2020

Word count: ca. 40000

AUTHOR'S DECLARATION

I declare that the work in this dissertation was carried out in accordance with the requirements of the University's Regulations and Code of Practice for Research Degree Programmes and that it has not been submitted for any other academic award. Except where indicated by specific reference in the text, the work is the candidate's own work. Work done in collaboration with, or with the assistance of, others, is indicated as such. Any views expressed in the dissertation are those of the author.

SIGNED: ..... DATE: .....

ACKNOWLEDGEMENTS

I would like to gratefully acknowledge my mentor Fabrizio Scarpa, for his incomparable supervision and support throughout my PhD programme. A special thank you to Dmitry Ivanov, for contributing to this project with his special knowledge of composites materials. I also wish to acknowledge the European Union's Horizon 2020 research and innovation program for the financial support and the UK Engineering and Physical Sciences Research Council (EPSRC) for the materials and testing infrastructure support.

Finally, I extend my gratitude to my family, for significantly contributing to the completion of this ardours journey.

BRISTOL, SEPTEMBER 2020 R.P.

Abstract

The integration of vibroacoustics constraints in the design of sandwich panels is nowadays of utmost importance. Countless industrial sectors and applications now require multi-functionality in terms of mechanical, vibrational and acoustical performances. The main challenge dwells in the fact that good mechanical properties of a sandwich panel are normally related to poor acoustic performances. Numerous solutions have been proposed to enhance their vibroacoustic properties, ranging from porous and viscoelastic insertions or layers to Helmholtz resonators. However, the main drawback of such additions is the increase of weight which undermines the lightweight advantage of the panel. Thus, the complexity of designing structures which are mechanically and vibroacoustically efficient at the same time is further aggravated by the necessity of maintaining the additional mass at low levels.

This thesis illustrates the development of a novel sandwich panel for vibroacoustics applications with emphasis on vibration damping, paramount indicator of vibroacoustics performances of sandwich structures. The design strategy adopted revolves around the utilisation of novel materials and viscoelastic inserts as *passive* damping mechanisms. Specifically, a flax-fibre reinforced composite laminate is chosen for the square-cell core and the skins. Natural-fibre composites generally provide higher vibration energy dissipation than commercial materials traditionally used for sandwich and composite structures. Carbon-nanotube reinforced viscoelastic inserts are embedded in critical locations within the lattice core — junction corners between interlocking walls — to further increase its vibration damping capabilities and, by consequence, to potentially increase its strength as well. Restrictions to the value of additional mass brought by the inserts are imposed to ensure the preservation of the lightweight advantage of the sandwich panel.

Mechanical static analyses are carried out to guarantee good-quality structural performances. The quasi-static flatwise compression characterisation of bare and insert-reinforced core specimens shows that both configurations outperform other comparable benchmark cases present in open literature, in terms of normalized stiffness and strength. The reinforced configuration, in particular, has 24.5% higher normalized strength compared to the bare panel.
Two different types of tests are performed to investigate vibroacoustic performances of the sandwich panels. Results of out-of-plane vibration transmissibility tests show that the bare configuration outperforms that with inserts due to Coulomb dry friction effects which are triggered during the test at the interlocking areas between walls. On the other hand, the reinforced panel offers the highest viscoelastic damping values under free vibrations. In this case, indeed, bending deformation shapes are excited and the dry friction mechanisms in the bare lattice are not initiated.

Table of Contents

List of Tables

List of Figures

Figure **Page**

CHAPTER 1

INTRODUCTION

Contents

1.1 Thesis scope and main findings

SANDWICH panels have been extensively adopted in a variety of industrial fields during the last eighty years due to multiple reasons. Firstly, they provide good mechanical performances conferred by the high specific bending stiffness [1]. Such characteristic originates in the peculiar configuration of this type of structure, consisting of two face skins separated by a low-density core. The latter can traditionally be a porous layer, a cellular structure or balsa wood [1, 2]. Another reason for the extensive acceptance of sandwich panels lies in their high versatility due to the broad variety of materials and configurations that can be adopted as core and skins [3]. This feature makes them attractive in an assortment of fields. From the aerospace to the transport sectors, from packaging to goods transportation, sandwich panels are mainly exploited for applications where low weight and high performances are fundamental requirements.

However, the great mechanical properties of sandwich panels are often in conflict with their vibroacoustics performances [4, 5], since the sound transmission characteristics are negatively influenced by their low effective mass. Nowadays, structure-borne sound transmission is becoming an important quality criterion for any type of lightweight and stiff structural panel. The interest for the challenging integration of vibroacoustic constraints in the design process of sandwich

panels is hence growing accordingly. For this reason, research has been focusing on the inclusion of vibroacoustics constraints in the design process to obtain multi-functional structures that are both mechanically and acoustically efficient [3, 6–10].

Generally, coincidence phenomena due to the matching of phase velocity of structural waves propagating within a structure and incident acoustic pressure waves from the fluid medium causes reduced impedance and high sound radiation [11]. Structurally efficient systems such as sandwich panels with cellular or truss-lattice types of cores are generally acoustically poor due to their low critical frequencies which are caused by the low mass to stiffness ratio [11, 12]. Conversely, a soft and heavy monolithic panel is acoustically efficient but structurally useless in an aircraft. Novel cell topologies [3, 9, 13], poroelastic and auxetic insertions [14, 15], multilayered cores [16], Helmholtz resonators [17–19] are just few of the solutions that are being researched to improve vibroacoustics characteristics of sandwich panels with cellular or truss-lattice cores. However, the main drawback is that the related added weight can undermine the lightweight advantage of the panel [20].
One other technique that has been explored in literature to enhance the vibroacoustics quality of such structures consists of damping their motions by means of highly damping and viscoelastic materials [15, 21]. With this method, rather than working primarily on shifting the coincidence frequencies or including acoustic absorbers within the panel, damping is utilized to lessen the adverse effects of coincidence, such as the sound radiation of the panel in correspondence of these frequencies. Nevertheless, achieving high values of stiffness and damping at the same time with low added mass represents a significant challenge at the design level [11]. This is the area of development within which this thesis takes place.

1.1.1 Scope

This thesis illustrates the development of a novel sandwich panel for vibroacoustics applications with focus on vibration damping. This, as introduced in the previous section, is one paramount indicator of vibroacoustics performances of sandwich structures [22, 23], especially in applications concerning their dynamic behaviour at low frequency bandwidths of excitation. The strategies adopted to develop this panel are based on *passive* mechanisms: the use of novel materials and inclusion of passive dampers. At the same time, limitations are set on the additional mass brought to the panel by the passive dampers, and static investigations ensure that the structure guarantees good structural performances. Because the attention is mainly focused on materials, the topology of the core and the geometry of the panel are fixed.
Sandwich panels consist of several parts and hence different aspects related to those must be considered to meet our goals. Therefore, the following paragraphs describe the main features of the panel and the strategies behind their choice.

Core topology As previously introduced, generally speaking the core of a sandwich panel can traditionally be a porous layer, balsa wood or a cellular lattice. The latter is defined by

classes of cell topologies that have been successfully applied during the years. In particular, high-density rectangular lattices are preferable to hexagonal configurations for shock loads as they combine resistance to crushing and energy absorption with in-plane stretching strength [24–26]. Rectangular lattices are also relatively easy to manufacture; thus, they are ideal for exploring novel classes of materials as core platforms. For the aforementioned reasons, the core adopted in this study is a rectangular lattice and, to further simplify, its cells are square.

Core walls and skins material In this work, a flax-fibre reinforced composite material is adopted for both the walls of the cellular core and the skins of sandwich panels. The reason for this is that natural-fibre composites have been extensively evaluated during the last decade not only for their low environmental impact, but also for the higher vibration energy dissipation they provide compared to commercial materials traditionally used for sandwich and composite structures [27–30]. Indeed, vibration damping is paramount in vibroacoustics applications and the materials that have been traditionally adopted as core walls and skins (aluminium, Nomex, Kevlar, glass- or carbon-fibre reinforced composites) possess low values of viscoelastic loss factor [22]; this feature confers some limited vibration damping performances to the entire cellular structure.

Viscoelastic inserts As previously introduced, insertions such as porous materials, viscoelastic inserts or Helmholtz resonators can be embedded within a sandwich panel as passive mechanisms to improve its vibroacoustics characteristics. In this thesis, Carbon-nanotube (CNT) reinforced viscoelastic inserts are embedded in critical locations within the lattice core with the specific purpose of increasing its vibration damping capabilities with a very low weight penalty and, by consequence, to potentially increase its strength as well. Indeed, viscoelastic inserts for vibration damping have been widely and successfully evaluated in open literature [15]. In this thesis, local viscoelastic reinforcements are deposited at critical locations within the lattice core to make the best use of the energy absorption capabilities they provide: such locations are the junction corners between core walls, which have been demonstrated to be optimal sites to embed elastomeric insertions [31, 32]. The viscoelastic material adopted for the inclusions is a CNT-reinforced resin. CNTs are renowned for providing high vibration damping thanks to the stick-slip mechanism which dissipates energy at the nanotube scale by interfacial friction between the CNT's outer surface and the surrounding polymer [33–35]. In particular, adhesion between CNT and matrix is one of the most important factors on stiffness and damping characteristics of the resin. On the other hand, the strategic placement of the inserts at the junction areas of the walls allows to also potentially increase the out-of-plane (OOP) strength of the lattice: indeed, there is experimental evidence in literature that the junction corners between core walls are the best locations for this purpose as well [36, 37]. Figure 1.1(a) shows the reinforced lattice topology and its geometric characteristics, while figures 1.1(b) and 1.1(c) describe the deposition mechanism of the CNT resin by means of a 3D printed injection device. An example of the viscoelastic inclusion at a wall

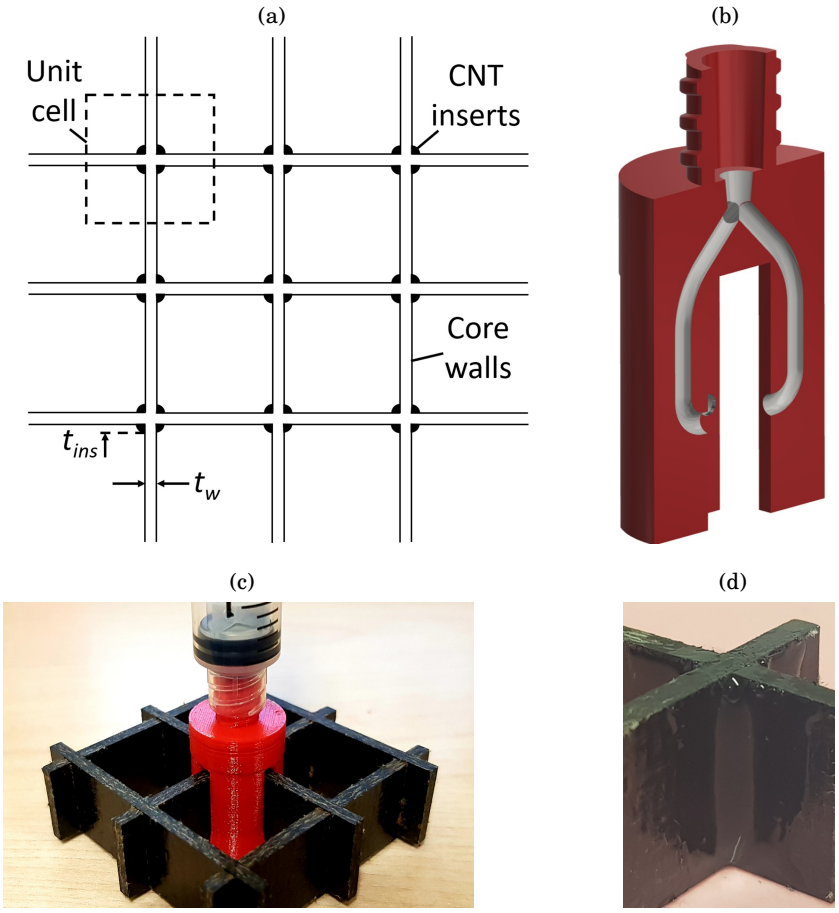

FIGURE 1.1. (a) Top-view representation of sandwich core with inserts and geometric characteristics. (b) CAD model of 3D-printed injection mould for CNT-resin deposition—AutoCAD 2017. (c) CNT-resin injection mechanism. (d) Example of viscoelastic insert at the core walls junction.

junction is shown in figure 1.1(d).

1.1.2 Main findings

Following, a summary of the milestones accomplished in this work.

- A novel natural-fibre based sandwich panel with distributed CNT viscoelastic inserts for vibroacoustics applications is developed: materials are characterized by mechanical and thermo-mechanical tests before proceeding with the design of the viscoelastic inserts.

- A manufacturing procedure for the sandwich panel with CNT resin depositions is successfully developed. The technique allows a fast and efficient process: it is possible to easily manufacture even large-scale sandwich panels.

- Core specimens with and without CNT inserts (from now on indicated as *reinforced* and *bare*, respectively) are tested by OOP flatwise compression tests. They outperform other benchmark cases present in open literature in terms of normalized OOP stiffness and strength. Furthermore, the reinforced configuration has 24.5% higher normalized strength—with 25% increase of relative density—compared to the bare panel.

- OOP vibration transmissibility tests are performed on small-scale sandwich panel specimens. When subjected to this type of OOP excitation, the bare panel—whose core is made by simply interlocking the composite walls without applying any resin/glue at the junctions—outperforms the reinforced panel. Indeed, Coulomb dry friction intervenes in this case, offering much higher mechanical energy dissipation than the reinforced configuration: with the experimental settings that will be discussed in detail in Chapter 6, the bare specimens show 14.4% loss factor at the resonance frequency, compared to 2.74% of the reinforced.

- Bare and reinforced large-scale sandwich panels are characterized by free vibration tests. The response of each plate to a white noise excitation applied at its centre is measured in terms of frequency response functions and deformation shapes. By evaluating the loss factor at the peaks of resonance, it is possible to verify that in this specific case the reinforced panel offers higher viscoelastic damping than the bare one. In this type of test, the deformation shapes are bending ones and the dry-Coulomb friction mechanism between interlocking walls of the bare panel is not "activated". Contrarily, the CNT inserts offer an increase in loss factor of about 8% at the first peak of resonance and 15% at the second one.

1.2 Thesis outline

This thesis is structured into three main parts. Firstly, materials for core walls, skins and viscoelastic inserts are characterized by mechanical and thermo-mechanical tests (Chapters 3 and 4). Once the materials are fully characterized, Finite Element models can be developed and the panel be designed. Hence, the second part of this thesis (Chapter 5) consists of the design and manufacturing methodologies of the entire sandwich panel with CNT-resin depositions. Finally, the last part (Chapters 6 and 7) describes vibroacoustics numerical and experimental analyses performed on sandwich panel specimens of different scales. At the same time, because the sandwich core must provide structural integrity along with good vibroacoustic properties, quasi-static OOP compression tests are executed on core lattices.
To summarize, the work carried out during this PhD project is described in nine chapters as follows.

Chapter 2 firstly explores background on vibrations, different types of vibration damping and techniques for its measurement. Afterwards, it summarizes the literature of research on natural fibres, viscoelastic inserts and the application of CNTs for damping purposes. Finally, rectangular lattices for sandwich cores are examined.

Chapter 3 describes methodologies, techniques and procedures adopted for mechanical and thermo-mechanical characterization tests of the materials constituting the sandwich panels.

Chapter 4 presents the results of mechanical and thermo-mechanical tests of which methods are discussed in Chapter 3. The characterization is performed not only on the natural-fibre composite and the CNT-reinforced resin, but also on the pristine, unreinforced resin in order to quantify the effect of CNTs inclusion.

Chapter 5 illustrates the design procedure of the viscoelastic inserts. Firstly, the dimensions of inserts are defined by setting a limit on the percentage of added mass that they bring to the panel. A technique for the deposition of CNT resin is developed and presented and the manufacturing procedure of entire bare and reinforced sandwich panels is shown. Secondly, a probabilistic design analysis is performed in order to assess the effect of geometric uncertainties of the shape of inserts on the unit cell global properties.

Chapter 6 concerns methodologies, techniques and procedures for quasi-static, dynamic and acoustic experimental and numerical characterization of bare and reinforced sandwich panel specimens.

Chapter 7 shows the results of quasi-static, dynamic and acoustic characterization tests and simulations, of which methods are discussed in Chapter 6. Results obtained for bare and reinforced sandwich panels are compared.

Chapter 8 provides a discussion of the results showed in Chapters 4 (mechanical and thermo-mechanical characterization of materials) and 7 (quasi-static, dynamic and acoustic characterization of sandwich panel specimens).

Chapter 9 draws the thesis to a conclusion with a summary of the results and a discussion on potential future research and development directions.

CHAPTER 2

BACKGROUND AND LITERATURE REVIEW

Contents

2.1 Introduction

SANDWICH panels are widely used in a variety of industrial fields. The main motive for this is saving weight, as they provide a very high stiffness-to-weight ratio. Another fundamental reason is the versatility that characterizes this type of structures: a broad variety of materials and configurations can be utilized for different scopes, due to the peculiar configuration of a sandwich panel. In fact, the latter consists of two flat plates (skins) connected to a low-density core, which is usually a porous layer, a cellular structure or balsa wood. Strength and shear modulus of a cellular structure are usually considerably higher than a foam's [1]: hence, in cases where core material mechanical properties govern the design of the sandwich panel, cellular structures are more appropriate. On the other hand, porous materials can be adopted in lightly loaded, insulating panels. Nevertheless, it is not uncommon to see combinations of these configurations: cells of cellular cores can, for instance, be filled with foam inserts or other insulating materials, providing good structural properties and fair insulation performances at the same time. Finally, balsa wood can be sometimes preferred to cellular cores because of their excellent strength-to-weight and stiffness-to-weight ratios. Indeed, sandwich panels produced with balsa core are found in major load-bearing applications, such as hulls of ships and aircrafts [38–40]. In this thesis, focus is on sandwich panels with cellular cores. Figure 2.1 represents schematically their typical configuration: here, the core is a honeycomb lattice connected to the facings by means of adhesive layers.
From the historical standpoint, the first known man-made sandwich structure was built in 1845 and was part of a tubular railroad bridge in Wales consisting of a large rectangular tube through which trains ran. The top compressive panel of the tube had two flat plates connected to a square cell egg-crate wood core. Another important date in the history of sandwich panels is 1919, with the first sandwich panel utilized in the aircraft industry: it was fabricated by using thin mahogany facings bonded to a balsa wood core and was used as primary structure on seaplane pontoons. Later on, during World War II, the military aircraft industry adopted plywood facings on balsa wood core for applications in Italian seaplanes. Finally, a paramount development for sandwich panels technology happened in 1945, when the first all-aluminum panel was made (i.e. aluminum facings bonded to an aluminum honeycomb) [1].

If, from one side, sandwich panels have been widely studied and exploited during the last century because of the high mechanical performances they offer, from the other side the same cannot be said about sound insulation and vibration damping properties they provide, which are usually very poor [6]. Sometimes, these performances can be improved by adopting passive, weight-increasing solutions [14, 15, 41], hence reducing the main advantage sandwich panels offer: light weight. For this reason, as noise reduction and vibration suppression are becoming important quality criteria not only in aircraft design but also in all transportation sectors, the improvement of vibration and acoustic performances in sandwich panels represents nowadays a major challenge.

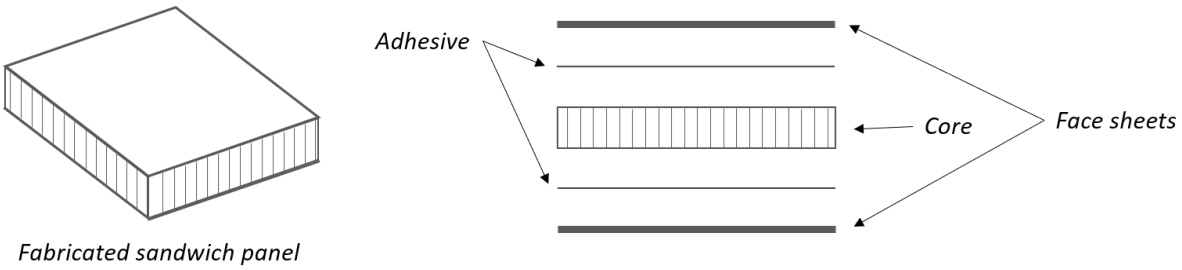

FIGURE 2.1. Schematic representation of a sandwich panel with cellular core.

In particular, vibration damping plays a vital role in the vibroacoustic behaviour of sandwich panels and hence it is one of the major indicators to consider when designing structures for vibroacoustics applications: passive damping properties of composite sandwich panels are crucial because they affect the sound transmission loss of the panel, especially in the critical frequency range, and the vibration response to excitation [22].
Consequently, next sections explore basic concepts of vibration (section 2.2) and different mechanisms through which damping in vibrating systems dissipates mechanical energy (section 2.3). Sections 2.4, 2.5 and 2.6 focus respectively on natural fibres, viscoelastic inserts and CNT-reinforced resins, with a particular focus on their application in sandwich panels and their contribution to vibration damping. Finally, section 2.7 summarizes the literature on rectangular lattices and their application as cores in sandwich panels.

2.2 Introduction to Vibration, Vibration Control and Noise Control

This section will introduce basic vibration principles, equations and nomenclature. In order to do so, the following subsections consider the simple case of a single degree-of-freedom system.

2.2.1 Equation of Motion for undamped single-DoF systems

The equation of motion of an undamped single degree-of-freedom (DoF) mass-spring system (figure 2.2) consisting of a rigid mass m supported by a spring k is:

$$m\frac{d^2x(t)}{dt^2} + kx(t) = f(t) \tag{2.1}$$

where $x(t)$ is the mass displacement from equilibrium, $d^2x(t)/dt^2$ is its acceleration and $f(t)$ the excitation force. Particularly of interest is the case in which the excitation is harmonic and can be expressed as $f(t) = F\sin(\omega t)$, where ω is the frequency [rad/sec]. Then the displacement from equilibrium position is

$$x(t) = \frac{F\sin(\omega t)}{k - m\omega^2} \tag{2.2}$$

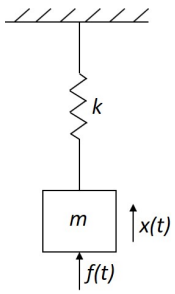

FIGURE 2.2. Schematic representation of an undamped single-DoF mass-spring system.

This equation describes what is known as the *steady-state* response of the system, which is the response when all transient effects have been dissipated. This can happen only if there is damping in the system: in this case, if the excitation $F\sin(\omega t)$ starts at $t = 0$, then it can be demonstrated that the full solution is:

$$x(t) = \left[\frac{F\sin(\omega t)}{k - m\omega^2} + Ae^{-\zeta\omega_0 t}\sin(\omega_0 t)\right]H(t) \tag{2.3}$$

being A the initial amplitude of the transient term, $\omega_0 = \sqrt{k/m}$ the natural frequency of the system and $H(t)$ the Heaviside step function,

$$H(t) = \begin{cases} 1 \text{ for } t > 0, \\ 0 \text{ for } t < 0 \end{cases} \tag{2.4}$$

and ζ the damping coefficient, assumed to be very small but finite. Depending on the value of ζ, after a sufficiently long time the transient term is dissipated through each cycle of response becoming infinitesimal and only the steady-state term remains, giving equation 2.2.
It is possible to notice that for $\omega = \omega_0 = \sqrt{k/m}$ the response $x(t)$ of the system is infinite: if excited at this particular frequency, the infinite amplitude is built up through each cycle as energy is inputted into the system and it is achieved after an infinite amount of time. In practice, the system will break before the amplitude reaches infinity.
More complicated structures with more DoFs behave similarly but multiple resonances can be observed and each one of them is associated with a certain deformation mode, typically known as *mode of vibration* or *natural mode*.
The vibration response of a structure can be controlled in many ways. Very stiff and massive structures, for example, may have so high natural frequencies that all vibrations the structure normally undergoes are within an acceptable level [42]. For instance, many structures that were built in the 19th Century are on a massive scale and have relatively few vibration problems. Building massive structures is, however, very expensive and hence cannot be a definitive solution to vibration control problems. Conversely, the tendency nowadays is to build very light structures at the expense of an even lower stiffness, causing resonances to often arise where excitation forces are high. Hence, structures have to be designed to avoid vibration problems as much as possible:

resonance frequencies and their corresponding modes are calculated and structural changes are applied to ensure safety in the expected operational conditions of the system. Furthermore, damping treatments and devices are widely used for control of vibration, either at the design stage or as solution to problems that might emerge later during production or construction.
On the other hand, noise control issues cannot be treated with the same approach. In some cases for example, noise is generated by a source (such as gas turbine engines) and is then transmitted into the surrounding atmosphere: here, the only control can be at the source itself or by applying barriers between source and receiver. Only structure-borne noise, which is generated by interactions of vibrating structural members with the surrounding atmosphere, can be controlled by damping, changes in mass and/or stiffness and inclusion of barriers.

2.2.2 Equation of motion for single-DoF systems with viscous damping

Vibration damping and the different types of energy dissipation mechanisms will be explored in depth in next sections. For now, let us consider the case of linear viscous damping, for which the equations of motion are simple and linear. A viscous damper is a device that creates forces at each one of its ends opposing the relative velocity between the ends themselves. Forces amplitudes are proportional to the relative velocity by a factor denoted by c. Generally, viscous dampers utilise a viscous flow through a piston to create the opposing force and can be developed and applied in cases where damping forces are applied between two points in a structure. Examples are automotive hydraulic shock absorbers and pneumatic door jambs.
Figure 2.3 shows a schematic representation of a single-DoF mass-spring-damper system. The equation of motion of this system is

$$m\frac{d^2x(t)}{dt^2} + c\frac{dx(t)}{dt} + kx(t) = f(t) \tag{2.5}$$

where the sum of inertial, damping and stiffness forces balances the external force, $f(t)$. In the simple case of an harmonic excitation $f(t) = F\sin(\omega t)$, the steady-state solution $x(t)$ representing the displacement from the equilibrium position is [42]:

$$x(t) = \frac{F\sin(\omega t - \psi)}{\sqrt{(k - m\omega^2)^2 + (c\omega)^2}}, \tag{2.6}$$

where ψ is the phase lag between applied force and steady-state response and is such that $\tan\psi = c\omega/(k - m\omega^2)$. Comparing equation 2.6 to the undamped steady-state solution, it is clear that the presence of c limits the response amplitude at resonance, especially if the value of c is not small. By introducing the damping ratio or damping coefficient $\zeta = c/2\sqrt{km}$, the ratio of peak amplitude at resonance to peak amplitude at zero frequency is equal to $1/2\zeta$. Finally, $\zeta = 1.0$ defines the so-called critical damping condition.

2.2.3 Inertial forcing

This section considers a particular case of the damped single-DoF system introduced in previous section, in which the dynamic load is caused by motion of the supports of the system itself.

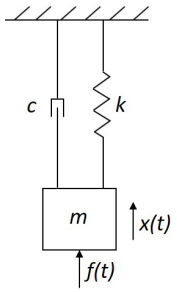

FIGURE 2.3. Schematic representation of a single-DoF mass-spring system with viscous damper.

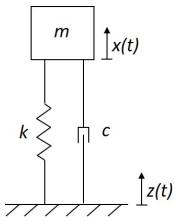

FIGURE 2.4. Schematic representation of a single-DoF mass-spring system with viscous damper subjected to base motion.

Measurements performed on such system allow to evaluate its transmissibility ratio which, as it is shown later in this section, is a fundamental indicator of its vibration behaviour. Indeed, transmissibility tests will be performed on the novel natural composite-based sandwich panels, as shown in Chapters 6 and 7.
When the dynamic load is given by motion of the supports of the system, the external force on the oscillator is the inertial force resisting the ground acceleration,

$$f(t) = -m\frac{d^2z(t)}{dt^2} \tag{2.7}$$

where $z(t)$ is the base motion [43]. Figure 2.4 shows a representation of such system. The equation of motion of this system can hence be written as

$$m\left(\frac{d^2x(t)}{dt^2} + \frac{d^2z(t)}{dt^2}\right) + c\frac{dx(t)}{dt} + kx(t) = 0 \tag{2.8}$$

or, equivalently, as

$$\frac{d^2x(t)}{dt^2} + 2\zeta\omega_0\frac{dx(t)}{dt} + \omega_0^2x(t) = -\frac{d^2z(t)}{dt^2} \tag{2.9}$$

Equation 2.9 is independent of the mass term. Therefore, systems with different masses and equal natural frequency and damping ratio have the same behavior and respond in the same way to the same motion of the support.

In the particular case of sinusoidal motion of the base, $z(t) = \overline{Z}cos(\omega t)$, the base acceleration is $d^2z(t)/dt^2 = -\overline{Z}\omega^2 cos(\omega t)$. In this case the equation of motion can be expressed as

$$m\frac{d^2x(t)}{dt^2} + c\frac{dx(t)}{dt} + kx(t) = m\overline{Z}\omega^2 cos(\omega t) = mZ(\omega)\omega^2 e^{i\omega t} + mZ^*(\omega)\omega^2 e^{-i\omega t} \tag{2.10}$$

Therefore, the steady-state response is a function of the frequency of the base motion, ω, and can be expressed as $x(t) = X(\omega)e^{i\omega t} + X^*(\omega)e^{-i\omega t}$. The positive and negative exponents terms are independent of each other and can be analyzed separately.

Considering the particular part of the solution (persistent excitation and ignoring the transient response term), the response of the system will be harmonic and the "positive exponent" part of the steady-state response will have a form $Xe^{i\omega t}$. Substituting this expression into equation 2.10, the frequency response function is

$$\frac{X(\omega)}{Z(\omega)} = \frac{m\omega^2}{(k - m\omega^2) + i(c\omega)} = \frac{\Omega^2}{(1 - \Omega^2) + i(2\zeta\Omega)} \tag{2.11}$$

where $\Omega = \omega/\omega_0$ and

$$\left|\frac{X(\Omega)}{Z(\Omega)}\right| = \frac{\Omega^2}{\sqrt{(1 - \Omega^2)^2 + (2\zeta\Omega)^2}} \tag{2.12}$$

Finally, the motion of the system can be evaluated with respect to a fixed point by considering the so-called total motion, which is the sum of base motion and motion relative to the base, $z(t) + x(t)$. It is hence possible to define the *transmissibility ratio*, $\mathrm{T}(\Omega, \zeta)$, as follows.

$$\mathrm{T}(\Omega, \zeta) = \left|\frac{X + Z}{Z}\right| = \frac{\sqrt{1 + (2\zeta\Omega)^2}}{\sqrt{(1 - \Omega^2)^2 + (2\zeta\Omega)^2}} \tag{2.13}$$

The transmissibility ratio determines the ratio between the total response amplitude $\overline{X + Z}$ and the base motion $\overline{Z}$. It is a paramount indicator of the vibration transmission behaviour of a structure and therefore part of the characterization of the novel natural-composite sandwich structures will be centered around its numerical and experimental evaluation (Chapters 6 and 7). Its analytic formulation has been here introduced for the sake of completeness but it will not be applied in this work. The vibration transmissibility of sandwich panel samples will be evaluated numerically and experimentally in Chapter 7 and therefore next section introduces procedure and formulations for its experimental evaluation.

2.2.4 Experimental evaluation of vibration transmissibility of a system with inertial forcing

Vibration transmissibility tests contemplate shaker-excited SDOF systems which can provide accurate measurements of amplitude and phase over a wide frequency range [42]. This type of test method, widely applied in open literature [42, 44–46], is also well-known as standing wave resonance method [47] and is similar to the ISO 13753 procedure for antivibration glove

materials. Figure 2.5 shows a schematic representation of such system: the specimen is subjected to excitation at the base by an electromagnetic shaker and the acceleration is measured at base and top of the specimen. Other than the mass of the specimen, m, the mass of the accelerometer at the top (or other means of measuring acceleration) and any mass/weight added on the sample must be taken into consideration, M.

The equation of motion of such system can be expressed as:

$$(M + m/3)\frac{d^2x(t)}{dt^2} + k^*[x(t) - x_0(t)] = 0 \tag{2.14}$$

where k^* is the complex stiffness of the system. In case of harmonic excitation, the displacement at the base can be written as $x_0(t) = X_0 e^{i\omega t}$ and the free response at the top as $x(t) = Xe^{i\omega t}$. Thus,

$$X = \frac{X_0 k(1 + i\eta)}{k(1 + i\eta) - (M + m/3)\omega^2} \tag{2.15}$$

The resonance peak amplitude, A, is determined as the ratio of the accelerations measured by the accelerometers, $A = |X/X_0|$. Furthermore, the modulus k at the resonance frequency ω_R (radians/second) is evaluated as:

$$k = (M + m/3)\omega_R^2 \tag{2.16}$$

and the loss factor η as:

$$\eta = \frac{1}{\sqrt{A^2 - 1}}. \tag{2.17}$$

This method allows to evaluate very accurately and with a simple, straightforward procedure the values of loss factor and complex modulus at the resonance frequency. Its advantages and disadvantages are therefore evident since, in order to evaluate these values for a range of frequencies rather then one single frequency, the mass at the top of the specimen must vary accordingly. However, the mass value can only be determined within some limit: lowest limits are imposed by any cut-off frequencies of the shaking table and regardless, the minimum value is the mass of the accelerometer. Furthermore, M should be such to not interfere with any resonances of the rig/base plate. Finally, high values are limited by creep/toppling phenomena which might become important for some systems.

2.3 Vibration Damping

This section introduces different mechanisms through which damping in vibrating systems dissipates mechanical energy. The reason for reviewing these processes is that generally they all contribute to the overall damping levels in a system and, throughout this thesis, it will be demonstrated how different mechanisms intervene in the response of the structures as they undergo different types of deformation.

Damping is the phenomenon by which mechanical energy is dissipated in dynamic systems [48].

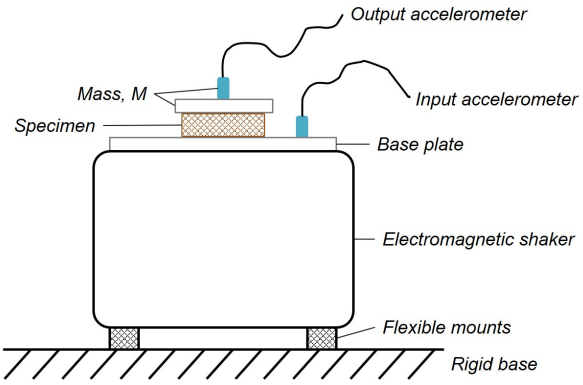

FIGURE 2.5. Structural-scale tests: schematic drawing of shaker-excited SDOF system tests (OOP vibration transmissibility).

This is typically due to the conversion of mechanical energy into internal thermal energy. There are forms of inherent mechanical energy dissipation in any dynamic system. However, in cases where the level of inherent damping is not adequate for a proper functioning of the system, external damping sources may be added. Generally speaking, there are three main mechanisms which contribute to energy dissipation in mechanical systems:

1. Internal damping (i.e., of material);

2. Structural damping (i.e., at joints and interfaces);

3. Fluid damping (i.e., through fluid-structure interactions - FSI).

Internal material damping is due to dispersion of mechanical energy within the material itself and can be caused by various microscopic and macroscopic phenomena. Structural damping derives from the relative motion between components at common points of contact, joints or supports. Finally, fluid damping results from drag forces and dynamic interactions of a mechanical system that moves in a fluid.
As introduced in previous section, the danger of resonances lies in the fact that the response of a structure is amplified when excited at its resonance frequencies. If resonance cannot be avoided by design (e.g., by controlling the stiffness and/or the mass properties or by somehow isolating the system from the excitation), then external dampers can be added to enhance the dissipation of mechanical energy. These devices can be classified into three categories:

1. Passive dampers, dissipating energy without an external power source or actuators;

2. Active dampers, consisting of sensors measuring the response at each instant of time and actuators applying forces to oppose the measured vibration response. They need an external source of power;

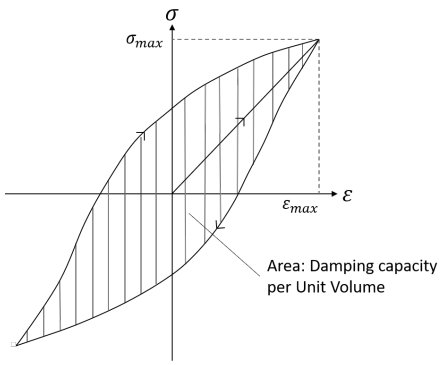

FIGURE 2.6. Typical hysteresis loop for mechanical damping.

3. Semi-active dampers, where active control enhances the damping properties of passive elements [23].

In the following paragraphs, material and structural damping are explored in more detail. These are the two energy dissipation mechanisms that will be encountered in this thesis.

2.3.1 Material Damping

Internal damping of materials is associated with energy dissipation mechanisms that depend on the characteristics of the material itself. They can be due to microstructure defects, such as grain boundaries and impurities; thermoelastic effects, caused by local temperature gradients resulting from nonuniform stresses, as in vibrating beams; eddy current effects in ferromagnetic materials; dislocation motion in metals; chain motion in polymers [48]. Because of the variety of internal damping origins—due to the wide range of engineering materials typically used—there is no general, single model that can describe the internal damping properties of all materials sufficiently well. Generally speaking, internal material damping can be classified into two main categories: viscoelastic and hysteretic. It should be clarified that all mechanisms of internal damping are related to hysteresis loop phenomena and hence the term "hysteretic" damping used for the second category can be quite misleading. In fact, the stress-strain ($\sigma - \epsilon$) relation at any point in a vibrating continuum system is characterized by a hysteresis loop (figure 2.6). The area defined by the curve gives the per-unit-volume damping capacity, d, which is the energy dissipation per unit volume, per stress cycle:

$$d = \oint \sigma \, d\epsilon \tag{2.18}$$

Contrarily to what happens for a pure elastic force, a damping force cannot be a function of the only displacement (q). In fact, such a force would be the same regardless of the direction of motion, meaning that in a loading-unloading cycle the same path would be travelled in both directions and there would be no hysteresis: the net work done in one cycle would be zero. Conversely, a force which is a function of both q and its first derivative, $\dot{q}$, will have different values in the two directions of motion. Hence, there will be a hysteresis loop correlated to the energy dissipation

(i.e., work done against the damping force). A damping force has then to depend somehow on the relative velocity. For example, as it will be shown later, *Coulomb* friction is independent of the amplitude of $\dot{q}$ and depends on its sign (i.e., direction).
For a **linear viscoelastic material**, the $\sigma - \epsilon$ relationship is given by a linear differential equation with respect to time. The Kelvin–Voigt model is traditionally used to express the $\sigma - \epsilon$ relation for these materials:

$$\sigma = E\epsilon + E^* \frac{d\epsilon}{dt} \tag{2.19}$$

in which E is Young's modulus and E^* is a time-independent viscoelastic parameter. $E\epsilon$ represents the elastic contribution of which, as previously noticed, the cyclic integral is null.
For viscoelastic damping materials, hence, the internal damping force is function of the frequency of variation of the strain (or frequency of harmonic motion). A simple model sometimes adopted for the $\sigma - \epsilon$ relationship is:

$$\sigma = E\epsilon + \frac{\tilde{E}}{\omega} \frac{d\epsilon}{dt} \tag{2.20}$$

which is identical to equation 2.19 in case the viscoelastic parameter E^* depends on the frequency of motion.
For some types of materials the dependence of the damping force on the frequency of variation of the strain is not very significant: in these cases the internal damping is known as **hysteretic**. In the simplified case of harmonic motion it is possible to demonstrate that the hysteretic damping can be represented by a complex modulus of elasticity of which the real part is the linear elastic modulus or Young's Modulus (energy storage), while its imaginary part represents the hysteretic loss modulus (energy dissipation). Thus, the $\sigma - \epsilon$ relation can be expressed as

$$\sigma = E(1 + i\eta)\epsilon \tag{2.21}$$

and, similarly, the relation between shear stress and strain as

$$\tau = G(1 + i\eta)\phi \tag{2.22}$$

where G is the shear modulus. η is the loss factor and is one of the many ways of representing damping in vibration analysis (this will be explored in more detail in section 2.3.1).

2.3.2 Structural Damping

This type of damping has origin in friction mechanisms (due to relative motion between two or more parts of a structure or system), impacts or intermittent contacts at joints. As for the internal material damping, it is nearly impossible to develop an analytic model describing all types of structural damping in a satisfactory manner due to its dependency on the particular characteristics of the parts or components of the system. In fact, even though some models do exist for specific cases, the most efficient, common and truthful method for evaluating structural

damping is by experimental measurement. Also in this case, however, the procedure is not straightforward: measured damping values contemplate overall damping levels in a mechanical system, hence the structural damping component alone has to be calculated by subtracting the other types of damping (assessed in environment-controlled experimental tests, known from existent data, etc.) from the measured value. Contribution of internal damping is, however, usually not significant when compared to structural damping.

Slip damping is one of the major types of structural damping and is due to interface shear acting at a structural joint. Depending on factors such as joint forces and surface characteristics and materials, part of slip damping is caused by Coulomb dry friction directly. Corrosion phenomena can be a consequence of the action of slip damping at the joint, thus it is common to utilize damping layers to prevent and/or reduce joints deterioration.

As slip damping acts at a joint, the damping force varies due to local deformations which naturally happen with slipping. Figure 2.7(a) represents a hysteresis loop for this case, in which the arrows show the direction of relative velocity. Figure 2.7(b) shows a hysteresis loop in case of idealized Coulomb friction, in which the friction force is constant in each direction of motion. In this idealized case, the constitutive relation between damping force f and relative velocity at the joint $\dot{q}$ is as follows:

$$f = c\ \mathrm{sgn}(\dot{q}) \tag{2.23}$$

where c is a friction parameter. Structural damping due to local deformation can be represented by the simplified model shown in figure 2.7(c),

$$f = c|q|\mathrm{sgn}(\dot{q}) \tag{2.24}$$

In all previous equations, the signum function is defined as

$$\mathrm{sgn}(v) = \begin{cases} +1 \text{ for } v \geq 0, \\ -1 \text{ for } v < 0 \end{cases} \tag{2.25}$$

It is important to highlight that friction damping models are hereby shown for the sake of completeness, albeit they are not applied in this work.

Interface Damping is one type of structural damping paramount in engineering applications. It originates at the interface of two sliding surfaces, such as in bearings, screws and guideways. It was first formally taken into consideration by Da Vinci in the 1500s and then by Coulomb in the 1700s. The simplified model used by them is the well-known Coulomb friction model:

$$f = \mu R \mathrm{sgn}(v) \tag{2.26}$$

in which f is the frictional force opposing motion, R is the normal reaction force between sliding surfaces, v the relative velocity and μ the friction coefficient. The signum function emphasizes

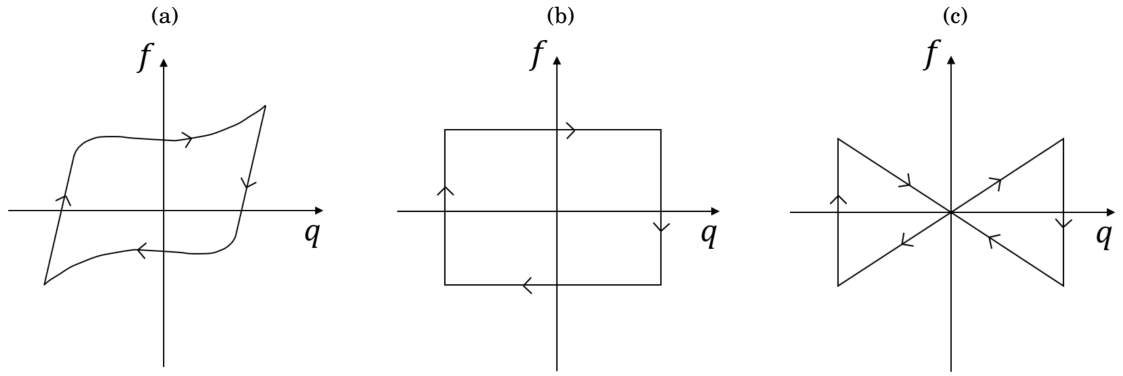

FIGURE 2.7. Representative hysteresis loops. (a) Typical structural damping, (b) idealized Coulomb dry friction damping and (c) simplified model of structural damping due to local deformation.

the fact that frictional forces act in opposite direction to the friction coefficient. Clearly, this model is very simple and cannot provide truthful estimations in all cases of interface damping. Generally, other factors that intervene are loading conditions, material and surface characteristics, lubrication, geometries and amplitude of velocity and therefore more complete and complicated models exist [48].

2.3.3 Representation of Damping in Vibration Analysis: Loss factor

The loss factor is a very common and useful method to compare damping capacity of systems and it is the one that will be utilized in this thesis (mostly in Chapters 6 and 7).
The *damping capacity* of a device (damper) is defined as the energy dissipated in one cycle of motion and, therefore, it is the area of the hysteresis loop in the displacement-force plane:

$$\Delta U = \oint f_d \, dx \tag{2.27}$$

The *specific damping capacity*, on the other hand, is indicated as

$$D = \frac{\Delta U}{U_{max}} \tag{2.28}$$

being U_{max} the initial total energy of the system. The *loss factor*, then, is defined as the specific damping capacity per radian of the damping cycle:

$$\eta = \frac{\Delta U}{2\pi U_{max}} \tag{2.29}$$

An equivalent definition of η is the ratio of dissipated power P_D to the product of total mechanical stored energy E_{tot} and the angular frequency ω [49, 50]. It can be shown that the loss factor for a viscous damped simple oscillator is expressed as [48]

$$\eta = \frac{2\omega\zeta}{\omega_n} \tag{2.30}$$

Table 2.1: Expressions for equivalent viscous damping ratio for different damping mechanisms in case of harmonic excitation. x_0: amplitude of steady-state vibrations. Reproduced from [48]

Damping Type	Equivalent Damping Ratio ζ_{eq}
Viscous	ζ
Hysteretic	$\frac{c}{2\omega_n\omega}$
Structural	$\frac{c}{\pi\omega_n\omega}$
Structural Coulomb	$\frac{2c}{\pi x_0\omega_n\omega}$

Table 2.2: Loss factor typical values for some common materials. Reproduced from [48]

Material	Loss Factor $\eta \cong 2\zeta$
Aluminium	2x10^{-5} to 0.002
Concrete	0.02 to 0.06
Glass	0.001 to 0.002
Rubber	0.1 to 1.0
Steel	0.002 to 0.01
Wood	0.005 to 0.01

For free decay of the system and for low damping values $\omega = \omega_d \cong \omega_n$, where ω_d is relative to the case of damped response. Similarly, in case of forced oscillations the worst response condition occurs at when $\omega = \omega_d \cong \omega_n$: this is the condition that must be considered with regard to energy dissipation. In both cases, the loss factor in case of viscous damping is approximately

$$\eta = 2\zeta \tag{2.31}$$

where ζ is the damping ratio, as defined in section 2.2. This relation is accurate within 5% for $0 \leq \eta \leq 0.3$. For higher values of loss factor, the relation defined by Nashif *et al.* [51] and Graesser and Wong [52] is more precise [49]

$$\eta(\omega) = 2\zeta(\omega)\sqrt{1-\zeta(\omega)^2} \tag{2.32}$$

For other types of damping, equation 2.31 is still valid when substituting the equivalent damping ratio, ζ_{eq} to ζ. Indeed, while for linear viscous damping the mathematical expression is fairly simple, other types of damping are usually represented by equivalent viscous damping terms in simplified dynamic models. Equivalent viscous damping is such that its energy dissipation per cycle is equal to that for original damping. Table 2.1 summarizes expressions for the equivalent damping ratios for common types of damping. Table 2.2 shows typical loss factor values for common materials.

2.3.4 Measurement of Damping

As introduced in previous sections, there are many parameters by which energy dissipation mechanisms can be represented in a system (e.g., specific damping capacity, loss factor, damping

ratio, Q-factor). At the same time, there are different types of damping that can act in a system or machine and, hence, several models to describe it (e.g., viscous, hysteretic, structural, fluid). Therefore, how damping is measured experimentally depends first of all on the model that is used to represent it in order to describe satisfactorily the phenomenon of energy dissipation. Once the model is decided, the parameter to be measured has to be defined. However, not only developing a realistic model for a complex system is extremely complicated, but also the experimental determination of its parameters can be very challenging. The reasons for this are multiple. One fundamental issue lies in the impossibility of identifying the contributions of the various mechanisms of damping from the overall measurement. Another problem is that measurements should always be performed in the actual operating conditions: for example, if fluid damping is eliminated during the measurement then the latter does not represent faithfully the operating conditions. Furthermore, the interacting effects between different damping types could be neglected if they are not all taken into account: overall damping in a system is not equal to the sum of individual damping values when they are acting independently and nonlinear effects could also intervene.

Generally speaking, two main categories of damping measurements can be identified. Time response methods consider the time response of the system to a transient excitation. Examples are the Logarithmic Decrement and the Step-Response methods, which assume that the system is a single-DoF oscillatory system with viscous type of damping and it is excited by an impulse and a unit-step excitation, respectively. On the other hand, frequency-response methods are based on the frequency-response function (FRF) of the system and the amplitude of resonance peaks. Examples are the Magnification Factor and the Bandwidth methods [48]. Another type of damping measurement is the power injection method (PIM), which is based on steady-state input to the system and measurement of the stored energy: the dissipated energy is compared to the system's maximum strain energy under steady-state vibration [53]. Finally, in hysteresis loop methods the area of the hysteresis loop in the displacement-force plane is equal to the damping capacity ΔU: the work done by conservative forces (e.g., gravity, inertia, elasticity and so on) in one cycle of motion is null and hence the net work must be equal to the work done by damping forces only [48].

In this thesis, only the FRF-based Bandwidth method is used to evaluate damping values of the natural-fibre sandwich panels. This will be explored in more detail in Chapter 6, which presents the methodologies and techniques utilized for the dynamic characterization of the sandwich panels.

2.4 Natural-fibre Reinforced Composites

As introduced in Chapter 1, most of the components of the novel sandwich panels developed in this thesis consists of natural fibre-based composite laminates. The reason behind this choice is the intrinsically high vibration energy dissipation they offer compared to commercial materials,

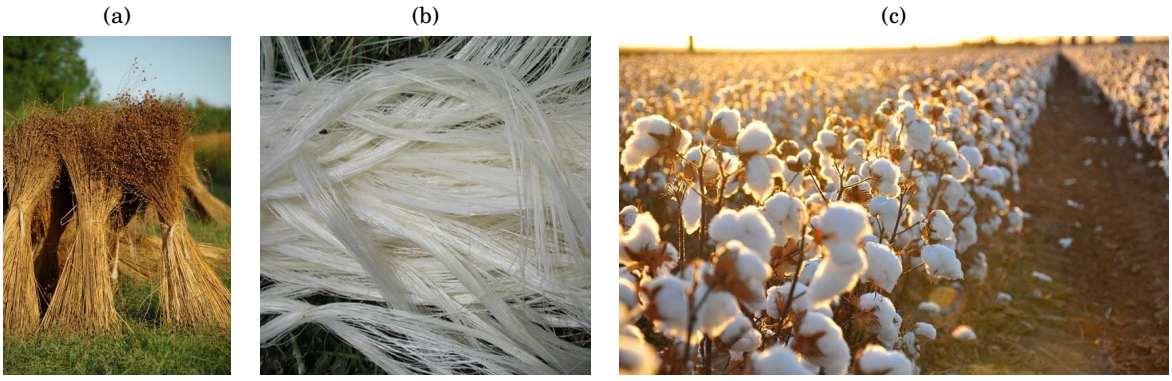

FIGURE 2.8. Examples of natural fibres used in industry. (a) Flax during harvest (bast fibres type), (b) raw sisal fibres (leaf fibres type) and (c) cotton (seed fibres type).

especially those traditionally utilized for sandwich panels. This section, therefore, reviews different types of natural fibres which are most commonly used in industrial applications. Advantages and disadvantages related to their adoption are also examined. Finally, relevant literature regarding the mechanical energy dissipation provided by natural fibres is reviewed.

This century has witnessed exceptional accomplishments in green technology thanks to the blooming of eco-friendly bio-composites from plant-derived fibre (natural/bio-fibre) and crop-derived plastics (bio-plastic). Such advancement is due to the growth in environmental and sustainability awareness [30]: research and development of high-performance materials deriving from natural means is increasing all around the globe owing to the importance of breaking any dependence on fossil fuel resources [54, 55]. Bio-based materials include products made of renewable agricultural and forestry feed stocks, including wood, grasses, crops and crops by-products [28], whose production requires little energy and does not produce CO_2: instead, CO_2 is used while oxygen is released back into the environment. Other advantages their adoption may provide are low specific weight (resulting in high specific strength and stiffness), high vibration energy dissipation properties, low production costs, process-friendliness, possibility of recycling and good thermal and acoustic insulation characteristics [56].

Many examples where groups of cells contribute to strength and stiffness can be found in nature. Cellulose is a natural polymer with high strength and stiffness per weight and it is the building material of long fibrous cells. Usually these cells can be found in stem, leaves and seeds of plants [57]. Following, a few examples are reported.

Bast fibres (flax, hemp, jute, kenaf) The structure of bast fibres is here briefly introduced to familiarize with its basic components. This facilitates the understanding and interpretation of results of thermal and thermomechanical characterization of the natural-fibre laminates presented in Chapters 3 and 4.

Plants bast consists of a wood core surrounded by a stem. The latter contains fibre cells or filaments bundles and each filament is made of cellulose and hemicellulose bonded together by

a lignin or pectin matrix. Pectin surrounds the bundle of fibres, holding them on to the stem and, during the retting process, is removed to allow separation of bundles from the rest of the stem (scutching). In order to make a composite, fibres are then impregnated with a resin and the weakest component in the final material is the lignin between cells. For this reason, the bundles are sometimes pre-treated to separate the cells and remove the lignin in between, resulting in a stronger composite.
Flax (figure 2.8(a)) and hemp fibres have replaced glass fibres in many applications especially in automotive industry [57]. They are amongst the strongest and stiffest natural fibres and although their mechanical properties are usually lower than those of glass fibres, they are also about 50% lighter and hence their specific properties are comparable to the stated values of glass fibres [58]. Furthermore, they can be grown in moderate climates and hence many countries have started to produce them for industrial purposes. Jute, on the other hand, is grown in warmer climates. It is cheap, reasonably strong and resistant to decomposition and is therefore mainly adopted in packaging applications.

Leaf fibres (sisal, abaca (banana), palm) Leaf fibres are usually coarser than bast's and are mainly applied in ropes and coarse textiles. Sisal fibres (figure 2.8(b)), obtained from agave leaves, are the most important among them because of their relatively high stiffness. Sisal is, in fact, often applied with flax fibres in hybrid mats composites to improve their permeability when the mat is impregnated with resin.

Seed fibres (cotton, coir (banana), kapok) It is well known that cotton is the most used seed fibre (figure 2.8(c)), as it is adopted for textiles anywhere in the world. Other types of seed fibres can be applied as stuffing materials, except for coir (the fibre of coconut husk). The latter is, in fact, very thick, coarse and durable and therefore applied in ropes, matting and brushes.

Natural-fibre based materials present also many problems and disadvantages. They, for instance, have usually low mechanical properties in terms of both stiffness and strength and especially regarding impact performances; their quality varies substantially according to unpredictable influences of weather, local environmental conditions, fibre type, processing approaches and so on; they easily absorb moisture, causing fibres to swell; costs fluctuate depending on harvest results and agricultural politics; maximum processing temperatures are limited; they generally have poor durability, even though this can be consistently improved by several types of fibres treatments; they have low fire resistance. Because of the generally low mechanical properties, natural-fibre composites have been mainly applied in secondary load bearing structures: in this sense, these materials have already found many industrial applications [59–62] like automotive interiors and non-critical packaging. Nevertheless, while originally bio-composites were mostly intended to be used in such applications with minor strength requirements, current environmental threat is making them attractive also in load-bearing applications [28]: natural

fibre-reinforced composites are gaining ground as promising materials also for aircrafts and spacecrafts [63] and therefore development of a deeper understanding of these materials is paramount. This is reflected in the increasing number of publications concerning natural fibres and natural-fibre composites characterization during the last couple of decades [64–74] including reviews [56, 75–81] and books [29, 82–86].

Vibration damping As introduced in previous paragraphs, one important reason why natural fibres have been so widely studied in the last decade is the intrinsically high vibration energy dissipation they offer compared to commercial materials, especially those traditionally utilized for composite structures and sandwich panels [22] (e.g., aluminium, Nomex, Kevlar, glass- or carbon-fibre reinforced composites). Duc *et al.* [66] studied mechanical and damping characteristics of unidirectional (UD) and twill 2x2 flax-fibre (FF) reinforced thermosets (epoxy) and thermoplastics (polypropylene (PP) and poly lactic acid (PLA)) composites. These were compared to carbon- (CF) and glass- (GF) fibre-reinforced epoxy composites. The Authors showed that the specific mechanical properties of the UD FF composite were comparable with those of the GF composite. Furthermore, dynamic mechanical analysis showed that FF composites present higher damping than the synthetic CF and GF: the addition of UD FF to epoxy resin brought a 100% increase in loss factor compared to the only matrix and the GF-epoxy composite and, among all composites investigated, FF/PP showed the highest damping at 25°C and 1 Hz. The Authors also found that the best compromise between stiffness and damping is given by FF/PLA composites. Kumar *et al.* [70] carried out an experimental study on free vibration performance of short sisal- and banana-fibre polyester composites. The impact of fibre length and weight percentage was analyzed and it was found that an increase in fibre content has a positive impact on both mechanical and damping properties. Prabhakaran *et al.* [87] performed an experimental study on the sound and vibration absorption of FF composites compared to GF composites. Once again, the superior acoustic absorption and vibration damping provided by the FF samples was confirmed. Similarly, Petrone *et al.* [88] performed experimental modal analysis on two sandwich panels with the same core but different materials for the composite skins—FF/polyethylene (PE) and GF/PP. The Authors estimated the vibration damping by using reverberation time measurements and found the FF/PE panel damping to be twice that of GF/PP samples within the entire frequency range examined. Rahman *et al.* [89] investigated the effect of fibre content and fibre orientation on the dynamic behaviour of FF/PP composites by using impulse hammer techniques. Natural frequencies and loss factors were evaluated from resonance peaks in the FRFs. The Authors showed that there are significant variations in both natural frequencies and loss factors depending on the fibre orientation. Composites with fibres at 45°, 60° and 90° showed to have approximately the same natural frequencies. Composites with differing fibre orientations exhibited different loss factors (generally lying in the range of $2-7\%$) for the various modes of vibration and the maximum loss factor was in case of fibres at 45°. Furthermore, it was shown that the loss factor decreases slightly by increasing fibre content. Longana *et al.* [90] also applied HiPerDiF

(high performance discontinuous fibre, [91]) architectures to produce high-performance hybrid composites with discontinuous FF and reclaimed CF with high levels of alignment. Those samples showed that both a reduction in percentage of CF and an increase in the FF content lead to higher vibration damping.
Outcomes of these studies experimentally demonstrated that FF-reinforced composites can be a commercially viable material for applications in which noise and vibration are significant issues and which require an important amount of damping.

2.4.1 Application of Natural-fibre Composites in Sandwich Panels

There have been many applications of natural-fibre based materials in the automotive industry, for both interior and exterior vehicle components. Indeed, they allow reduction in overall weight of the car and at the same time increase in its fuel efficiency and sustainability. Furthermore, for vibration and noise applications, the intrinsically high vibration damping of natural fibres can confer good damping performances to the entire structure. The use of natural materials in automotive applications is not a new idea: in the 1930s and 1940s, Henry Ford strongly advocated the use of natural materials, including hemp, producing reinforced soy resin composites in the manufacture of exterior body panels. If it had not been for the long material cure time and the difficulty in molding, Ford's idea for alternative materials may have been implemented [29, 92]. Only in the recent years, however, a significant number of multinational companies, such as Daimler Chrysler, Mercedes Benz and Toyota, have applied natural-fibre composites into their products and plan to further increase their use in future [92]. For example, Mercedes [80] used jute-based composites applied to the door panels of the E-class, banana-fibre composites for the A-class and other bio-composites for the S-class. The Araco Corporation in Japan presented the Grasshopper as a fully electric vehicle in 2003. This vehicle's body is entirely made from plant-based composites (mainly kenaf) [30]. Jaguar and Land Rover [93] developed a prototype car door from FF/PP and both reported that the natural-fibre component offers excellent performance compared to current parts: Land Rover's prototype is approximately 60% lighter than the equivalent steel part for the same stiffness, while Jaguar's is 35% lighter than a GF-filled PP component with same thickness.
Fundamental research on the use of natural fibre-based materials in primary load bearing applications has intensified in the last decade due to increasing demands for greater environmental protection. Many researchers showed that natural-fibre composites can offer comparable properties to conventional-fibre composites. Mallaiah *et al.* [94] compared the properties of bio-based and synthetic fibre based sandwich structures and demonstrated that a hybrid structure based on bamboo and GF offers higher values of core shear stress and face bending stress than structures manufactured from either pure glass or bamboo fibres. Rao *et al.* [95] conducted a linear elastic finite element analysis on a hollow core sandwich structure manufactured from a sisal fibre composite. They found that the specific shear strength of the core is more than twice that associated with an unreinforced PP core. Rao *et al.* [96] used both experimental tests

and numerical modelling techniques to characterise the bond strength and energy absorption capabilities of recyclable sandwich panels made from sawdust PP composites. Hao *et al.* [97] explored the compression behavior of eco-friendly natural fibre-based isogrid lattice cylinders made of pineapple leaf fibres and phenol formaldehyde resin matrix. Results showed that the most important factor influencing special load and stiffness is the number of circumference divisions and indicated that the lattice cylinder can be treated as a truss core combined with skins to manufacture a hierarchical sandwich structure with the potential to be used as structural component in buildings. Petrone *et al.* [27] studied natural-fibre cores based on FF and PE matrix composites. By performing experimental modal analyses, the Authors found that the modal damping of the unreinforced core is higher than that of fibre-reinforced cores, suggesting that in this case the main influence on damping may be due to the viscoelastic properties of the matrix. However, a core made of only resin presents poor mechanical properties: the Authors measured 100% higher mechanical properties and 40% lower damping when reinforcing the resin with FF. A solution to reduce this gap was presented, that is filling the cores with wool fibres: this results in minimal weight increase and unchanged mechanical properties and brings higher acoustic absorption properties and damping. Zuhri *et al.* [98] investigated numerically and experimentally the out-of-plane compression characteristics of square and triangular lattices based on FF-reinforced PP and PLA polymers. They were manufactured using a simple slotting technique and were tested in compression mode at quasi-static rates of strain. The Authors found that the PP structures offer much higher strength and energy-absorbing characteristics than the PLA cores. Furthermore, compression strength and energy-absorption characteristics of the square-cell cores are significantly higher than those of their triangular counterparts. Stocchi *et al.* [99] explored a core made of a natural-fibre reinforced composite consisting of vinyl ester (VE) matrix reinforced with jute fabric. Experimental tests were conducted to characterize the elastic response of the cores under quasi-static flatwise compression and showed that the failure mechanisms were yarn pull-out and fibre breaking: the large thickness of the walls of this core inhibited buckling. When compared in terms of the specific strengths, the jute/VE cores showed similar performances to commercially available counterparts, suggesting that jute-reinforced cores have the potential as alternative to standard cores in static load bearing applications.

2.5 Viscoelastic inserts in sandwich panels

Viscoelastic inserts for passive vibration damping have been widely and successfully evaluated in open literature [100]. Passive damping mechanisms (defined in section 2.3) have been dominant in the non-commercial aerospace industry since the early 1960s. However, the use of surface damping treatments in the automotive, commercial airplane and other industries has only been possible during the last couple of decades thanks to advancements in cost-effective manufacturing processes suitable to high-volume production [23]. Clearly, these types of passive damping devices and treatments are recommended for structural components that do not carry primary loads:

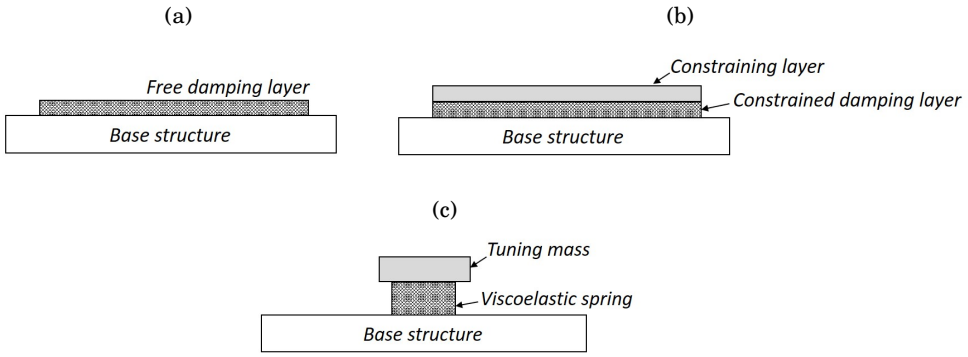

FIGURE 2.9. Schematic representation of Passive Vibration Damping Mechanisms. (a) Free-Layer Damping, (b) Constrained-Layer Damping and (c) Tuned Viscoelastic Damper.

for load carrying members, the design must always first accomplish strength and stiffness requirements over damping benefits.

Several ways are available to exploit viscoelastic materials for energy absorption purposes [101]. Some of the most studied and traditionally applied methods are based on free-layer damping (FLD), constrained-layer damping (CLD) and tuned viscoelastic damping (TVD) technologies—figure 2.9.

In FLD devices (figure 2.9(a)), a portion of a structure is covered by a damping material which can either be sprayed or bonded by means of an adhesive. As the system deflects in bending, the viscoelastic layer deforms mostly in extension and compression and, hence, the resulting hysteresis loop of cyclic stress and strain dissipates mechanical energy. Kerwin [102] and Ross [103] firstly performed vibration analyses of a beam with an FLD layer and found that the system's loss factor increases with thickness, storage modulus and loss factor of the viscoelastic layer. They also showed that, for full coverage of the layer, damping performances do not depend on the mode of vibration. Nevertheless, it is possible to optimize a partial coverage for one or more modes [104–106].

In a CLD device (figure 2.9(b)), the viscoelastic material (e.g., a damping tape) is forced to deform in shear, as the base structure undergoes bending vibrations, due to the presence of the stiff upper layer (e.g., a thin metal foil). The CLD design is more effective than the FLD since more energy is dissipated into heat by the shearing forces acting within the viscoelastic layer. The symmetric configuration—in which base and constraining layer have equal thickness and stiffness—is the most effective design as in this case shear deformation in the core layer is maximum. CLDs have been widely studied by Scarpa and Tomlinson [107], who evaluated the deposition of damping material with the aim of providing maximum damping at the frequency of excitation and temperature of the operating environment. Ghiringhelli *et al.* [14] applied a concept similar to CLDs to metal–polymer–metal sandwich configurations which can be applied to structural elements in aircrafts for enhanced damping performances. In this study, different

numbers of layers and types of structural materials (e.g. aluminum alloy and carbon composites) were considered, whereas only styrene–butadiene rubber was adopted for the viscoelastic layer. The Authors experimentally demonstrated that this solution is particularly effective to improve dynamic and acoustic performances of thin and moderately thick panels (i.e., panels prone to bending vibration transmission). In particular, multiple stacking has been shown to produce higher damping than a single, equivalent layer of viscoelastic material. Weight penalties are, on the other hand, unavoidable, as well as the decrease of bending stiffness properties.

TVD devices (figure 2.9(c)) are usually applied to reduce vibration/noise associated with a single frequency or a narrow band of frequencies. If properly tuned, they eliminate an unwanted resonance by splitting the original peak into two, one below and one above the initial resonance frequency, and by decreasing displacement amplitudes thanks to the addition of damping. TVDs are effective when located at points of highest displacements (anti-nodes). A controlling factor in the design of these devices is the operating temperature range: the TVD should operate far from the glass transition region of the viscoelastic material as here, although damping is high, the stiffness changes rapidly with temperature. This means that any temperature changes caused by internal heating due to energy dissipation alters the dynamic stiffness significantly and may cause the TVD to detune. In fact, the best region to use elastomeric materials for TVDs is the rubbery region, where small changes in temperature do not have important effects on the stiffness.

In recent years, however, researchers have studied and developed several other concepts of viscoelastic inserts for passive vibration damping, especially for composite laminates and as insertions in sandwich panels. For instance, Bhattacharya *et al.* [108] explored the effect on vibration damping of the shape of viscoelastic inserts embedded within laminated composite beams. Boucher *et al.* [15] showed that partial filling of honeycomb cores with damping material is more efficient than their complete filling in terms of damping performances and density characteristics. A rise up to 45% in damping-to-mass ratio was demonstrated using specific optimal insert designs. Agnese and Scarpa [109] performed a numerical and experimental study of star-shaped biphase composites cells and demonstrated that non-conventional inclusions in a low-stiffness-ratio biphase composite structure can dissipate higher level of strain energy than composites with classical cylindrical inclusions. Aumjaud *et al.* [110] performed a comparative numerical study between CLD devices and Double Shear Lap-Joint (DSLJ) dampers, which are embedded within structures. It was shown that DSLJs are more efficient than CLD structures for cantilevered beams and plates and are comparable in terms of performance when operate in simply supported beams and plates. Scarpa *et al.* [21] and Rajasekaran *et al.* [111] showed that, in sandwich core lattices, the junction corners between walls are optimal locations to embed elastomeric insertions to make the best use of the energy absorption capabilities they provide (figure 2.10): by placing the inserts in these specific positions, there is a potential increase in the vibration damping capabilities of the entire structure.

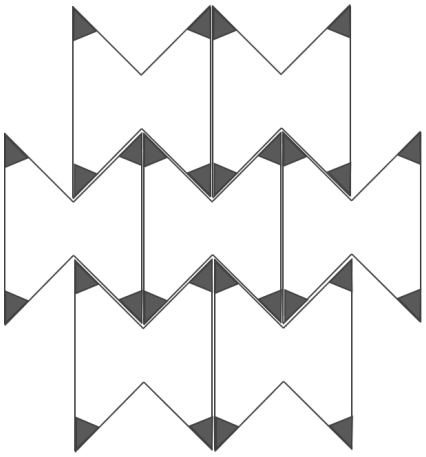

FIGURE 2.10. Inclusion of viscoelastic inserts at the walls junction areas of a cellular auxetic core structure.

2.6 CNT-resins and vibration damping

Since they were first discovered in 1991 [112], carbon nanotubes (CNTs) have been extensively studied in open literature due to the many interesting properties they possess. From a mechanical standpoint, their elastic modulus is of the order of magnitude of 1 TPa [34], which is higher than any materials' elastic modulus [113]. Furthermore, the electric current carrying capacity of CNTs is of the order of $10^{11} - 10^{12}$ A/cm^2, substantially higher than any values typically found for known conductive materials [114]. Researchers have been exploring many ways for exploiting the superlative properties of CNTs in both macroscopic and microscopic applications. For instance, they have been widely studying CNT-based composites, where they take advantage of the CNTs conductivity and high aspect ratio to generate highly conductive plastics [115]. Similarly, their massive thermal conductivity can also be used to generate thermally conductive composites [116]. Regardless, probably the most promising area of research involves the mechanical enhancement of plastics by adding CNTs as reinforcing fillers. By including 0.1% of CNTs to epoxy resin, Xu *et al.* [117] obtained a 20% increase in its elastic modulus. Allaoui *et al.* [118] obtained a 100% rise in elastic modulus by adding 1.0% CNTs to epoxy resin. Other than the elastic modulus, also other mechanical properties such as strength and toughness have been demonstrated [119] to increase by adding CNTs [120].

Nonetheless, there are many problems related to the use of CNTs and issues which prevent to realize their full potential. Firstly, their characteristic small size represents a fundamental difficulty from a practical point of view: it is, for example, extremely challenging to control their manipulation (placement, movement, welding, etc.). Furthermore, in composites applications, CNT-matrix adhesion and CNT dispersion in the matrix represent big challenges which limit their potential: CNT pullout from matrix material has been widely experimentally observed and reported in open literature [121]. Moreover, CNTs have a tendency to adhere to each other and

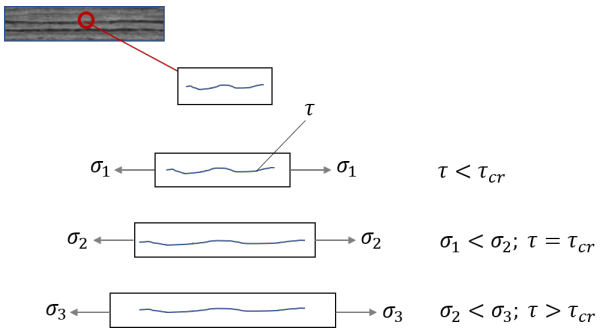

FIGURE 2.11. The schematic of "stick-slip" mechanism acting between CNTs and matrix in a CNT-composite.

agglomerating, hence making very hard to obtain a composite with uniform dispersion [34]. Thus, the Young's modulus of the final CNT composite can easily not be as enhanced as expected.
Another fundamental mechanical property of CNTs is the structural damping they provide in CNT composites, which brings the interesting possibility of exploiting CNTs for passive vibration control applications. By adding multi-walled nanotubes (MWNTs) to epoxy resin, Koratkar *et al.* [122] observed up to 200% increase in damping and 30% increase in the baseline bending stiffness with minimal increase in structural weight. Likewise, Rajoria and Jalili [123] showed experimentally a 140% rise in damping ratio by dispersing single-walled nanotubes (SWNTs) in epoxy resin. Zhou *et al.* [124] introduced the idea of the interfacial "stick-slip" energy dissipation mechanism acting between CNTs and matrix, thus causing vibration energy dissipation, by adopting a micro-mechanical approach and modelling analytically a four-phase composite system made of resin, voids and randomly oriented bonded and debonded CNTs. The stick-slip mechanism can dissipate energy on the micro-scale due to poor adhesion between CNTs and surrounding polymer matrix. This mechanism is well described in [34]. Under the action of normal tensile stress σ, a CNT-composite elongates and the matrix applies shear stress τ on the nanotube, thus causing load transfer—figure 2.11. As a consequence, normal strain appears in the CNT and it starts elongating. If the applied stress σ is small, the CNT stay bonded to the matrix and they deform together as the strains are equal in both phases (sticking phase). However, if the applied σ increases, the shear stress on the nanotube increases accordingly, hence resulting in a bigger elongation of matrix and CNT. There is a certain value of τ (known as critical shear stress, τ_{cr}), at which the CNT debonds from the matrix: as the shear stress increases over τ_{cr}, the matrix basically "flows" over the CNT's surface. The strain in the nanotube stays constant at its maximum value, whereas the strain in the matrix increases (slipping phase). At this stage, there is no load transfer happening between matrix and CNTs. Instead, energy dissipation happens at the micro-scale due to this slippage phenomenon, hence causing damping in the system. Rajoria and Jalili [34] performed structural vibration tests on CNT-epoxy sandwich steel beams to characterize stiffness and damping properties. They in particular analyzed the effects of factors such as CNT proportion, CNT type and frequency dependence on these properties and

found that the storage modulus of epoxy is not fundamentally impacted by the addition of CNTs, whereas the loss modulus can be affected. By including 5.0 wt% (weight percentage) MWNTs to epoxy, up to 700% increase in damping ratio was found. By analyzing the forced vibration tests results, it was found that, in general, higher damping occurs at higher modes of vibration.

2.7 Sandwich core topology: rectangular lattices

As introduced in Chapter 1, the topology of the sandwich panel core that has been adopted in this thesis is a square-cell rectangular one. One important reason for such choice is that it is a simple geometry, relatively easy to manufacture and therefore ideal for exploring novel classes of materials as core platforms. Apart from this practical motivation, the mechanical performance of the rectangular or square-cell topology (especially in terms of out-of-plane (OOP) and the response to impact properties) has been widely reported in open literature and it has been shown that high-density rectangular lattices are preferable to hexagonal configurations for shock loads as they combine resistance to crushing and energy absorption with in-plane (IP) stretching strength. Dharmasena *et al.* [125] showed that square lattice honeycombs exhibit strengths that are 27% higher than triangular ones. Xue and Hutchinson [24] performed a comparative study of metal sandwich plates under blast loads. The sandwich panels considered in that paper included three different types of cores: a folded plate, a pyramidal truss and a square-cell honeycomb. The results were compared against those from monolithic beams of equal mass by using 3D finite element simulations. Xue and Hutchinson not only demonstrated that the sandwich panels can sustain larger blast loads than an equivalent solid plate with equal weight, but they also showed that the square honeycomb and folded plate topologies outperform the truss core one. Fleck and Deshpande [25] developed an analytical procedure to analyze the dynamic response of metallic sandwich beams subject to air and water blasts by including fluid-structure interaction effects. The Authors presented performance charts for a wide range of core topologies. In both load cases and for the same mass of the sandwich beams, square-cell honeycombs show better performances than the hexagonal cores. Xue and Hutchinson [126] developed and proposed a continuum constitutive model for square honeycomb cores, which is able to represent the structure under multi-axial stressing conditions. Rathbun *et al.* [127] presented an experimental and numerical study on stainless steel sandwich panels with square honeycomb cores and solid monolithic beams of equivalent weight under impulses representing those associated with nearby explosions/shocks. They proved that the sandwich structure responds with smaller displacements than the solid beam, particularly at low impulses. Côté *et al.* [26] carried out an analytical and experimental analysis of stainless steel square-cell honeycomb cores manufactured by interlocking steel strips and by brazing the final assembly. OOP compressive tests showed that the peak strength is fairly insensitive to the ratio between core height and cell width and to the presence of face skins when the relative densities of the core are lower than 0.2. Hayes *et al.* [128] performed an experimental characterization of IP and OOP compressive behavior and energy absorption under quasi-static

and dynamic loads of extruded square-cell honeycomb cores with 0.25 relative density. In that case the cores were made of maraging steel and were obtained via a novel process based on the extrusion of oxide powders, followed by reduction in hydrogen.
All things considered, high-density rectangular lattices are preferable to hexagonal configurations for shock loads as they combine resistance to crushing and energy absorption with IP stretching strength. Rectangular lattices are also relatively easy to manufacture and this makes such configuration ideal to experiment novel classes of materials as core platforms.

2.8 Conclusions

Sandwich panels have been widely used in the last century as primary and secondary load bearing structures. Their exceptionally good mechanical performances come, however, with very poor vibration and acoustics properties. With the goal of designing structures that are both mechanically and vibro-acoustically efficient, damping materials, novel cell topologies, viscoelastic, poroelastic and auxetic insertions, multilayered cores, Helmholtz resonators and many other solutions are currently being investigated in open literature.
Natural-fibre based composites represent one promising alternative to traditionally adopted materials for sandwich panels' core walls and skins: other than contributing to vibration energy dissipation, they represent an environmentally friendly solution which is also associated with low costs and reduced weights and is therefore attractive to many industrial sectors. For these reasons, a flax-fibre based composite is adopted as material for skins and core walls of the novel sandwich panel developed in this thesis.
On the other hand, viscoelastic inserts and CNT-reinforced resins constitute potential solutions to vibration damping absorption issues and can therefore be employed in sandwich panels to improve their vibration and acoustic performances: a CNT-reinforced resin is, in fact, adopted as material constituting viscoelastic inserts embedded within the novel natural fibre-based sandwich panel.
A fundamental point in this thesis is experimenting novel classes of materials as core platforms for sandwich panels, in order to produce a structure which is efficient from the vibroacoustic point of view and, at the same time, provides structural integrity. In this sense, rectangular lattices are preferable to hexagonal configurations as they not only combine resistance to crushing and energy absorption with in-plane stretching strength, but are also relatively easy to manufacture. A square-cell lattice is therefore chosen as topology for the core of the sandwich panel developed in this thesis.

Next chapter introduces methodologies and procedures utilized for the mechanical, thermo-mechanical, thermal and rheological characterization of the materials adopted for the novel sandwich panel.

CHAPTER 3

CHARACTERIZATION OF MATERIALS: METHODS

Contents

3.1 Introduction

THIS chapter presents comprehensive descriptions of methodologies, techniques and procedures for the mechanical, thermal, thermo-mechanical and rheological characterization of the materials adopted for the novel natural-fibre sandwich panel with CNT-inserts. The first section presents the materials and describes manufacturing/curing techniques. The second section focuses on the mechanical characterization (i.e. tensile and three-point-bending tests) from which the elastic properties of the materials are retrieved. Finally, last section presents

the methodologies adopted for thermal, thermo-mechanical and rheological characterization (i.e. Thermal Gravimetric Analysis, Differential Scanning Calorimetry, Dynamic Mechanical Analysis and Rheological tests). For the sake of clarity, results of the tests described in this chapter will be presented separately in Chapter 4.

3.2 Materials and manufacturing methodology

3.2.1 Evopreg PFC-flax natural-fibre composite for core walls and skins

The material adopted in this work for skins and core walls of the sandwich panel is a natural-fibre composite made of flax fibres in poly (furfuryl alcohol) resin (PFA). Specifically, the composite material is a prepreg provided by Composites Evolution Ltd, UK: Evopreg PFC-flax, Biotex flax 400 g/m^2 with fibres arranged in a balanced 2x2 twill fabric.
The Evopreg PFC-flax is chosen amongst other similar composites with the goal of obtaining high-performance bio-based composite laminates ensuring good mechanical properties along with their intrinsically high vibration damping. In particular, the reason behind the choice of flax fibres—amongst other types of natural fibres—lies in the fact that they provide the highest mechanical properties [129] and, due to their high specific stiffness and strength, have widely replaced glass fibres in many industrial applications.
On the other hand, PFA resin is a relatively new introduction for composites products and mainly used during the last decade as a matrix in natural-fibre composites [64, 65]. Indeed, PFA is a bio-based resin made from crop waste and therefore, used together with natural-fibre reinforcements, constitutes a 100% bio-composite. Its polymerization is mediated by acid catalysts or temperature and yield a hard, rigid and highly cross-linked macromolecular structure with uniquely high temperature properties. This makes PFA a high-performance thermoset resin with notable fire-resistant properties and gives it the ample potential to be used as alternative to non-renewable resource based resinous products demanding durability and structural strength such as epoxy and phenol [64, 130].

Lamination and curing Initial investigations on the curing process of the composite are performed starting from the recommendations provided by the supplier. The suggested curing techniques are standard methods such as vacuum bag/oven, autoclave and press moulding. The recommended ramp rate is $1 \div 3\,^{\circ}$C/min and the advised pressure 3.5 bar. The cycle is characterized by a first dwell at 80 °C for 30 minutes and a second, longer one at the PFA curing temperature, 140 °C, for 45 minutes. Therefore, initial lamination and curing attempts are made according to these parameters by using vacuum-bag/autoclave techniques. Some tries are also made by using a hot-press since it does not necessarily require a vacuum bag and hence could be a more practical solution for the composite curing. However, as it is shown in Appendix A, laminates prepared with this technique present poor quality mechanical properties. For this reason, laminates are

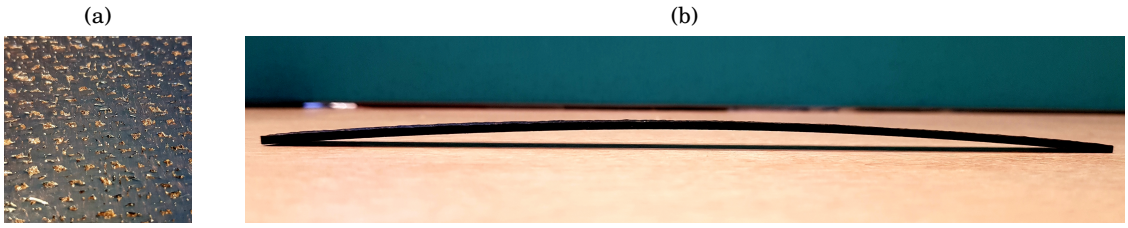

FIGURE 3.1. Cured laminates, initial investigations: (a) high void content and (b) bending effects due to poor compaction levels.

cured with vacuum-bag/autoclave techniques, as this is the procedure amongst the available options which ensures highest quality for the flax-PFA final plates.

At the stage of initial investigations, several technical challenges are encountered. The main difficulty experienced is the poor compaction level achieved with the cycle recommended by the supplier due to the high porosity of the natural fibres, as shown in figure 3.1(a). As a consequence, the first laminates manufactured show very pronounced out-of-plane bending – figure 3.1(b). This is substantially improved by paying specific attention to the pre-compaction of the lay-up: every one, two and four plies both a manual roll and vacuum are employed to increase compaction levels by allowing air release from the prepreg plies. Moreover, an aluminium plate is placed on the laminate upper face to favour the application of uniform pressure and improve even further the levels of surface finishing and compaction.
Additionally, the supplier's recommended curing cycle is modified via a trial and error process until high levels of compaction and statistically reliable mechanical properties are achieved. The final curing cycle is: heat rate of 0.5°C/min, 110-minute dwell at 80°C, 95-minute dwell at 140°C and pressure of 6.9 bar. Figure 3.2 shows the definitive autoclave curing cycle compared to the recommended.
A second, main issue that is encountered regards the flatness of the final plate. Figures 3.3(a) and 3.3(b) show initial manufacturing attempts. Here, the cured plates, of two and three plies respectively, show evident twisting and bending. This phenomenon is probably related to any deviation of the fibres from the 0/90° orientation and properties variations from ply to ply: a non-perfect allignment of the natural fibres causes warpage in directions other than longitudinal and transverse and the cured laminate stabilises in the state of minimum potential energy. Another factor most likely contributing to the plates distortion is the resin shrinkage during curing, aggravated by moisture loss associated with both the PFA and the flax. In a typical curing profile, the uncured resin is in a liquid form during the heating ramp, expanding thermally as the temperature increases. At the isothermal dwell, however, polymerisation occurs: chemical crosslinks cause volumetric shrinkage which is then followed by a thermal contraction of the resin as the solid composite is cooled to room temperature. During this last stage, residual internal stress builds in the material leading to issues such as warpage of the final composite laminate [131]. Due to the high levels of crimp and irregularities of the flax fibres woven

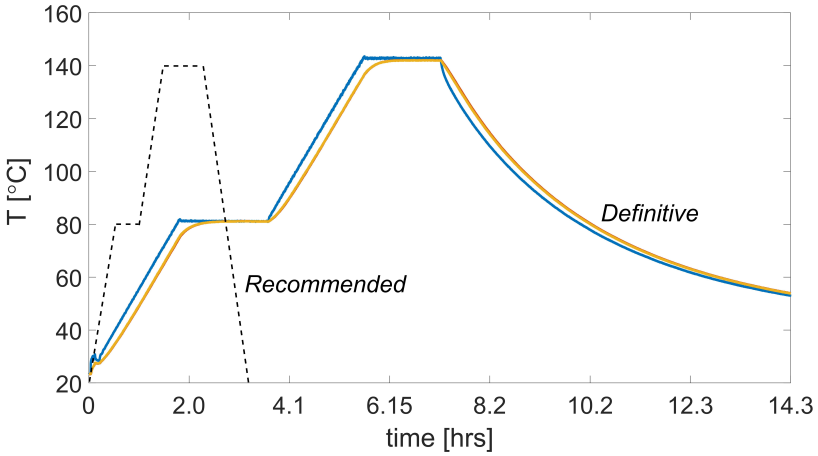

FIGURE 3.2. Autoclave curing process: final temperature cycle (solid line) at 6.9 bar pressure versus temperature cycle recommended by the supplier (dotted line) at 3.5 bar. Blue curves: nominal temperature. Orange and yellow curves: temperature measured by the thermocouples.

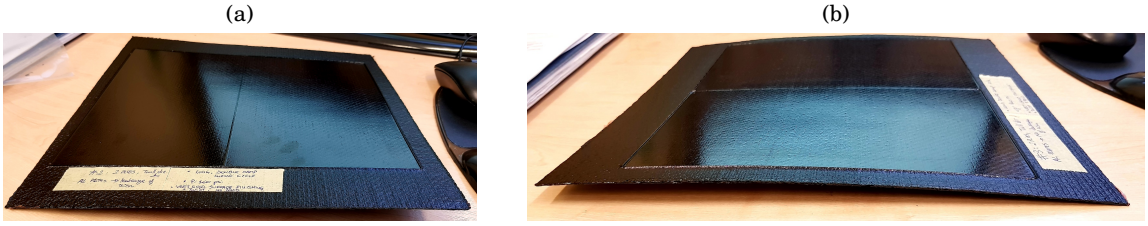

FIGURE 3.3. Cured laminates, initial investigations: (a) two- and (b) three-ply laminates.

architecture, the fabric is unable to resist any distortion due to the resin shrinkage. This may result in differences on top and bottom faces of the laminate in terms of thermal stresses, resin content and, therefore, overall flatness.

The effect of such distortions on the flatness of the laminate is minimised by making a symmetric and balanced sequence. As each layer contains fibres both at 0° and 90°, the only characteristic direction that can be used as a reference for the stacking sequence is the twill-fabric orientation, that is the 45° diagonal orientation of weave cross-overs—figure 3.4(a): plies are stuck in a symmetric and balanced sequence taking as reference the twill direction, thus minimising any distortion due to properties variations and fibres alignment irregularities from ply to ply. Furthermore, to account for possible through-the-thickness unevenness within each ply, two plies are placed with the front side upwards and two with the back side upwards, symmetrically with respect to the middle plane—figure 3.4(b). Consequently to these observations, the final stacking

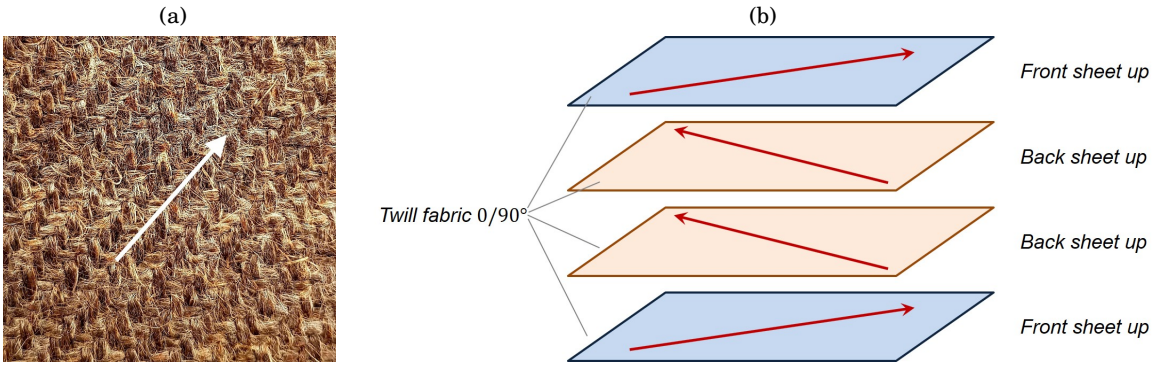

FIGURE 3.4. (a) Uncured Evopreg PFC-flax and (b) lamination stacking sequence. Arrows indicate the twill direction.

sequence must include a minimum of four plies to achieve a flat configuration. A four-layer laminate has a thickness of 2.3 mm (0.05 mm standard deviation).

Figure 3.5 shows a schematic representation of a composite lay-up and vacuum bag tooling. Following, the lamination procedure of a four-layer laminate is described step by step:

- The plies are cut from the prepreg roll, figure 3.6(a);
- Vacuum is applied to each ply for 15 minutes, figure 3.6(b);
- The plies are laid up two at a time; compaction levels are further improved by applying pressure manually by means of a roll – figure 3.6(c)—and employing vacuum for 15 minutes;
- The two laminates are laid-up to form the final laminate of 4 plies according to the stacking sequence presented in figure 3.4(b); once again, manual compaction first and vacuum then are applied, this time for a longer period of time (30 minutes);
- The pre-compacted laminate is prepared for the autoclave process: it is positioned in the middle of a tool plate on release film and its edges are surrounded by cork to prevent resin leakage during curing. The cork is perfectly aligned to the laminate, as it defines its final shape. More layers of release film separate the laminate and the aluminium plate, which has same dimensions as the plies. A layer of breather cloth covers the entire plate, vacuum valves are positioned at its corners and tacky tape is applied along the edges as a sealant for the bagging film – figure 3.6(d);
- Vacuum is applied through the valves: once verified with a pressure gauge that a pressure of at least −28 mmHg is reached (figure 3.6(e)), thermocouples are applied on top of the bag to monitor the temperature cycle and the layup is ready for the autoclave process.

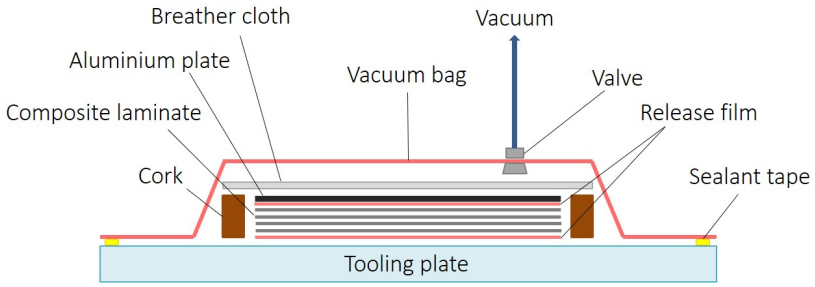

FIGURE 3.5. Simplified representation of composite lay-up and vacuum-bag tooling. Release film provides easy release between two layers; the aluminium plate is used for better surface finishing and uniform pressure; breather cloth allows air permeability; the vacuum bag applies vacuum pressure over the entire laminate; cork prevents the resin to flow from the edges; sealant tape is used to seal the bag to the tooling plate; valves connect the pumps to apply the vacuum.

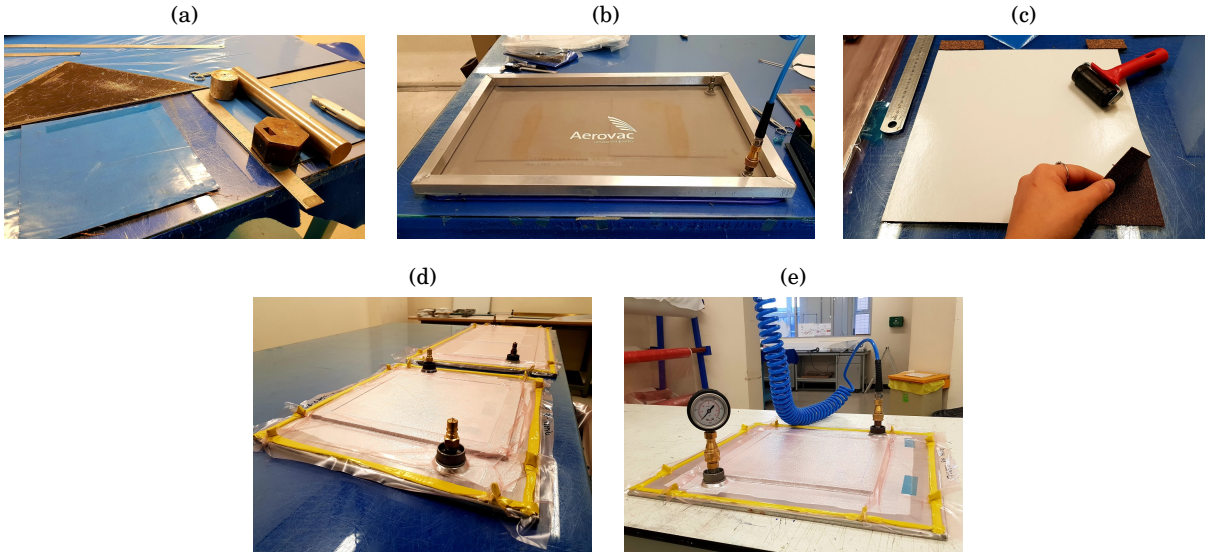

FIGURE 3.6. Flax/PFA composite lay-up process. (a) Plies are manually cut from the prepreg roll. (b) Vacuum is applied to each ply. (c) Plies are laid up two by two and vacuum is applied to each pair. All the plies are then stuck in sequence and vacuum is applied once again. (d) After applying layers of release film, breather cloth and bag film, the bag is sealed and vacuum is applied by means of specific valves. (e) Vacuum pressure is verified to reach -28 mmHg by means of a pressure gauge.

3.2.2 CNT-resin for viscoelastic inserts

The resin adopted for the viscoelastic inserts of the sandwich panel is obtained by mixing Nanocyl SA EPOCYL^{TM} 128 – 06 with Super Sap CLV Epoxy Bio-Resin (SS CLV - Entropy Resins, Gugeon Brothers Inc, MI). EPOCYL^{TM} 128 – 06 is a masterbatch of Bisphenol-A (Bis-A) epoxy resin

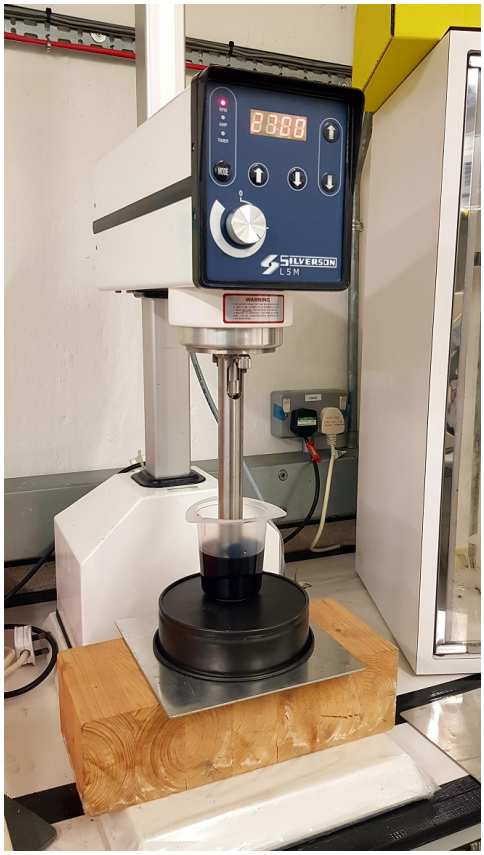

FIGURE 3.7. Mixing of EPOCYL 128-06 CNT paste with SS CLV Epoxy Bio-resin by means of Silverson's high shear rotor/stator laboratory mixer at 50 rpm.

with high concentrations of multi-walled CNTs (MWNTs). SS CLV provides a clear, low-viscosity bio-derived epoxy system, suitable to the present application. The EPOCYL paste is diluted into the SS CLV resin according to a dilution factor of 6, which is that recommended by the supplier (1 unit volume of solute, 5 unit volumes of solvent). Mixing is performed by Silverson's high shear rotor/stator laboratory mixer at 50 rpm speed (figure 3.7) and the heat generated in the stirring process favors the homogeneity of the resin. The concentration of CNTs in the final resin is 0.477 wt%.
Finally, all pristine and CNT-resin samples are cured at room temperature in 24 hours.

3.3 Mechanical characterization

Following sections describe the methodologies adopted for the mechanical characterization of materials, which is performed in order to retrieve their elastic properties. Indeed, these are fundamental values to measure when studying any material, and are particularly relevant to our purposes since they will be used in Chapters 5 and 6 to implement numerical models of the sandwich panels.

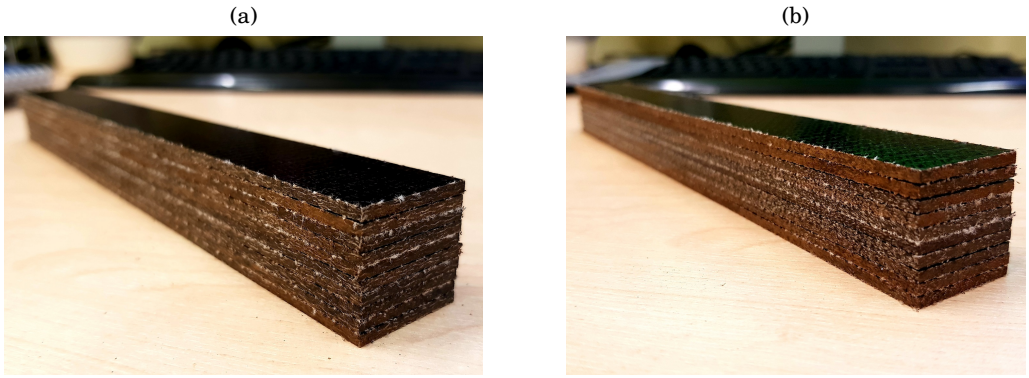

FIGURE 3.8. Evopreg PFC-flax specimens for tensile characterization with fibre orientation at (a) 0/90° and (b) ±45°.

3.3.1 Tensile testing

Experimental tensile tests allow to directly measure ultimate tensile strength, failure strength, maximum elongation and reduction in area, from which it is possible to determine Young's modulus, Poisson's ratio and yield strength [132]. Tests are performed on the materials presented in sections 3.2.1 and 3.2.2, respectively the flax-PFA composite—Evopreg PFC-flax—and the CNT-reinforced SS CLV Epoxy Bio-resin. The pristine SS CLV resin is also tested, in order to quantify the effect of the CNTs on the resin mechanical properties. All tensile tests and data processing are performed according to ASTM standards by means of a Shimadzu UK Limited long-stroke tensile testing system with 10 kN load cell. All data is processed in MATLAB R2018a environment and undergoes the Chauvenet criterion [133] to identify outliers to exclude from the determination of the statistical mechanical properties.
Since tensile characterization tests of the Evopreg PFC-flax and the SS CLV-Epoxy Bio-resin follow different ASTM standards, following sections present separately the respective methodologies.

3.3.1.1 Evopreg PFC-flax

Tensile tests on the Evopreg PFC-flax composite are performed according to the ASTM D3039 / D3039M-17 (Standard Test Method for Tensile Properties of Polymer Matrix Composite Materials) on batches of samples with fabric orientation 0/90° and ±45°. Specimens have rectangular shape with thickness 2.3 mm, width 25 mm and height 250 mm—figure 3.8. It should be explicitly noticed that albeit the standard suggests 2.5 mm thick samples, 2.3 mm (four plies) is the closest value achievable in the present case: four plies, indeed, correspond to the closest thickness to that required by ASTM while guaranteeing symmetry and balance requirements—section 3.2.1. Specimens are cut from composite laminates by means of a diamond blade. Ten specimens for each fibre orientation configuration batch are tested.
Figure 3.9(b) shows the experimental setup for tensile testing. The testing machine's cross-bar

(a) (b)

FIGURE 3.9. (a) Evopreg PFC-flax tensile characterization setup. (b) Detail on one tested sample of the marked points for strain measurement. Shimadzu testing machine with a 10 kN load cell—Digital Image Correlation (DIC) Video Gauge^{TM}.

displacement rate is 2 mm/min as for ASTM standards. Emery cloth is used for gripping the samples as a practical substitute to end tabs. Longitudinal and transverse strains are measured by Imetrum Limited's video-gauge—Digital Image Correlation (DIC) Video Gauge^{TM} software using a 3D Precision Displacement Tracker.

The strain range in which the material has elastic behaviour—and therefore used for the calculation of the Young's Modulus—is $\epsilon \in [0.1 \div 0.3]\%$ as for ASTM standards. The strain ϵ evaluated here is the engineering nominal strain, $\epsilon = \Delta L/L_0$, being L_0 the gauge length and ΔL the displacement increment. On the other hand, the stress σ is the engineering stress given by the ratio between the applied force and the initial section area. The Poisson's ratio is also evaluated according to the procedure indicated in the ASTM standard, that is from the linear regressions of transverse and longitudinal strains in the linear range. The Poisson's ratio is effectively determined as minus the ratio of the delta transverse strains and the delta longitudinal strains at the extreme values of the regression lines. These are found by evaluating a first linear relation, $y = b_1 x$, where b_1 is the slope or regression coefficient evaluated from the data. The fit is then improved by including a y-intercept b_0 as $y = b_0 + b_1 x$. To find the better fit, the coefficient of determination is evaluated: R^2 is one measure of how well a model can predict the data, and falls between 0 and 1. It is calculated from the ratio between the residual sum of squares and the total sum of squares. The higher the value of R^2, the better the model is at predicting the data. Figure 3.10 shows examples of longitudinal and transverse strain curves in the linear elastic range. First strains regression lines are indicated as "Slope". The fit is then improved by including a y-intercept, indicated as "Slope & Intercept".

The in-plane shear modulus is evaluated according to the ASTM D3518 / D3518M standard

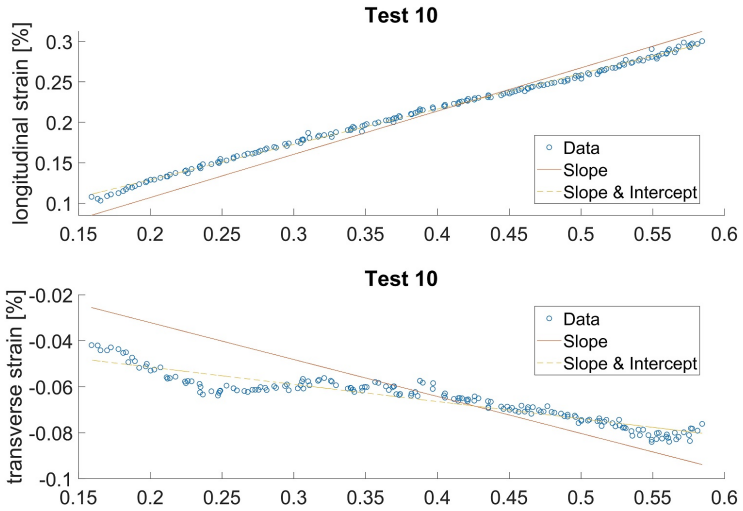

FIGURE 3.10. Example of regression lines for longitudinal and transverse strains measured in a tensile test on Evopreg PFC-flax with fibre orientation 0/90°.

(Standard Test Method for In-Plane Shear Response of Polymer Matrix Composite Materials by Tensile Test of a ±45° Laminate) by post-processing stress and longitudinal and transverse strains from tensile tests on samples with fabric orientation at ±45° degrees. Explicitly, it is evaluated as the Chord Shear Modulus of Elasticity:

$$G_{12}^{\text{chord}} = \frac{\Delta\tau_{12}}{\Delta\gamma_{12}} \tag{3.1}$$

applied over a 4000 $\mu\epsilon$ engineering shear strain range, starting with the lower strain point at 1500 $\mu\epsilon$. Indeed, this range corresponds approximately to the normal strain range of 1000 to 3000 $\mu\epsilon$ used to calculate the tensile chord modulus of elasticity in Test Method D3039/D3039M. $\Delta\tau_{12}$ is the difference in applied engineering shear stress between the two shear strain points and $\Delta\gamma_{12}$ the difference between the two engineering shear strain points (nominally 0.004). The shear stress at any required data point is calculated as:

$$\tau_{12_i} = \frac{P_i}{2A}, \tag{3.2}$$

where P_i is the force at i-th data point and A the initial cross-section area. The engineering shear strain at each required data point is evaluated as:

$$\gamma_{12_i} = \epsilon_{X_i} - \epsilon_{Y_i}, \tag{3.3}$$

where ϵ_{X_i} and ϵ_{Y_i} are the longitudinal and transverse normal strains at i-th data point, respectively.

3.3.1.2 Pristine and CNT-resin

Tensile tests on pristine and CNT-reinforced SS CLV Epoxy Bio-resin are performed according to the ASTM Standard D638-14 (Test Method for Tensile Properties of Plastics). The dog-bone-shaped specimens are made by curing at room temperature in a dedicated silicone mould—figure 3.11(a). Some preliminary tests on tabbed samples show that end tabs are not required for these specimens and, therefore, are not applied on the samples for the actual tests. Six specimens are prepared and tested for each of the two resins. The testing machine's cross-bar displacement rate is 5 mm/min. No emery cloth or end tabs are used for gripping the samples, as no evident slippage happens between the dog-bone specimens' ends and the grips. The elastic behaviour strain range is $\epsilon \in [0.1 \div 0.3]\%$ as for the standards. Similarly to the tests on the Evopreg PFC-flax, the strain ϵ considered here is the engineering nominal strain, $\epsilon = \Delta L/L_0$, being L_0 the gauge length and ΔL the displacements increment. Once again, the stress σ is the engineering stress, that is the ratio between the applied force and the initial section area.
For the two resins, only tensile characteristics are evaluated (i.e. the Young's Modulus, Tensile Strength and Elongation).

For quality control, the experimental values are then compared to analytic predictions according to the model of Halpin and Tsai [134, 135] with Thostenson's correction [136]. For random orientation of the CNTs, the Young's Modulus of the composite material can be expressed as following:

$$\frac{E}{E_{pristine}} = \frac{3}{8}\left[\frac{1+\zeta\eta_L V_{NT}}{1-\eta_L V_{NT}}\right] + \frac{5}{8}\left[\frac{1+2\eta_T V_{NT}}{1-\eta_T V_{NT}}\right] \tag{3.4}$$

where:

$$\eta_L = \frac{E_{eff}/E_{pristine} - 1}{E_{eff}/E_{pristine} + \zeta}, \tag{3.5}$$

$$\eta_T = \frac{E_{eff}/E_{pristine} - 1}{E_{eff}/E_{pristine} + 2}, \tag{3.6}$$

$$\zeta = \frac{2L}{D}. \tag{3.7}$$

Here, D and L are the nanotubes outer diameter and length respectively; $E_{pristine}$ is the Young's Modulus of the pristine resin and V_{NT} the volume fraction of the filler. The latter can also be expressed in function of the weight fraction w_{NT} and the pristine resin and CNTs densities:

$$V_{NT} = \left[\frac{\rho_r}{w_{NT}} - \rho_r + 1\right]^{-1}; \tag{3.8}$$

$$\rho_r = \frac{\rho_{NT}}{\rho_{pristine}} \tag{3.9}$$

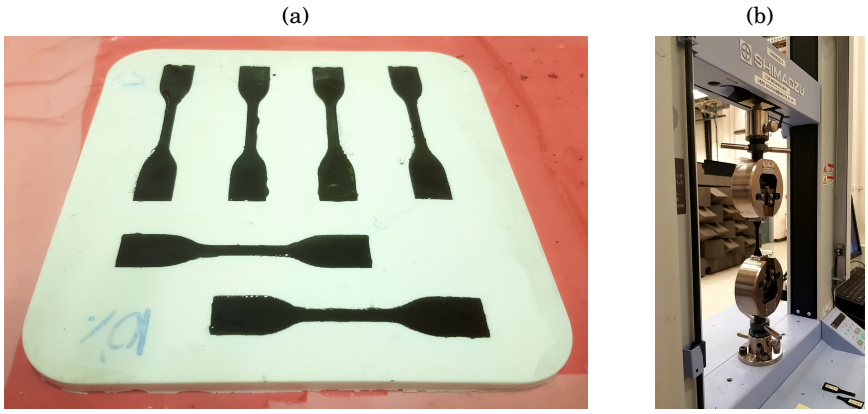

FIGURE 3.11. Tensile tests on CNT-reinforced SS CLV Epoxy Bio-resin: (a) dog-bone-shaped specimens cured in an open silicone mould; (b) experimental setup. Shimadzu testing machine with 10 kN load cell.

The effective Young's Modulus E_{eff} in previous equations accounts for the structure of the nanotube in terms of constituent properties, nanotube geometry and structure. As firstly introduced by Thostenson and Chou [136], the elastic modulus of the nanotube is modelled by considering that its outer wall acts as an effective solid fibre with the same deformation behaviour and same diameter and length. E_{eff} is hence evaluated according to the micromechanics approach described in [136] as:

$$E_{eff} = \frac{4t}{D} E_{NT}, \tag{3.10}$$

Where E_{NT} and t are the Young's Modulus of the nanotubes and their wall thickness, respectively.

The MWNTs characteristics that are used in the equations above are values typically found in literature [120, 137]. For what concerns the Young's Modulus E_{NT}, its typical values are very sensitive to a variety of factors, such as defect concentration, process of production of the nanotubes and type of measurements. Albeit graphite has an in-plane modulus of 1.06 TPa [138], E_{NT} values that have been experimentally measured in open literature present indeed very large variations in estimates, ranging from 0.3 and 1.3 TPa [139–143]. For our estimates, a value of 1 TPa is assigned to E_{NT}. Regarding the geometric characteristics of MWNTs, the outer layer's typical thickness is 0.34 nm and the nanotube typical length 10 μm. Outer and inner diameter, D and D_i respectively, are assumed to be 15 nm and 5 nm. With these geometric values, the nanotube density is evaluated as [136]:

$$\rho_{NT} = \frac{\rho_g (D^2 - D_i^2)}{D^2}, \tag{3.11}$$

being ρ_g the density of fully dense graphite, 2.25 g/cm^3. As the pristine resin's nominal density is 1.15 g/cm^3 (from data sheet), the resulting value of ρ_r is 1.74.

(a) (b)

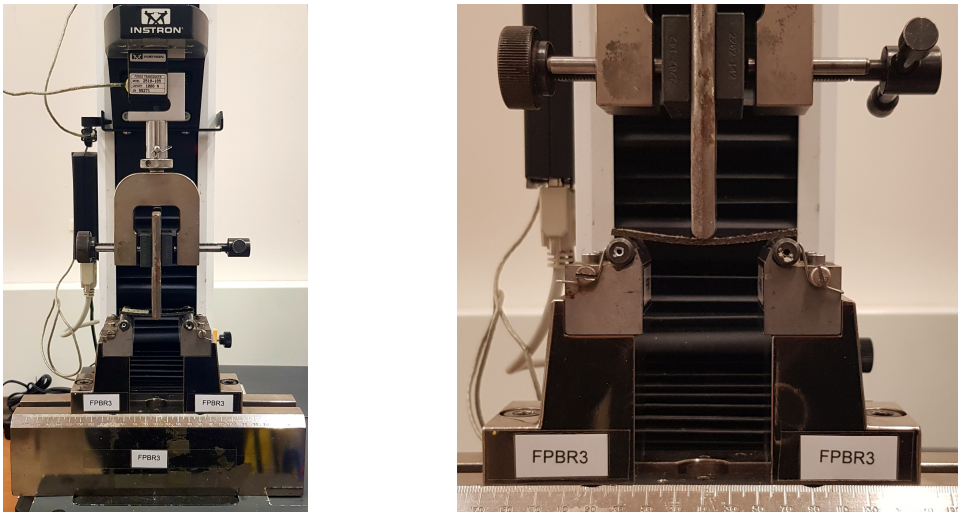

FIGURE 3.12. Evopreg PFC-flax three-point-bending characterization with fibre orientation 0/90°. Instron testing machine with 1 kN load cell.

3.3.2 Three-point-bending testing

Three-point bending flexural tests provide values for the modulus of elasticity from the flexural stress–strain response of the material [144]. They are performed on the Evopreg PFC-flax composite with an Instron testing machine with 1 kN load cell (figure 3.12). The specimens are cut out of 0/90° four-ply laminates by means of a diamond blade. Tests and data processing are performed according to the ASTM D7264 / D7264M-15 (Standard Test Method for Flexural Properties of Polymer Matrix Composite Materials). The main advantage of this type of test is the ease of the specimen preparation and testing. Indeed, the samples are simply rectangular-shaped. Their dimensions are such that the flexural properties are determined accurately from the tests: the standard support span-to-thickness ratio guarantees that failure occurs at the outer surface of the specimens, due only to the bending moment. Indeed, shear deformations can significantly reduce the apparent modulus of orthotropic laminates when the support span-to-thickness ratio is low. For this reason, a high support span-to-thickness ratio is recommended for flexural modulus determinations. The standard span-to-thickness ratio is 32:1, the standard specimen thickness is 4 mm, and the standard specimen width is 13 mm, with the specimen length being about 20% longer than the support span. If the standard specimen thickness cannot be obtained, an alternate specimen thickness can be used while maintaining the support span-to-thickness ratio 32:1 and specimen width. As in the present case the laminate's thickness is 2.3 mm, the support span is set to 73.6 mm and therefore the specimen length to 88 mm.
Specimens are easily positioned on the testing apparatus, as they are simply laid down on the supports. However, specific attention must be paid to correctly aligning and centering the sample on the supports and the loading shaft at the centre of the specimen.

As for the tensile tests, all data are processed in MATLAB R2018a and the Chauvenet criterion is applied to define the outliers to not be considered in the evaluation of the statistic properties. Finally, the strain range in which the material has elastic behaviour and therefore used for the evaluation of the Elasticity Modulus is $\epsilon \in [0.1 \div 0.3]\%$.
Three batches (six specimens each) of Evopreg PFC-flax samples are tested:

1. Batch 1: “bare” specimens;

2. Batch 2: the face under compression loading is covered by a layer of pristine SS CLV;

3. Batch 3: the face under tensile loading is covered by a layer of pristine SS CLV.

The reason for testing also the last two configurations is that, as it will be described in detail in section 5.3, a layer of pristine SS CLV resin is applied to the flax-PFA skins of the sandwich panel to glue them to the core. It is, therefore, of interest to assess the impact of the resin on the composite’s mechanical properties.

3.4 Thermal, thermo-mechanical and rheological characterization

Thermal and thermo-mechanical characterization is performed on both the Evopreg PFC-flax and the pristine and CNT-reinforced SS CLV Epoxy Bio-resin. Rheology investigations are also carried out on the two resins. More in detail, Thermal Gravimetric Analysis allows to determine limits on the temperature ranges to adopt in the other tests. Differential Scanning Calorimetry is carried out to assess the characteristic temperatures of the materials (glass transition and curing). Dynamic Mechanical Analysis is performed to evaluate the damping characteristics of the materials. Particular attention is paid to the CNTs contribution to the damping of the SS CLV resin and, for all materials tested, to the mean damping ratio at room temperature. The latter will, in fact, be assigned as material property in FE numerical models for dynamic analyses simulations. Furthermore, the average values of Storage Modulus at room temperature are compared to Elasticity Modulus values from tensile and three-point-bending testing. Finally, rheological tests are performed on the two resins to quantify the increase of viscosity due to the presence of CNTs in the SS CLV resin. This is very relevant to our scope, as the inclusion of CNTs allows the resin to be viscous enough to form the inserts in the sandwich panel: as it will be shown from the results of the rheological tests (section 4.3.2.4), the pristine resin’s viscosity is very low and it is not possible to hold the shape of the inserts as it cures with the deposition technique that is developed in the present work. This will be discussed in detail in Chapter 5 (section 5.3.2), where the methods for CNT-inserts deposition are presented.

3.4.1 Thermal Gravimetric Analysis

Thermal gravimetric analysis (TGA) is a method of thermal analysis in which the mass of a sample is measured over time as the temperature changes [145]. This measurement provides information about physical phenomena, such as phase transitions, as well as chemical phenomena including thermal decomposition and solid-gas reactions (e.g., oxidation or reduction).
TGA tests are performed on cured samples of the Evopreg PFC-flax and the pristine and CNT-reinforced SS CLV Epoxy Bio-resin by means of a Netzsch STA 449 *F3 Jupiter*® thermal analyzer with liquid nitrogen cooling system. For all tests, temperature ranges from 0°C to 800°C with 10°C/min heat rate. The mass loss first derivative (DTGA) is evaluated from the measured mass loss. Data for the DTGA is smoothed with local regression techniques by using weighted linear least squares and a second degree polynomial model, with a span of 6% of the total number of data points.

3.4.2 Differential Scanning Calorimetry

Differential Scanning calorimetry (DSC) is a thermo-analytical technique which measures the difference in the amount of heat required to increase the temperature of a sample and reference (usually air) as a function of temperature [146]. Both the sample and reference are maintained at nearly the same temperature throughout the experiment.
DSC tests are performed by means of a TA Instruments Inc Differential Scanning Calorimeter Q2000 in the National Composite Centre (NCC) facilities. The materials tested are the cured and uncured pristine- and CNT-resin. Mass of specimens varies between 8 and 10 mg. Samples tested from a cured state are cut into very small pieces to obtain an as much as possible uniform distribution of the material at the bottom of the pan. Temperature ramps are applied to both cured and uncured specimens, within the limits found from the TGA tests, i.e. up to 200°C. For the cured specimens, only a heating temperature ramp with 10°C/min heat rate is applied, whereas the uncured materials undergo a heat/cool/heat cycle, once again with 10°C/min heat rate.

3.4.3 Dynamic Mechanical Analysis

Dynamic mechanical analysis (DMA, also known as dynamic mechanical spectroscopy) is a thermo-mechanical technique used to characterize the viscoelastic behavior of polymers [147]. A sinusoidal stress is applied and the strain is measured, allowing to determine the complex modulus. The temperature of the sample or the frequency of the stress are usually varied, leading to variations in the complex modulus; this approach can be used to locate the glass transition temperature of the material, as well as to identify transitions corresponding to other molecular motions.
DMA tests are performed on the pristine- and CNT-reinforced SS CLV Epoxy Bio-resin as well as on the Evopreg PFC-flax composite with a TA Instruments Q800 DMA in the NCC facilities. Generally, DMA tests can be performed in different "modalities": tensile, compression, dual- and single-cantilever, three-point-bending. The latter is one of the most common modality, as it allows

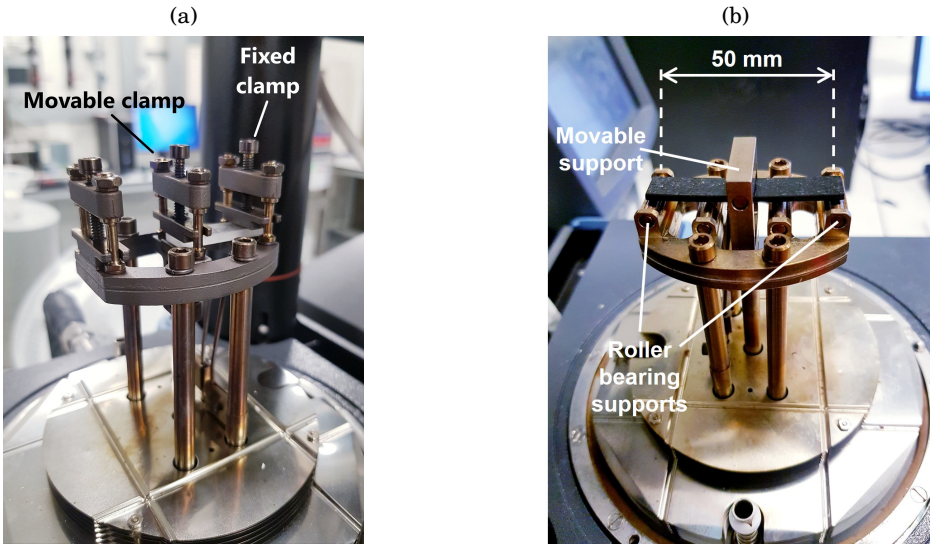

FIGURE 3.13. DMA tests on (a) SS CLV resin in single cantilever mode and (b) Evopreg PFC-flax in three-point-bending mode. TA Instruments DMA Q800.

to have the "truest" results. Indeed, it is possible to obtain a “pure” mode of deformation since clamping effects are eliminated and the 50 mm wide-apart clamps are provided with low-friction, roller bearing supports. However, because of the nature of this configuration itself, it is only suitable for stiff materials, such as composites. Dual-cantilever tests, on the other hand, are more suitable for less rigid materials, such as resins. Here, the ends of the sample are both clamped and the sample is loaded in the middle by means of an actuator. Finally, single-cantilever tests are a good compromise between three-point-bending and dual-cantilever modalities, as only one end of the specimen is clamped and the other one is loaded. Generally speaking, cantilever bending is a good general-purpose mode for evaluating thermoplastics and highly damped materials (e.g., elastomers). For these reasons, DMA tests on the resins are carried out in single-cantilever mode—figure 3.13(a). All tests are performed after mass and clamp calibration. A batch of five specimens for each resin is tested at a constant frequency of 1 Hz, constant amplitude of 15 μm (strain $\approx$ 2%), applying a temperature ramp from room temperature to 200°C, with heat rate of 5°C/min. The initial temperature is not controlled for these specific tests, as there is no cooling system connected to the DMA machine used. Instead, a fan is used to cool down the chamber between tests, making it impossible to start each one from exactly the same temperature (which is also always above room temperature due to residual heat in the chamber).

Finally, DMA characterization of the Evopreg PFC-flax is performed in three-point-bending mode (figure 3.13(b)). Similarly to the tests on the resins, a batch of five specimens is tested at a constant frequency of 1 Hz, constant amplitude of 15 μm (strain $\approx$ 2%), applying a temperature ramp from 25°C to 200°C, with heat rate of 5°C/min. All tests are performed after mass and clamp calibration. This time, the initial temperature is controlled by a nitrogen cooling system connected to the DMA machine used for these specific tests. Therefore, all samples are kept

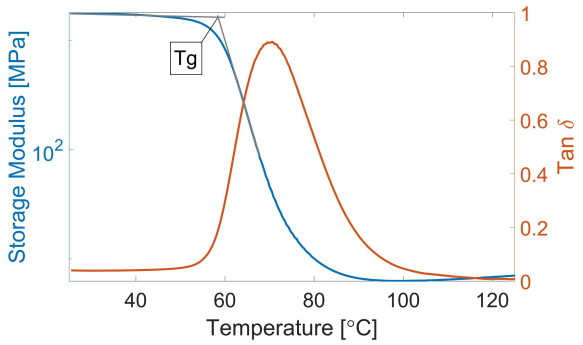

FIGURE 3.14. Identification of glass transition temperature Tg on DMA Storage Modulus curve.

isothermal at 25°C for two minutes before starting the temperature ramp.
For all tests, the glass transition temperature Tg is identified as per ASTM D7028-07 (Glass Transition Temperature (DMA Tg) of Polymer Matrix Composites by Dynamic Mechanical Analysis (DMA)) by plotting the logarithm of Storage Modulus and linear tanδ (δ is the angle between cyclic stress and strain) versus the linear temperature. During the glass transition, the storage modulus of the composite material is significantly reduced. The DMA Tg is determined to be the intersection of two tangent lines from the storage modulus by this test method. The first tangent line is selected at a temperature before the transition (in the present case, it is the temperature at the start of the cycle), whereas the second tangent line is constructed at the inflection point to approximately the midpoint of the storage modulus drop. The two tangent lines are intersected, and temperature corresponding to this intersection point is recorded as the DMA Tg—figure 3.14.

3.4.4 Rheological tests

Rheometry generically refers to the experimental techniques used to determine the rheological properties of materials, that are the relationships between stresses and strains and their derivatives [148]. Rheometry investigates materials in relatively simple flows like steady shear flow and small amplitude oscillatory shear. The choice of the adequate experimental technique depends on the rheological property which is to be determined. This can be the steady shear viscosity, the linear viscoelastic properties, the elongation properties, etc. In the present case, interest is in determining the complex viscosity in the linear viscoelastic range, in order to quantify the impact of the CNTs on the viscosity of the resin.
Rheological tests are performed with a TA Instruments Inc rheometer HR-1 at the NCC. Data is acquired by means of the software TA Instruments Trios V4 and post-processed in MATLAB R2018a. 40 mm diameter Aluminium plates are adopted for both the resins, as TA advises these larger plates—rather than the smaller 25mm-diameter ones—for low viscosity resins to guarantee higher oscillation torques. The gap between plates is set to 500 μm. Temperature nominally ranges from 25°C to 200°C, with 2°C/min heat rate, but in fact the test automatically stops (or is

stopped by the user) after reaching the curing of the resins.
Strain amplitude and frequency are such to work in the linear regions. Limits on usable ranges are also given from the minimum oscillation torque, which is 10 μNm. Clearly, ideally the same settings would be used for the two resins. However, different settings are adopted in order to work in the linear range of each resin and guarantee good quality, reliable data for all tests. For the pristine SS CLV, the strain amplitude is set to 15% and the angular frequency to 10 rad/sec. For the CNT-reinforced SS CLV the strain amplitude is 10% and the angular frequency 85 rad/sec. Finally, the stress signal is constantly monitored during the tests to ensure that acquisitions are significant: in the linear viscoelastic region, the stress signal is a sine wave and only if this is verified the rheology measurements are meaningful.

3.5 Conclusions

This chapter presented the materials constituting core walls, skins and viscoelastic inserts of the novel natural-fibre sandwich panel with CNT-inserts. The first section described in detail the techniques adopted for their manufacturing and curing processes. Definitive manufacturing methods include vacuum-bagging/autoclave techniques for the natural-fibre Evopreg PFC-flax composite and room temperature curing for the EPOCYL MWCNTs paste diluted in SS CLV Epoxy Bio-resin. The second part, instead, focused on the description of methods, apparatus and procedures used for mechanical, thermal, thermo-mechanical and rheological characterization of the materials.
Next chapter presents results of the characterization tests that were presented in this chapter for both the flax-PFA composite and the pristine- and CNT-reinforced resins.

CHAPTER 4

CHARACTERIZATION OF MATERIALS: RESULTS

Contents

4.1 Introduction

THIS chapter presents the results of materials mechanical, thermal, thermo-mechanical and rheological characterization tests of which methodologies and procedures were thoroughly described in Chapter 3. The chapter is structured in two main sections. First section shows the results of the aforementioned tests on the natural-fibre composite (Evopreg PFC-flax) adopted for the core walls and skins of the sandwich panel. The second part, instead, presents the results of the same tests performed on the CNT-reinforced SS CLV Epoxy Bio-resin utilized for the viscoelastic CNT-inserts in the sandwich panel. The CNT-resin performances are always compared to the pristine resin's in order to clearly quantify the effects of the CNTs on the resin's properties. Results will be further discussed in Chapter 8.

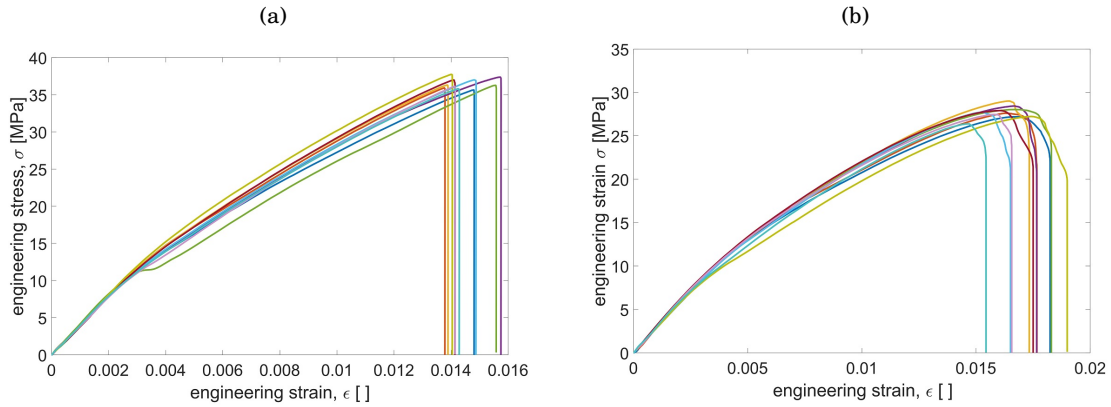

FIGURE 4.1. Stress-strain curves of Evopreg PFC-flax specimens. Autoclave-cured laminates with definitive temperature cycle and 6.9 bar pressure. Fibres orientation (a) 0/90° and (b) ±45°.

4.2 Evopreg PFC-flax natural-fibre composite

4.2.1 Mechanical characterization

4.2.1.1 Tensile tests

Figure 4.1 shows the $\sigma(\epsilon)$ curves for laminates with fibre orientation 0/90° and ±45° cured with the definitive cycle presented in section 3.2.1. In table 4.1, which summarizes the Evopreg PFC-flax mechanical properties, it is possible to appreciate the statistic reliability of data, with low standard deviation and coefficient of variation (CV). Table 4.1 also presents the values of Poisson's ratio and Shear Modulus, evaluated as per the procedures described in section 3.3.1.1.

4.2.1.2 Three-point-bending tests

Three-point-bending flexural tests are performed on the Evopreg PFC-flax composite according to the methodologies described in section 3.3.2. As already introduced, on two of the three batches pristine SS CLV Epoxy Bio-resin is applied on one face of the specimen and cured at room temperature. For batch 2, loading is applied on the face with the resin, whereas for batch 3 it is applied on the opposite face. Figure 4.2(a) shows stress-strain curves for bare samples (batch 1). Figures 4.2(b) and 4.2(c) show the curves for batches 2 and 3, respectively.
The results are briefly summarized in Table 4.1 together with all the mechanical characteristics of the Evopreg PFC-flax laminate measured by experimental testing. Three-point-bending tests on the three batches of specimens are indicated as "3PB - 1, 2, 3". For batch 1, the Elasticity Modulus is evaluated according to both Euler-Bernoulli (EB) [149] and Timoshenko (T) [150, 151] theories. As the difference between the two is evidently negligible, for batches 2 and 3 the Modulus is evaluated according to EB only. Mechanical properties of batches 2 and 3 differ of a very little amount: there is not enough experimental evidence to assess that there is a difference between

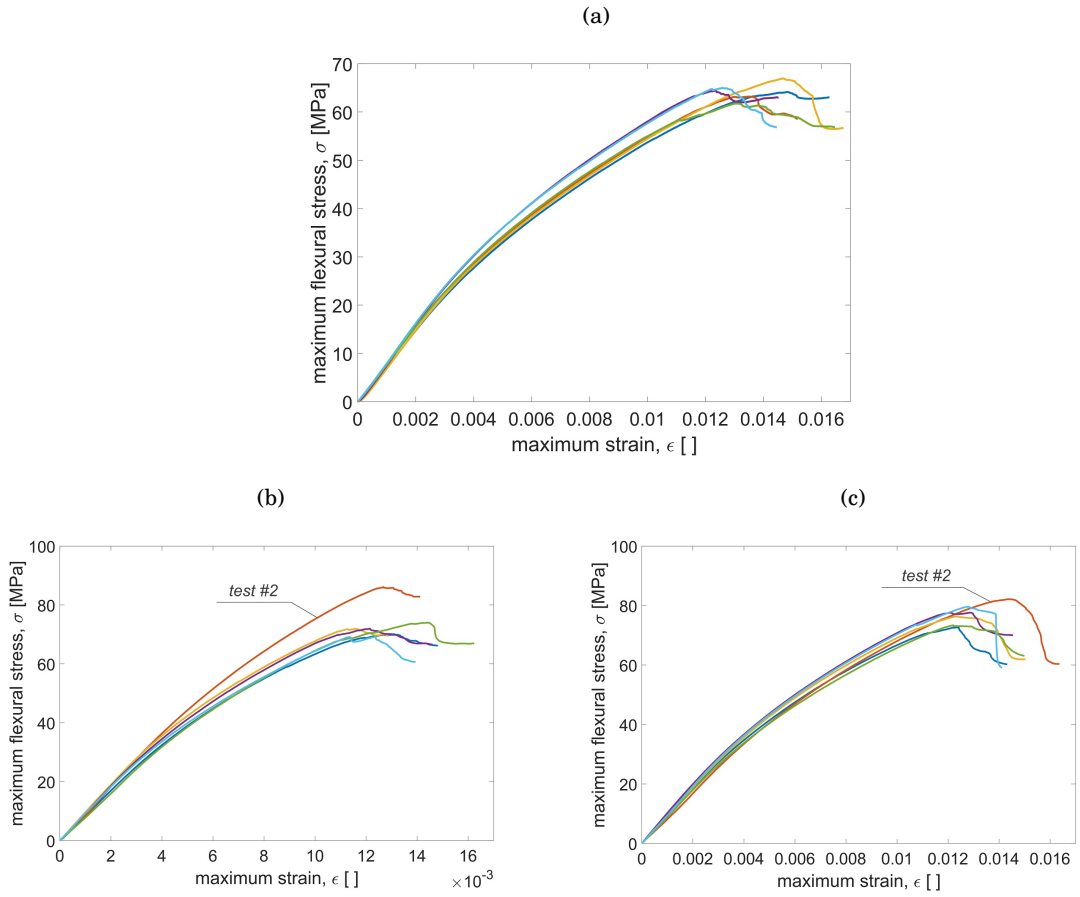

FIGURE 4.2. Three-point-bending tests stress-strain curves of Evopreg PFC-flax laminates. Fibres orientation 0/90°. (a) Bare samples, (b) samples with SS CLV resin on face under compression loading, (c) samples with SS CLV resin on face under tension loading. Tests number 2 in (a) and (b) are outliers according to Chauvenet [133].

batches 2 and 3, as the values are within the statistic scatter. An increase of stiffness of 15% is assumed when the resin is added on either one of the laminate's faces. This is taken into account in the Finite Element models of the sandwich panels that will be presented in Chapters 5 and 6. Finally, it can be noticed that the flexural stiffness is almost double the tensile stiffness measured with tensile tests. As it will be discussed in detail in Chapter 8, this discrepancy might be related to the high levels of weaving and misalignment of fibres in the flax/PFA fabric.

4.2.2 Thermal and thermo-mechanical characterization

4.2.2.1 TGA

TGA analyses on the Evopreg PFC-flax composite are performed following the methods indicated in section 3.4.1. Figures 4.3(a) and 4.3(b) show the percentage of mass loss and its first derivative, DTGA, as the temperature increases.

Table 4.1: Summary of experimentally measured mechanical properties of Evopreg PFC-flax laminates cured with vacuum-bagging/autoclave techniques.

	Fibres 0/90°	Mean	Standard Deviation	Coefficient of Variation
Tensile tests	Young's Modulus [GPa]	3.69	0.111	3.01%
	Tensile Strength [MPa]	33.5	0.652	1.95%
	Yield Stress [MPa]	22.2	0.977	4.40%
	Elongation [%]	1.45	0.0691	4.76 %
	Resilience [Mj/m^3]	0.0072	0.00011	1.51%
	Toughness [Mj/m^3]	0.277	0.0118	4.25%
	Poisson's ratio [ ]	0.336	0.114	33.9%
	Shear Modulus [GPa]	0.877	0.0601	6.86%
3PB - 1	Elasticity Modulus (EB) [GPa]	7.62	0.276	3.62%
	Elasticity Modulus (T) [GPa]	7.67	0.276	3.62%
	Flexural Strength [MPa]	64.3	1.73	2.69%
	Strain at peak [%]	1.35	0.1	7.73 %
3PB - 2	Elasticity Modulus (EB) [GPa]	8.79	0.538	6.12%
	Flexural Strength [MPa]	71.4	1.90	2.67%
	Strain at peak [%]	1.26	0.110	8.95 %
3PB - 3	Elasticity Modulus (EB) [GPa]	9.03	0.298	3.30%
	Flexural Strength [MPa]	76.9	3.65	4.74%
	Strain at peak [%]	1.25	0.0322	2.58 %
	Fibres ±45°	Mean	Standard Deviation	Coefficient of Variation
Tensile tests	Young's Modulus [GPa]	2.69	0.092	3.42%
	Tensile Strength [MPa]	25.4	0.660	2.60%
	Yield Stress [MPa]	17.8	0.833	4.68%
	Elongation [%]	1.62	0.0793	4.89 %
	Resilience [Mj/m^3]	0.0053	0.00009	1.70%
	Toughness [Mj/m^3]	0.289	0.0160	5.54%

It is possible to recognize three main behaviours, especially evident when analyzing the DTGA. These behaviours are due to the contributions of both the natural fibres and the PFA resin.
First of all, a weight loss around 100°C happens due to the evaporation of water that natural-fibres pores retain. At higher temperatures, degradation of the natural fibres begins and it mainly involves two steps. The first one is the thermal depolymerisation of the hemicellulose and the cleavage of glycosidic linkages of cellulose—starting around 230°C. The second one (300-350°C) is related to the decomposition of the α-cellulose [152]. Thermal decomposition kinetics of natural fibres is reviewed in detail by Yao *et al.* [153] for activation energy with dynamic TGA [154]. On the other hand, Burket *et al.* [155] investigated how, as the conversion of PFA polymer to carbon begins, weight loss occurs in two distinct temperature regimes. In the region of 300–400°C the by-products are primarily water (H_2O) and Carbon monoxide (CO). A second major weight loss occurs between 400°C and 600°C. Here, the production of CO increases, while H_2O is slightly suppressed. Generation of Methane (CH_4) and Carbon dioxide (CO_2) is also initiated in this region.
Summarizing what is observed in these TGA tests and what is known from literature, phase 1 may be due to the thermal depolymerisation of hemicellulose in the flax fibres, while phase 2 to

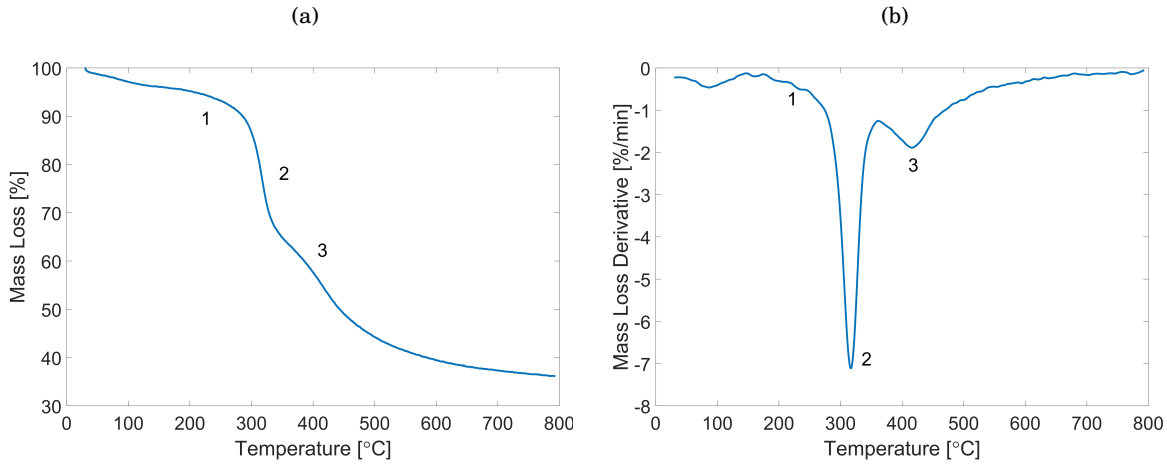

FIGURE 4.3. (a) TGA characterization of Evopreg PFC-flax and (b) first derivative of mass loss.

both flax fibres degradation and PFA polymer conversion to H_2O and CO. Finally, phase 3 may be related to increased production of CO due to PFA degradation [152, 154, 155].

4.2.2.2 DMA

Measurements resulting from DMA analysis cannot be taken into consideration to investigate the thermo-mechanical behaviour of the Evopreg PFC-flax composite. Indeed, probably due to the water content, high porosity and irregular resin distribution, thermal and mechanical transitions are not clearly identifiable. Even though the samples are oven-dried for three hours at 105°C prior the tests and kept sealed until loaded in the testing chamber, a main role in the irregular results might be played by the incomplete removal of fibre moisture. Hence, figure 4.4 is here reported only as a representative case.

For all samples, the value of the Storage Modulus continuously decreases as temperature increases, up to the glass transition region (ranging between 80°C and 140°C). The drop in the Storage Modulus at the glass transition is then followed by a further distinct drop happening between 150°C and 230°C, which can be attributed to the natural fibres degradation.

These findings are in line with open literature: Resch-Fauster *et al.* [156] observes irregularities in DMA-analyzed glass- and hemp-reinforced PFA due to high porosity and irregular resin distribution. As in the present case, a continuous decrease in storage modulus values is registered until glass transition. However, in [156] this is followed by an increase in stiffness due to PFA post-curing—which is not observed in the present case.

Regardless, it is possible to determine the mean value of $\tan\delta$ (being δ the angle between cyclic stress and strain) at room temperature, which will be an input for Finite Element models described in Chapter 6. For the Evopreg PFC-flax: $\tan\delta = 2\zeta = \eta = 0.0290$ (standard deviation 0.0061), being ζ the damping ratio and η the loss factor.

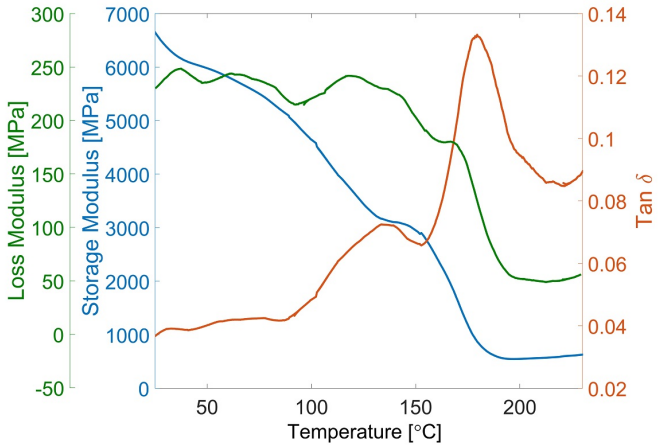

FIGURE 4.4. DMA tests on Evopreg PFC-flax—representative curves.

Finally, the average Storage Modulus at 25°C and frequency 1 Hz is compared to the Elasticity Moduli measured from tensile and three-point-bending testing. The Storage Modulus mean value of the Evopreg PFC-flax is 6.28 GPa (standard deviation: 0.245 GPa; CV: 3.9%), which is much closer to the Elasticity Modulus measured with the three-point-bending tests, 7.62 GPa, than to the one measured with tensile testing, 3.69 GPa. Once again, the discrepancy between Young's Modulus values as evaluated per tensile and three-point-bending tests is further discussed in Chapter 8.

4.3 CNT-reinforced SS CLV Epoxy Bio-resin

4.3.1 Mechanical characterization

4.3.1.1 Tensile tests

Tensile testing on the pristine and CNT-reinforced resins are performed following the methods described in section 3.3.1.2. Samples are prepared by curing the resin in an open mould and therefore present some irregularities in their geometric shape. This clearly causes a quite high variability in the results and for this reason they will be compared to analytic predictions later in this section. However, most of the variability regards the failure point, in terms of both stress and elongation. Conversely, the Young's Modulus—which is our primary interest as it will be an input value for FE models in next chapters—presents more consistent, reliable results.

Figure 4.5(a) shows the entire stress-strain curve for the CNT-reinforced SS CLV Epoxy Bio-resin in terms of mean curve and standard deviations. Figures 4.5(b) and 4.5(c) show the linear elastic range stress-strain curves of both pristine- and CNT-reinforced resins. The entire pristine resin's curves are not displayed, as the variability at failure makes them non-significant in this area. From the experimental tests, the pristine resin's Young's Modulus is 1.82 GPa (standard deviation: 0.0252 GPa; CV: 13.8%), whereas that of the CNT-resin is 1.99 GPa (standard deviation:

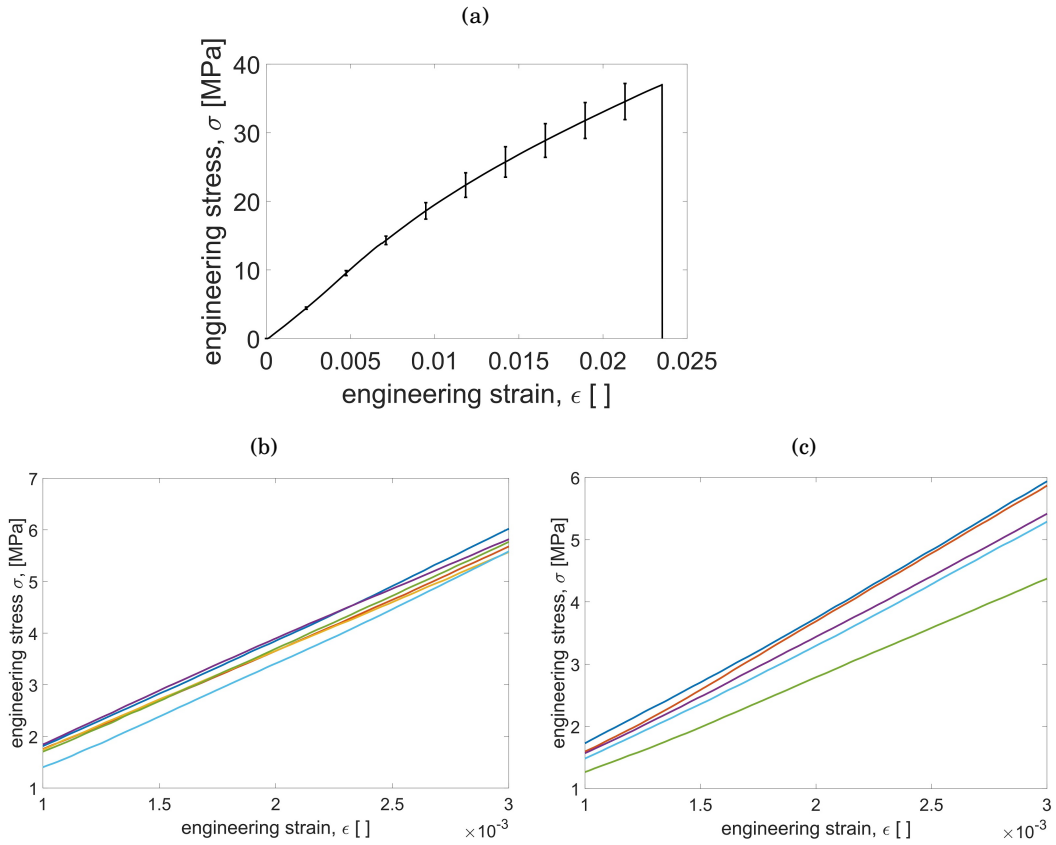

FIGURE 4.5. Tensile tests stress-strain curves of pristine and CNT-reinforced SS CLV Epoxy Bio-resin. (a) CNT-resin mean curve with standard deviations, (b) CNT-resin linear range curves, (c) pristine resin linear range curves.

0.0655 GPa; CV: 3.29%).

These experimental results are then compared to analytic predictions according to the model of Halpin and Tsai with Thostenson correction, as introduced in section 3.3.1.2. By inputting the measured Young's Modulus of the pristine resin, $E_{pristine}$ = 1.82 GPa, and the weight percentage of the CNTs (w_{NT} = 0.477 wt%) into the equations, the analytic model predicts an effective Young's Modulus of 1.92 GPa—figure 4.6. This prediction is very close to the measured value, 1.99 GPa, showing only 3.6% error with respect to experimental data.

4.3.2 Thermal, thermo-mechanical and rheological characterization

4.3.2.1 TGA

TGA characterization is performed according to the procedure described in section 3.4.1. Mass loss and first derivative of pristine and CNT-reinforced SS CLV Epoxy Bio-resin are shown in figures 4.7(a) and 4.7(b), respectively. No significant difference between the resins is detected, apart from a slight difference in the DTGA peak—the pristine resin's is slightly higher—and a minor difference in the DTGA "shoulder" after the peak.

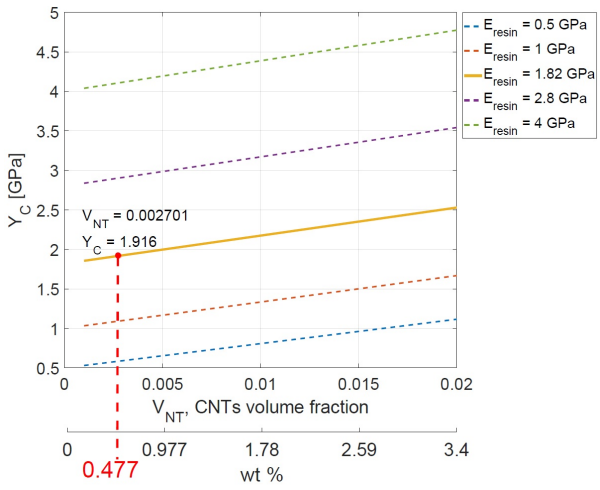

FIGURE 4.6. Analytic prediction of the CNT-resin Young's Modulus according to Halpin and Tsai model with Thostenson's correction (micromechanics approach). Curves in function of the pristine resin's Young's Modulus.

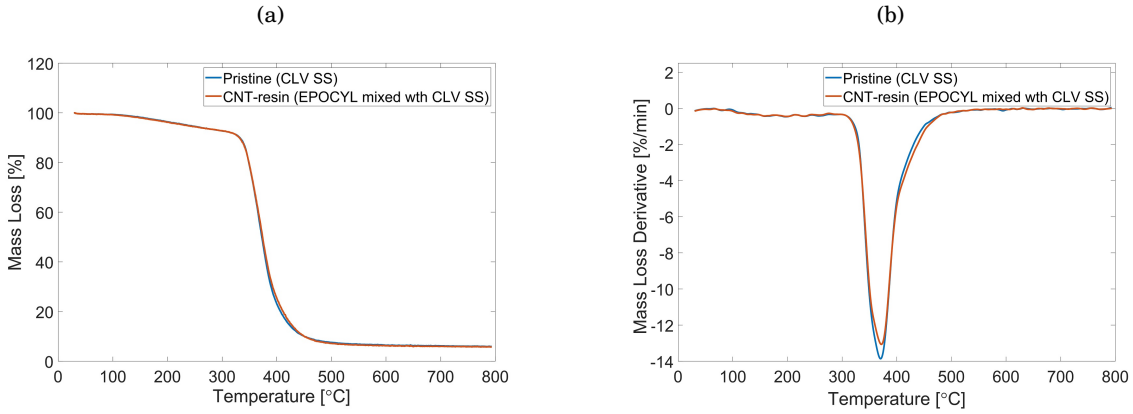

FIGURE 4.7. (a) TGA characterization of pristine and CNT-reinforced SS CLV Epoxy Bio-resin and (b) first derivative of mass loss.

4.3.2.2 DSC

DSC analyses are carried out according to the methods introduced in section 3.4.2. Initially, cured resins samples are analyzed and figure 4.8 shows the results. As evident from the curves, molecular relaxation happens around the glass transition making it appear as a melt and, therefore, preventing a clear identification of the Tg (Glass Transition Temperature), which is given by the change in the Baseline. For this reason, more tests are performed by applying heat/cool/heat cycles on the uncured resins. Results of the latter tests are shown in figure 4.9(a). Firstly, the uncured resins undergo a heating cycle. Pronounced exothermic peaks appear in the plots revealing the curing temperatures: curing happens around the same temperature for both the resins—114°C for the pristine and 113°C for the CNT-resin. Secondly, the resins are

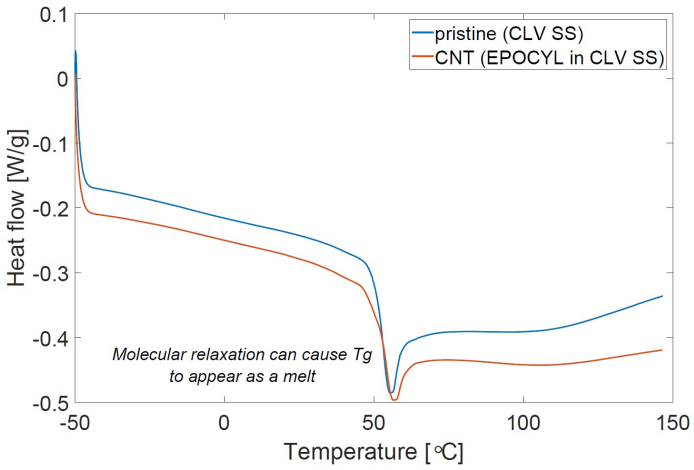

FIGURE 4.8. DSC characterization of pristine and CNT-reinforced SS CLV Epoxy Bio-resin—cured samples, heat cycle.

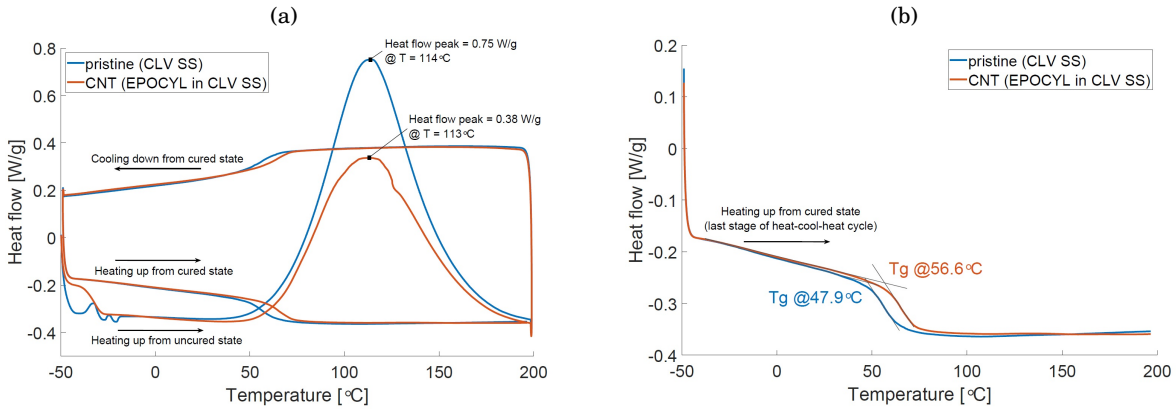

FIGURE 4.9. DSC characterization of pristine and CNT-reinforced SS CLV Epoxy Bio-resin—uncured samples, heat/cool/heat cycle.

cooled down before undergoing a new heating cycle in order to reveal the glass transition. This time, the transition is clearly visible and it is at 47.9°C for the pristine resin, 56.6°C for the CNT-resin—figure 4.9(b).

4.3.2.3 DMA

This paragraph presents the results of DMA tests performed on the pristine- and CNT-resin. Particularly, figure 4.10(a) shows representative curves of Storage Modulus, Loss Modulus and tanδ for the pristine SS CLV Epoxy Bio-Resin, whereas figure 4.10(b) displays the mean tanδ curves with respective standard deviations of the two resins.
The peak value of tanδ is 0.867 for pristine resin (standard deviation: 0.0283; CV: 3.26%), and 0.933 for the CNT-resin (standard deviation: 0.0431; CV: 4.62%). Therefore, including the CNTs

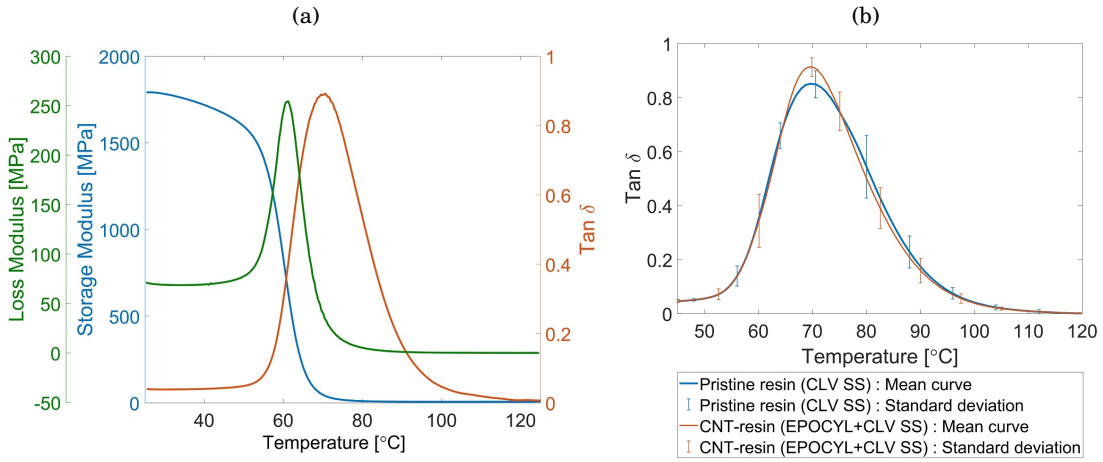

FIGURE 4.10. DMA characterization of pristine and CNT-reinforced SS CLV Epoxy Bio-resin. (a) Representative curves of Storage Modulus, Loss Modulus and tanδ for pristine SS CLV Epoxy Bio-Resin, (b) mean tanδ curves with standard deviations of the two resins.

in the resins allows an increase of 7.5% in the peak of tanδ.

The Tg is identified as described in section 3.4.3. For the pristine resin, it is 57.5°C (standard deviation: 0.572°C; CV: 0.99%), whereas for the CNT-resin it is 58.9°C (standard deviation: 1.41°C; CV: 2.43%). While the pristine-resin DMA Tg is very close to the DSC Tg value, 56.6°C, the CNT-resin DMA Tg is quite far from the DSC Tg, 47.9°C. The discrepancy is not surprising: the glass transition describes a range of behavior of which Tg is a single temperature indicator. DSC and DMA measure different processes and therefore the numbers can vary. In this perspective, the accordance between DMA and DSC Tg for the pristine resin is quite remarkable.

Similarly to what is done for the Evopreg in section 4.2.2.2, the mean tanδ value at room temperature and frequency 1 Hz is evaluated for the pristine and CNT resins as well, as they will be used as input for material damping properties in Finite Element models for dynamic simulations in Chapters 6 and 7. For the CNT-resin, $\tan\delta = 2\zeta = \eta = 0.0461$ (standard deviation 0.0057; CV: 12.4%). For the pristine resin, $\tan\delta = 2\zeta = \eta = 0.0402$ (standard deviation 0.0026; CV: 6.47%).

Finally, the room temperature Storage Moduli mean values of pristine- and CNT-resin are, respectively, 1.91 GPa (standard deviation: 0.348 GPa; CV: 18.2%) and 1.92 GPa (standard deviation: 0.512 GPa; CV: 26.8%). These mean values are very close to the ones measured with the tensile tests (1.82 GPa and 1.99 GPa, respectively), confirming the reliability of the experiments. However, it is also worth noticing that the standard deviations here are quite high. This is due to the fact that, as previously explained, samples for DMA testing are made in the laboratory by curing the resins in an open silicone mould. This means that specimens sections may have geometric irregularities that lead to inaccuracies in the Storage and Loss Modulus measurements.

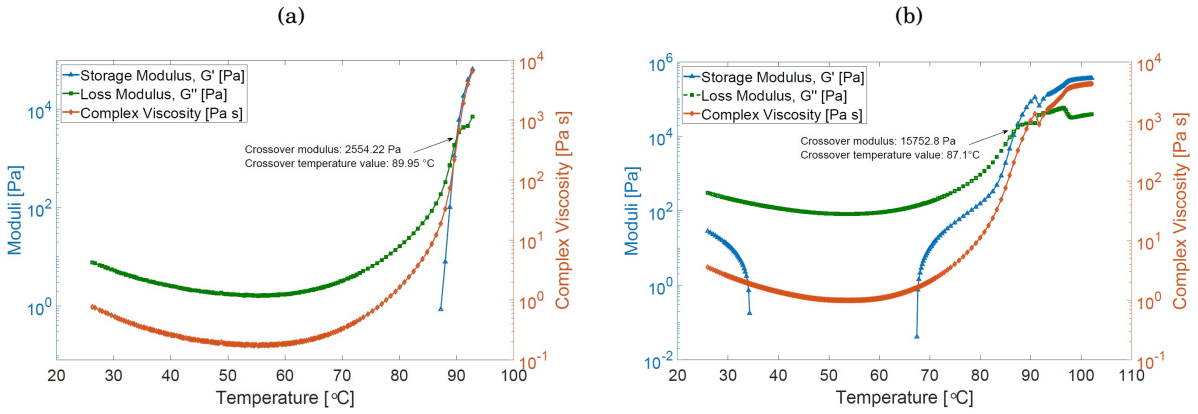

FIGURE 4.11. Rheology characterization of (a) pristine- and (b) CNT-reinforced SS CLV Epoxy Bio-resin.

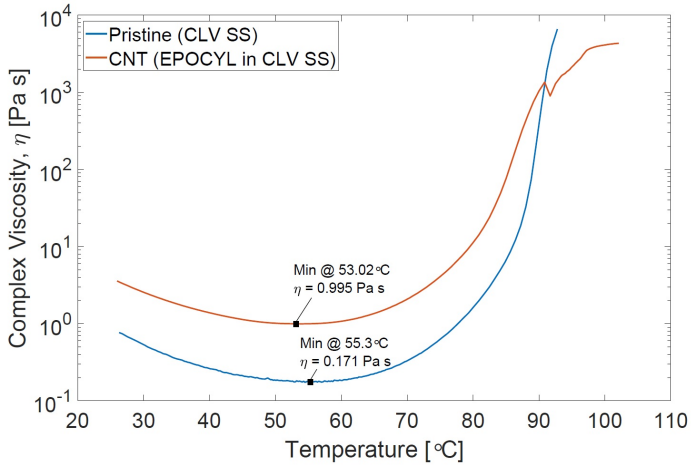

FIGURE 4.12. Rheology characterization of pristine- and CNT-reinforced SS CLV Epoxy Bio-resin: Complex Viscosity.

4.3.2.4 Rheology

Finally, rheology tests are performed on the resins with and without CNTs in order to quantify the effect of the latter on the resin's viscosity. The methods follow those described in section 3.4.4. Figures 4.11(a) and 4.11(b) show Storage and Loss Moduli and the Complex Viscosity for the pristine and CNT-reinforced resins, respectively. Storage Modulus values are not recorded for wide ranges of temperatures, that is when they are very low. In the plots, values of the Crossover modulus and the respective crossover temperature are indicated. This is the point where, as the resin cures, the Storage Modulus becomes higher than the Loss Modulus.
Figure 4.12 compares the Complex Viscosity of the pristine- and CNT-resin and indicates their minimum values, together with the temperatures at which they occur: at their respective minimum values, the complex viscosity of the CNT-resin is 5.8 times the pristine one's.

4.4 Conclusions

This chapter presented the results of mechanical, thermal, thermo-mechanical and rheological testing performed on the materials adopted for the novel natural-fibre sandwich panel with CNT-inserts. Firstly, the Evopreg PFC-flax (flax/PFA composite used for core walls and skins) and the CNT-reinforced SS CLV Epoxy Bio-resin (CNT-resin adopted for the viscoelastic inserts) were experimentally characterized to retrieve their mechanical properties. Indeed, these will be used in Chapters 5, 6 and 7 for numerical FE models of the sandwich panel and analytic formulations. For what concerns the pristine and CNT-reinforced resins, Young's Modulus values (evaluated by tensile tests) are 1.82 GPa and 1.99 GPa, respectively. These results are supported by analytic predictions according to Halpin-Tsai model, which shows 3.6% error with respect to experimental data. The flax/PFA composite was characterized by both tensile and three-point-bending tests. High discrepancy was detected between results of these tests, since the value of Flexural Modulus, 7.62 GPa, is about twice the Tensile, 3.69 GPa. Secondly, thermal and thermo-mechanical characterization allowed a deeper understanding of the materials behaviour and helped to identify their characteristic transitions with increasing temperatures. More in detail, preliminary TGA tests were performed to identify the limits within which to perform the other tests. DSC and DMA results were significant only for the resins and good agreement was found between Tg values evaluated by these two tests. For the pristine- and CNT-resin, Tg values detected by DSC are 47.9°C and 56.6°C, whereas the curing temperatures are 114°C and 113°C, respectively. On the other hand, Tg values detected by DMA are 57.5°C (pristine) and 58.9°C (CNT). DMA tests also allowed to quantify the effect of CNTs on the peak of $\tan\delta$, which increases of 7.5% when including the filler. Mean values of damping ratios at room temperature and 1 Hz frequency were also estimated from DMA results, since they will be used in the FE models for dynamic analyses in Chapters 6 and 7. In order to confirm the reliability of the tests, for both the resins and the Evopreg PFC-flax, Storage Modulus mean values at room temperature and 1 Hz frequency from DMA were compared to the Tensile and, for the composite only, to the Flexural Modulus. While good agreement was found for the resins (1.91 GPa and 1.92 GPa for pristine and CNT-resin, respectively), the composite Storage Modulus was found to be in the same range as the Flexural value, hence dissimilar from the Tensile (6.28 GPa). Finally, rheology studies were performed on the pristine- and CNT-resin to quantify the CNTs contribution to the resin Complex Viscosity. At their respective minimum values, the CNT-resin viscosity is almost 6 times the pristine-resin.

After the mechanical and thermo-mechanical characterization of materials, their mechanical properties are known and can be utilized as input for numerical models. Hence, next chapter presents an FE probabilistic design analysis study of the geometric uncertainties of the viscoelastic insert, the design of the insert itself and the manufacturing process of the entire sandwich panel.

CHAPTER 5

DESIGN AND MANUFACTURING OF NATURAL-FIBRE SANDWICH PANEL WITH CNT-INSERTS

Contents

5.1 Introduction

In CHAPTERS 3 and 4, materials constituting the natural-fibre sandwich panel with CNT-inserts were extensively characterized by mechanical and thermal test campaigns. This allows to proceed with the manufacturing of the sandwich panels prototypes, followed by a numerical analysis of manufacturing uncertainties of the CNT-inserts, based on Finite Element (FE) models that contemplate the material properties measured experimentally. Geometric and materials properties of the sandwich panel walls are fixed and kept constant throughout the

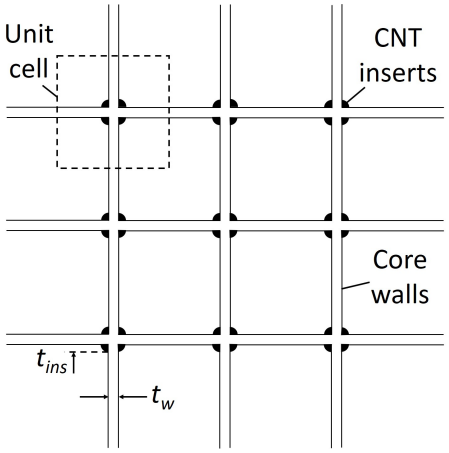

FIGURE 5.1. Schematic in-plane drawing of the core of a sandwich panel with CNT-inserts.

study: the core topology consists of a square-cell rectangular lattice with width of the unit cell $l = 20\,\text{mm}$, out-of-plane height $h_{core} = 15\,\text{mm}$ and walls thickness $t_w = 2.3\,\text{mm}$. The latter is dictated by the thickness of the laminate constituting the walls, which is made of the flax-PFA composite (Evopreg PFC-flax) introduced in Chapter 3. In particular, in section 3.2.1 it was discussed that the minimum number of plies ensuring flat plates is four, corresponding to a thickness of the laminate of 2.3 mm. Figure 5.1 shows a schematic in-plane drawing of the core lattice.

This chapter is structured in two main parts. The first section describes manufacturing procedures and techniques for sandwich panel specimens and shows how each component (i.e. core, inserts and skins) is produced. In particular, the inserts dimensions are fixed by setting a limit to the maximum percentage of mass added to the lattice core. Afterwards, the second section describes a probabilistic design analysis performed to determine the impact of the inserts geometric uncertainties on the global mechanical properties of the unit cell. Methods are presented first, followed by results of the simulations.

5.2 Manufacturing of sandwich panel

Following sections show manufacturing and assembly procedures of the sandwich panel components. They also describe the design procedure of the CNT-inserts and their deposition techniques. Samples of several sizes for different types of tests (which will be described in Chapters 6) are produced. Furthermore, depending on the type of test specimens either consist of the rectangular lattice alone or are provided with face skins. In all cases, the reinforced configuration (that is the structure with the viscoelastic CNT-inserts) is compared to a baseline structure, that is the panel with no inserts.

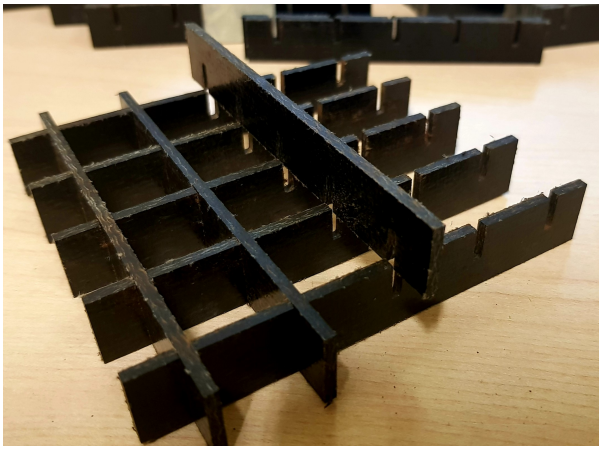

FIGURE 5.2. Assembly of the sandwich core (flatwise compression tests specimen): interlocking of grooved strips.

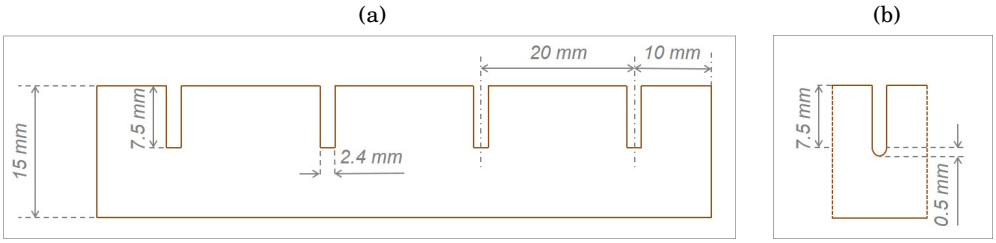

FIGURE 5.3. Schematic drawing of core strips geometry. The total width of the strip is not indicated as it depends on the IP dimensions of core specimens.

5.2.1 Core

This section describes the manufacturing of the base structure of the sandwich panel core, which is the bare layout with no viscoelastic depositions. It consists of a square-cell lattice whose walls are grooved strips interlocked with each other—figure 5.2. No glue is used at the junctions. Strips are cut from Evopreg PFC-flax laminates with fibre orientation 0/90° and therefore fibres in the lattice core are parallel its in-plane (IP) and OOP directions. Figure 5.3(a) shows the geometry of strips. The strip width varies depending on the IP size of the panel specimen. The grooves are as wide as the laminate thickness—to allow the interlocking and, at the same time, to prevent any play or looseness—whereas their depth is half the core's height. From a technical manufacturing standpoint, the grooves have to be slightly deeper than this since it is not possible to generate perfectly square corners with a blade—figure 5.3(b). The distance between grooves is 20 mm, which is the IP width of a unit cell. The relative density of this core (ratio of lattice density, ρ, to wall material density, ρ_s) is $\rho/\rho_s = (2t_w l - t_w^2)/l^2 = 0.23$.

For small-scale samples, cutting is performed manually by means of a blade using water as coolant system. On the other hand, for large-scale sandwich panels cutting is performed by means of numerically-controlled water jet techniques. In both cases, using water-based processes

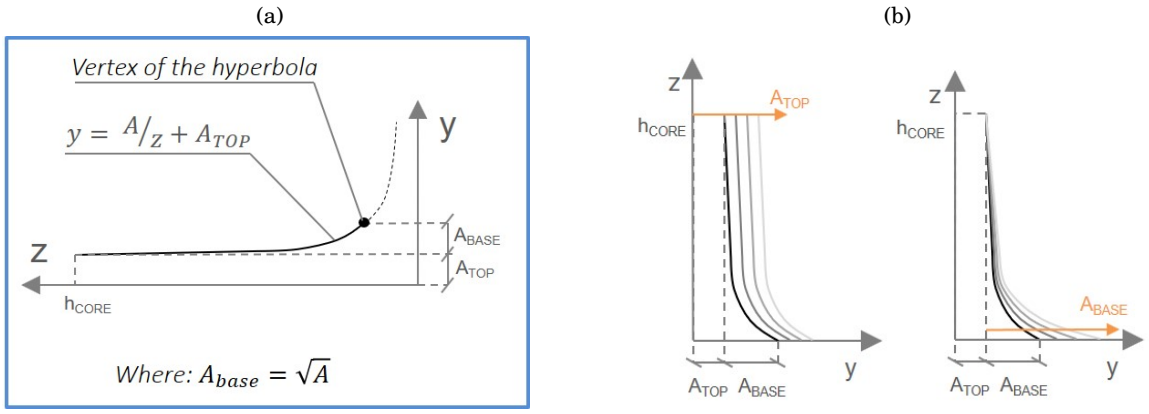

FIGURE 5.4. Qualitative drawing of the insert's hyperbolic geometry. The RI variables for PDS analyses are indicated: A_{base} and A_{top}.

on natural-fibre laminates is not ideal since the fibres inevitably absorb humidity in the process. There are, however, no other valid alternatives in the available laboratory facilities and, hence, components are oven-dried for a few hours—depending on the size of the pieces—at 105°C after cutting, to remove most of the moisture absorbed by the fibres.

As previously introduced, specimens both without and with inserts are manufactured. Next section describes the CNT-resin deposition procedure adopted to obtain the inserts within the core lattice.

5.2.2 Skins

Similarly to the core strips, skins are cut from Evopreg PFC-flax laminates with fibre orientation 0/90°. Prior to gluing it to the core, one of the faces of each skin is treated with sand paper to obtain a more rough surface and hence favour the adhesion between components. It is then glued to the core by applying pristine SS CLV Epoxy Bio-resin. The skins are attached one at time. This choice is due to the practical fact that it is ideal for the skin to be underneath the core as the resin cures to avoid any dripping of glue through the lattice. Firstly, the resin is roughly spread on the treated surface of the skin by means of a brush. It is then distributed more evenly by using a large roll, which also helps to eliminate any resin in excess. Finally, the core is aligned on the skin and an aluminium plate and weights are positioned on top of the assembly to favour its flatness and bonding of components. Once the first skin is attached to the core and the resin is completely cured, the same process is performed with the second skin.

5.2.3 Design of the CNT-inserts

The design of the novel sandwich panel developed in this thesis involves primarily the definition of the inserts characteristics, considering that core and skins properties are fixed and kept unaltered. The geometry of a cylindrical insert is completely described by only one variable—that is the diameter of its circular section—given that its height is equal to that of the sandwich

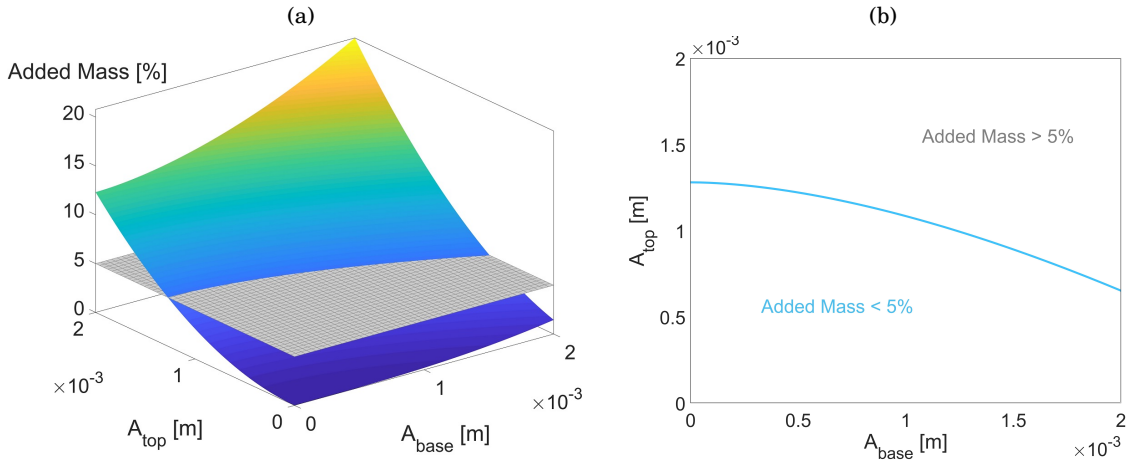

FIGURE 5.5. Analytic prediction of mass percentage added by the inserts to the sandwich panel core in function of the inserts dimensions.

panel core. However, the action of gravity affects the shape of the insert after the CNT-resin has been deposited at the walls junction corner and before it cures completely, thus generating a non-uniform distribution. This will be clearer in section 5.3.2, which shows the deposition technique of the CNT-resin. The profile of such a distribution can be approximated by a hyperbolic shape as shown in figure 5.4, where its main geometric characteristics are also indicated.

The design space of such geometric parameters of the insert is determined by establishing a limit on the percentage of mass added by the viscoelastic depositions to the sandwich panel core. Indeed, as observed in section 2.1, weight increment is a fundamental parameter to control when applying any type of insertion in a sandwich structure to improve its sound insulation and/or vibration damping [14, 15, 41]. Therefore, in this study the CNT-inserts are designed by establishing a maximum value for the percentage of added mass of 5%.

Figure 5.5(a) shows the analytic percentage of added mass in function of the characteristic dimensions of the insert. It is calculated as:

$$\text{Added Mass } [\%] = 100 * \frac{M_{walls+inserts} - M_{walls}}{M_{walls}}, \tag{5.1}$$

where the insert volume is evaluated as a solid of revolution of the hyperbolic profile (refer to figure 5.4):

$$M_{insert} = \rho_{resin} \pi \int_{A_{base}}^{A_{base}+h_{core}} \left[\left(\frac{A_{base}{}^2}{z} + A_{top} \right)^2 \right] dz \tag{5.2}$$

Figure 5.5(a) also displays the maximum percentage of added mass: the intersection between the two surfaces identifies the curve circumscribing the design space—figure 5.5(b).

At the manufacturing level, there is little control on A_{base}: this variable is, in fact, a result of how uniformly the resin spreads along the corner rather than an input parameter (details on the manufacturing techniques of the inserts will be explained in section 5.2.3). Therefore, by setting a

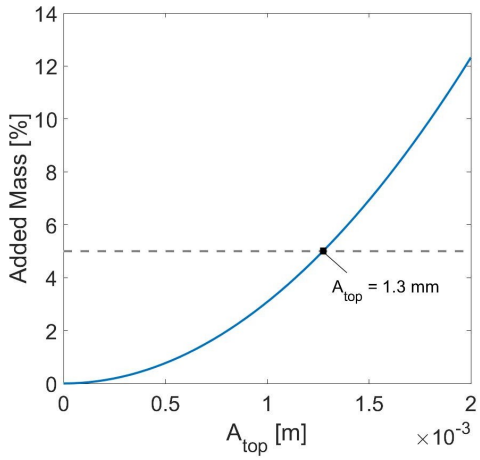

FIGURE 5.6. Analytic prediction of percentage of mass added by *cylindrical* inserts to the sandwich panel's core as a function of the insert's thickness A_{top}.

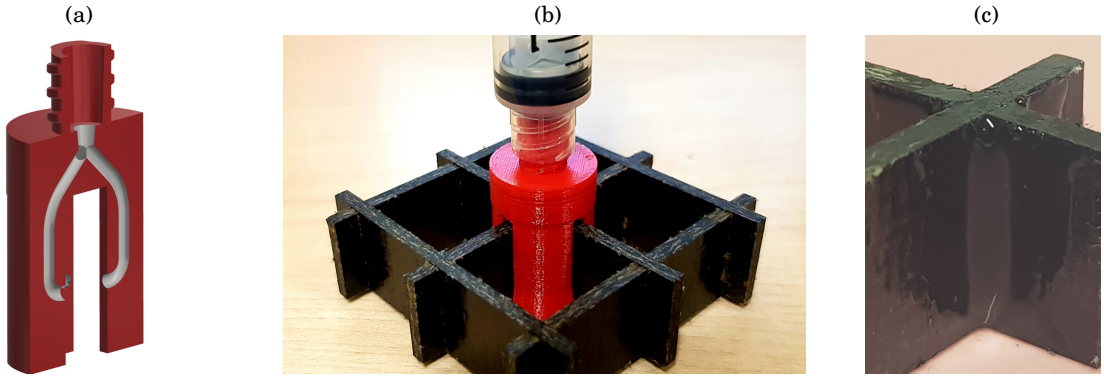

FIGURE 5.7. (a) CAD model of 3D-printed injection mould for CNT-resin deposition; (b) CNT-resin injection; (c) example of viscoelastic insert at the core walls junction.

nominal thickness of the insert, the corresponding volume of resin will distribute along the corner, resulting in certain final values of A_{top} and A_{base}. It is, hence, possible to consider an equivalent cylindrical insert with $A_{base} = 0$, corresponding to that nominal thickness value. In this case, the design space is reduced to a curve, as it is shown in figure 5.6, and the maximum percentage of added mass dictates straightforwardly the volume of the insert—$\pi r^2 h_{core} = 79.6\,\text{mm}^3$—which is that corresponding to a cylindrical insert with radius r equal to a nominal thickness of 1.3 mm.

5.2.4 Deposition of CNT-inserts

The viscoelastic inserts are manufactured by injecting CNT-reinforced resin at the corners of wall junction areas by means of a specifically designed 3D printed injection mould device applied to the tip of a medical syringe—figure 5.7(a). After sucking the resin into the syringe, the mould is mounted at its tip and positioned at the junction between crossing walls, figure 5.7(b). By pressing the plunger, the resin flows into the mould, then splitting into four channels—each one

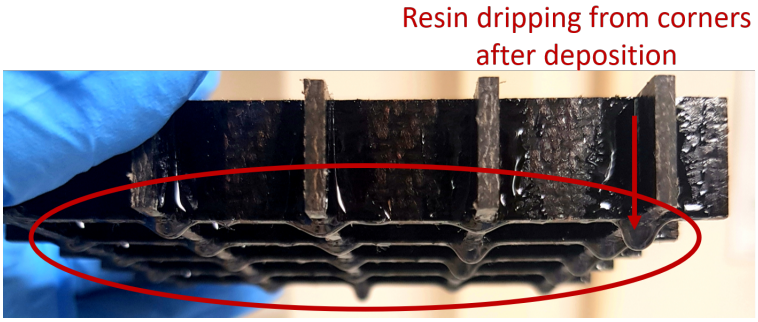

FIGURE 5.8. Sandwich cores reinforced with pristine SS CLV Epoxy Bio-resin: resin dripping under the effect of gravity.

directed towards one of the four corners of the unit cell. These channels end at half the height of a cavity, which is a hollow quarter of cylinder: here, the resin spreads uniformly upwards and downwards along the corner, thus shaping the insert. Once the resin has been injected, the syringe with the mould is pulled away from the junction and the resin is left to cure for about 24 hours—figure 5.7(c). During the first few hours after the resin deposition (hence, when it is still mostly uncured), the core is turned upside down at least twice in order to ensure an as uniform through-the-thickness distribution of the resin as possible.

The inner cavities of the mould—i.e. the hollow quarters of cylinder which shape the insert—have a ray of 1.5 mm. As shown in section 5.2.3, the insert thickness is set to 1.3 mm (corresponding to 5% added mass). The cavities are, however, slightly oversized to account for adhesion phenomena acting between their inner walls and the external layers of the resin in contact with them. The 1.5 mm value is found by trial and error, by measuring the added mass for different values of cavity widths.

Finally, it is important to notice that, for the sake of completeness a second reinforced configuration should be considered, that is a core with viscoelastic inserts made of unreinforced SS CLV Epoxy Bio-resin. However, such configuration is not manufacturable within the limits imposed by the resin deposition technique developed in this work. Indeed, as the rheology investigation showed in section 4.3.2.4, the pristine resin has much lower viscosity values than its CNT-reinforced version. This prevents the resin from keeping the shape of an insert: once deposited at the corner, the resin flows downwards, dripping from the core under the effect of gravity and leaving only a thin layer of resin on the walls—figure 5.8. Consequently, the use of a filler is essential in order to obtain a well-shaped insert with the deposition technique developed in this study.

5.2.5 Large-scale sandwich panels

As for small-scale specimens, two panels are manufactured: one structure is provided with the CNT-viscoelastic inserts, whereas in the other one core strips are simply interlocked with neither inserts or any kind of gluing resin applied at the junctions.

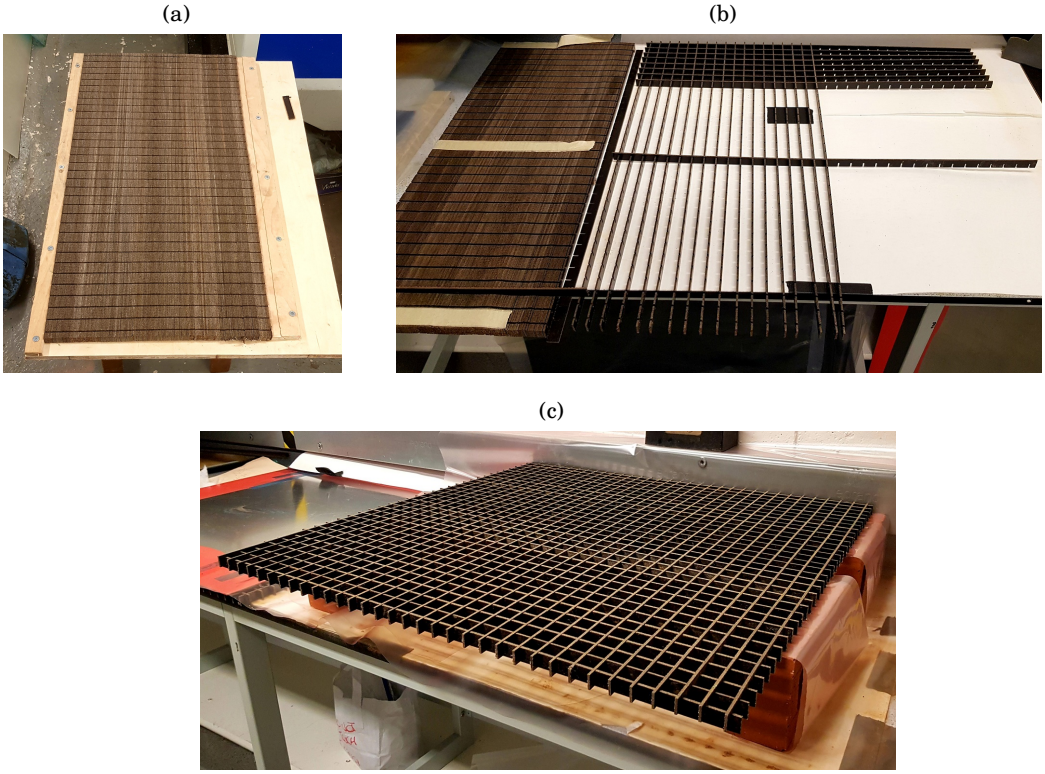

FIGURE 5.9. Large-scale sandwich panels core strips interlocking: (a) core strips before interlocking; (b) core assembly process; (c) assembled core (bare configuration).

Overall, 136 core strips and 4 skins are cut out of eight 700 mm x 700 mm Evopreg PFC-flax laminates by means of numerically controlled water jet techniques. Specifically, four out of eight laminates are used for the skins and the remaining plates for the core strips. The maximum laminate dimensions are dictated by the largest available tool plate for autoclave curing, which is 800 mm wide. Considering the space occupied on the tool plate by cork and tacky tape, the maximum width of the composite plates is 700 mm. The edges of cured laminates are then trimmed to remove any irregularities or resin in excess at the borders, thus allowing to obtain 680 mm x 680 mm sandwich panels.

Albeit the procedure to assemble these panels is not different from that used for smaller ones, some adjustments are made due to their large dimensions. For what concerns the lattice core (figure 5.9), for instance, most grooves have to be manually widened by means of a diamond file to allow the slotting: on a large scale, errors due manufacturing accumulate from slot to slot and, when strips are positioned to assemble the core, many grooves end up to be not perfectly aligned. The CNT-resin is then injected into one of the two cores in small areas at a time (figure 5.10). Finally, skins are attached according to the procedure described in section 5.2.2—figure 5.11. Major attention is paid to the alignment of components and their bonding, which are favoured by a large aluminium plate and several weights positioned at the top of the assembly.

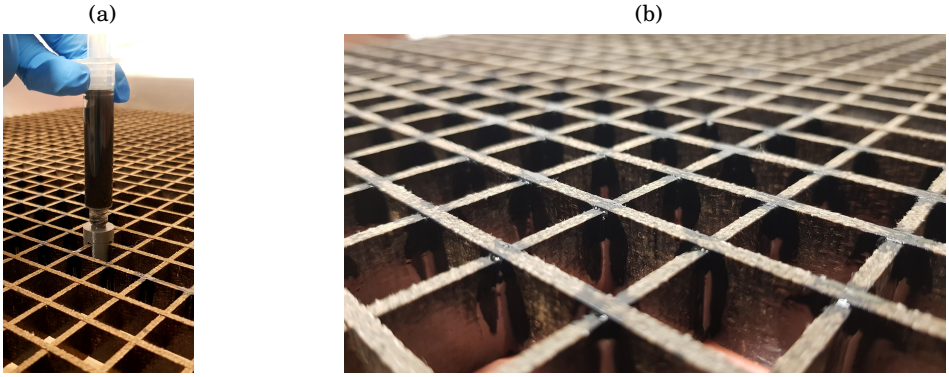

FIGURE 5.10. Large-scale sandwich panels: CNT-reinforced resin injection at core walls junction areas. (a) injection process; (b) final reinforced core.

FIGURE 5.11. Large-scale sandwich panels: treatment of one surface of each skin with sand paper for better bonding with the core.

Table 5.1 shows a summary of the sandwich panels characteristics. In particular, it is possible to observe that the resin used for the lattice-to-skins bond adds a negligible amount of mass to the panel (6 gr for each skin, about 0.24% added mass to the sandwich panel).

5.3 Probabilistic design analysis

The shape—and therefore the thickness—of the CNT-resin inserts are highly uncertain input parameters due to multiple manufacturing-related factors, such as the volume of resin ejected from the syringe, the timescales of deposition, the distribution of CNTs in the resin and its viscosity. A probabilistic design analysis is hence required to assess the effect of uncertain input parameters on the mechanical performances of the sandwich panel unit cell.
Generally, a probabilistic design analysis allows to determine the extent to which uncertainties affect the results of an FE analysis. Statistical distribution functions describe uncertain parameters and it is possible to verify how large is the scatter of the output parameters—in other words, how robust they are with respect to the random input (RI) variables.

Table 5.1: Characteristic weights of large-scale sandwich panels—Analytic estimates vs measured values.

		Estimated	Measured
Core	Bare core weight [kg]	2.000	2.099
	Reinforced core weight [kg]	2.106	2.196
	Core strips per panel	68	68
Inserts	CNT-resin weight [kg]	0.106	0.0970
	Added mass	5.3%	4.62%
	Inserts per panel	1156	1156
Skins	Average weight (no gluing resin) [kg]	1.414	1.471
Skins	Average weight (with gluing resin) [kg]	-	1.477
Sandwich panel	Bare [kg]	4.829	5.053
	Reinforced [kg]	4.935	5.154

Next sections describe the FE model of the unit cell and methods and results of the probabilistic study.

5.3.1 FE model of unit cell

Shear characteristics are paramount indicators of the mechanical performances of sandwich panels [1], and the out-of-plane (OOP) Shear Modulus is therefore used as control parameter in the probabilistic design analysis. At this stage, numerical models of the unit cell do not include the sandwich panels skins since it is well-known in literature that the main contribution to global shear characteristics in a sandwich panel is given by its core [1].
Numerical analyses are performed in ANSYS Parametric Design Language (ANSYS Mechanical APDL R15). The unit cell FE model is entirely parametric to allow to implement loops of simulations where any properties can vary arbitrarily. As introduced in section 5.1, however, the initial design choice for this study is to keep unchanged the base structure of the core.

Figure 5.12 shows the FE model of a quarter of the unit cell for clarity reasons, but in fact the entire cell is modelled by symmetrically mirroring this quarter. Three different configurations—i.e., the cell with different geometric characteristics of the insert—are displayed to take into account the fact that, from the manufacturing standpoint, once the CNT-resin is deposited at the corner of the walls junction it is subjected to the effects of gravity, hence resulting in a non-uniform distribution. Figure 5.12(a) shows the particular case of a cylindrical distribution, while figures 5.12(b) and 5.12(c) display two representative cases of slight and pronounced hyperbolic shapes, respectively. Among these three cases, the one most representative of the manufactured inserts is (b), the slightly hyperbolic profile. Indeed, while gravity definitely has an effect on the CNT-resin as it cures, the latter is characterized by high viscosity levels and hence the thickness of the insert is quite uniform along the core junction, becoming larger only towards the base of the core. In case (c), instead, the CNT-resin drops so heavily towards the base that there is only a

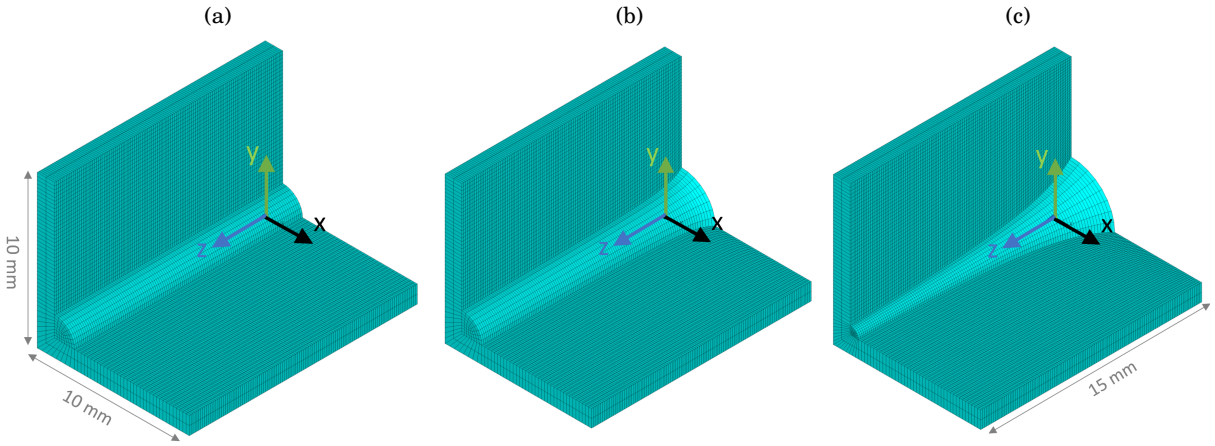

FIGURE 5.12. APDL parametric FE model of one-quarter unit cell of the core of the sandwich panel. Three representative cases of insert configuration: (a) cylindrical with radius $A_{top} = 1.3\,mm$, (b) slightly hyperbolic with $A_{top} = 1.3\,mm$ and $A_{base} = 1\,mm$ and (c) prominently hyperbolic with $A_{top} = 0.1\,mm$ and $A_{base} = 2.9\,mm$.

very thin layer of resin at the top of the core, which does not represent our specimens.

SOLID185 elements are adopted to model all components of the cell. SOLID185 is used for 3-D modeling of solid structures and it is defined by eight nodes having three degrees of freedom each, which are the translations in x, y, and z directions [157]. In particular, elements of the composite walls are *layered* structural solids (SOLID185 with layered option activated) to simulate the composite lay-up. The elements size is determined by following two criteria: not only the mesh has to be found convergent, but it needs to be fine enough to provide an accurate representation of the hyperbolic distribution. Since at this stage the FE model represents the only unit cell and therefore is quite light, the element size is set to 0.25 mm (corresponding to a total number of elements of 5520). Elements dimensions vary slightly along the insert, as the mesh becomes coarser towards the vertex of the hyperbola.
For what concerns the material properties, core walls consist of the four-layer 0/90° Evopreg PFC-flax composite of which the mechanical properties are summarized in table 4.1 in Chapter 4. Specifically, the fine mesh allows to have four through-the-thickness elements, so that each element has one layer with fibres at 0/90° (each layer of the composite laminate consists, in fact, of 2x2 twill fabric). The material properties of the insert are isotropic. The Young's Modulus is that measured by tensile tests (section 4.3.1.1), whereas the Poisson's ratio has a typical 0.3 value. Finally, the density is 1150 kg/m^3 as per data sheet.

The OOP Shear Modulus is evaluated by performing static analyses which simulate a single-lap shear test, similarly to the procedures described in [158, 159]. Periodic boundary conditions are applied to the four edges of the unit cell, by specifying that all degrees of freedom on one edge are equal to the corresponding ones on the opposite edge. Nodes on one of the transverse faces ($z = 0$) are fixed, whereas on the opposite transverse face ($z = h_{core}$) they are rigidly connected

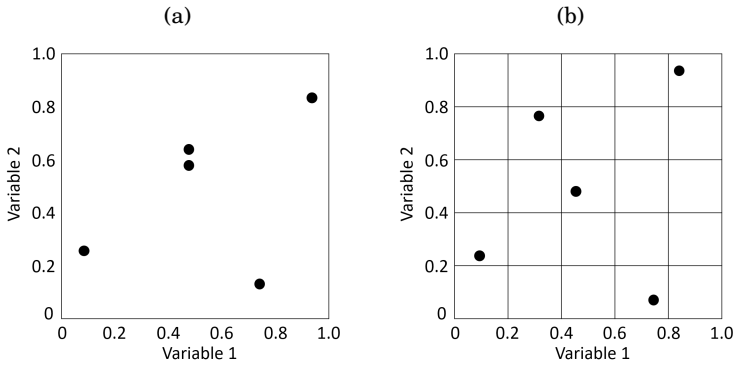

FIGURE 5.13. Representation of sampling techniques for Monte Carlo Method simulations: (a) Direct and (b) Latin Hypercube Sampling.

and their OOP displacements and rotations are set to zero. Finally, loading is assigned as a transverse force acting on nodes at $z = h_{core}$.

5.3.2 Probabilistic design analysis: methods

Probabilistic design analyses are performed with the Probabilistic Design System (PDS) tool in ANSYS Mechanical APDL [157]. Although every characteristic of the unit cell—and hence, of the FE model—is subjected to scatter (for instance, the dimensions of walls and insert, their stiffness, density and all material properties), in this PDS study only the characteristic dimensions of the insert are subjected to scatter, since they are the most uncertain parameters mainly due to manufacturing factors. All the other properties are considered deterministic values. As introduced in section 5.3.1, the output parameter of this study is the OOP Shear Modulus, G_{ZY}, which is a fundamental design parameter for sandwich constructions since it is responsible for the shear core resistance in bending behaviour for first-order sandwich theory [160, 161].

The algorithm used by the ANSYS PDS module is based on Monte Carlo Method (MCM) simulations, which involve random sampling of certain probability distributions. The main idea is repeating the experiment many times using the Law of Large Numbers and/or other methods of statistical inference [162]. MCM techniques mimic the uncertainties present in manufacturing processes, meaning that it "virtually" manufactures components one after the other. The uncertain parameters slightly vary from component to component, following a certain statistical distribution. This method offers many advantages. Firstly, assuming that the deterministic model is correct and a very large number of simulation loops are performed, the probabilistic results are always correct. However, as it is not possible to compute infinite simulation loops, it is assumed that the limited number of loops is statistically representative (this assumption can be verified by means of the confidence limits). Furthermore, the simulation loops are independent from each other, meaning that each loop does not depend on the results of any other loops.
There are two forms of MCM analyses, the Direct Monte Carlo Sampling and the Latin Hypercube Sampling (LHS) [163]. In the first type, one simulation loop represents one component subjected to

a particular set of loads and boundary conditions. This technique is not computationally efficient as it has no "memory": new sample points are generated without taking into account previously generated ones and two or more sampling points could be very close to each other in the space of all input variables, not providing any new information of the component's behaviour—figure 5.13(a). Conversely, LHS technique is more advanced and efficient as it has "memory": it avoids repeating samples that have already been evaluated. The key of this method is stratification of the cumulative probability distribution: the cumulative curve is divided into equal intervals and each sample is randomly taken from each interval (which also forces the tails of the distribution to participate to the sampling process). Figure 5.13(b) shows a Latin Square, which is a grid of samples positions containing only one sample in each row and each column. A Latin Hypercube is a generalization to an arbitrary number of dimensions: each sample is the only one in axis-aligned hyperplane containing it. LHS requires much fewer simulation loops than Direct Sampling (20% to 40% less). Therefore, MCM algorithm with LHS technique is used in the present study.

The first and most important step that is executed in the analyses is verifying the convergence level of the output parameter. Indeed, in order to verify whether the number of MCM simulations is sufficient, the unit cell Shear Modulus is plotted against the number of simulations: convergence is achieved if the curve approaches a plateau. The confidence bounds are also displayed and show the accuracy of the requested curve: as the number of simulation loops increases, their width is reduced.
Another method for making sure convergence is reached is by showing the histograms of the RI variables. A histogram is derived by dividing the range between minimum and maximum values into equal-size intervals. The software then calculates how many samples fall within each interval. If the number of simulation loops is sufficient, the histogram bars are close to the distribution function curve, are quite smooth and do not present large gaps.
Once verified that convergence is reached, the trends are post-processed. First of all, the probabilistic sensitivities are evaluated. Probabilistic sensitivities are very different from deterministic ones, as they measure how much the range of scatter of an output parameter is influenced by the scatter of the RI variables. Therefore, both the slope of the gradient and the scatter range of the RI variables have an influence on probabilistic sensitivities. To display the sensitivities, PDS groups the RI variables into one group having a significant influence on a particular random output variable and one with insignificant variables. This is based on a statistical significance test, which tests the hypothesis that the sensitivity of a particular RI variable is zero and then calculates the probability that this is true. If such a probability exceeds a certain significance level (i.e. the hypothesis is likely to be true) than that variable is rather insignificant. PDS displays a bar chart with RI variables with the highest sensitivity in the leftmost position, and the others follow to the right. This chart shows absolute values, i.e. taking signs into account: a positive (negative) sensitivity shows that increasing the value of the RI variable the value of the random output parameter for which the sensitivities are plotted increases (decreases). A pie

chart is also displayed, where the sensitivities are relative to each other.
PDS analyses are performed on the unit cell FE model described in section 5.3.1. As discussed in sections 5.1 and 5.3.1, walls properties are assumed to be deterministic, whereas the insert geometric dimensions are considered as the RI variables: figure 5.4 shows the two RI variables, A_{base} and A_{top}. The CNT-resin deposited at junction corners between walls is affected from gravity as it cures, resulting in a non-uniform distribution that is modeled with a hyperbolic shape. The effect of the uncertainties of such a distribution is studied, verifying its impact on the global properties of the unit cell, the OOP Shear Modulus G_{ZY}. Both the RI variables are assigned as a Gaussian distribution. It should be clearly stated that characteristic scatter in fillet's dimensions is not measured experimentally. However, due to the high viscosity of the CNT-resin the shape of inserts is only slightly affected by gravity effects, and hence their average thickness A_{top} is close to the nominal value, while A_{base} is usually small. Indeed, referring to figure 5.12, the manufactured inserts shape is much closer to case (b) - where the hyperbolic shape differs from the nominal, cylindrical one only due to a slight increase of the section area at the base - than case (c) - where the resin drops heavily towards the base of the cell, thus leaving a very small amount at the top. For this reason, a mean value equal to the nominal thickness of the cylindrical insert, $\mu = 1.3\,\text{mm}$ is assigned to the A_{top} distribution, with standard deviation $\sigma = 0.2\,\text{mm}$, while for A_{base} $\mu = 1\,\text{mm}$ and $\sigma = 0.2\,\text{mm}$. A hundred MCM simulation loops are performed.

5.3.3 Probabilistic design analysis: results

Figure 5.14 shows the mean value of G_{ZY} as a function of the number of simulation loops. As the plateau zone is approached around loop fifty, from which the confidence bonds width is also reduced, a hundred simulation loops certainly ensure good convergence levels and are statistically representative. This is double-checked in the histogram plots of the RI variables shown in figures 5.15(a) and 5.15(b): the histogram bars follow the Gaussian nominal distributions smoothly and with no gaps.

Once verified the convergence level, data trends are post-processed. Figure 5.16 represents the probabilistic sensitivities of the OOP Shear Modulus. It is clear that, albeit both RI variables are significant, G_{ZY} is much more sensitive to uncertainties in A_{top} than in the "extra" material that differentiates the hyperbolic distribution from the cylindrical, A_{base}.

The fact that A_{base} is not significant to the global mechanical properties of the unit cell is positive from the manufacturing standpoint. Indeed, albeit the inserts might not be perfectly cylindrical due to the effect of gravity and thus present a certain variability in their shape, this does not affect significantly the core global properties.

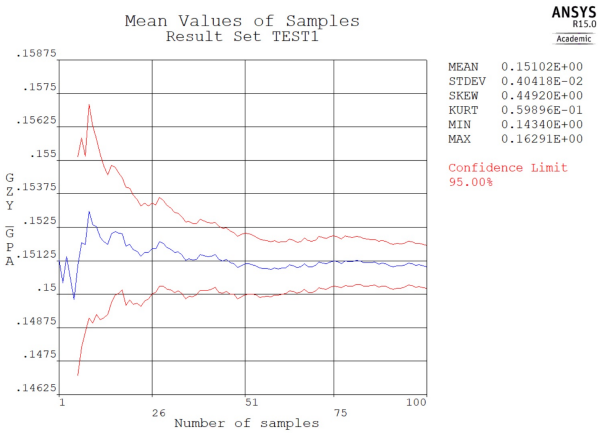

FIGURE 5.14. PDS analyses convergence check: output parameter G_{ZY} [GPa] mean values versus the number of loops.

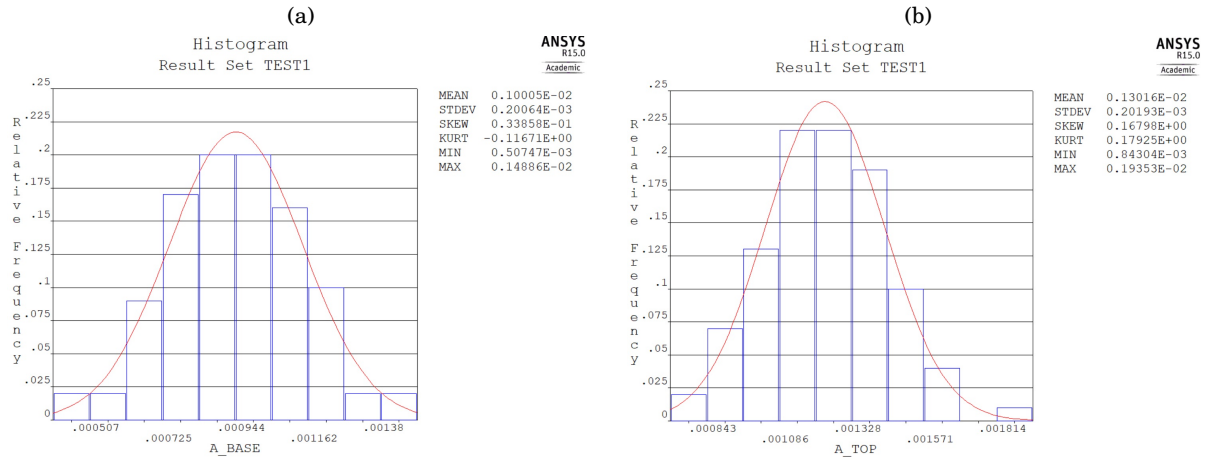

FIGURE 5.15. PDS analyses convergence check in case of output parameter G_{ZY}: RI variables histograms.

5.4 Conclusions

This chapter described the procedure adopted to design the viscoelastic inserts of the novel natural-fibre sandwich panel, the manufacturing procedures and techniques of panels specimens and a probabilistic design study of uncertain parameters due to manufacturing-related factors. The insert's thickness was defined by setting a limit of 5% to the percentage of mass added to the lattice core by the inserts. In the manufacturing process, attention was paid to obtain a homogeneous distribution of the resin through the thickness of the lattice core. Regardless, a probabilistic design analysis was performed to check the significance of the inserts geometric uncertainties to the global properties of the sandwich core unit cell. It was verified that the deviation of the shape of the insert from the cylindrical one due to gravity effects is only marginally significant to the unit cell global properties.

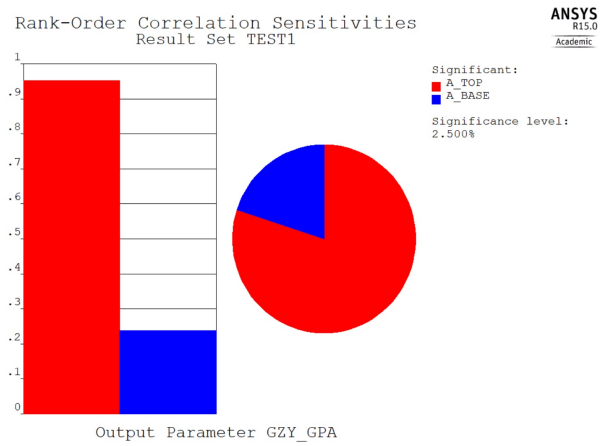

FIGURE 5.16. PDS analyses trends post-processing: output parameter G_{ZY} probabilistic sensitivities.

Next chapter will present numerical and experimental procedures adopted for static, dynamic and acoustic characterization of sandwich panel specimens.

CHAPTER 6

EFFECTS OF CNT-INSERTS ON STATIC, DYNAMIC AND ACOUSTIC PERFORMANCES OF NATURAL-FIBRE SANDWICH PANEL: METHODS

Contents

6.1 Introduction

IN PREVIOUS chapters, materials constituting the novel natural-fibre based sandwich panel with CNT-inserts were investigated in terms of manufacturing/curing techniques, mechanical and thermo-mechanical properties (Chapters 3 and 4). Afterwards, FE models of the sandwich panel unit cell were implemented and the inserts were designed by setting a limit on the percentage of additional mass (Chapter 5). Several sandwich panels specimens were then manufactured for different types of experimental tests.

This chapter presents methods, techniques and procedures adopted for the quasi-static, dynamic and acoustic characterization of bare and reinforced sandwich panel specimens. In the

first section, focus is on quasi-static out-of-plane (OOP) characterization of core lattices under flatwise compression loading: techniques adopted for experimental tests as well as for analytic and numerical predictions are presented. In the second part, methods used for numerical and experimental dynamic characterization of the entire sandwich panels are described. Finally, last section explores methods adopted for the acoustic measurements by means of an impedance tube.

6.2 Quasi-static flatwise compression tests

The novel sandwich panel developed in this work is specifically designed for vibroacoustics applications: its constituting materials are, indeed, chosen due to their well-known high mechanical energy dissipation properties. Nevertheless, the cores of these sandwich structures must provide structural integrity along with the good vibroacoustic performances. Highly damping materials like natural composites might decrease the overall mechanical efficiency of the core lattices because of their general lower stiffness and strength compared to traditionally adopted core materials: as a matter of fact, natural fibres have been and still are extensively adopted in industry, but mainly in secondary load bearing applications like automotive interiors and non-critical packaging [59–61]. For these reasons, OOP compression characterization is executed on the core lattices along with the vibration and acoustic tests: OOP compression strength is, in fact, one of the key metrics to assure for structural integrity [1] and a paramount investigation for quality assurance.
This section describes the methodologies adopted for quasi-static flatwise compression characterization of bare and reinforced sandwich panels cores. Lattice samples are built according to the manufacturing process described in section 5.2. Following paragraphs present FE models and settings of flatwise compression simulations, formulations for analytic assessments and techniques and setup of experimental validation.

6.2.1 Analytic formulations

Failure mechanisms of high-density honeycomb cores ($\rho/\rho_s > 0.1$) under compression loads can be very different from low-density cores ($\rho/\rho_s < 0.1$), such as Nomex or aluminium honeycombs manufactured by sheet corrugation or expansion methods. Under OOP compression loading, these structures are characterized by linear elastic behaviour before elastic buckling leads to non-linear behaviour [164]. In this case, the maximum load is identified at the beginning of the folding collapse mode. Instead, high-density honeycombs loaded in the OOP direction can be characterized by fracture failure. This happens when the net section stress in the plane normal to the load direction exceeds the fracture stress of the core walls material [2]. In this study, the fracture stress of the bare lattice core is approximately estimated from the tensile strength value. Indeed, albeit compressive tests on the Evopreg flax/PFA laminates would provide more precise assessments of the OOP compression characteristics of the cores, compression strength and damage behaviour go beyond the objectives of the modelling and usually tensile tests provide

sufficiently accurate evaluations of such properties without running into the complexity of compression testing. Therefore, the fracture stress of the bare lattice core is evaluated as:

$$\sigma_z = \sigma_{fs}\frac{\rho}{\rho_s} \tag{6.1}$$

where the core walls material fracture stress σ_{fs} is simply scaled by a factor equal to the lattice relative density, ρ/ρ_s. Following the same approach, the bare core's OOP stiffness can be approximately evaluated from the walls solid tensile modulus E_s as:

$$E_z = E_s\frac{\rho}{\rho_s} \tag{6.2}$$

Similarly, the insert-reinforced core properties are evaluated as:

$$\sigma_z = \frac{A_w * \sigma_{fs} + A_i * \sigma_{fi}}{A_{cell}}; \quad E_z = \frac{A_w * E_s + A_i * E_i}{A_{cell}} \tag{6.3}$$

In previous equations, $A_w = 2t_w l - t_w^2$ and $A_i = \pi t_{ins}^2$ are the walls and insert's transverse areas respectively, being t_w the thickness of the core walls, t_{ins} the thickness of the insert at one corner of the walls junction and l the width of a unit cell; σ_{fi} and E_i are the CNT-resin's strength and tensile stiffness, respectively, and $A_{cell} = l^2$ is the transverse area of a unit cell.

6.2.2 FE modelling

Non-linear static simulations are performed in ANSYS Mechanical APDL R15 to predict the OOP characteristics of bare and reinforced core samples. FE models derive from those of the unit-cell described in section 5.3. However, the insert shape is here simplified as an equivalent parallelepiped with same volume as the cylindrical-shaped insert. This simplified model of the unit cell allows to have a lighter mesh for the full-scale lattice (5x5 cells), which is obtained by shifting the cell along the two in-plane orthogonal directions - figure 6.3.
In order to define the minimum number of elements which allows to have accurate numerical results, a Mesh Convergence study is performed. A Mesh Convergence study verifies that results converge to a solution as the mesh becomes finer, and it also provides a justification for Mesh Independence and unnecessary additional refinement:

- Mesh Convergence: The response of the system converges to a repeatable solution as the element size decreases.
- Mesh Independence: Following convergence, additional mesh refinement does not affect results.

The study is performed on the model of the bare panel specimen utilized for flatwise compression characterization.

Using an iterative method, the number of elements increases along each side of the specimen—walls thickness, unit cell semi-width and core height. The complexity of the model (i.e. number of

	Case		1	2	3	4	5	6	7	8	9
FEA Mesh Characteristics	Number of divisions	Thickness	2	2	2	2	4	4	4	8	8
		Width	2	2	4	8	8	16	24	24	32
		Height	2	3	6	12	12	24	32	32	48
	Number of elements		800	1200	4800	19200	38400	153600	230400	614400	1228800
FEA Results	Max displacement x 10^{-6} [m]		-3.579	-3.600	-3.633	-3.644	-3.651	-3.656	-3.657	-3.660	-3.661
	Error [%]		-	0.60	0.90	0.33	0.18	0.14	0.03	0.07	0.02
	Computational time [min]		0.02778	0.02778	0.05556	0.1111	0.2778	1.111	2.361	10	26.03

FIGURE 6.1. Case studies and results of Mesh Convergence analysis.

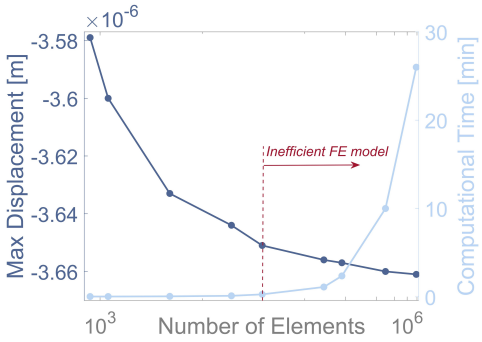

FIGURE 6.2. Results of Mesh Convergence analysis. Maximum displacement and computational time vs increasing number of elements (x axis in logarithmic scale).

elements) and the response of interest (maximum OOP displacement under a unitary pressure load) are recorded. Figure 6.1 shows the mesh size vs deflection and solve time for each case study. Figure 6.2 presents the relative curves, where the x axis (number of elements) is plotted with a logarithmic scale.

By analysing the Convergence study results, it is clear that by decreasing the elements size the mesh becomes very inefficient starting from Case 4, as the complexity of the model increases noticeably without providing any essential contribution to the accuracy of results. Therefore, for both bare and reinforced configurations, the FE models utilized to simulate flatwise compression tests are based on the mesh of Case 4, with an average element size of 1.25 mm. In particular, due to the presence of the insert, the reinforced models have a slightly finer mesh in correspondence of the insert itself and through the walls thickness.

Figure 6.3 shows the final mesh of unit cells and entire specimens. The bare unit cell is modelled with 768 elements and 1313 nodes while the bare lattice with 19200 elements and 31265 nodes; for the reinforced configuration, the cell model has 1296 elements and 1850 nodes, whereas the entire lattice 32400 elements and 44250 nodes.

For what concerns the material properties, multilinear isotropic hardening models are adopted in the plastic range: for each material (i.e., the 0/90° Evopreg PFC-flax laminates for lattice walls and the CNT-reinforced SS CLV Epoxy Bio-resin for the insert CNT-resin), twenty discrete points

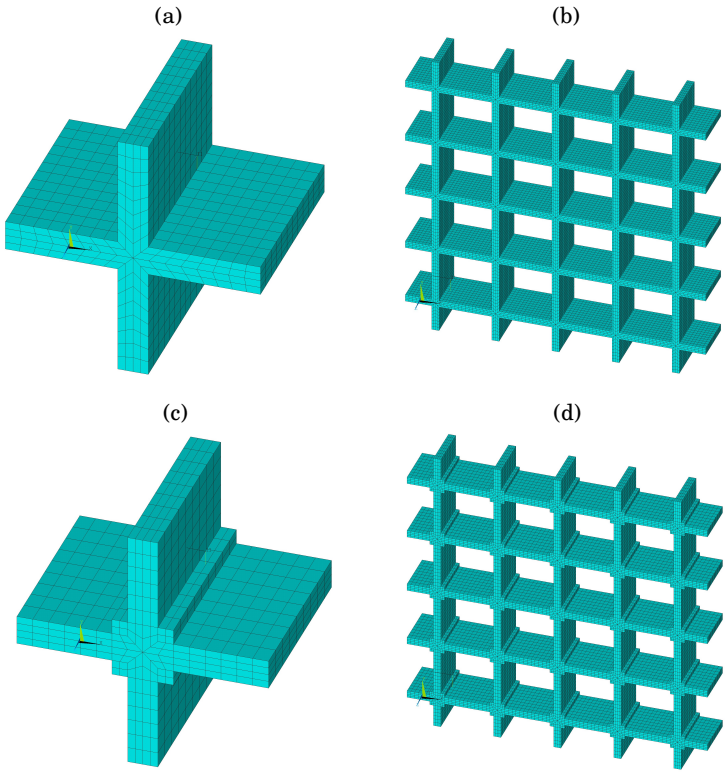

FIGURE 6.3. FE model of bare and reinforced core for flatwise compression simulations: (a) bare, unit cell; (b) bare, entire lattice; (c) reinforced, unit cell; (d) reinforced, entire lattice.

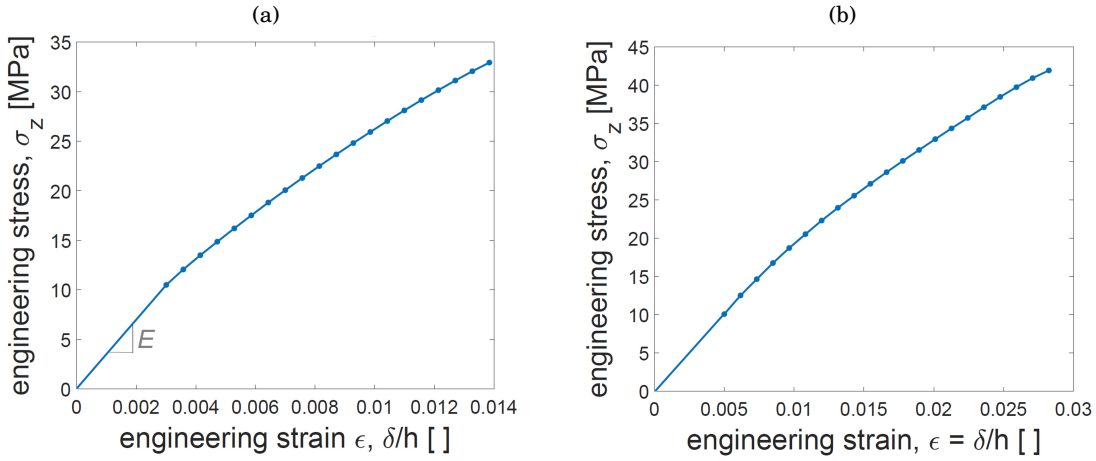

FIGURE 6.4. Multilinear hardening models for (a) Evopreg PFC-flax and (b) CNT-reinforced SS CLV Epoxy Bio-resin from ASTM tensile tests average curves.

are taken from the experimental mean stress-strain curves measured in the tensile tests – figures 6.4(a) and 6.4(b).

Three different models are considered for each one of the two configurations. The first one (Model 1) is that of the entire lattice. Here, the OOP displacement u_z degree of freedom at $z = 0$, i.e. one of the two transverse faces, is constrained to zero, whereas in-plane u_x and u_y displacements of these nodes are allowed. The central node of the face at $z = 0$ has all degrees of freedom constrained to zero. On the other side, the OOP displacements u_z of all nodes at $z = h_{core}$, i.e. the opposite transverse face, are coupled and only the central node of this face has the in-plane u_x and u_y displacements constrained to zero.
The second and third models both contemplate only the unit cell of the periodic structure. However, in these models two different sets of boundary conditions are applied in order to verify which one of them better represents the behaviour of the entire periodic specimen.
The boundary conditions applied to the faces at $z = 0$ and $z = h_{core}$ are the same in these two models. At $z = 0$, the u_z degree of freedom of all nodes is constrained to zero, whereas the central node of this face is fixed—all degrees of freedom are constrained to zero. At $z = h_{core}$, all nodes have coupled OOP displacements, u_z, while the central node of this face has the in-plane u_x and u_y displacements constrained to zero.
What differentiates the two FE models is the set of boundary conditions applied to the four edges of the cell to simulate the presence of adjacent cells. In particular, in the second model (Model 2) sliding boundary conditions are applied to the edges—i.e., the displacements in the orthogonal direction to the edge's face are constrained to zero. In the third model (Model 3), in-plane degrees of freedom of nodes on the edges' faces are coupled. The real behaviour of the lattice structure is expected lie between that of these two models of the unit cell, since the absence of face skins allows in-plane displacements to happen, but at the same time they are limited by the presence of adjacent unit cells. Large deflections are allowed for these non-linear analyses. Small deflection and small strain analyses assume that displacements are small enough that the resulting stiffness changes are insignificant. Instead, by allowing large deflections the solution contemplates stiffness changes resulting from changes in element shape and orientation due to large deflection, large rotation and large strain and, therefore, results are more accurate. Allowing large deflections requires an iterative solution and it needs the load to be applied in small increments [157]. For this reason, a static pressure load is applied to the nodes at $z = h_{core}$ incrementally, by dividing it into sub-steps.

Once the simulation is solved, stress values are evaluated by averaging mean reaction forces along the z-axis and by homogenizing over the cross-section area of the cell or lattice. More explicitly, z-components of reactions at $z = 0$ are averaged. The mean value is hence multiplied by the number of nodes at $z = 0$ and, for the unit cell models only, by the ratio between the transverse areas of lattice and unit cell - that is the number of unit cells contained in the core specimens. The mean reaction force is then divided by the cross-section area to evaluate the value of stress.

FIGURE 6.5. Setup of quasi-static OOP flatwise compression tests on sandwich panels cores.

6.2.3 Setup for experimental validation

Quasi-static OOP flatwise compression tests are performed on bare and reinforced core specimens by means of an Instron 600DX testing machine. For each configuration, five specimens with non-stabilized faces (i.e. only cores, no skins adopted) are tested. The samples have a transverse area of 100 mm x 100 mm, containing 25 unit cells (5 for each in-plane, orthogonal direction) - figure 6.5.

Experimental tests and data processing are performed according to the ASTM C365/C365M - 16 (Standard Test Method for Flatwise Compressive Properties of Sandwich Cores) and all data is post-processed in MATLAB R2018a.

The linear elastic range used for the evaluation of the Compression Modulus is $\epsilon \in [0.6 \div 1.6]\%$ for the base configuration, $\epsilon \in [2 \div 3]\%$ for the inserts reinforced configuration. The strain plotted in the $\sigma(\epsilon)$ curves is the engineering strain, $\epsilon = \delta/h$, being $h = h_{core}$ the initial core height. Finally, all data undergoes the Chauvenet criterion [133] to define the outliers to not be considered in the evaluation of the batches statistic properties.

6.3 Dynamic characterization

Two different types of dynamic tests are performed: OOP vibration transmissibility tests on small-scale sandwich panels and frequency response analyses on large-scale panels. The following sections explore methods adopted for numerical predictions and experimental validation for these two types of tests.

6.3.1 OOP vibration transmissibility of small-scale sandwich panels

The analytic definition of vibration transmissibility ratio for single-degree-of-freedom (SDOF) systems and the formulations and procedure for its experimental evaluation were shown in detail in sections 2.2.3 and 2.2.4. This section briefly summarizes the experimental tests procedure.

Vibration transmissibility tests contemplate shaker-excited SDOF systems which can provide accurate measurements of amplitude and phase over a wide frequency range [42]. Figure 6.6 shows a schematic representation of such system: the specimen is subjected to excitation at the base by an electromagnetic shaker and the acceleration is measured at base and top of the specimen. Other than the mass of the specimen, m, the mass of the accelerometer at the top (or other means of measuring acceleration) and any mass/weight added on the sample must be taken into consideration, M.

The resonance peak amplitude, A, is determined as the ratio of the accelerations measured by the accelerometers, $A = |X/X_0|$, where X is the free response measured at the top of the specimen and X_0 that measured at the base. Furthermore, the modulus k at the resonance frequency ω_R (radians/second) is evaluated as:

$$k = (M + m/3)\omega_R^2 \tag{6.4}$$

and the loss factor η as:

$$\eta = \frac{1}{\sqrt{A^2 - 1}}. \tag{6.5}$$

Next sections will present methods adopted for FE modelling of vibration transmissibility tests and procedures for experimental characterization.

6.3.1.1 FE modelling

FE simulations of OOP vibration transmissibility tests are performed in ANSYS Mechanical APDL on the lattice core unit cell model described in section 6.2.2, this time provided with face skins. Figure 6.7 shows the corresponding meshes utilized for bare and reinforced configurations. Mechanical properties of materials are assigned as per results of materials experimental characterization. Specifically, damping is assigned as internal material damping and the values are those from DMA tests at room temperature and 1 Hz frequency, reported in sections 4.2.2.2 and 4.3.2.3. Perfect bonding is assumed between components - i.e. between interlocked walls,

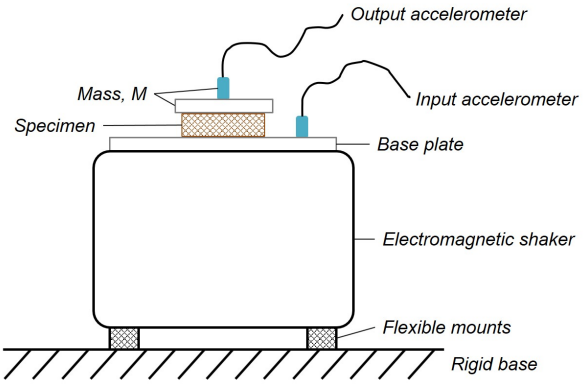

FIGURE 6.6. Structural-scale tests: schematic drawing of shaker-excited SDOF system tests (OOP vibration transmissibility).

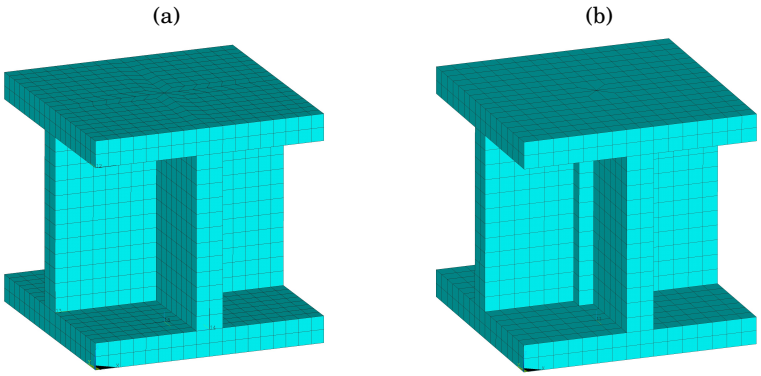

FIGURE 6.7. Vibration transmissibility FE simulations: mesh of (a) bare and (b) reinforced unit cells.

core and skins, insert and walls - and the reinforced configuration is represented by means of a parallelepipedic insert equivalent in volume to the cylindrical one. To approximate the presence of the surrounding structure, sliding boundary conditions are applied to the four edges of the cell. On the other hand, special attention is paid to the boundary conditions at the top and bottom faces. The nodes at the top of the unit cell are linked via master-slave multi-point constraints (MPC) connection (CERIG rigid region in APDL), the master node being the one at the centre of the face. Thereby, the mass M (given by the weight placed at the top of specimen and the top accelerometer, as described in previous section) is applied to the master node of such rigid connection as a MASS21 element. Since results of simulations will be compared to experimental outcomes, the properties of this element - i.e. the mass value - are evaluated by considering the mass utilized in the experimental tests. In particular, by assuming that in the experimental tests the mass on the specimen is distributed uniformly on its transverse area, M is given by the experimental mass scaled by the ratio of transverse areas of specimen and unit cell— $50.8 * 50.8$ mm^2/$20 * 20$ mm^2 = 6.45. For what regards the bottom face, a master-slave

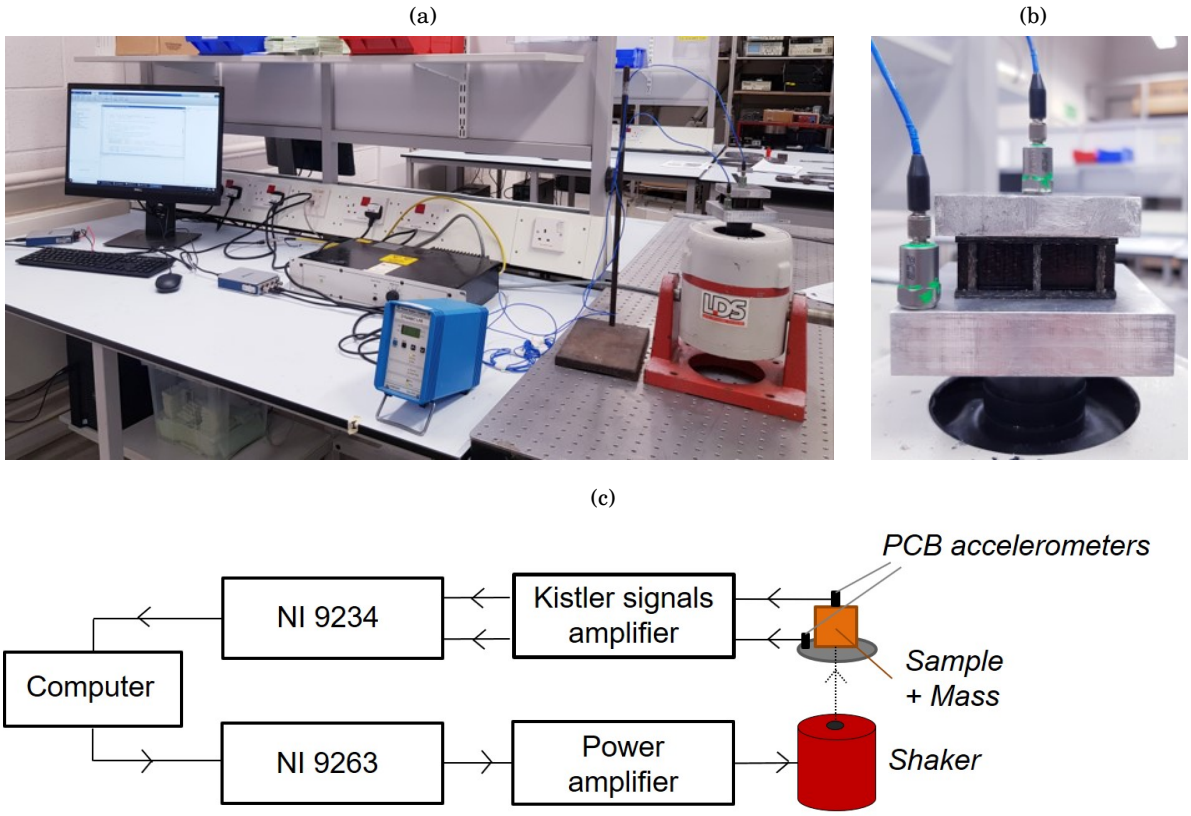

FIGURE 6.8. (a) Experimental setup of vibration transmissibility tests and (b) detail of the specimen configuration. (c) Schematic representation of experimental setup.

MPC connection is applied also to its nodes: a harmonic excitation is applied to the system by imposing an harmonic displacement between 0 and 10 kHz to the master node of this MPC. 1000 substeps are evaluated in the frequency range and the frequency step is decreased to 1 Hz around the resonance peak to capture it with precision. Finally, vibration transmissibility spectra are evaluated from the ratio between top and bottom OOP displacements.

6.3.1.2 Experimental tests

Figure 6.8 shows the experimental setup of vibration transmissibility tests. The instrumentation consists of:

- Lyng Dynamic System (LDS) electromagnetic shaker and power amplifier;
- Support table with Newport I-2000 Vibration Isolation Stabilizers;
- Four-channel signal acquisition module, National Instruments (NI) 9234 (accelerations: analog to digital signals);
- Voltage output module, NI 9263 (excitation: digital to analog signal);

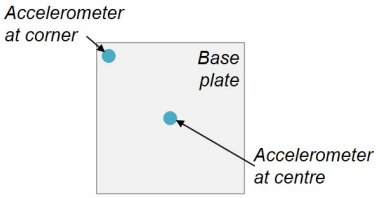

FIGURE 6.9. Preliminary investigations of vibration transmissibility experimental tests: analysis of resonances of the rig.

- Kistler signals conditioning system for accelerations;
- Computer for controlling the shaker and processing output data.

The specimens adopted for these experimental tests are one bare and one reinforced sandwich panels. These same specimens are used for acoustic characterization tests (which will be presented in section 6.4), hence their in-plane area is dictated by the dimension of the inner cavity of the impedance tube, which is 50.8 mm x 50.8 mm.

Prior performing the actual tests on the sandwich panels specimens, some preliminary investigations are carried out on the bare sandwich panel sample.
The first preliminary investigation to be performed is on the rig only, i.e. with no specimen mounted on it. In order to investigate any resonances or anomalous behaviour of the rig, the two accelerometers are placed at the centre and at one corner of the base plate (figure 6.9) and the transfer function in terms of amplitude (transmissibility) and phase is evaluated.
All the other preliminary examinations are performed with the bare specimen mounted on the rig according to the setup displayed in figure 6.8. Thus, a study of bonding techniques between sample and mass at the top is conducted. While the bottom face of the specimen is bonded to the base plate by means of superglue, the top surface and the mass are attached by means of a very strong and thin type of double-sided tape applied to one of the surfaces of the mass. To prevent any movements between the two pieces, a drop of superglue is deposited at the centre of the top surface of the specimen.
Successively, the response of the specimen to different types of excitation (Gaussian noise and stepped-sine) are compared. For what concerns the stepped-sine excitation, a 50 Hz step is adopted in the entire range, save the frequency span surrounding the peak of resonance for which a finer step is utilized. The sine wave measurements last 10 seconds, albeit only the steady-state response (1 second measured at the end of the time signal to make sure that all transient effects have been dissipated, see section 2.2) is used to evaluate the Transfer Function between input and output signals. Regarding the Gaussian noise excitation, each measurement lasts 20 seconds. The specimens then undergo Gaussian noise excitation with increasing amplitude levels amplitudes (0.1 V, 0.5 V and 1 V) to determine any non-linearities of the specimens themselves.
Finally, a series of experiments with different masses placed at the top of the sample is performed

to select the one to use for the actual tests.
Results of these initial investigations will be presented in next chapter (section 7.3.1). Following, the definitive settings adopted for the actual tests after these preliminary studies are reported. The frequency range is set to $0-6000$ Hz with sampling frequency of the input signal set to 25600 Hz. Superglue is adopted to attach all the components - i.e. the specimen to the base plate and the mass, one accelerometer to the base plate, one accelerometer to the top mass. Finally, Gaussian noise with amplitude 1 V and a mass of 129 gr are adopted.

For what concerns the post-processing of data, signal processing is executed in Matlab environment. For the stepped-sine excitation, signals are filtered with a band-pass Hamming filter of 30^{th} order. The Frequency Response Function is computed for signals at each single frequency in terms of single-sided spectrum (that is, the negative side of the spectrum can be recovered by simply mirroring the positive side). Finally, the vibration transmissibility is evaluated as the ratio between the maximum amplitudes of output and input signals at each frequency value.

6.3.2 Frequency response analyses of large-scale sandwich panels

Frequency response tests are performed on one bare and one reinforced large-scale sandwich panels (transverse area 680 mm x 680 mm) in the Ecole Centrale de Lyon facilities (Laboratory of Tribology and Systems Dynamics, LTDS).

The frequency response of the system is evaluated both numerically and experimentally and the resulting spectra are compared. Essentially, a frequency response function (FRF) is a representation of the relationship between input and output of two points in a system.
The basic formula for a frequency response function $H(f)$ is

$$H(f) = \frac{Y(f)}{X(f)} \tag{6.6}$$

$Y(f)$ and $X(f)$ are respectively the output and the input to the system in the frequency domain, that is the Fourier Transform of the corresponding signals in time domain, X(t) and Y(t). Details of the techniques according to which FRFs are evaluated from numerical analyses and experimental tests are described in the following sections.

6.3.2.1 Numerical assessments

FE models of the two sandwich panels (implemented in ANSYS Mechanical APDL R15) are based on the unit cells described in section 6.3.1.1 for the OOP vibration transmissibility simulations. However, the mesh utilized in this case is considerably coarser (figures 6.10(a) and 6.10(b)), in order to reduce the high computational cost which is due to the large dimensions of the sandwich panels. Indeed, the unit cell is shifted along the two in-plane orthogonal axes 34 times to obtain the final panel (total number of unit cells: 1156). With this coarser mesh, the bare unit-cell

model contains 238 nodes, while the entire panel model 203188. Similarly, for the reinforced configuration the unit-cell model has 398 nodes, whereas the entire panel model 370196. All simulations are run in free-free boundary conditions.

Modal analysis simulations are performed first to extract eigenvalues and eigenvectors in the frequency range $0-1000$ Hz. For this analysis, the damping of the systems is neglected: it is, in fact, useful to analyze damped systems by neglecting damping terms at first, in order to explore fundamental dynamic properties such as the modal characteristics (undamped natural frequencies and mode shapes) [48]. Preconditioned Conjugate Gradient (PCG) Block Lanczos method [157] is adopted to extract the first twelve modes (six rigid and six elastic modes). This method internally uses the Lanczos algorithm [165] combined with the PCG iterative solver. It is the best method to use to extract few modes (up to 100) of very large models (even with more than $1,000,000$ degrees of freedom) [166].
Once the system natural frequencies are known, harmonic analyses are performed by assigning internal material damping ratios, ζ, to the model. These values are retrieved from the DMA results by averaging $\tan\delta$ values at room temperature and 1 Hz frequency. For the Evopreg PFC-flax, $\tan\delta = 2\zeta = \eta = 0.0290$ (standard deviation 0.0061) - section 4.2.2.2 - whereas for the CNT-resin $\tan\delta = 2\zeta = \eta = 0.0461$ (standard deviation 0.0057) - section 4.3.2.3. Full-harmonic analyses are performed in the same frequency range as the modal ($0-1000$ Hz) with 200 substeps (i.e. every 5 Hz), by applying a unitary cyclic excitation load at the centre of one of the skins of the sandwich panel and by reading the cyclic response at the central node of the opposite skin. The load amplitude is maintained the same for all substeps ("stepped" load). The FRF is then plotted as the output displacements spectrum. Results of these preliminary analyses are used to define the number of acquisition points for the experimental grid. This is because usually 6 to 10 points per wavelength are necessary in order to capture a sine wave. Since the number of wavelengths increases towards high frequencies, the acquisition grid is such to have 6 to 10 points per wavelength at the highest frequency of the range investigated, that is 1000 Hz.

6.3.2.2 Experimental investigations

In the frequency response experimental investigations, the sandwich panels are hung to a fixed support structure by means of thin plastic strings to resemble free-free boundary conditions. The test instrumentation consists of three "groups" of equipment.
Power input:

- Controller-Dynamic Signal Analyzer;
- Data Physics Power Amplifier;
- Data Physics Modal Shaker (cut-off 3000Hz);
- 1 BNC connector;

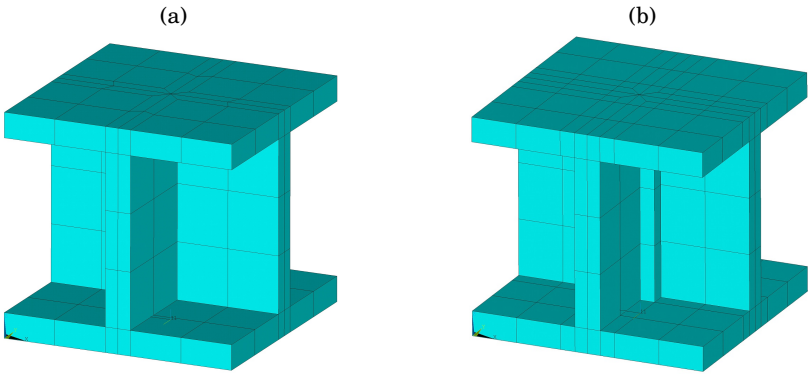

FIGURE 6.10. Modal and harmonic analysis simulations: FE models of (a) bare and (b) reinforced unit cells. These are shifted along the x- and y-axis to generate the full sandwich panels models.

Transducer:

- Mechanical Impedance Sensor PCB Piezotronics (piezoelectric transducer for force and acceleration);
- ICP signal conditioner;
- 2 Microdot cables and 2 BNC connectors;

Frequency response measurement:

- Polytec Scanning Vibrometer laser to measure and analyse vibrations;
- Reflective adhesive paper (20 vertical grid lines) - 19.6 gr, 0.3% added mass to each panel.

A schematic representation of the experimental setup is shown in figure 6.11, whereas figure 6.12 shows some pictures of instrumentation and test setup. The acquisition grid consists of 20x21 points and is marked on the panels by means of vertical strips of reflective paper. The latter allows the laser beam to be mostly reflected back to the Vibrometer and hence to ensure high signal quality. Pseudo-random noise excitation with signal amplitude 0.5 V is used and 40 averages are made for each acquisition point. As for the numerical simulations, $0-1000$ Hz frequency range is addressed, with 1600 frequency lines (sample frequency 2.56 kHz, resolution 625 mHz and sample time 1.6 seconds). The duration of each test is 7.5 hours.

Input and output measurements are used to estimate the FRF, $H(f)$. Two of the most used formulations for $H(f)$ are $H1(f)$ and $H2(f)$, which are used extensively for hammer impact or resonance analyses. Generally, $H1(f)$ is used when the output to the system is expected to be noisy compared to the input, whereas the $H2(f)$ frequency response function is used when the input is expected to be noisy when compared to the output. $H1(f)$ is defined as

$$H1(f) = \frac{S_{xy}(f)}{S_{xx}(f)} \tag{6.7}$$

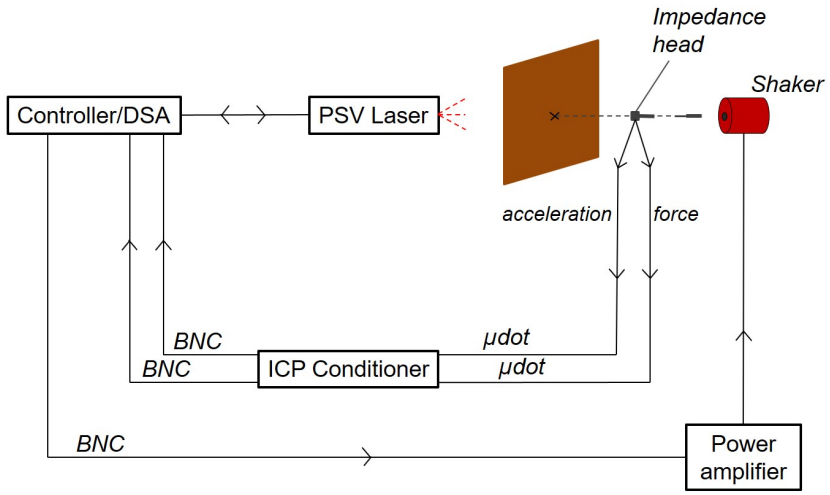

FIGURE 6.11. Frequency response experimental analysis: schematic drawing of measurement setup.

where $S_{xy}(f)$ is the Cross Spectral Density in the frequency domain of X(t) and Y(t) and $S_{xx}(f)$ the Auto Spectral Density in the frequency domain of X(t). On the other hand, $H2(f)$ is defined as

$$H2(f) = \frac{S_{yy}(f)}{S_{yx}(f)} \tag{6.8}$$

where $S_{yx}(f)$ is the Cross Spectral Density in the frequency domain of $Y(t)$ and $X(t)$ and $S_{yy}(f)$ the Auto Spectral Density in the frequency domain of Y(t). Furthermore, since a measure of the input-output behavior of a system always contemplates some noise in the input and output measurements, another important spectrum called the Coherence Function is evaluated. It is defined as

$$\gamma^2 = \frac{|S_{xy}(f)|^2}{S_{xx}(f)S_{yy}(f)} \tag{6.9}$$

and it is a real-valued spectrum measuring how much of the measured output is actually caused by the measured input. Its dimensionless amplitude varies between 0 and 1. In case of a linear system where measurements are not contaminated by noise, the measured output is everything that it is input in the system and the Coherence is 1. In a non-linear system in which there is noise at the input and/or output, it is less than 1. Consequently, a Coherence equal to 0 indicates that input and output are totally unrelated. Therefore, departures from unity can be symptom of input noise, output noise, nonlinear process or any combination of these.

For what concerns data processing, experimental data is post-processed in MATLAB R2018a and a Savitzky-Golay digital filtering [167] is applied to the signals. The FRF is measured in terms of $H1(f)$ (velocity over force) from the vibrometer and force sensor measurements. The Coherence function is also plotted to ensure good quality of measurements.
Finally, damping corresponding to the examined modes is evaluated. The loss factor at resonance

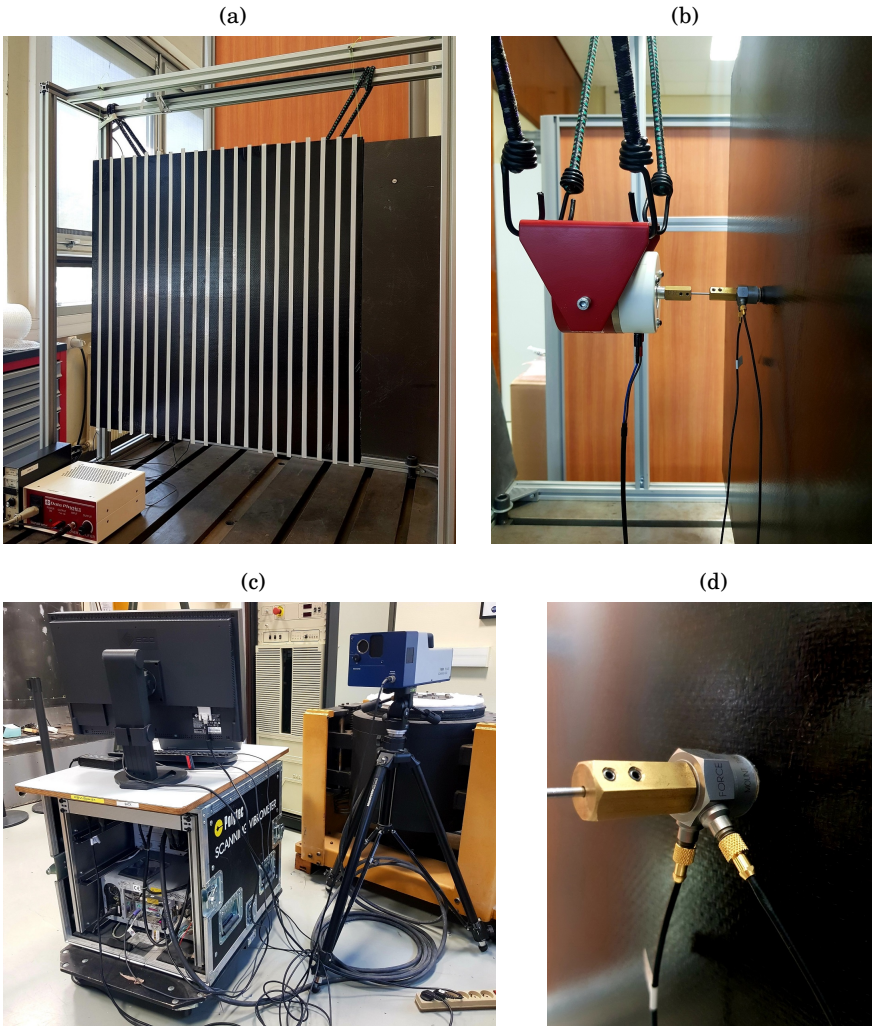

FIGURE 6.12. Frequency response experimental analysis: pictures of experimental setup. (a) Sandwich panel structure with free-free boundary conditions; (b) Data Physics Modal Shaker applied at the centre of the panel; (c) Polytec Scanning Vibrometer laser; (d) detail of the Mechanical Impedance Sensor PCB Piezotronics (piezoelectric transducer for force and acceleration).

is evaluated by the frequency-response based Half-Power Method (or 3-dB method or Bandwidth method), which was briefly introduced in section 2.3.2 among other common methods for damping estimation. Bandwidth (half-power) $\Delta\omega$ is defined as the width of the frequency-response magnitude curve when the magnitude is $1/\sqrt{2}$ times the peak value [48]. Since a factor of $\sqrt{2}$ corresponds to 3 dB, the bandwidth corresponding to a resonance is given by the width of the magnitude plot at 3 dB below that resonant peak. Referring to figure 6.13, this very consolidated method estimates the loss factor at each resonant frequency as

$$\eta = \frac{\Delta\omega}{\omega_r} = \frac{\omega_2 - \omega_1}{\omega_r}, \tag{6.10}$$

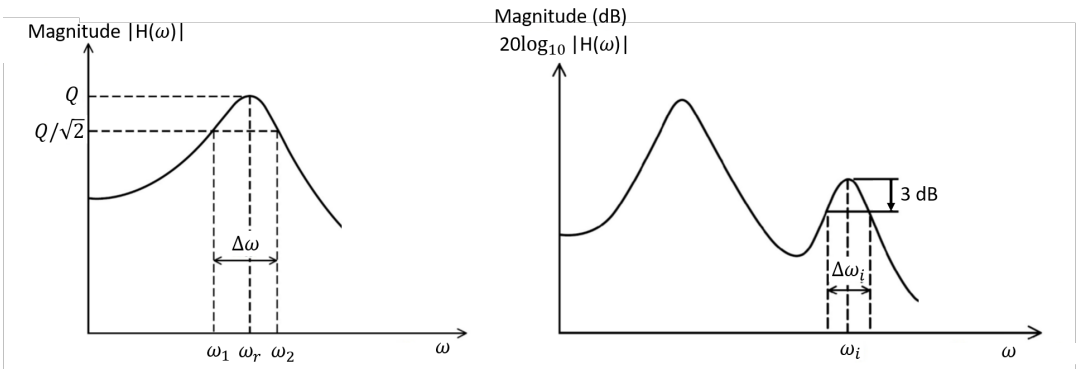

FIGURE 6.13. Bandwidth (Half Power) Method for damping measurement applied to (left) single- and (right) multi-DoF systems.

where ω_r is the resonance frequency and $\omega_{1,2}$ are the frequency values at which the amplitude of the response is

$$A = \frac{A_{peak}}{\sqrt{2}}. \tag{6.11}$$

These values are simply found by interpolating the FRF average curves around the resonance peaks.

The bandwidth method of damping measurement indicates that the bandwidth at a resonance is a measure of the energy dissipation in the system in the neighborhood of that resonance [48]. The simplified relationship given above is valid for low damping, however, and is based on linear system analysis.

6.4 Acoustic tests

Acoustics tests are performed on small-scale bare and reinforced sandwich panel specimens according to ASTM E2611-09 (Standard Test Method for Measurement of Normal Incidence Sound Transmission of Acoustical Materials Based on the Transfer Matrix Method). An in-house-built Kundt's tube is adopted for the tests. The tube is built as for the standard and is provided with four microphones and a digital frequency analysis system. Figure 6.14 shows a schematic drawing of the measurement setup. The tube has a squared section with inner cavity dimensions 2 in x 2 in. This dictates the size of specimens, which must fit into the tube without allowing any gaps at the boundaries that would deeply affect the acoustic measurements. For this reason, skins and core strips are manufactured with the same dimensions as the tube's inner cavity with high levels of precision. Where necessary, they are then carefully adjusted with sand paper to fit into the cavity (this usually means performing slight adjustments on two of the four edges of the sandwich specimens). For each one of the two configurations, three samples are tested. Five measurements are taken for each sample after re-positiong, with the purpose of taking into account not only manufacturing-related but also positioning-related variability.

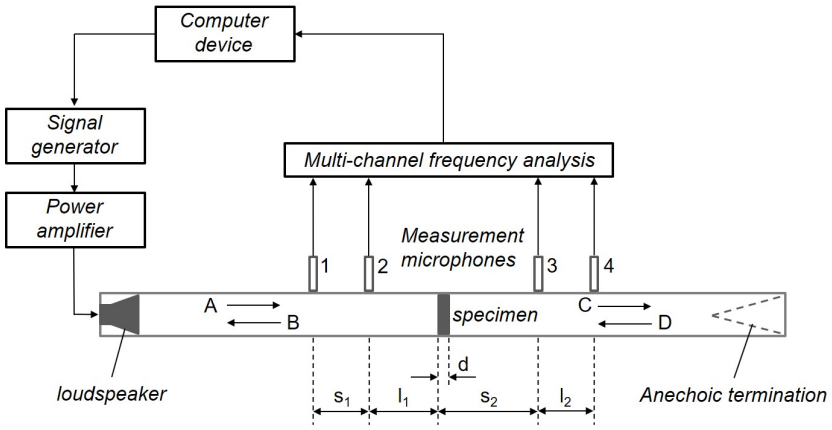

FIGURE 6.14. Acoustic impedance tube tests: schematic drawing of measurement setup.

The signal is a random noise with uniform spectral density across the frequency range. Four microphones record data with a sampling frequency of 41958 Hz. Finally, a Hanning window with 50% overlapping is applied to the signals.

The Normal Incidence Transmission Loss, TL_n, is determined as:

$$TL_n = 20log_{10}\left|\frac{1}{t}\right|, \tag{6.12}$$

where t is the Transmission Coefficient. The latter is evaluated as for the standards by applying the two-load method to determine the Transfer Matrix, TM. The method involves performing measurements with two different terminations to have four linear equations that can be solved to evaluate the four unknown TM elements. In this study, anechoic and open tube terminations are utilized. The TL then relates the acoustic pressure and particle velocity on front and back surface of the specimen. Once the TM is known, its coefficients are used to calculate the Transmission Coefficient, hence the TL_n. Details of the mathematical formulations from the ASTM standard are reported in Appendix B.

6.5 Conclusions

This chapter described the methodologies adopted for static, dynamic and acoustic experimental characterization of bare and reinforced sandwich panels. For the quasi-static OOP flatwise-compression characterization, methods for analytic and numerical predictions were also presented, whereas for dynamic vibration tests on small- and large-scale sandwich panels techniques for numerical assessments were also explored.

Next chapter presents the experimental results of the tests introduced in this chapter, comparing them - where possible - to analytic and/or numerical predictions.

CHAPTER 7

EFFECTS OF CNT-INSERTS ON STATIC, DYNAMIC AND ACOUSTIC PERFORMANCES OF NATURAL-FIBRE SANDWICH PANEL: RESULTS

Contents

7.1 Introduction

IN THIS chapter, results of quasi-static, dynamic and acoustic experimental tests on bare and reinforced sandwich panels are presented. Where possible, experimental results are compared to analytic and/or numerical assessments. Methods, procedures and techniques utilized for these tests were described in detail in Chapter 6. In the first section, results of the quasi-static flatwise compression analytic predictions, numerical simulations and experimental tests on bare and reinforced core specimens are compared. Afterwards, results of dynamic investigations are presented: outcomes of vibration transmissibility tests on small-scale sandwich panels and harmonic frequency response tests on large-scale panels are compared to their respective numerical predictions. Finally, last section shows results of acoustic Kundt's tube experimental tests on small-scale sandwich panels.

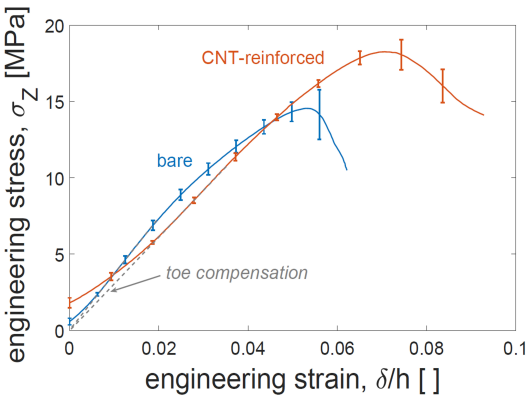

FIGURE 7.1. Quasi-static OOP flatwise compression tests: $\sigma(\epsilon)$ curves for bare and reinforced core configurations (mean curves with standard deviations).

7.2 Quasi-static flatwise compression characterization of core lattices

Figure 7.1 displays results of the OOP compression tests on bare and reinforced lattice cores in terms of stress-strain mean curves with standard deviations. Bare and reinforced lattices fail by material fracture at 147 and 183 kN respectively. Thus, the reinforced core shows an increase of 24.5% in failure stress compared to the bare one, with a 25% increment of relative density. It is possible to notice that the curves in figure 7.1—especially the one relative to the reinforced lattice—do not start from zero. This is likely due to manufacturing-related factors, and especially to imperfect flatness levels of the specimens which cause the system to undergo an initial adjustment phase as soon as some load is applied to the lattice.
Figures 7.2(a), 7.2(b) and 7.2(c) show two representative cases of failed specimens. It is possible to observe that cracks propagate along in-plane directions through the length of a core strip. In the bare lattice, cracks are quite "discontinuous" through the walls junction areas, whereas in the reinforced lattice they propagate more continuously through these zones—which is probably due to the presence of the CNT-resin at the junction.

Results of numerical simulations are compared to the experimental curves in figures 7.3 and 7.4. As explained in paragraph 6.2.2, Model 1 refers to the entire lattice, Model 2 to a unit cell with more "rigid" boundary conditions (sliding boundary conditions at the cell edges—i.e., displacements in the orthogonal direction to the edge's face constrained to zero) and Model 3 to a unit cell with more "soft" boundary conditions (coupled in-plane degrees of freedom of nodes on the edges' faces).
One first, very evident aspect that can be observed, is that the failure point under compression loading cannot be predicted with accuracy with the non-linear FE models that have been here utilized: plastic behavior of materials in tension cannot be used to describe the compression damage accumulation that is detected experimentally.

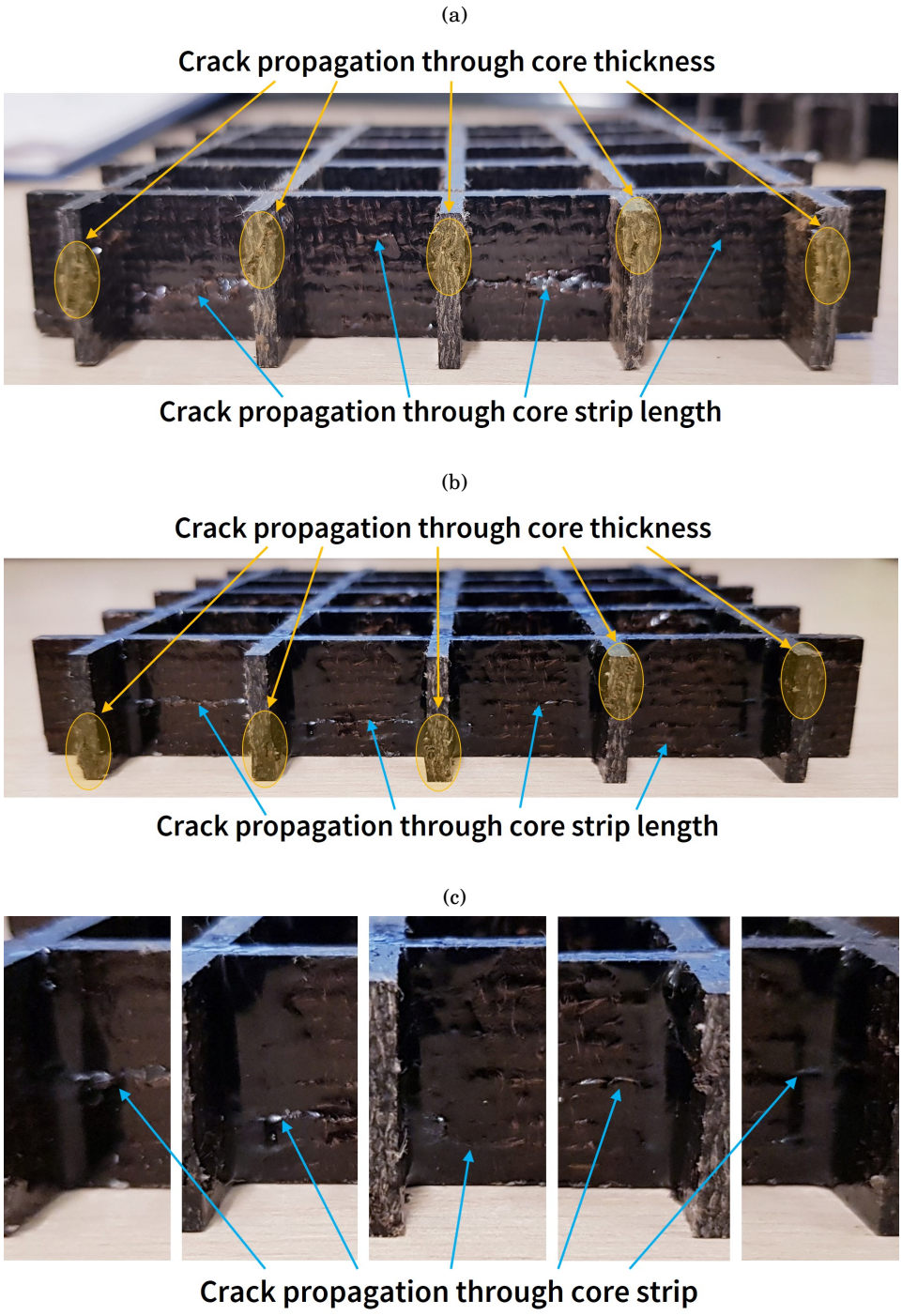

FIGURE 7.2. Examples of failed core samples under quasi-static OOP flatwise compression loading. (a) Bare and (b) reinforced configurations. (c) Detail of inserts areas.

These models, however, provide acceptable predictions of the $\sigma - \epsilon$ curve up to about $\epsilon = 0.2$. For the bare lattice, the numerical curve of Model 1 falls between the curves given by Model 2 and

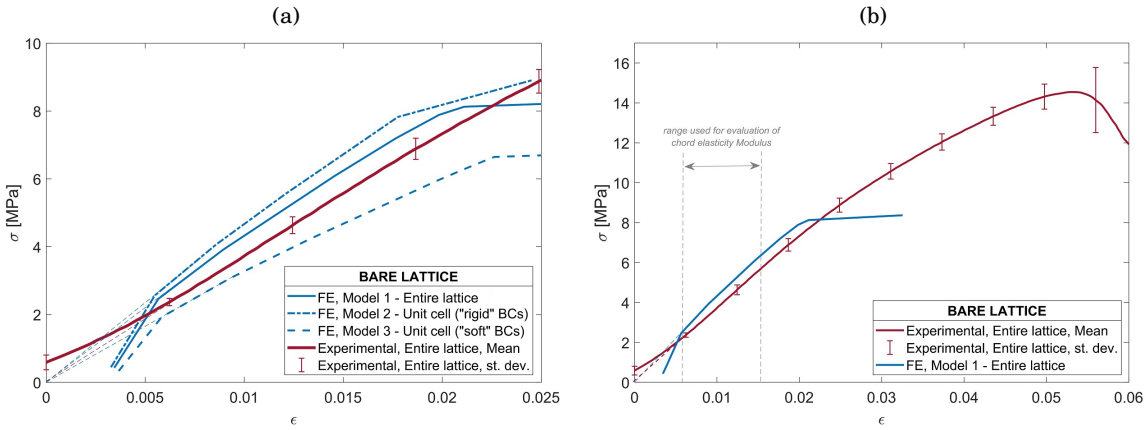

FIGURE 7.3. Sigma-epsilon curves resulting from nonlinear static FE simulations of the OOP flatwise compression tests on *bare* core specimens. (a) Comparison of different FE models and (b) entire experimental curve with most reliable numerical prediction.

3—figure 7.3. Model 1 also provides the most reliable numerical prediction, since it is the closest to the experimental results. Furthermore, Model 2 provides a more accurate assessment of the elasticity modulus than Model 3. For the reinforced lattice, results differ highly from those of the bare configuration, since in this case the model most faithfully representing the experimental behaviour is Model 3—figure 7.4. From these numerical assessments and especially from the differences in the results provided by Models 2 and 3, it is therefore evident that the compaction response of samples can be highly dependent on friction levels between the tooling plate and the sample.

Another aspect that can be noticed from figures 7.3 and 7.4 is that, for both bare and reinforced configurations, the tracts of numerical curves at low strains (up to about 0.5%) is not detected experimentally.

Finally, table 7.1 summarizes analytic and numerical assessments of bare- and reinforced-core mechanical properties comparing them with the experimental values. The numerical results reported here are those given by Model 1 for the bare lattice and Model 3 for the reinforced, which are the most accurate numerical assessments respectively.

In general, there are important discrepancies between the analytic and numerical models, and the experimental results: models do not give acceptable predictions for the strength of the structures and the characteristic strain values. Most likely, the biggest factor contributing to this is that the materials models used to simulate the structure compression behaviour are taken from experimental *tensile* characterization.

These results and the discrepancies between them will be further investigated and discussed in much more detail in Chapter 8.

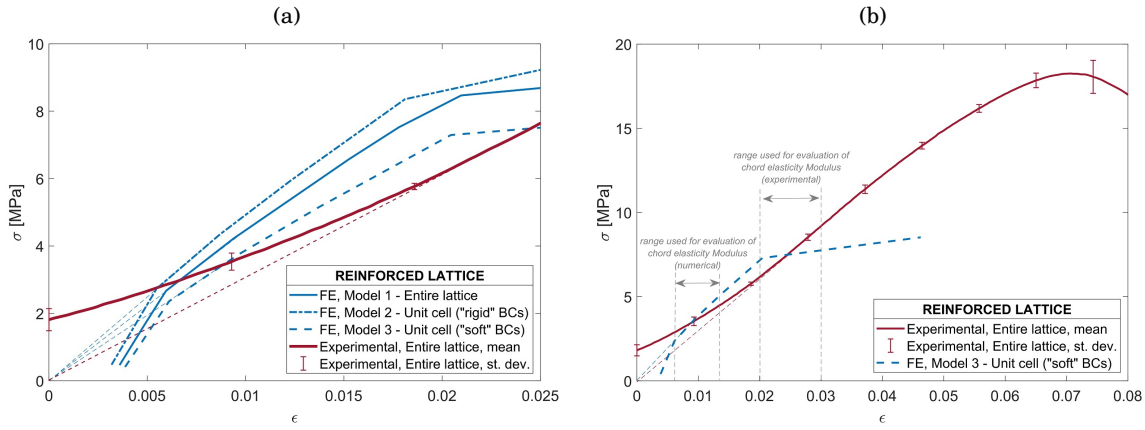

FIGURE 7.4. Sigma-epsilon curves resulting from nonlinear static FE simulations of the OOP flatwise compression tests on *reinforced* core specimens. (a) Comparison of different FE models and (b) entire experimental curve with most reliable numerical prediction.

Table 7.1: Comparison between analytic, numerical and experimental results of quasi-static OOP flatwise compression tests on bare and CNT-reinforced core specimens.

		Analytic	FE model	Tests
Bare	Failure stress [MPa]	7.71	7.9	14.7
	Compression Modulus [MPa]	848.7	442.9	374
Reinforced	Failure stress [MPa]	8.20	7.3	18.3
	Compression Modulus [MPa]	863.0	343.4	303

7.3 Dynamic characterization of sandwich panels

This section presents the outcomes of dynamic characterization of the natural-fibre based sandwich panels. As explained in section 6.3, OOP vibration transmissibility tests on small-scale specimens and frequency response analyses on large-scale panels are performed. For both types of tests, experimental results are compared to numerical assessments. Where necessary, the FE models are then updated and tuned to the experimental results in order to have a faithful numerical representation of the experimental tests.

7.3.1 OOP vibration transmissibility: FE simulations and experimental tests

OOP vibration transmissibility tests, also known as standing wave resonance method analysis [47], are executed according to the procedure described in sections 2.2.4 and 6.3.1. To start with, this section presents results of some investigation tests of the experimental set-up. Indeed, prior carrying out the actual tests on the sandwich panels specimens, a series of initial analyses have to be carried out. First of all, the rig alone is studied in order to identify any possible anomalous behaviours, resonances and so on acting in the examined frequency range. Figure 7.5(a) shows the Transfer Function (TF) of the base plate only, according to setup and

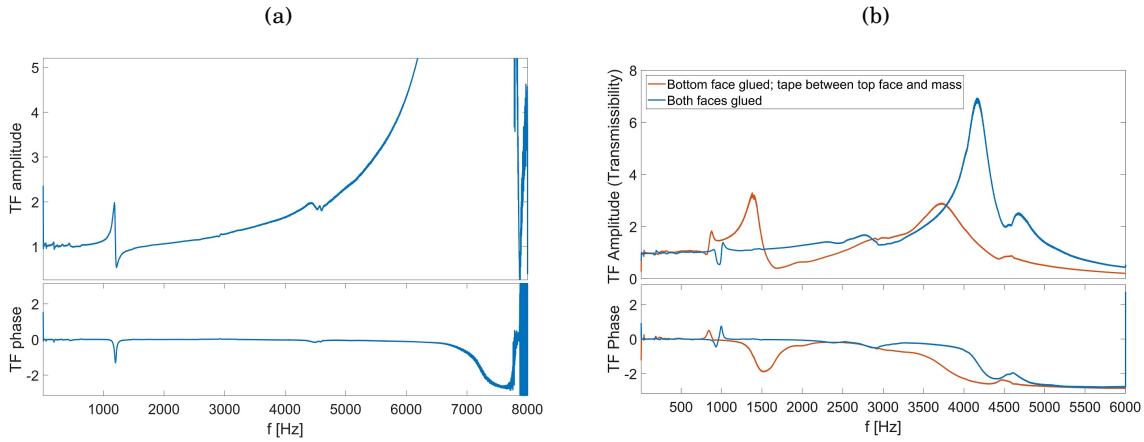

FIGURE 7.5. Experimental set-up tests. (a) Experimental rig. TF between accelerometers at centre and corner of base plate. Gaussian noise with 1 V amplitude. (b) Investigation of bonding techniques between specimen and top mass. Gaussian noise with 1 V amplitude (base acceleration rms 0.28 g). Mass at top of specimen: 129 gr.

methodologies described in section 6.3.1.2. Here, the TF is evaluated from the acceleration signals measured at one corner and at the centre of the base plate. It is possible to see that a first resonance of the plate is identified around 1100 – 1200 Hz. Some irregularities are also observed at 3000 Hz and 4500 Hz, whereas measurements become non-reliable after 6000 Hz. Therefore, in the actual tests the peak of transmissibility must not interfere with the resonances of the rig and must not fall after 6000 Hz: the mass mounted at the top of the sample must be such to avoid any overlap/interference with these frequency ranges. Besides, attention must be paid to measurements around 3000 Hz and 4500 Hz, where the rig presents some irregularities.

A second key aspect that is investigated concerns the technique used to bond the specimen to base plate and top mass. To isolate the effects, two configurations are examined. The first one contemplates a bare panel specimen attached to the base plate by means of superglue and to the top mass by means of a strong type of double-sided tape. A drop of superglue is deposited between sample and top mass as well to prevent any movements between components. In the second configuration, on the other hand, the bare specimen is attached to both base plate and top mass by means of superglue only. As introduced in section 6.3.1.2, a mass of 129 gr is placed at the top of the specimen and the excitation is Gaussian noise. Results from this analysis are shown in figure 7.5(b). It is clear that the introduction of a thin layer of tape compromises the reliability of measurements remarkably as it introduces a source of viscoelastic damping into the system. As a result, superglue is adopted for all remaining tests as technique for bonding the specimens to base plate and top mass.

Once determined the frequency range and the bonding technique, investigations are performed to compare the response of the specimen to Gaussian noise and stepped-sine excitation. Indeed,

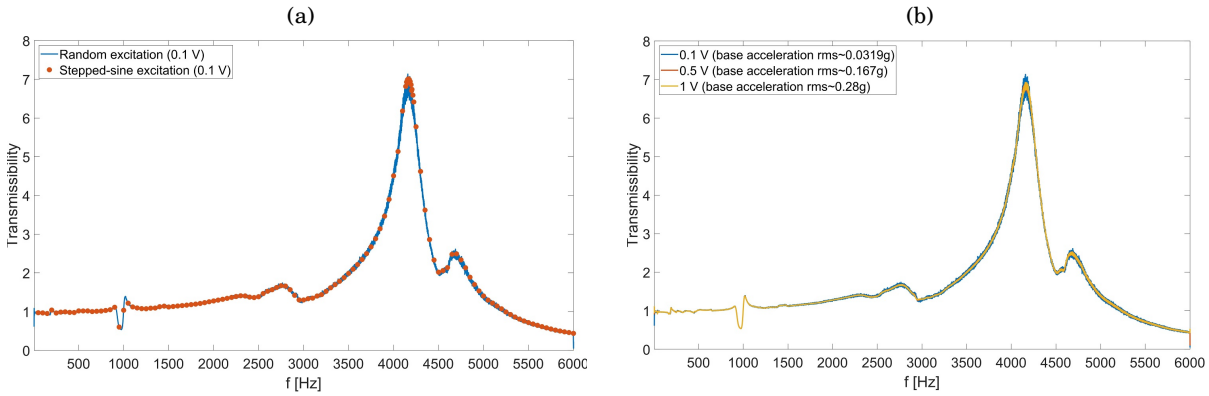

FIGURE 7.6. Tests of experimental set-up. (a) Response to different types of excitation. Excitation amplitude: 0.1 V (base plate acceleration rms 0.0319 g). (b) Linearity of sample. Mass at top of specimen: 129 gr.

single frequency sine waves allow to have more precise measurements since at each frequency the structure is subjected to a pure sine wave: by measuring the steady-state response and filtering the signals to exclude any source of noise, very high quality acquisitions can be made. However, this type of test is very time consuming by nature. On the opposite, by using Gaussian noise excitation all frequencies are excited at once, allowing to have much quicker results. For this reason, preliminary investigations are performed to check the reliability of measurements with Gaussian noise compared to those with stepped sine. As figure 7.6(a) displays, no significant differences are detected between the two cases. Therefore, Gaussian noise excitation is adopted for the remaining experiments.

In order to exclude any effects due to non-linearities of the specimen, some measurements are performed by increasing the amplitude of the input excitation and measuring any differences in the response. Figure 7.6(b) shows the results: acquisitions become more clear as the amplitude of excitation increases, but no effects of non-linearities are detected. Hence, higher amplitude of the input excitation (corresponding to a root mean square of base plate acceleration of 2.76 m/s^2) is used in the remaining tests to have clear measurements.

Finally, the behaviour of the system with several top masses is investigated to select one or more to use for the actual tests. As previously explained, the mass must be such to avoid any interference between the resonance of the specimen and that of the rig. Figure 7.7 shows the TF obtained with three different masses. Evidently, only the 129 gr one meets the requirements. Thus, this is used for the actual tests.

Figure 7.8 shows the experimental results of vibration transmissibility analyses on bare and reinforced panels. It can be observed that the configuration without inserts has a remarkably lower peak of transmissibility than that with CNT-inserts. Hence, under this particular type of OOP excitation and with these boundary conditions, the bare panel provides higher levels

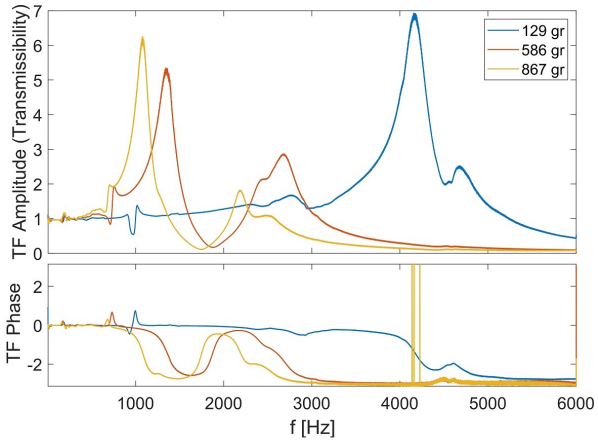

FIGURE 7.7. Effect of different masses at top of specimen. Excitation type: Gaussian noise with 1 V amplitude (base plate acceleration rms 0.28 g).

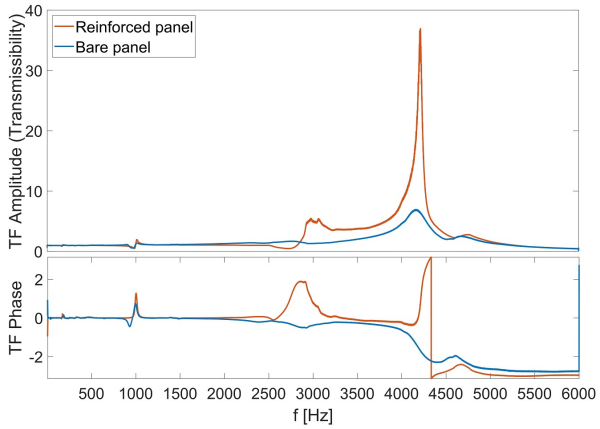

FIGURE 7.8. Results of vibration transmissibility experimental tests on bare and reinforced panels. Gaussian noise with 1 V amplitude. Mass at the top: 129 gr.

of mechanical energy dissipation than the reinforced. This is explained by the fact that the core strips in the bare panel are not glued at the junctions, thus allowing Coulomb dry friction phenomena to act in between interlocked walls. As it will be discussed in more detail in section 8.3, this mechanism is activated whenever the sandwich panel is subjected to this type of uniform OOP excitation, causing high levels of energy dissipation. Contrarily, by depositing the CNT-resin for the viscoelastic inserts at the junctions between walls, it glues the interlocked walls and hence prevents any Coulomb dry friction phenomena: in this specific load case, the viscoelastic damping provided by the inserts does not represent a relevant contribution to the overall vibration damping levels of the natural-fibre sandwich panel, which are dominated by structural damping instead. FE simulations of the standing wave resonance tests are also performed, according to the FE model described in section 6.3.1.1. Figure 7.9 shows the results for bare and reinforced configurations with several values of mass applied to the top of the specimen. At this stage,

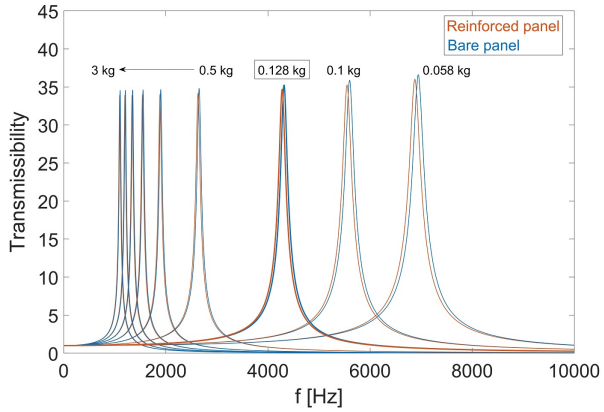

FIGURE 7.9. Results of vibration transmissibility FE simulations of bare and reinforced panels with several masses applied at the top.

the FE model of the bare configuration does not take into account the friction mechanisms between interlocking walls since perfect bonding is assumed between all components. In fact, FE simulations results show very similar curves for the bare and the reinforced case, with a slight decrease in both the resonance frequency and the peak of transmissibility due to the contribution of the viscoelastic inserts. While the bare panel FE model does not represent well the experimental tests, numerical results for the reinforced configuration agree with the experimental ones. In order to have a better representation of the OOP vibration tests for the bare configuration as well, the FE model is tuned to the experimental results by assigning a value of material damping to the entire model which is that found from the peak of transmissibility assessed experimentally (0.0725). By performing the FE simulations on this updated model, the resulting numerical curve agrees much better with the experimental behaviour. Figure 7.10 shows a comparison between experimental and numerical results of OOP vibration transmissibility tests, where the numerical curve relative to the bare panel is that obtained with the tuned model. Finally, table 7.2 summarizes experimental and numerical values of resonance frequencies, amplitudes of peak of transmissibility and loss factors for bare and reinforced panels. The loss factor is evaluated according to equation 2.17 introduced in section 6.3.1 from the amplitude of the peak of transmissibility. Table 7.2 also shows the values of amplitude of Complex Stiffness, as per formula 2.16, where the mass of bare and reinforced specimens is 30.009 gr and 31.142 gr, respectively. Hence, the Young's Modulus is calculated by applying the classic relation between Young's Modulus and stiffness for purely axial deformation, $K = EA/H$.

For the sake of completeness, values of the loss factor are also estimated by applying the Half-Power Method which was introduced in section 6.3.2.2. Table 7.3 compares the values obtained from the amplitude of the peak of transmissibility with those evaluated by Half-Power Method. For the numerical curves, it is evident that both methods give comparable results, whereas for the experimental curves the Half-Power Method loss factor's value is less than half that evaluated from the amplitude of the peak of transmissibility. The reason for this is that, probably due to

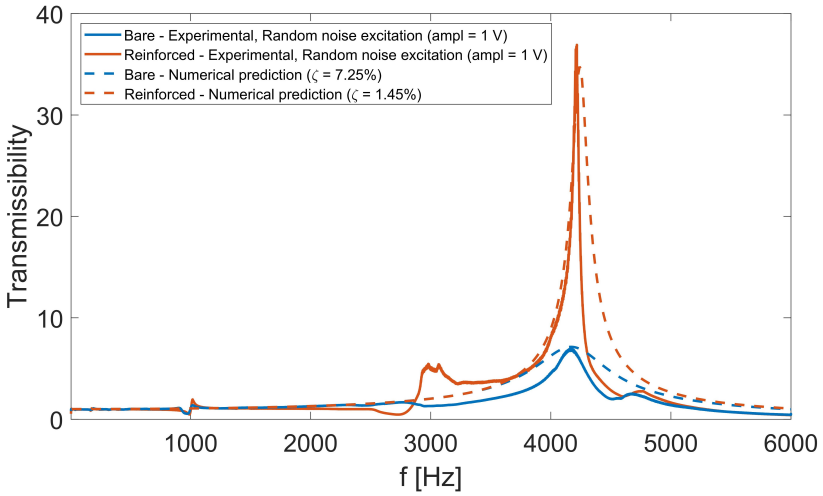

FIGURE 7.10. Comparison between experimental and numerical results of vibration transmissibility tests. Mass at the top: 129 gr.

		f [Hz]	A [ ]	η [ ]	K [N/m]	E [MPa]
Bare	Tests	4165 Hz	7.01	0.144	9.52e+07	723
	FE	4170 Hz	7.13	0.142	9.49e+07	721
Reinforced	Tests	4214 Hz	35.7	0.0274	9.82e+07	746
	FE	4240 Hz	34.8	0.0287	9.84e+07	747

Table 7.2: OOP vibration transmissibility: summary of results of experimental tests and FE simulations.

		η (Peak Amplitude Method)	η (Half-Power Method)
Bare	Tests	0.144	0.0586
	FE	0.142	0.145
Reinforced	Tests	0.0274	0.0104
	FE	0.0287	0.0294

Table 7.3: Loss factor values evaluated from the vibration transmissibility tests and FE simulations by two different method: from the amplitude of the peak of transmissibility and by applying the Half-Power Method.

experimental factors, in the experimental curves it is possible to observe a very steep drop after the peak (especially for the reinforced panel), and hence the width of the curves around resonance is narrower than the numerical ones. Therefore in our specific case the more reliable method to measure the loss factor is by calculating it from the amplitude of the resonance peak.

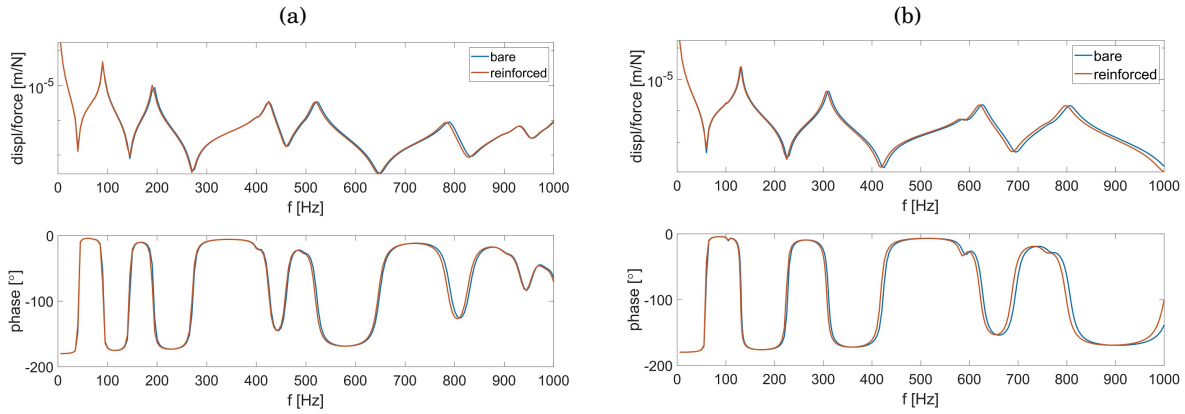

FIGURE 7.11. Harmonic FE simulations on large-scale sandwich panels: FRF H1 at the centre of the plates (displacement/force). Young's Modulus of Evopreg PFC-flax from (a) tensile and (b) three-point-bending characterization tests.

7.3.2 Frequency response analyses of large-scale panels

7.3.2.1 FE simulations

Modal numerical analyses are performed on FE models of the bare and reinforced large-scale sandwich panels, with the settings described in section 6.3.2.1. These first simulations allow to identify the natural frequencies and the corresponding elastic modes of the panels in the frequency range 0 – 1000 Hz. Two FE models per configuration are considered: in the first, the Tensile Modulus from tensile tests is assigned as Young's Modulus of the flax/PFA composite, whereas in the second one the Flexural Modulus from three-point-bending tests is assigned to the composite material. For all configurations, the first six elastic modes are shown in table 7.4. From a preliminary analysis of the natural frequencies, it is clear that the inserts have bigger impact at higher frequencies and, as the inserts bring additional mass to the panel, generally the effect is that of a decrease of the natural frequencies compared to the bare configuration.

Harmonic analyses simulations are then performed with the same FE models of the large-scale panels, with settings described in section 6.3.2.1. As for the modal analysis, two FE models for each configuration are analyzed, with the value of Young's Modulus of the flax/PFA composite from tensile and three-point-bending tests. Results shown in figure 7.11.

7.3.2.2 Experimental validation

Figure 7.12 compares results of the frequency-response tests on the large-scale bare and reinforced sandwich panels. As observed from the numerical simulations results, the effect of inserts is more significant at higher frequencies. Figures 7.13(a) and 7.13(b) show a reconstruction in Matlab of the first four excited elastic modes (modal shapes at the first four peaks of resonance) for both configurations. By comparing experimental and numerical FRFs, it is possible to observe a high discrepancy between the number of resonance peaks that are captured in the examined

Table 7.4: Numerical assessment of first six elastic mode shapes of bare and reinforced sandwich panels with Young's Modulus from tensile and three-point-bending (3PB) tests—ANSYS Mechanical APDL R15.

	Elastic mode		Bare Tensile	Reinforced Tensile	Bare 3PB	Reinforced 3PB
1	1^{st} torsional 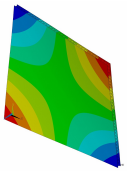	f :	41.6 Hz	40.6 Hz	59.5 Hz	56.7 Hz
2	1^{st} bending (saddle) 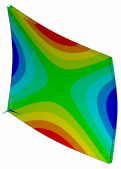	f :	79.4 Hz	77.4 Hz	114.1 Hz	109.6 Hz
3	2^{nd} bending (tympanum) 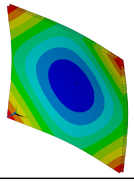	f :	98.8 Hz	95.5 Hz	142.0 Hz	134.5 Hz
4	3^{rd} bending (anti-symmetric) 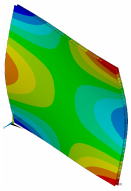	f :	119.7 Hz	116.6 Hz	171.9 Hz	164.3 Hz
5	3^{rd} bending (anti-symmetric) 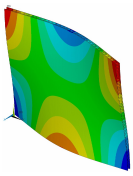	f :	119.7 Hz	116.6 Hz	171.9 Hz	164.3 Hz
6	4^{th} bending (symmetric) 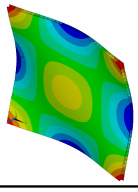	f :	206.7 Hz	201.7 Hz	297.9 Hz	284.3 Hz

frequency range, especially for the model with composite's Elastic Modulus equal to the value measured experimentally by tensile tests: numerical and experimental results are, indeed, much closer when referring to the FE model contemplating the Flexural Modulus. There are many

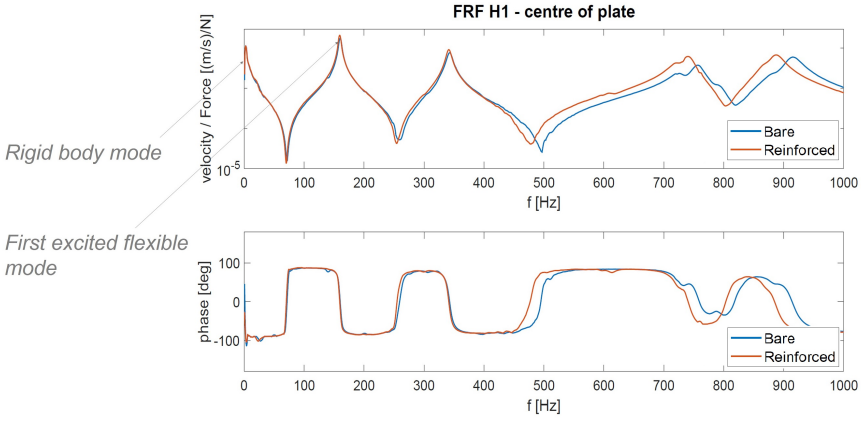

FIGURE 7.12. Experimental results of frequency response analysis on large-scale bare and reinforced sandwich panels: FRF H1 Bode plots at the centre of the plates.

factors that may contribute to this inconsistency and they will be explored in detail in Chapter 8. However, it is worth reporting here that good agreement between numerical and experimental data is achieved by tuning the FE model to the experimental results: by increasing the Young's Modulus value of the flax/PFA composite to 9.6 GPa, the numerical curves shift towards higher frequencies as shown in figure 7.14.

Loss factor values at resonance peaks are evaluated by applying the Half-Power Method to the experimental FRF curves, as introduced in section 6.3.2.2. Nevertheless, the only peaks that can be analysed with this method are the first two, since peaks at higher frequencies tend to be very close. Figure 7.15(a) shows the average FRF spectrum (H1, displacement over force) for bare and reinforced configurations. In figures 7.15(b) and 7.15(c), the Half-Power Method is applied to the first and second resonance peaks of the average FRF spectrum and values of ω_1 and ω_2 are evaluated from each peak, as per equation 6.11. Table 7.5 summarizes resonance frequencies and corresponding loss factor values, evaluated as per equation 6.10. While resonance frequencies do not differ significantly for bare and reinforced panels, the increase in damping given by the inserts is evident: at the first peak, the loss factor is 8.33% higher for the configuration with inserts compared to the bare, while for the second peak is 15.3% higher. Once again, it is possible to appreciate how the inserts have more impact at higher frequencies. Finally, it is worth noting that the bare panel loss factor value at the first resonance is remarkably close to the mean loss factor value of the Evopreg PFC-flax from DMA at room temperature and 1 Hz frequency—$\eta = 0.0290$, section 4.2.2.2.

7.4 Acoustic tests

Impedance tube acoustic tests are executed on small-scale specimens of the bare and reinforced sandwich panel according to the settings described in section 6.4. As introduced in that section, three samples are tested for each configuration. Each sample is re-positioned ten times within

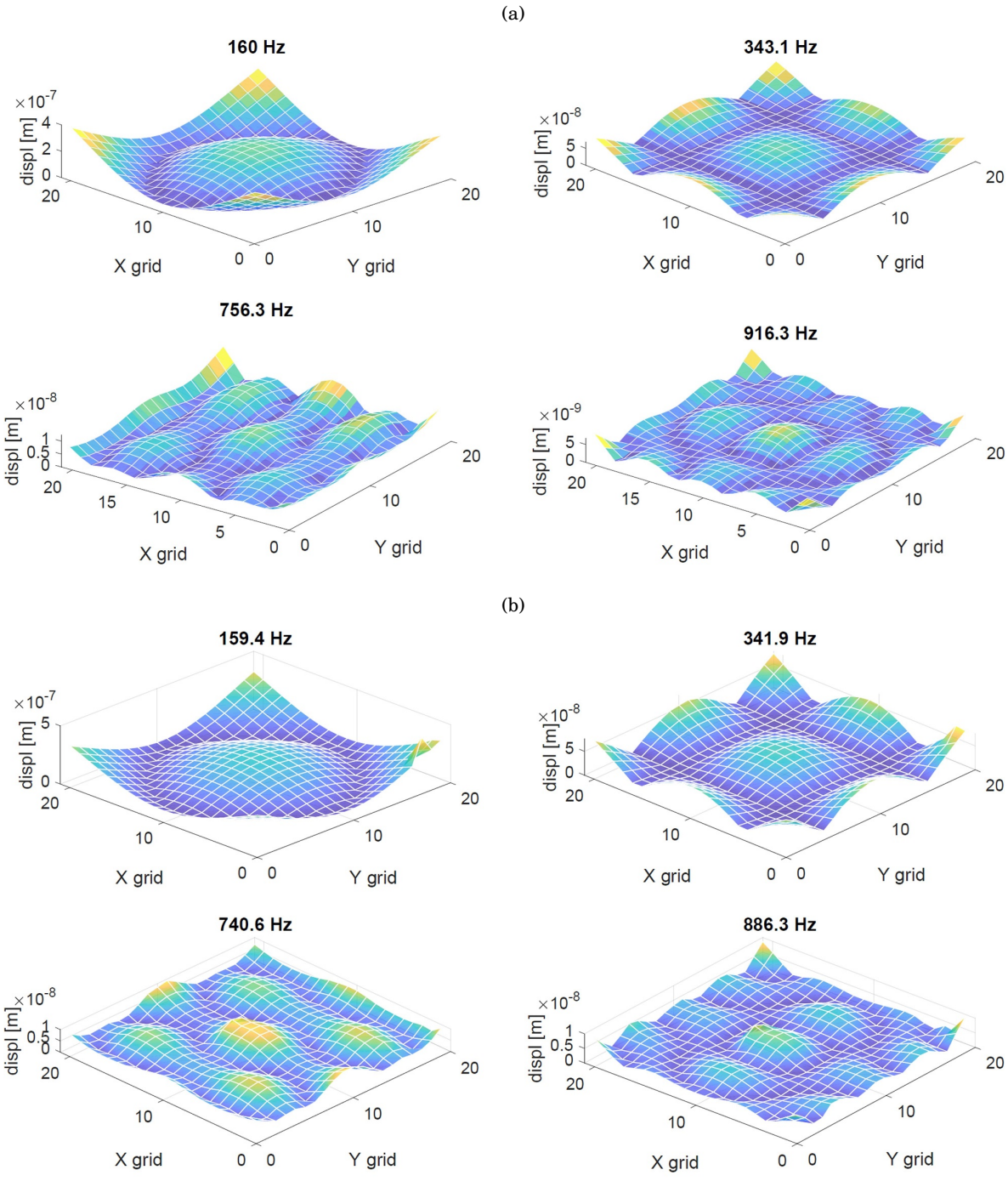

FIGURE 7.13. Experimental modal shapes at resonance peaks of (a) bare and (b) reinforced configurations (measured with laser vibrometer).

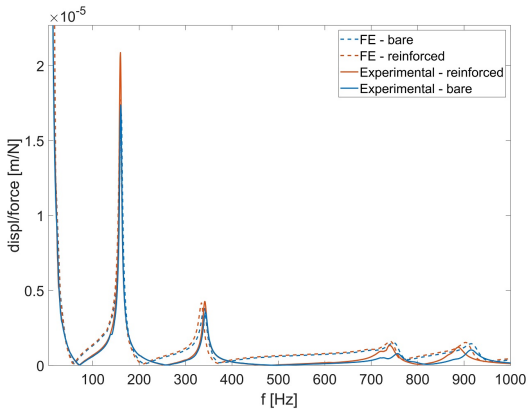

FIGURE 7.14. Results of frequency-response simulations and tests on large-scale sandwich panels—FRF H1 at centre of plates (displacement/force). Numerical results from model with composite Young's Modulus of 9.6 GPa.

Table 7.5: Frequency response measurements on large-scale sandwich panels: damping at the first two resonances of bare and reinforced configurations—Half-Power Method.

	Resonance frequency		Loss factor, η		Inserts contribution
	Bare	Reinforced	Bare	Reinforced	to Damping ratio, ζ
1^{st} resonance	159.3 Hz	160.1 Hz	0.0289	0.0312	+8.33%
2^{nd} resonance	341.2 Hz	342.6 Hz	0.0249	0.0286	+15.3%

the tube (five times for each one of its two OOP orientations) to take into account uncertainties in the sample positioning and possible OOP effects due to irregularities from manufacturing. Hence, in figure 7.16 results for each sample are represented by a mean curve with standard deviations in order to show the variability of measurements with respect to the specimen positioning.

Acoustic tests do not show any significant differences between the two configurations. Even though the TL mean curves are lower for the configuration with inserts than the bare one, there is not enough experimental evidence that the core with inserts shows lower TL effectively: the mean values are, indeed, within the statistic scatter and it is not possible to state that there is experimental evidence of property reduction. This is likely explained by the fact that the TL is mostly determined by the bulk properties of a structure or material: it is then principally affected by geometry and density characteristics of the sandwich panels and since the CNT depositions do not alter the bulk characteristics of the sandwich panel significantly, acoustic transmission properties are not altered.

7.5 Conclusions

This chapter presented the results of experimental tests on bare and CNT-reinforced sandwich panels according to the methodologies that were thoroughly described in Chapter 6. Sandwich panel specimens underwent quasi-static, dynamic and acoustic experimental tests and in most

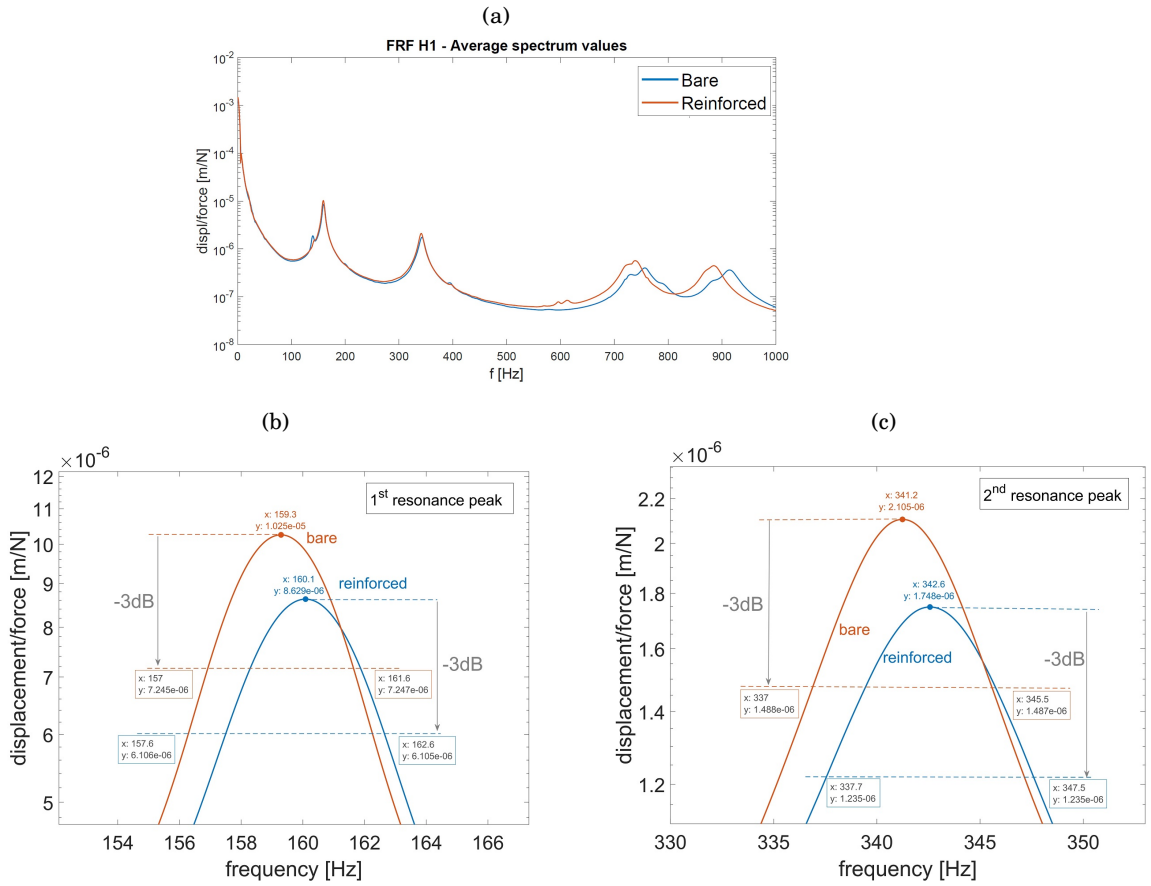

FIGURE 7.15. Frequency response experimental measurements on large-scale sandwich panels: average FRF spectrum (H1, displacement over force) of bare and reinforced configurations. (a) Full spectra; Half-Power Method applied to the first (b) and second (c) resonance peaks.

cases the experimental results were compared to analytic and/or numerical assessments.

Quasi-static flatwise compression tests showed that the reinforced configuration has 24.5% higher failure stress—even with 25% increase of relative density—compared to the unreinforced specimens.

Two different types of dynamic tests were executed respectively on small- and large-scale sandwich panels. First of all, OOP vibration transmissibility tests, carried out on small-scale panels after a stage of preliminary investigations, showed that the bare specimens outperform the CNT-reinforced ones when subjected to this type of OOP excitation: Coulomb dry friction effects act in between interlocking walls of the bare specimens, causing high levels of energy dissipation and hence of vibration damping. With a mass of 129 gr mounted at the top of the specimens, the bare configuration showed 14.4% loss factor at the resonance frequency of 4165 Hz, compared to the 2.74% at 4224 Hz of the CNT-reinforced specimen. Good agreement was found between experimental tests and FE numerical simulations for the panel with insert. However, FE models

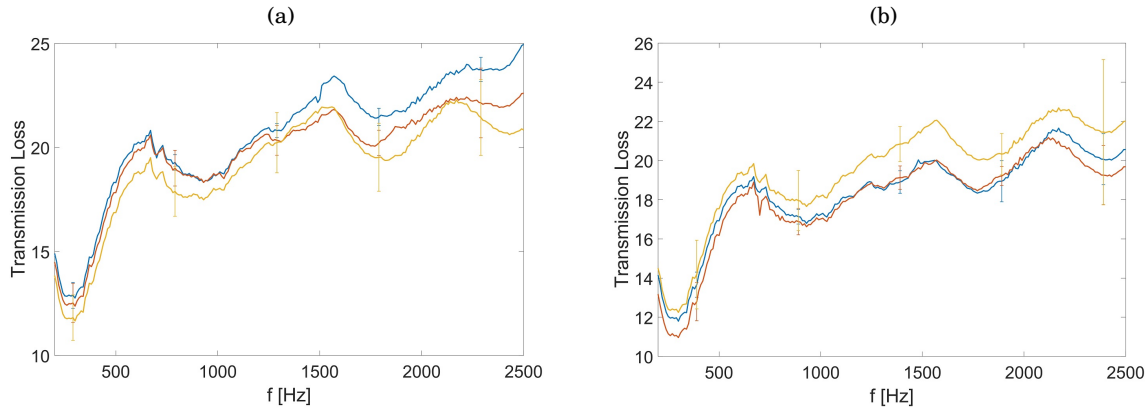

FIGURE 7.16. Results of impedance tube acoustic tests on (a) bare and (b) reinforced sandwich panel specimens. The mean curves are relative to the re-positioning of each specimen in between acquisitions.

had to be tuned to the experimental results for the bare specimen, as at this stage they assume perfect bonding between interlocked walls. By assigning a hysteretic value of damping ratio equal to that evaluated experimentally from the resonance peak, good agreement was found between experimental and numerical curves. Secondly, frequency response tests were performed on large-scale sandwich panels. In this case, the panel with viscoelastic inclusions showed the highest loss factor values at resonance peaks. Specifically, the CNT configuration offers a rise in loss factor of 8.33% at the first peak and 15.3% at the second one. Resonances at higher frequencies could not be analyzed with the Half-Power Method, as modes overlap and corresponding peaks are note clear. Good agreement between experimental and numerical results was found after tuning the FE models to the experimental results by increasing the flax composite stiffness.
Finally, impedance tube acoustic tests were performed on small-scale sandwich panels. Albeit the mean curves of bare and reinforced specimens differ, values are within the statistic scatter and hence there is no experimental evidence of change in the TL.

CHAPTER 8

DISCUSSION OF RESULTS

Contents

8.1 Introduction

THIS thesis explored successive steps of development of the novel natural-composite sandwich panel reinforced with CNT-resin inserts. Firstly, mechanical and thermo-mechanical characteristics of constituent materials were investigated. Afterwards, the viscoelastic inserts were designed and sandwich panel specimens of different dimensions were manufactured. Bare panels without inserts were also produced as control specimens. Finally, tests at a structural scale allowed to characterize quasi-static, dynamic and acoustic behaviour of the panels and to quantify the effects provided by the inserts by comparing results given by bare and insert-reinforced configurations.

This chapter provides a comprehensive discussion of the main results presented in this thesis and is structured into two main parts.In the first section, outcomes of some of the quasi-static characterization tests are discussed: mechanical tests on the natural flax/PFA composite (which were presented in Chapter 4) are examined, followed by a discussion of the OOP flatwise

compression tests of sandwich core lattice specimens (presented in Chapter 7). Second part focuses on discussing results of the dynamic tests that were presented in Chapter 7.

8.2 Quasi-static mechanical tests

8.2.1 Mechanical characterization of Evopreg PFC-flax

This section goes through one main area of discussion regarding the natural-composite material utilized for the skins and lattice core walls in the sandwich panels, which is the discrepancy between Young's Modulus values as measured from tensile and three-point-bending tests.
Overall, the mechanical properties of the Evopreg PFC-flax laminate evaluated from tensile tests are fairly low compared to values of similar laminates that can be found in some open literature cases. It is important to stress, however, the high reliability of the tensile tests performed in this thesis as they are performed by following the ASTM D3039/D3039M—17 specifications to the letter and results present very good statistic properties.

Natural-fibre based composites are generally characterized by a wide variability in terms of their mechanical performances due to a number of factors (e.g., unpredictable influences of weather, local environmental conditions, fibre type, processing approaches, moisture absorption and so on). Hence, it is possible to also find open literature cases of similar laminates with mechanical properties comparable to the Evopreg. The only laminates from literature that should be considered for comparison are those with a 2x2 twill type of fabric and comparable density to the present case: in fact, not only fabrics usually present lower mechanical properties than unidirectional laminates, but the level of weaving in yarns may influence the mechanical properties (a high level of weaving is related to greater misalignment within the yarn and hence to poorer mechanical characteristics) [62]. However, even comparing the Evopreg PFC-flax laminate properties to cases of similar laminates only, it is possible to appreciate that its value of Young's Modulus evaluated by tensile tests is quite low, probably due to its high level of crimp: Duc *et al.* [66] measured the properties of flax-Epoxy, flax-PLA and flax-PP composite laminates with 2x2 twill fabrics (300 g/m^2 areal weight) and they are respectively 7.9, 8.8 and 5.8 GPa, against 3.69 GPa measured for the Evopreg flax-PFA. On the other hand, Fiore and Calabrese [68] performed some mechanical characterization tests on two twill weave woven fabrics based composites: jute supplied by Composites Evolution and flax supplied by Lineo (Valliquerville, France), having areal weight of 400 g/m^2 and 320 g/m^2, respectively. For both, epoxy resin was used as matrix. By performing quasi-static flexural tests according to ASTM D790 standard, it was found that the Flexural Modulus of the jute laminate is 4.36 ± 0.19 GPa, whereas that of the flax laminate is 3.75 ± 0.47 GPa. These values are quite close to the Young's Modulus value of the Evopreg PFC-flax laminate found by tensile characterization.

The Young's Modulus value from tensile tests is also much lower than that from three-point-bending tests: the Flexural Modulus, 7.62 GPa, is about twice the Tensile Modulus, 3.69 GPa. It is important to stress that for the bending tests no independent strain measurements are performed.

Strain values are indeed evaluated from the displacements recorded by the testing machine and, hence, in principle their values might be inaccurate. Nevertheless, as for the tensile tests, results of three-point-bending tests also present very good statistic characteristics (section 4.2.1.2) and their reliability is confirmed by DMA tests (section 4.2.2.2). DMA characterization of the Evopreg laminate samples is, indeed, performed in flexural mode. Clearly, DMA provides inaccurate measurements of Storage and Loss Moduli since they are usually subjected to several sources of error depending on the precision of samples geometry (hence, accuracy in the manufacturing process) and of the measurement of their dimensions. However, DMA tests can provide an approximate estimation of the magnitude of Storage and Loss Moduli. The Evopreg PFC-flax Storage Modulus mean value at room temperature and 1 Hz frequency is 6.28 GPa (CV: 3.9%), which is much closer to the Flexural Modulus measured by three-point-bending tests, 7.62 GPa, than the Tensile Modulus value.
Similar—if not even larger—discrepancies have been measured in open literature in comparable cases. Fiore *et al.* [67] performed quasi-static tensile and three-point-bending tests on two composite laminates consisting of bidirectional flax fabrics and epoxy matrix—figure 8.1(a). The first one (indicated as 'F220') is a balanced twill fabric with areal weight of 220 g/m^2, whereas the second one (indicated as 'F150') is an unbalanced plain weave fabric with areal weight 150 g/m^2. Tensile tests on these composites showed a Young's Modulus for the F150 and F220 laminates of 1.79 ± 0.04 GPa and 4.5 ± 0.15 GPa, respectively. Interestingly, the Flexural Modulus values are 7.41 ± 0.39 GPa and 5.35 ± 0.21 GPa, respectively: for the F150 composite, the Flexural Modulus is about four times the Tensile one, whereas for the F220 the difference is of about 20%, which is what one would normally expect. One explanation for the higher value of Flexural Modulus in case of the Evopreg PFC-flax and the F150 composite from [67] could be related to the fact that in both cases the yarns of fibres in the fabric are very thick and close to each other. This is evident from figures 8.1(a) and 8.1(b), which show the F220 and F150 woven fabrics and the uncured Evopreg PFC-flax prepreg, respectively. In the cured laminates, the yarns dimensions are hence comparable to those of the laminate's section, figure 8.2: the high level of weaving—and hence misalignment of fibres—could be the cause of the low tensile properties of the composite.
Nevertheless, in this thesis the mechanical characterization of materials is only performed to provide input for the elastic modelling of the sandwich panels, hence the discrepancy between tensile and three-point-bending tests results is not examined in depth.

Elastic models of sandwich panels are built by assigning the Young's Modulus value from tensile tests to core walls and skins. With this setting, numerical simulations of different types of tests provide results with fluctuating reliability. Simulations of OOP flatwise compression tests provide values which are quite far from the experimental ones, but very close to the analytic predictions by Gibson's formulae [2]. This will be discussed in more depth in section 8.2.2. On the other hand, numerical simulations of OOP vibration transmissibility tests provide results very close to the experimental ones. Finally, as it will be further discussed in section 8.4, when

(a)

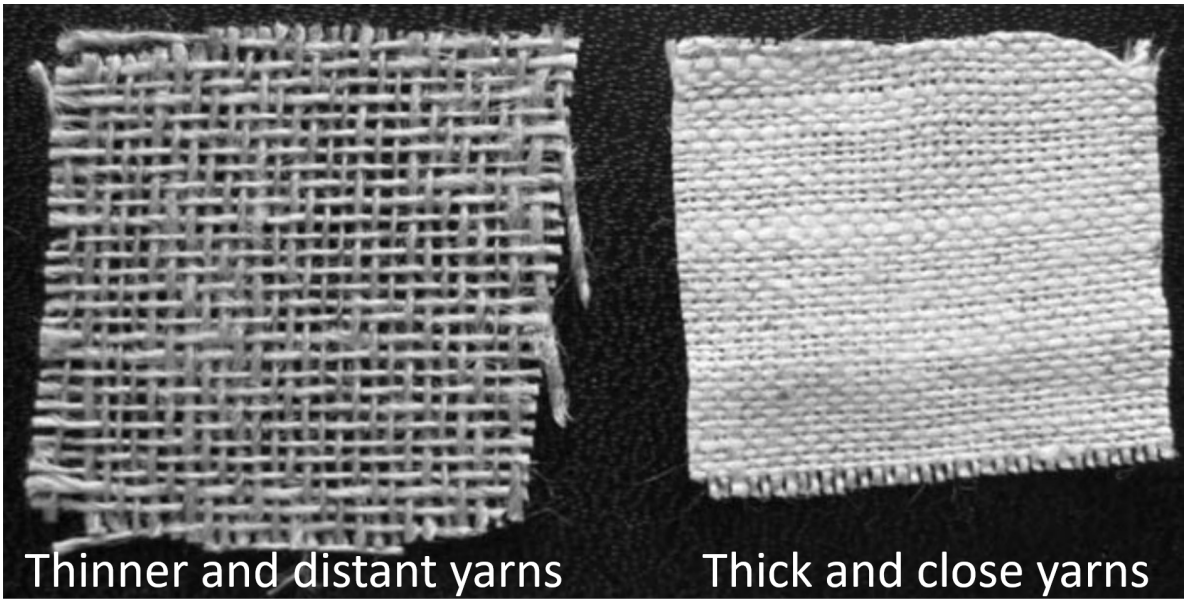

(b)

FIGURE 8.1. (a) Wave architectures of F220 (left) and F150 (right) woven fabrics. Reproduced from [67]. (b) Wave architecture of 2x2 Twill Evopreg PFC-flax.

the Tensile Modulus value is assigned to the FE model, frequency response simulations on large-scale sandwich panels provide results far from the experimental ones. Instead, numerical

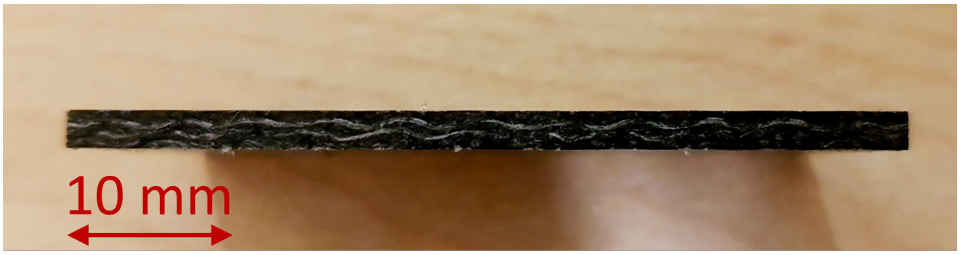

FIGURE 8.2. Transverse section of Evopreg PFC-flax composite laminate.

Table 8.1: Comparison between analytic, numerical and experimental results of quasi-static OOP flatwise compression tests on bare and CNT-reinforced core specimens.

		Analytic	FE model	Tests
Bare	Failure stress [MPa]	7.71	7.9	14.7
	Compression Modulus [MPa]	848.7	442.9	374
Reinforced	Failure stress [MPa]	8.20	7.3	18.3
	Compression Modulus [MPa]	863.0	343.4	303

and experimental results are much closer when assigning the Flexural Modulus value. From these observations, it is possible to ascertain that when the panel undergoes uniform OOP deformations (i.e., OOP flatwise compression and vibration transmissibility), numerical models with stiffness from tensile tests provide more reliable results. Conversely, when it is subjected to flexural deformations (as in the frequency response tests), numerical models contemplating the stiffness from three-point-bending tests provide higher agreement with the experimental results.

8.2.2 Flatwise compression properties of bare and CNT-reinforced sandwich cores

Quasi-static flatwise compression tests on sandwich cores present quite controversial results at a first glance, as they are far from analytic and numerical predictions despite their good statistic reliability.

Table 8.1 (reproduced from section 7.2) shows a summary of the experimental outcomes together with analytic predictions according to the formulas introduced in section 6.2.1 and numerical simulations on the FE models described in section 6.2.2.

For what concerns the failure behaviour of the lattices, analytic failure stress values are 7.71 MPa (bare) and 8.20 MPa (reinforced), whereas the numerical ones 7.9 MPa and 7.3 MPa, respectively. For both configurations, these predictions are much lower than the experimental mean values of 14.7 MPa (CV 6.78%) and 18.3 MPa (CV 4.15%), respectively.
From the analysis of the experimental values only, the reinforced core shows an increment of 24.5% in failure stress compared to the bare configuration, with 25% higher relative density. The deposition of the CNT-resin, therefore, has a strengthening effect probably due to the improvement of interfacial bonding and load transfer at the walls junction areas. This is in line with the

experimental observations found in open literature, as the junction corners between core walls are the best locations for viscoelastic depositions to increase the core strength [36, 37].
The discrepancies with the analytic and numerical assessments are most likely due to several different factors. First of all, numerical simulations assume that the composite follows a multilinear isotropic hardening rule in the plastic range. This is an obvious limitation, since plasticity is adopted to model damage process in the composite material: non-linearity is, indeed, due to progressive cracking of off-axis weft yarns and utilizing plasticity to model the composite's behaviour is a very strong simplification. Numerical models can therefore provide acceptable predictions of the lattice behaviour under flatwise compression loading at low strains, but the failure process cannot be assessed with reliability.
Secondly, both analytical and numerical assessments are done by considering the tensile properties of the composite material: the analytic formula, indeed, considers its failure stress under tensile loading and the numerical models contemplate the multilinear stress-strain curve also measured in the tensile characterization. The tensile failure stress is generally lower than the compression one, since under compression loading there usually are strain hardening effects, i.e., an increase in the strength and hardness of the material due to mechanical deformations in its microstructure. The FE models consider homogenized properties of the composite material rather than its microstructure and micromechanics in compression and at failure and this might explain the higher failure stress and elongation values.
Another factor that might play a fundamental role in the high discrepancy between predictions and measured value of failure stress is related to the cutting process of grooved core strips from flax/PFA laminates. Indeed, the cutting is performed by means of a blade using water as coolant system. The material is not fully immersed in water and is in contact with it for a short amount of time. Moreover, it is dried in the oven at 105°C for 3 to 5 hours after the cutting. However, residual humidity trapped inside the fibres may not only contribute to decreasing the stiffness [168], but also to increase the compressive strength. There is, indeed, experimental evidence in open literature that water can cause swelling of natural fibres, leading to higher mechanical properties: in natural fibres such as flax or jute, swelling of the fibres fills the voids/gaps in the composite and may generate radial pressure which results in higher strength [169].

For what regards the compression Modulus, the analytically predicted values are 848.7 MPa (bare) and 863.0 MPa (reinforced), whereas numerical values are 484.9 MPa and 343.4 MPa, respectively. The experimental values are 373.5 MPa (CV 1.06%) and 303.0 MPa (CV 9.23%), respectively. Also in this case, there are different factors to take into account and observe.
First of all, the value of compression Modulus measured experimentally is lower for the configuration with inserts than the bare one. Regardless, there is not enough experimental evidence that the core with inserts shows lower stiffness effectively: albeit the mean value in the first case is slightly smaller than that of bare core, the values are within the statistic scatter and it is not possible to state that there is experimental evidence of property reduction. The ab-

sence of increase in stiffness in the experimental tests is likely due to materials, geometric and manufacturing-related factors.
Secondly, another aspect that is worth observing in relation with the reinforced lattice is that the numerical model which best represents the experimental behaviour is that of the unit cell with "soft" boundary conditions (Model 3) rather than that of the entire lattice (Model 1). The lattice hence behaves in a much softer manner than what predicted numerically and this lower stiffness of the structure is well simulated by applying soft boundary conditions to the unit cell. This soft behaviour is likely due to CNT-resin permeation effects at the junction areas between the crossing walls, and to interactions between the CNT-resin itself and the composite matrix. Moreover, while the FE model assumes perfect bonding between inserts and walls, in reality there might intervene debonding phenomena between the components under compression. Finally, there is the possibility of some residual gas trapped within the CNT-resin, also contributing to a softer behaviour than the numerical predictions.
Lastly, the discrepancy between analytic, numerical and experimental values of the compressive Modulus are probably due to a combination of different factors. For the sake of clarity, they are listed separately below.

- As for the failure stress, analytic predictions of the Modulus are made by considering the material tensile Young's Modulus rather than its compressive properties.

- From the analysis of the numerical stress-strain curves in section 7.2, the linear part of the curve at low strains corresponds to a high Modulus value due to the linear behaviour of the composite material. This part of the curve corresponds to the linear range of the tensile stress-strain curve given in input as multilinear hardening model and therefore agrees with the analytic assessments of the compression Modulus (the numerical value of the Modulus in this range is 909.8 MPa for the bare lattice and 872.2 MPa for the reinforced). Such behaviour at low strains is not detected experimentally. This is partly related to the fact that the FE models contemplate tensile properties of the materials rather than compressive, and the compressive behaviour of the composite material at low strains is unknown. Another important factor to consider is the possible presence of manufacturing imperfections of the samples, especially in their flatness levels. At low strains there might be some instabilities effects as the flat plates of the testing machine are aligning with the sample faces, hiding the "real" behaviour of the material under compression in this region.

- Natural-fibre composites usually show lower compressive modulus than tensile: Van Vuure *et al.* [69] showed that the compression to tensile stiffness ratio of flax- and bamboo-reinforced composites is about 60%.

- Finally, as introduced above, the cutting of flax/PFA laminates is performed by means of a blade using water as coolant system and residual humidity trapped inside the fibres may contribute to decreasing the stiffness as well [168].

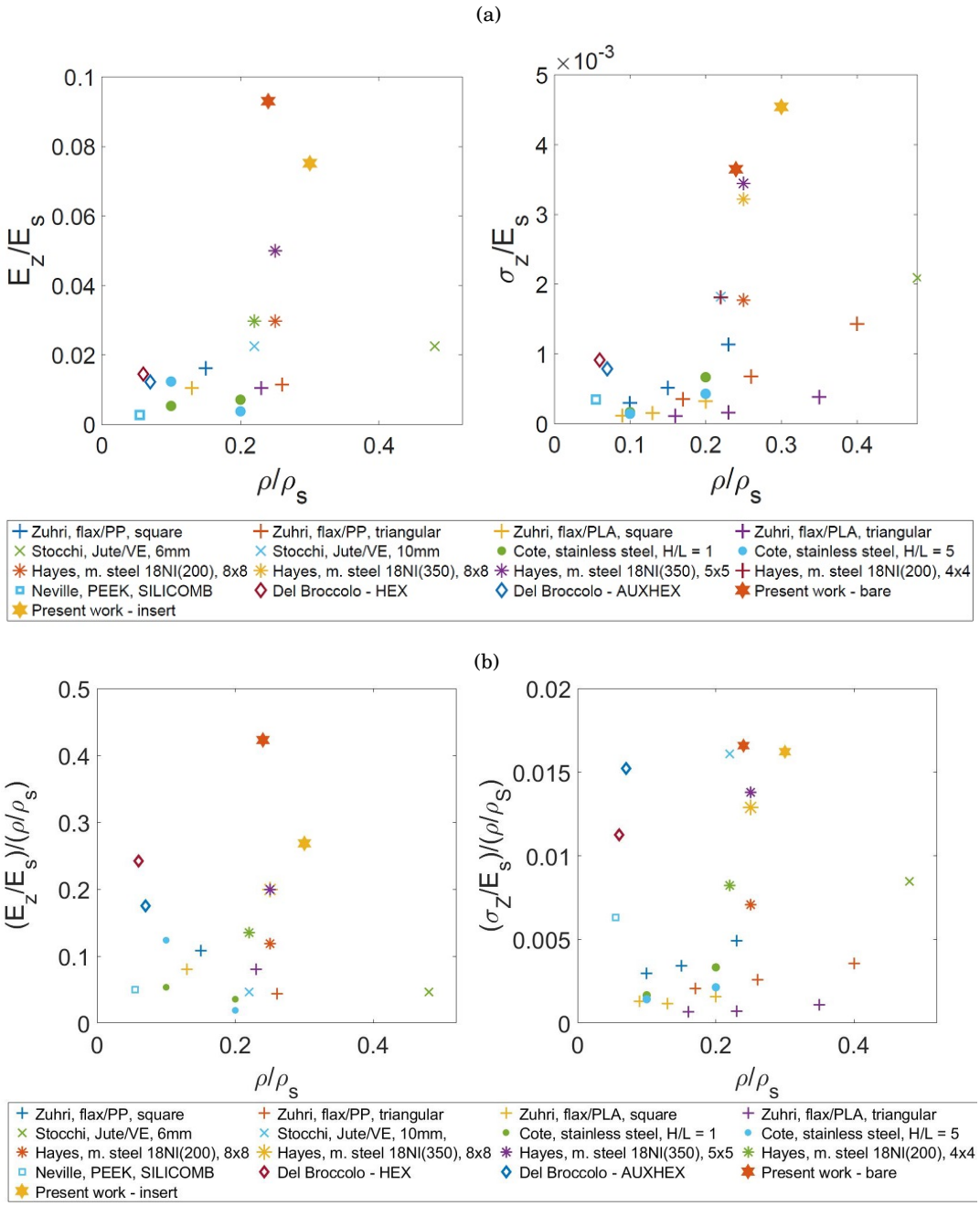

FIGURE 8.3. Quasi-static flatwise compression performance charts: OOP stiffness and failure stress of bare and reinforced lattices compared to open-literature cases. Normalization with respect to (a) walls solid Tensile Modulus and (b) walls solid Tensile Modulus and relative density.

8.2.2.1 Comparison with literature cases: performance charts

The lattices OOP mechanical properties are compared to other literature cases in the performance charts in figures 8.3(a) and 8.3(b). Since the charts contemplate different types of cellular lattices,

compression stiffness and failure stress are normalized to the Tensile Modulus of core walls material, E_s, in figure 8.3(a) and to both E_s and the relative density in figure 8.3(b). This is a conventional method for presenting results in performance charts since with this normalization differences in terms of materials and/or topologies of the cellular structures are taken into account [170]. Following, a brief review of the benchmark cores from open literature utilized in the performance charts.

Zuhri *et al.* [98] investigated the compression characteristics of square- and triangular-cell honeycomb cores reinforced with flax fibres in Polypropylene (PP) and Poly(lactic acid) (PLA) polymers. Stocchi *et al.* [99] examined hexagonal-cell honeycomb cores of jute fibres in vinyl ester (VE) matrix with two different cell dimensions, 6 mm and 10 mm. Côté *et al.* [26] evaluated the OOP compression behaviour of metallic honeycombs with square cells and two different height-to-cell-length (H/L) values. Hayes *et al.* [128] examined the mechanics of linear cellular alloys (LCA), considering two different grades of maraging steels and several cell array configurations (4x4, 5x5, 8x8). In [170] the transverse properties of Kirigami zero-ν Polyether ether ketone (PEEK) honeycombs have been explored, where the zero-ν behaviour is obtained using the SILICOMB geometry. Del Broccolo *et al.* [171] has additionally performed a comparative study between PEEK hexagonal (HEX) and AUXHEX configurations (the latter is a type of topology which confers zero-ν behaviour to the structure).

The flax/PFA lattices presented in this thesis appear to possess outstanding performances in terms of normalized stiffness and failure stress when compared to the other literature cases. It is worth observing how normalized stiffness values are high despite the impact of humidity, as explained above. While the compression stiffness of the reinforced configuration is however lower than the one of the bare core, one can notice from figure 8.3 that both bare and reinforced configurations perform remarkably better than the other cases considered. It is also worth noticing how the normalized failure stress is significantly higher in the flax/PFA cores than for the flax fibres composites with thermoplastic matrix (PLA and PP) lattices (square and triangular unit cells). The latter cases have similar relative densities to the flax/PFA lattices developed in this work. Likewise, flax/PFA cores perform better than the Jute fibres with thermoset resin (VE). From these observations, it is possible to ascertain that the PFA resin might play an important role in the unusually great compression characteristics of the flax/PFA cores shown in this work.

8.3 Dynamic vibration tests on sandwich panels

This section will discuss some aspects concerning the dynamic performances of bare and CNT-reinforced sandwich panels. As presented in Chapters 6 and 7, two types of dynamic tests were performed: OOP vibration transmissibility tests on small-scale specimens and frequency response analyses on large-scale panels. In both cases, experimental results were compared to numerical predictions and, where necessary, numerical models were tuned to respective tests results. Following, a more detailed discussion of the dynamic tests outcomes.

In section 7.3.1, results of vibration transmissibility tests showed that sandwich panels without CNT-resin depositions outperform the reinforced ones. Indeed, the loss factor at resonance—evaluated from the resonance peak amplitude—is 14.4% for the bare configuration and 2.74% for that with inserts. Results suggest that with this specific configuration of load and boundary conditions, Coulomb dry friction intervenes at the junctions between crossing walls, hence providing a higher contribution to overall mechanical energy dissipation values than that given by internal material damping: indeed, as shown in sections 5.2.1 and 5.2.4, bare cores are assembled by simply interlocking the walls in correspondence of grooves, whereas the CNT-resin acts as a glue in the reinforced configuration and any dry friction effects between crossing walls is blocked.

In the frequency response analysis tests, large-scale sandwich panels (the manufacturing of which is described in section 5.2.5) are in free-free boundary conditions and therefore are free to deform with flexural bending deformation modes (the experimental setup is described in detail in section 6.3.2.2). The boundary conditions, hence, differ from those of the vibration transmissibility tests as the panels can now deform according to bending shapes as response to the excitation. It is, in fact, very well known in open literature that in the low frequencies range a sandwich panel behaves as a homogeneous panel and its bending characteristics dominate: this zone is controlled by the total section bending stiffness and the whole panel acts as if it were homogeneous [172]. Therefore, in this frequency range and with these boundary conditions, most of the strain energy is located in the skins rather then in the core and friction between interlocking walls is not "activated".
This hypothesis is supported by numerical simulations performed on unit cells subjected to static compression, bending and shear loading. Indeed, for linear analyses the location of maximal strain in the core lattice unit cell and insert is similar in static and dynamic cases, although absolute values may differ [15]. Contours of the elastic strain energy in the cell under each type of loading are shown in figure 8.4. It is possible to notice that in case of OOP compression the highest strain energy values are located in the core. Furthermore, core walls of the bare cell have overall higher levels of strain energy than the reinforced. From these observations it is possible to ascertain that, albeit this model assumes perfect bonding at the walls junction, when dry friction mechanisms intervene in the transmissibility tests they dissipates more energy than the viscoelastic inserts do—by internal material damping—in the reinforced panel. On the other hand, when the cell deforms in flexural bending, face skins are characterized by noticeably higher values of strain energy than core walls—figure 8.4(b)—and the friction mechanism at interlocking walls in not activated. The difference in strain energy between bare and reinforced configurations is small in this case—although slightly higher values can be observed in the reinforced cell. Nevertheless, when subjected to this type of deformation the reinforced configuration dissipates more energy than the unreinforced due to the higher internal material damping caused by the presence of viscoelastic inserts. This is reflected in the results of frequency response experimental tests: as shown in section 7.3.2.2, the reinforced panel provides an increase of damping of 8.33%

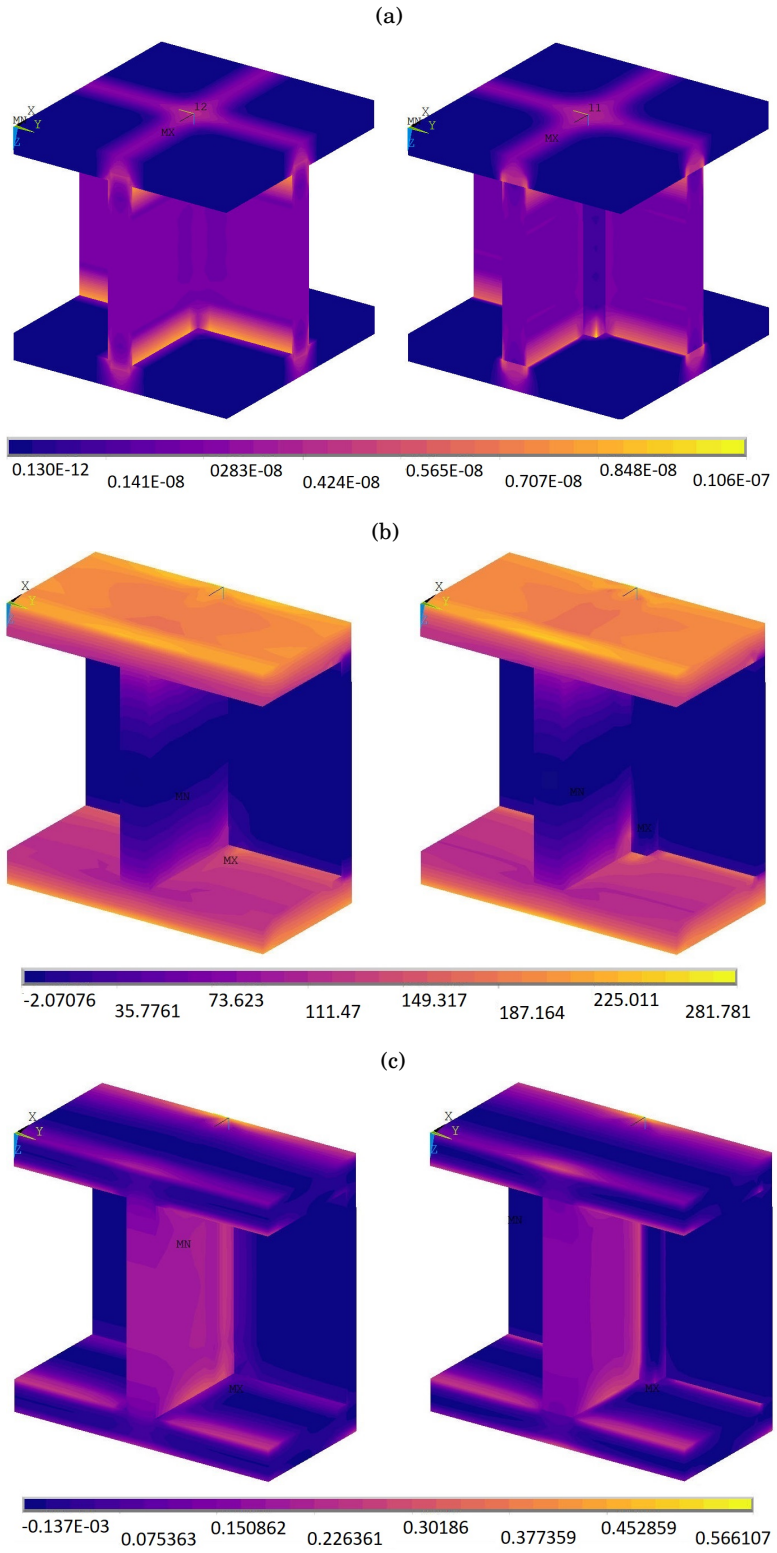

FIGURE 8.4. Elastic strain energy contour in bare and reinforced unit cells subjected to (a) pressure, (b) bending and (c) shear loading. In cases (b) and (c) half of the unit cell is modelled.

and 15.3% at the first two peaks of resonance respectively compared to the configuration without viscoelastic inserts. Finally, when subjected to OOP shear loading, the unit cell has comparable levels of elastic strain energy with and without insert, even though slightly higher values can be observed in the core walls of the bare unit cell. One interesting aspect about this case is related to the first (or shear) transition frequency of sandwich panels [172] and will be explored in more detail in section 9.2.2 as an intriguing future development.

One other aspect that must be discussed about outcomes of the frequency response analysis is the high discrepancy between experimental tests and numerical simulations, particularly when the FE model contemplates the flax/PFA composite Young's Modulus from tensile tests rather than from three-point-bending tests. This was already introduced in sections 7.3.2.2 and 8.2.1. By examining the numerical FRFs in the frequency range 0-550 Hz (figure 7.11(a) in section 7.3.2.1), it is possible to notice a similarity with the experimental FRFs in the entire range 0-1000 Hz (figure 7.12 in section 7.3.2.2), suggesting that the structure might be considerably stiffer than what is predicted numerically. Since in these tests the panels deform with bending shapes and it was experimentally shown that the Flexural Modulus of Evopreg PFC-flax laminates is about two times the Tensile (as discussed in section 8.2.1), further simulations are performed by assigning the Flexural Modulus value as stiffness of the Evopreg PFC-flax. In this case, numerical results are closer to the experimental curves—figure 7.11(b). The numerical model is then tuned to experimental results by increasing the Evopreg PFC-flax Young's Modulus even further, until good agreement is found—figure 7.14. The final value of Young's Modulus assigned to the sandwich panels core and skins is 9.6 GPa. The fact that such value is higher than the Flexural Modulus from three-point-bending tests might be due to stiffening effects introduced by gluing core to skins and using weights to impose a correct alignment of components and overall flatness.
A second factor that differentiates numerical and experimental outcomes in this study is found with a more attentive study of the deformation shapes at resonance frequencies. Indeed, some deformation shapes corresponding to resonances in the numerical FRFs appear as antiresonances in the experimental FRFs. An example is the tympanum mode, which corresponds to the first antiresonant frequency—around 70 Hz—in the experimental FRFs, figure 8.5. As explained in [173], when the measurement is performed at the driving point it is normal to have a successive changes in resonances and antiresonances in the FRF. Wahl and Schmidt [173] also demonstrated that the antiresonance frequencies of a system are equal to the resonance frequencies of the same system in which a stiff constrain of displacement is applied to the excitation point. Therefore, one explanation for the discrepancy might be a high sensitivity to the boundary conditions: the modal shaker at the back of the panel may interfere with the system, thus causing destructive interference between the external driving force and the system itself (in fact, the measured amplitude of vibrations drops to almost zero). For the sake of clarity, figure 8.5 shows the experimental FRFs and the corresponding deformation shapes measured at resonance and antiresonance frequencies.

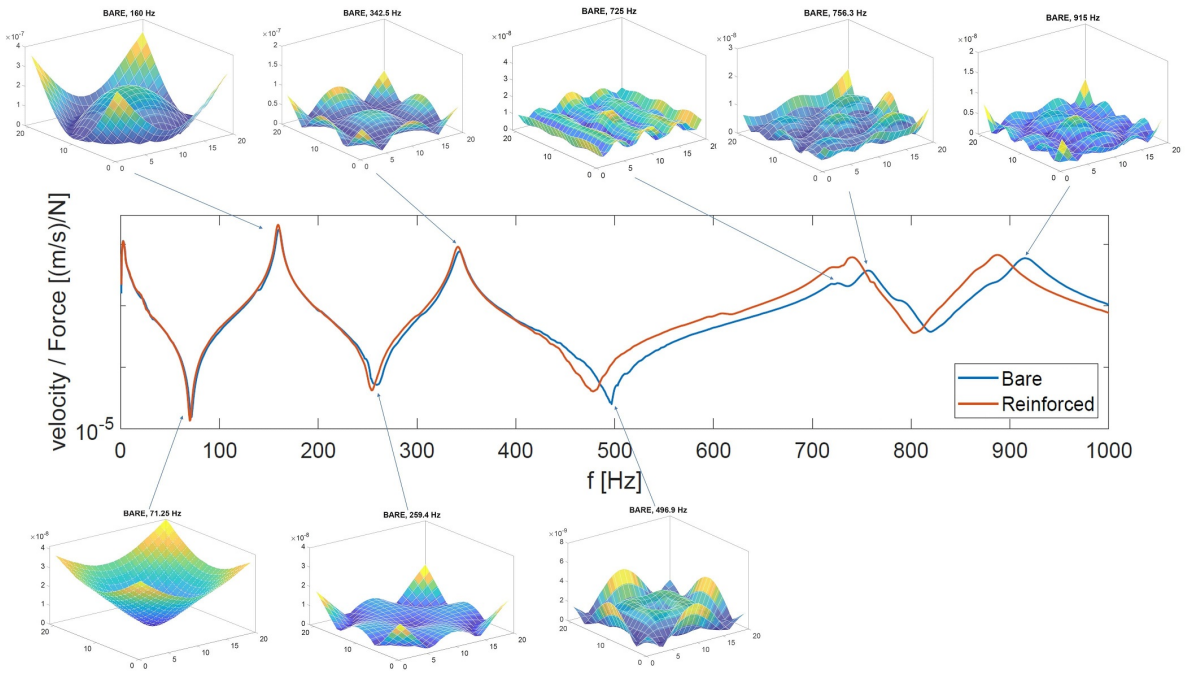

FIGURE 8.5. Frequency response tests on large-scale sandwich panels: FRF H1 at the centre of the plates. The deformation shapes captured at resonant and antiresonant frequencies are displayed.

8.3.0.1 Comparison with literature cases

In this section values of loss factor measured for the Evopreg-PFC flax sandwich panels are compared to literature cases of different types of bio-based composite structures.

Petrone *et al.* [27] experimentally investigate two flax-fibre based sandwich panels. Both panels face skins consist of unidirectional (UD) glass fibre and PP resin composite laminates and the cores are cellular lattices with hexagonal topology. For the first panel, the core walls consist of a UD flax-fibre mat (180 gr/m^2 density) in PE resin, whereas for the second one of a random fibre mat (200 gr/m^2 density) in PE resin. Results of the modal analysis show that for both panels the modal damping ranges approximately from 0.01 to 0.03 in the frequency range 500 – 2000 Hz. By inserting wool fillers in the core cells, damping values increase going from 0.015 to 0.065 for the first panel and from 0.01 to 0.05 for the second one.

Monti *et al.* [174] investigate the vibration behaviour of bio-based composite beams up to 3000 Hz. The core consists of balsa wood panels and the face skins of a flax-fibre based composite with thermoplastic resin (Elium®). Different lamination sequences are adopted for the skins: UD 0°, UD 90°, UD ±45°, and cross-ply (CP) $[0/90]_s$, $[\pm 45]_s$. Similarly to the case of this thesis, all these laminates consist of four plies. The loss factor is evaluated both for the only laminates and for entire sandwich panels with balsa wood cores of several thicknesses (6.4 mm, 12.7 mm, 15.9 mm and 19.1 mm) and face skins CP $[0/90]_s$. Results show that for UD ±45° and UD 90°

Table 8.2: Comparison of flax/PFA sandwich panels loss factors with open-literature cases of bio-based sandwich panels and composite laminates.

Literature	Structure	Experimental test	η
Present work	Flax/PFA small-scale sandwich panel (bare)	Transmissibility	14.4%
	Flax/PFA small-scale sandwich panel (CNT-reinforced)	Transmissibility	2.74%
	Flax/PFA large-scale sandwich panel (bare)	Free Vibration (1^{st}, 2^{nd} peak)	2.89%, 2.49%
	Flax/PFA large-scale sandwich panel (CNT-reinforced)	Free Vibration (1^{st}, 2^{nd} peak)	3.12%, 2.86%
[27]	UD flax/PE sandwich beam	Free Vibration	3% – 6%
	Mat flax/PE sandwich beam		2% – 5%
	UD flax/PE sandwich beam with *wool*		3% – 13%
	Mat flax/PE sandwich beam with *wool*		2% – 10%
[174]	UD Flax/Elium® 0° laminate	Free Vibration	1.8%
	UD Flax/Elium® 45° laminate		4% – 6%
	UD Flax/Elium® 90° laminate		4% – 6%
	CP Flax/Elium® $[0/90]_s$ laminate		2%
	CP Flax/Elium® $[\pm 45]_s$ laminate		5.5% – 3.5%
	CP $[0/90]_s$ skins and balsa wood core sandwich beam		2%
[175]	Bamboo, cotton/VE skins sandwich panels	Clamped-clamped Vibration	2% – 5.5%

laminates the loss factor is about 6% at very low frequencies (up to 500 Hz) and diminishes to 4% in the remaining frequency range. For UD 0° and CP $[0/90]_s$ laminates it is about 2% at low frequencies and then settles at 1.8% towards higher frequencies. Finally, for CP $[\pm 45]_s$ laminates the loss factor is about 5.5% at very low frequencies before settling at 3.5% at higher values. Measurements performed on the sandwich beams with different thickness show that the loss factor curves are always comprised between the values of 2% and 3%.
Last literature case considered here is that of sandwich composite beams with balsa wood, Rohacell® 51 WF foam and pine wood cores [175]. This time, the face skins consist of bamboo and cotton fibres in VE resin. The laminates consist of four plies with stacking sequence $[0/90]_s$. The beams behaviour is analysed in the frequency range 250 – 4000 Hz. In all cases, the loss factor curves have parabolic trend and are comprised in the range of loss factor values 0.02 – 0.055.

Table 8.2 summarizes the loss factors of the flax/PFA sandwich panels of the present study and of the literature cases just described. From the comparison it is possible to highlight that the only literature case which presents a loss factor of the same range as the flax/PFA bare panel in the transmissibility tests is that of flax/PE sandwich beams with wool insertions.

8.4 Conclusions

This chapter provided a discussion of the most controversial results obtained in this thesis and presented in Chapters 4 and 7. The first section explored possible motivations for the low mechanical properties of the Evopreg PFC-flax laminate (composite utilized for core walls and skins in the sandwich panels) and the discrepancy between Tensile and Flexural Modulus measured experimentally in tensile and three-point-bending tests. Not only both tests present good statistic properties and, hence, high reliability, but results of three-point-bending tests are also supported by DMA tests, which are performed in bending mode. After comparing the present case with analogous open literature composites, one possible explanation that was provided for the low Tensile properties is related to the high levels of weaving and misalignment of fibres in the fabric, due to the fact that the yarns dimensions are comparable to the laminate thickness. Furthermore, under flexural loading, the thick bundles might undergo radial pressures on the compressed face and hence local stiffening effects, resulting in a higher Flexural Modulus. The agreement between numerical simulations and experiments when assigning the Tensile rather than the Flexural Modulus to the FE model was also explored. It was observed that, in general, when laminates mostly undergo in-plane deformations (such as in OOP flatwise compression or vibration transmissibility tests on the lattice cores) higher numerical-experimental agreement is obtained when assigning the Tensile Modulus value to the composite material in the FE model. Conversely, when the composite laminates are mainly subjected to flexural deformations (i.e., frequency response tests in free-free boundary conditions, where the response of the panel is dominated by bending shapes), higher reliability is reached when assigning the Flexural Modulus value to the composite laminate stiffness.

Flatwise compression properties of lattice cores were also explored, since results from the quasi-static experimental tests present low levels of agreement with analytic and numerical predictions despite their high statistic reliability. Factors that might contribute to these discrepancies were explored (materials, geometric and manufacturing-related aspects, water absorption by natural fibres and trapped humidity). The OOP mechanical properties of the natural fibre-based cores found experimentally were then compared against analogous data related to lab-scale cores available in open literature, showing that the flax/PFA composite core developed in this work features the highest normalized stiffness among the benchmark cases. The CNT-reinforced flax/PFA core also offers the highest normalized compression failure stress.

Finally, last section of this chapter discussed results of dynamic tests on entire sandwich panels. Besides investigating possible sources of discrepancies between numerical and experimental studies, the main point of discussion regarded the different sources of energy dissipation intervening in the bare and CNT-reinforced sandwich panels depending on loading and boundary conditions they are subjected to. OOP vibration transmissibility tests showed that when subjected to uniform OOP deformations, structural damping intervenes between interlocked walls in the bare panels, providing a significant contribution to vibration damping. On the other hand, when

the boundary conditions are such that panels are free to deform with flexural shapes, the friction mechanism at the junctions is not activated and internal material damping is the main source of mechanical energy dissipation. Hence, the configuration with inserts provides the highest vibration damping due to the viscoelastic inserts contribution.

Next chapter will draw this thesis to a conclusion by summarizing its main findings and exploring future areas of development.

CHAPTER 9

CONCLUSIONS AND FUTURE WORK

Contents

9.1 Summary and Review of Main Results

INCLUSION of vibroacoustics rules at early design stages of structures is becoming of great importance in many fields, from buildings and constructions, to automotive and aerospace industry. Indeed, structures which are designed to be mechanically efficient are often also characterized by poor vibroacoustic behaviour, especially in those cases where weight must be kept low and, at the same time, high mechanical properties must be ensured. Sandwich panels belong to this category and in fact the high specific bending stiffness is the main reason for which they are so widely adopted in many industrial fields. They are also extremely versatile due to the wide range of materials, configurations and many different types of inclusions that can be adopted depending on specific needs. Nevertheless, sandwich panels are usually characterized by very poor vibroacoustics efficiency which is why this aspect has been widely researched during the last couple of decades. Albeit many solutions have been demonstrated to be beneficial in this sense, they are usually weight-increasing fixes (e.g., viscoelastic inserts, porous fillers, Helmholtz resonators, etc.) and, hence, not ideal for the application in sectors with strict weight

requirements. On the other hand, substantial research has been focusing on the development of novel materials with higher viscoelastic damping than traditionally adopted solutions: these materials can be adopted as face skins and/or cellular core walls and thus have the potential to improve the vibroacoustics behaviour of a panel without compromising its weight. Examples are composite materials in which fibres are embedded in resins with nanoinclusions, causing damping to intervene on different scales to dissipate mechanical energy, or materials based on plant-derived sources, like natural fibres, which provide high energy dissipation by their own nature. The downside here, however, is that these materials are usually characterized by reduced mechanical properties and hence their adoption might compromise the stiffness-to-weight ratio and the structural integrity of the sandwich panel.

This thesis brought together many aspects relative to the development of a novel sandwich panel for vibroacoustics applications. The focus was primarily on researching novel materials rather than topology aspects and therefore the base configuration of the panel was fixed throughout the study: the two face skin are separated by a rectangular cellular core with square-cell topology, and dimensions of unit cell, thickness of core walls and skins were kept unchanged through the study. With the specific goal of designing a panel with high vibration damping properties, the material adopted for core walls and skins was a plant-derived composite consisting of flax fibres in PFA resin, a thermoset resin derived from crop waste. Furthermore, viscoelastic inserts consisting of a CNT-reinforced resin were deposited within the core and were designed by setting a maximum limit to the percentage of additional mass of 5%. The pristine resin adopted for the inserts was also a bio-derived resin.

In the entire study, a series of multidisciplinary aspects had to be explored. To start with, after choosing the materials, their manufacturing/curing techniques were investigated in order to set out the manufacturing process not only for the different components of the sandwich panels, but also for specimens for mechanical and thermo-mechanical characterization. Indeed, materials were not only mechanically characterized by tensile and three-point bending tests, but also TGA, DSC, DMA and rheology (only for the resins) tests allowed to have a wider picture of their thermo-mechanical behaviour. Methods and results of these characterization tests were explored in Chapters 3 and 4, respectively. The biggest remark about materials characterization that should be reiterated here concerns the substantial discrepancy between Tensile and Flexural Modulus of the flax/PFA composite (respectively evaluated from tensile and three-point-bending tests). Results from these tests are all highly reliable, due to both their good statistic properties and the fact that all experiments were performed by following respective ASTM standards to the letter. Three-point-bending tests outcomes were also confirmed by DMA tests in bending mode performed on the same material. Furthermore, numerical simulations of many tests performed at the structural scale (Chapters 6 and 7) provide results which are close to the experimental ones by considering either the Tensile or the Flexural Modulus as composite material stiffness depending on the type of deformations the structure (and hence the flax/PFA laminate) undergoes: when the

laminate is mostly subjected to in-plane deformations, then assigning the stiffness from tensile tests provides results closer to the experiments, whereas when it mainly undergoes flexural types of deformation the stiffness from three-point-bending tests provides more reliable numerical assessments. A possible explanation for this unusual behaviour of the flax/PFA laminate is given in section 8.2.1. High levels of weaving and misalignment of fibres can be observed in the flax/PFA fabric, due to the fact that the yarns dimensions are comparable to those of the laminate section: apart from generating low tensile properties, under flexural loading the thick bundles might generate "densification" phenomena and radial pressures on the compressed face and hence local stiffening effects, resulting therefore in a higher Flexural Modulus.

FE models with materials properties based on results from mechanical tests were implemented in Ansys Mechanical APDL and a probabilistic design study was carried out to study the impact of geometric uncertainties of the viscoelastic insert on global mechanical properties of the unit cell—section 5.3. This was done with the assumption that the properties of the lattice core base structure are deterministic variables. A manufacturing procedure for the entire sandwich panel was then developed in section 5.2 and specimens on several scales for different types of tests were produced. Control specimens without inserts were also manufactured (bare configuration). For these panels, the lattice core was made by interlocking crossing walls without applying any glue at the junction.

Different types of tests were performed on sandwich panels specimens. In order to demonstrate the structural integrity of the natural-composite based lattices, quasi-static OOP compression tests were carried out—sections 6.2 and 7.2 present methods and results, respectively—and the outcomes were compared to similar benchmark cases from open literature studies—figure 8.3 in section 8.2.2: the bare flax/PFA composite core developed in this thesis features the highest normalized stiffness among the benchmark cores, while the CNT-reinforced configuration offers the highest normalized compression failure stress. On the other hand, dynamic tests (sections 6.3 and 7.3) and impedance tube acoustic tests (sections 6.4 and 7.4) were also performed. As discussed in section 8.3, results of dynamic investigations suggest that different mechanisms intervene in the sandwich panels to dissipate mechanical energy, depending on the boundary conditions and load cases. When the panels are excited uniformly OOP, meaning that all points of the excited face are constrained to move together, the bare panel dissipates a great amount of mechanical energy by Coulomb dry friction mechanisms acting at the walls junction areas—figure 7.8 in section 7.3.1. In this case, indeed, experimental results suggest that the contribution of internal material damping to the overall loss factor is very small compared to the structural damping term. Conversely, when the sandwich panels are free to deform with flexural bending deformation modes, these friction phenomena at the walls junctions are not "activated" and the main energy dissipation mechanism is given by internal material damping. As introduced in section 8.3, it is well known in open literature that at low frequencies a sandwich panel behaves as a homogeneous panel and this frequency range is controlled by the total section bending

stiffness [172]. Therefore, in this configuration and in the examined frequency range, the panel with the viscoelastic inserts provides increased loss factor values with these specific boundary conditions due to the additional viscoelastic damping provided by the inserts—figure 7.15 and table 7.5 in section 7.3.2. Finally, impedance tube acoustic tests did not show any significant contributions by the inserts to the Transmission Loss of the panel—figure 7.16 in section 7.4.

9.2 Prospects of future research and development directions

9.2.1 Refinement of FE models: analysis of components contribution to overall damping levels

This section[1] provides an introduction to further developments of the FE models of bare and reinforced sandwich panels. In this thesis, in fact, damping was measured in terms of overall values, meaning that the contributions of single components and their interactions were not identified.

In order to quantify these contributions, numerical simulations should be performed by isolating different damping terms. The FE model of a unit cell must then contemplate the two face skins, the layer of glue (Super Sap CLV Epoxy Bio-Resin) between lattice and skins, the two interlocking walls, the contact between lattice walls (in the bare panel), the CNT-insert (in the reinforced panel). The most significant differences between these upgraded models and the ones adopted in this thesis would be the modelling of glue layers between lattice and skins (LS bond, present in both configurations) and of the joint between lattice walls (LL bond, in the bare panel).

Mechanical and internal material damping properties of the glue used for the LS bond are known, as this is the pristine resin that, filled with CNT inclusions, was also adopted for the CNT-inserts. Hence, its modelling and material properties assignment are straightforward. For what concerns the LL joint, instead, analytic and numerical dry-friction damping models currently available in open literature [176, 177] could be investigated and adopted. Since friction damping external to composite materials is an area relatively unexplored, alternative simplified modelling techniques of the joint could be taken into account and implemented at the same time. For example, one option could consist of modelling the bond with solid elements with material damping derived from the experimental value of vibration transmissibility peak amplitude (section 7.3.1). Figures 9.1 and 9.2 show examples of geometries for the LL and LS bonds, respectively. A second technique that could be adopted is applying spring-damper elements along the junction.

By performing FE simulations of the vibration transmissibility tests and the frequency response analysis and by comparing numerical and experimental results, it would be possible to explore the "location" of the damping, by identifying where the energy dissipation is predominant among the panel skins, the lattice, the insert and LL/LS bonds, and quantifying their contributions in

[1] The work introduced in this section as future development was carried out in parallel to the writing of this manuscript, within a research project in collaboration with QinetiQ Group PLC, headquartered in Farnborough, Hampshire, United Kingdom.

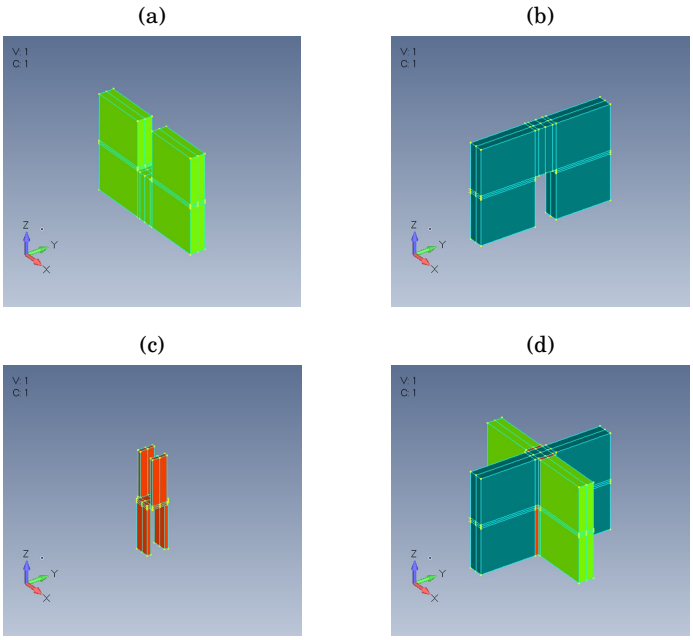

FIGURE 9.1. Geometry for refined FE model of the bare unit cell: lattice-lattice bond. (a) Lattice wall 1, (b) lattice wall 2, (c) lattice-to-lattice bond, (d) lattice walls with lattice-to-lattice bond. FEMAP CAE Software.

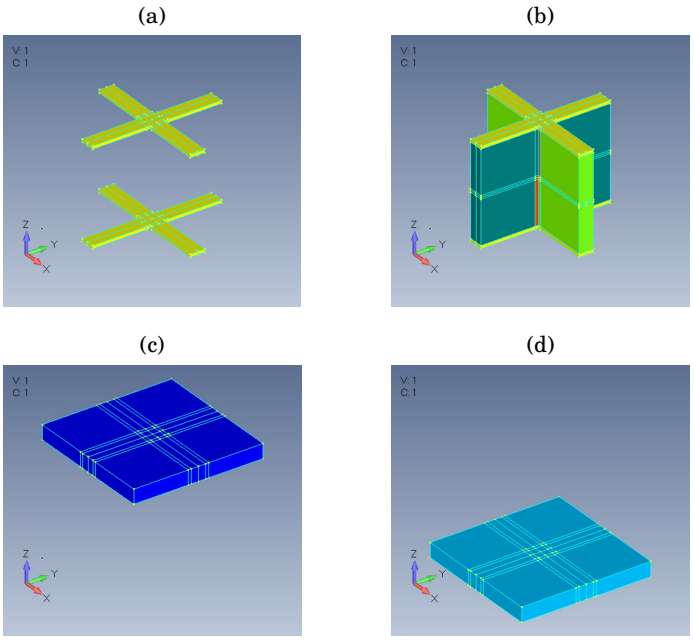

FIGURE 9.2. Geometry for refined FE model of the bare unit cell: lattice-skin bond. (a) Lattice-to-skin bonds, (b) bonded lattice walls and skin bonds, (c) top skin, (d) bottom skin. FEMAP CAE Software.

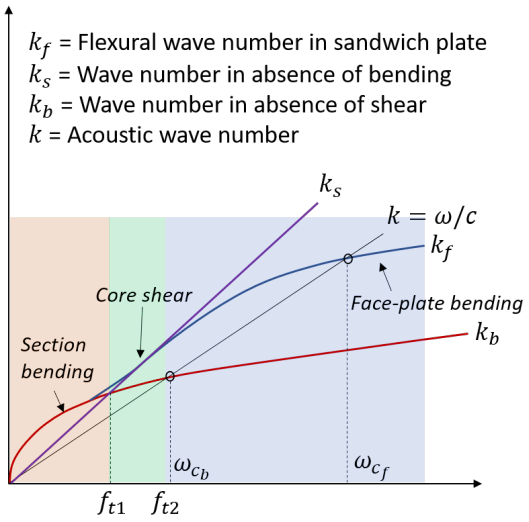

FIGURE 9.3. Typical dispersion curves of sandwich panels. The three main regions of vibroacoustic behaviour are highlighted.

the different case studies.

9.2.2 Further vibroacoustics investigations

Multiple vibroacoustics aspects are worth to consider for future investigations.

To start with, one interesting development could be performing an experimental study of the sound radiation resulting from structural vibrations of the two large-scale sandwich panels. Indeed, viscoelastic materials (applied to a structure as patches, inserts, layers, etc.) are well-known in literature for their consistent contribution to reducing sound levels radiated from a structure under vibrations [8, 100, 178]. Generally, sound radiation represents the final audible impression that one perceives due to structural vibrations [50]. Therefore, in case of the novel sandwich panels developed in this thesis, the evaluation of sound radiated from the panels without and with viscoelastic inserts would provide a more comprehensive study of their vibroacoustics performances.

A second development direction could be studying the vibroacoustic behaviour of the two sandwich panels in the range of frequencies dominated by core shear effects—i.e., after the shear transition frequency. Generally speaking, a transition frequency is the frequency at which a sandwich panel switches its current behaviour to another one. Fahy and Gardonio [172] defined three main regions of vibroacoustic behaviour of these structures and two transition frequencies, $f_{t,1}$ and $f_{t,2}$—figure 9.3. At low frequencies ($f < f_{t,1}$) the panel bending characteristics dominate: this zone is controlled by the total section bending stiffness and the whole panel acts as if it were homogeneous. In the middle region ($f_{t,1} < f < f_{t,2}$) the vibroacoustic behaviour is controlled by the core shear stiffness, whereas at $f > f_{t,2}$ the skin bending stiffness dominates. Therefore, $f_{t,1}$ is the first (or shear) transition frequency and defines the frequency at which the core shear becomes

important with respect to bending characteristics of the whole panel. The predominance of core shear effects is usually related to poor vibroacoustics performances of the sandwich panel and, generally, a higher $f_{t,1}$ value reflects an improvement in the sound transmission loss through the panel. For these reasons, the shear transition frequency is becoming an important design parameter for panels that need to be efficient from the vibroacoustic standpoint [4, 10, 179–181]. In figure 8.4(c) in section 8.3, slightly higher values of strain energy can be observed in the core walls of the bare unit cell compared to the reinforced. This suggests that when local modes intervene in the core shear-dominated region, mechanisms of Coulomb dry friction energy dissipation might be activated at the core walls junctions and therefore have beneficial effects on the vibroacoustic performances of the bare sandwich panel.

9.2.3 Improvement of manufacturing process and optimization of damping-to-mass ratio

Section 5.2 described the techniques adopted for the novel natural-composite sandwich panels manufacturing. With specific reference to the square-lattice core, slotted strips were cut either manually (for small panels) or with water jet technologies (for the two large-scale panels). Especially in case of small specimens, the manufacturing techniques can be improved by involving machines with higher precision to cut the slots, such as a milling machine. This might allow higher control on the slots width and, hence, on the gap between interlocking walls—which is mostly important for the sandwich panel without viscoelastic inserts.

Another aspect that could be further investigated in future concerns the design of the CNT-reinforced panel and is the optimization of the damping-to-mass ratio of viscoelastic inserts. In open literature, Boucher *et al.* [15] performed analytic and numerical study by investigating the optimization of the damping-to-mass ratio of viscoelastic inserts into a honeycomb lattice, proving that a partial occupation of the void could be more efficient on a density basis than full filling. The design of viscoelastic inserts inside honeycombs for damping applications was patented in [111]. This patent describes two types of inserts, a constrained layer of viscoelastic material within the ribs of the cell and a viscoelastic material inserted in the corner of the cell. Development of viscoelastic inserts in this thesis is performed on the basis of the latter approach. Considering these studies, the lattice filling might be optimised by the use of specific core designs or specific inserts. To avoid excessive increase in density, inserts may be deposited in a limited number of junctions rather than each one of them. Considering that the more strain energy is dissipated by the insert the more efficient it is, the aim is to find the optimal locations for the inserts under a variety of loading cases reflecting the deformation of the panel in a range of possible structural vibration modes. Some knowledge of the structural vibration modes of the sandwich panel is thus required. Indeed, locations of maximum strain vary depending on the deformation mode wavelength and the frequency range which is addressed. Hence, one approach might be aiming at specific frequencies and, depending on the corresponding wavelengths, verifying the areas of largest deformation which are the best for locating the damping inserts.

APPENDIX A

APPENDIX A

A.1 Evopreg PFC-flax composite curing: initial investigations

TENSILE tests on the Evopreg PFC-flax composite are performed on several batches of samples. As explained in section 3.2.1, these tests are initially used as a control method of the quality level of laminates as the parameters of the autoclave curing are being defined: better statistical characteristics and higher mechanical properties are noticeable in the stress-strain curves as, starting from the curing cycle recommended by the supplier, the heat rate is decreased, the dwell times are increased and the pressure applied is augmented. As an example, figure A.1 presents tensile test results of a laminate cured with a cycle similar to the definitive one presented in section 3.2.1, but with 3.5 bar pressure—that is the value recommended by the supplier—instead of 6.9 bar—that is the definitive cycle pressure. As evident from the curves, low pressure levels prevent the resin from spreading uniformly and penetrating fully into the flax fibres: low compaction causes high percentages of voids and defects, therefore less predictable mechanical properties.

As introduced in section 3.2.1, at the initial-investigation stage hot-press curing techniques are also explored. Figures A.2(a) and A.2(b) show results for hot-pressed composite laminates. The temperature cycle is that presented in section 3.2.1, whereas the applied force is 8 tons. Figure A.3 displays error-bar charts comparing mechanical performances of autoclave- and hot-press-cured Evopreg PFC-flax laminates. Briefly, compared to hot-press curing the autoclave techniques provide:

- Young's Modulus—higher mean values and smaller data ranges and standard deviations;
- Tensile strength—lower mean values and smaller data ranges and standard deviations;
- Elongation at break—lower mean values and smaller data ranges and standard deviations;

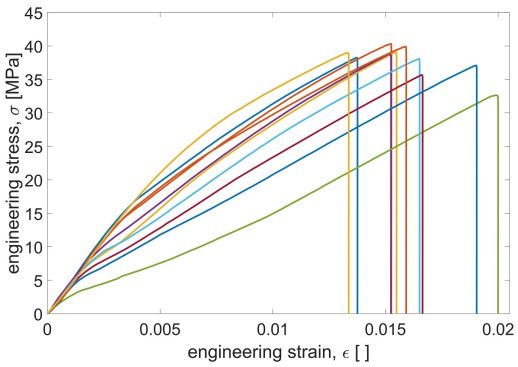

FIGURE A.1. Stress-strain curves of ten specimens cut from a low-compaction Evopreg PFC-flax laminate cured in autoclave with the definitive temperature cycle and 3.5 bar pressure. Fibers orientation 0/90°.

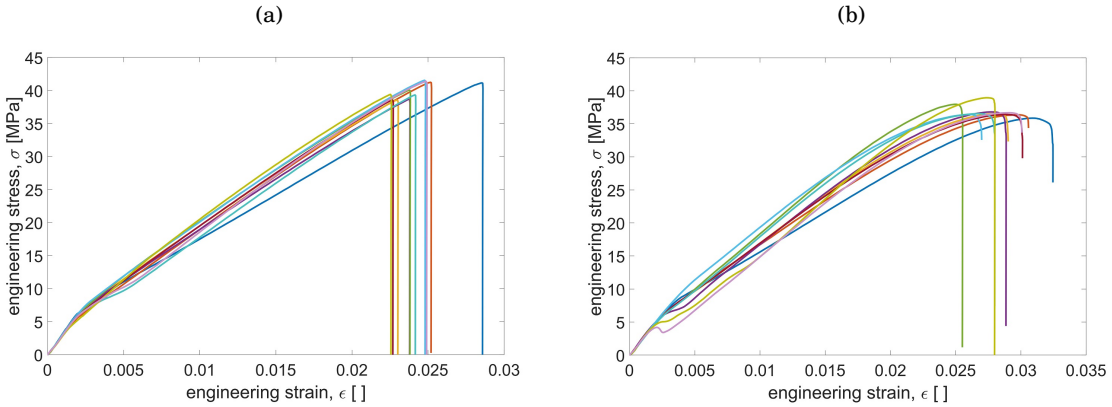

FIGURE A.2. Stress-strain curves of Evopreg PFC-flax specimens. Hot-press-cured laminates with definitive temperature cycle and 8 tons pressure. Fibers orientation (a) 0/90° and (b) ±45°.

- Overall, higher statistic reliability and better quality statistic properties.

It is clear not only that data for the hot-pressed laminates is less statistically reliable, but also that there is a degradation of mechanical properties compared to autoclave-cured samples. For this reason, vacuum bagging/autoclave methods are chosen as curing techniques for the Evopreg PFC-flax laminates.

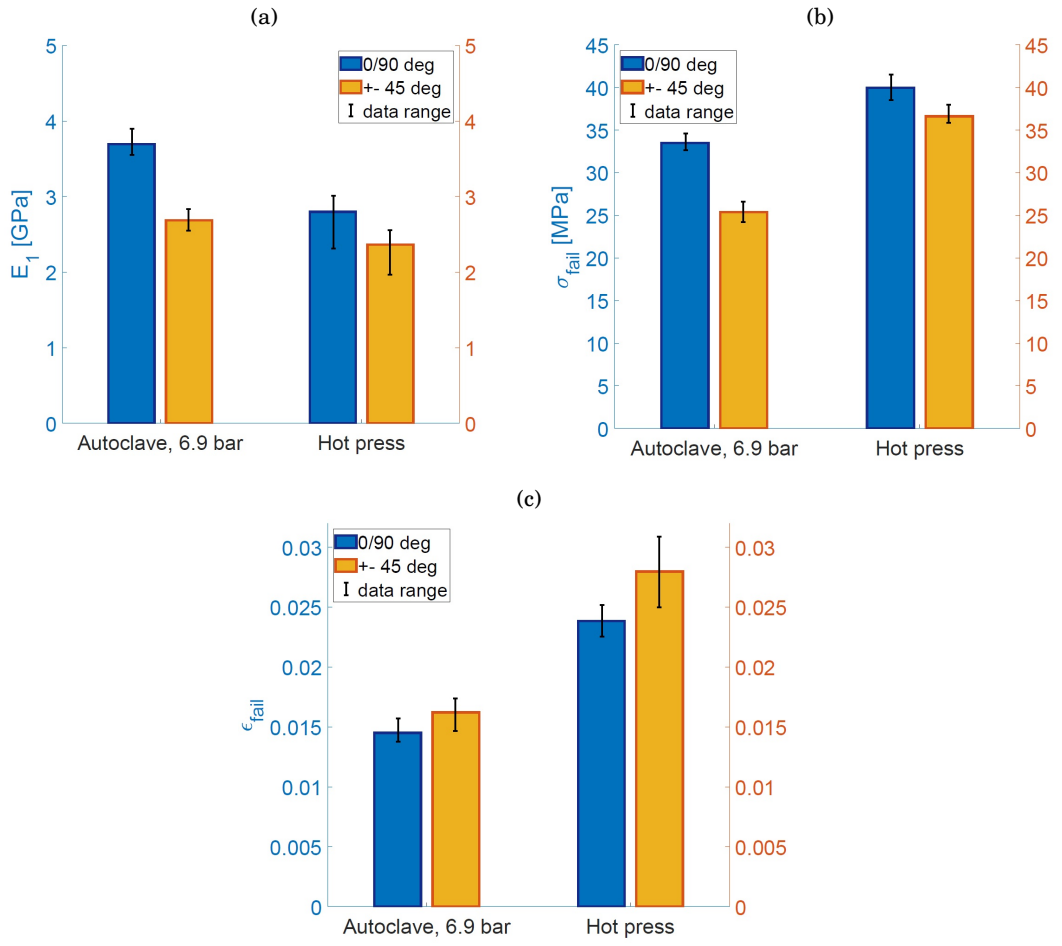

FIGURE A.3. Error-bar charts of mechanical characteristics of Evopreg PFC-flax laminates cured with different techniques: vacuum bagging/autoclave and hot press. Fibers orientation 0/90° and ±45°. (a) Young's Modulus, (b) tensile failure strength, (c) elongation at failure.

APPENDIX B

APPENDIX B

B.1 Measurement of Normal Incidence Sound Transmission Based on the Transfer Matrix Method

THIS method is reproduced from ASTM E2611-09 (Standard Test Method for Measurement of Normal Incidence Sound Transmission of Acoustical Materials Based on the Transfer Matrix Method). A schematic drawing of the measurements setup was shown in section 6.4 and it is reported here in figure B.1.

The sound transmission coefficient τ is a dimensionless property of a material in a specific frequency bandy and is defined as the ratio between airborne sound power incident on the material and the transmitted sound power:

$$\tau = \frac{W_i}{W_t} \tag{B.1}$$

Another property related to the incident and transmitted sound power is the sound transmission loss TL, defined as:

$$TL = 10 \log_{10}\left(\frac{W_i}{W_t}\right) = 10 \log_{10}\left(\frac{1}{\tau}\right) \tag{B.2}$$

TL_n represents the sound which impinges at an angle normal to the test specimen, as opposed to an arbitrary or random angle of incidence.
While the ASTM standard reports in detail how the apparatus needs to be built, test instrumentation to be adopted and test procedures, in this Appendix focus will be on the formulations utilized in this thesis for the estimation of the TM elements and, consequently, the sound properties of the structure.

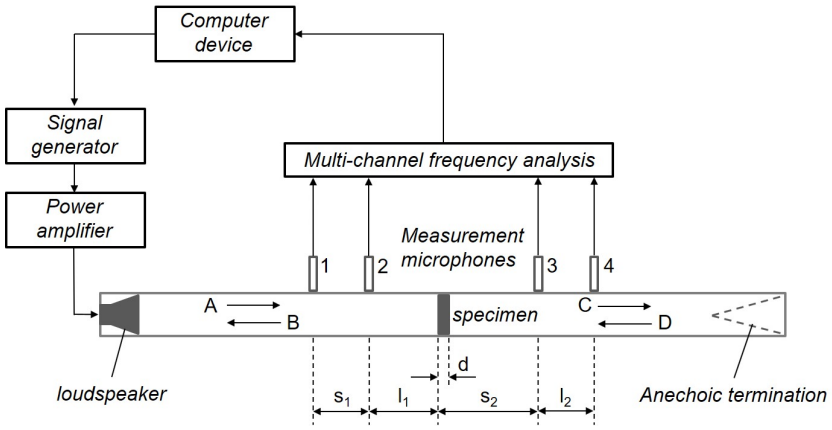

FIGURE B.1. Acoustic impedance tube tests: schematic drawing of measurement setup.

B.2 Transfer Matrix

According to the ASTM standard, two methods can be used to calculate the Normal Incidence TM: the Two-Load and the One-Load methods. Despite in this thesis only the first one is utilized, both will be briefly explored in the following sections.

B.2.1 Two-Load Method

A single transfer matrix (TM) measurement involves two different measurements with two different terminations of the impedance tube. The TM relates the acoustic pressure and particle velocity on front and back surfaces of the specimen. The tube must be configured with two different terminations (details are reported in the ASTM standard), which are here represented by indices a and b, in order to obtain four linear equations that can be used to solve the four unknown TM elements. The TM relation for termination a is:

$$\begin{bmatrix} p_a \\ u_a \end{bmatrix}_{x=0} = \begin{bmatrix} T_{11} & T_{12} \\ T_{21} & T_{22} \end{bmatrix} \begin{bmatrix} p_a \\ u_a \end{bmatrix}_{x=d} \tag{B.3}$$

Similarly, the TM relation for termination b is:

$$\begin{bmatrix} p_b \\ u_b \end{bmatrix}_{x=0} = \begin{bmatrix} T_{11} & T_{12} \\ T_{21} & T_{22} \end{bmatrix} \begin{bmatrix} p_b \\ u_b \end{bmatrix}_{x=d} \tag{B.4}$$

In the previous equations, case a could, for example, represent an "anechoic" termination and b a blocked or open one.
For each load case, the acoustic wave field inside the tube can be decomposed into forward and

backwards traveling waves on either side of the specimen (figure B.1):

$$A = j\frac{H_{1,ref}e^{-jkl_1} - H_{2,ref}e^{-jk(l_1+s_1)}}{2\sin ks_1} \tag{B.5a}$$

$$B = j\frac{H_{2,ref}e^{+jk(l_1+s_1)} - H_{1,ref}e^{+jkl_1}}{2\sin ks_1} \tag{B.5b}$$

$$C = j\frac{H_{3,ref}e^{+jk(l_2+s_2)} - H_{4,ref}e^{+jkl_2}}{2\sin ks_2} \tag{B.5c}$$

$$D = j\frac{H_{4,ref}e^{-jkl_2} - H_{3,ref}e^{-jk(l_2+s_2)}}{2\sin ks_2} \tag{B.5d}$$

In the previous equations, $H_{i,j}$ represent transfer functions of two microphone signals corrected for microphone response mismatch. For these transfer functions, the reference may be one of the four measurement locations, a separate measurement location removed from the original four, or the electrical signal provided to the source microphone. $k = 2\pi f/c$ is the wave number in air [m^{-1}], being f the frequency [Hz] and c the speed of sound [m/s]. Finally, l_i and s_i are geometric characteristics relative to the microphones positioning (see figure B.1).
For each one of the two load cases, the acoustic pressure and particle velocity on both faces of the specimen (at $x = 0$ and $x = d$) can be evaluated as:

$$p_0 = A + B \qquad p_d = Ce^{-jkd} + De^{+jkd} \tag{B.6a}$$

$$u_0 = (A - B)/\rho c \qquad u_d = (Ce^{-jkd} - De^{+jkd})/\rho c \tag{B.6b}$$

From pressure and particle velocity values in each load case, the specimen's TM can be calculated as:

$$T = \begin{bmatrix} \dfrac{p_{0a}u_{db} - p_{0b}u_{da}}{p_{da}u_{db} - p_{db}u_{da}} & \dfrac{p_{0b}p_{da} - p_{0a}p_{db}}{p_{da}u_{db} - p_{db}u_{da}} \\ \dfrac{u_{0a}u_{db} - u_{0b}u_{da}}{p_{da}u_{db} - p_{db}u_{da}} & \dfrac{p_{da}u_{0b} - p_{db}u_{0a}}{p_{da}u_{db} - p_{db}u_{da}} \end{bmatrix} \tag{B.7}$$

B.2.2 One-Load Method

For specimens that are geometrically symmetric (i.e., have same physical properties to the sound field on either side), the procedure of section B.2.1 can be simplified by recognizing that reciprocity places two constraints on the TM:

$$T_{11} = T_{22} \quad \text{and} \quad T_{11}T_{22} - T_{12}T_{21} = 1 \tag{B.8}$$

Thus allowing the TM elements to be determined by a measurement of the microphone transfer function with only one termination case, preferably the anechoic.

$$T = \begin{bmatrix} \dfrac{p_d u_d + p_0 u_0}{p_0 u_d + p_d u_0} & \dfrac{p_0^2 - p_d^2}{p_0 u_d + p_d u_0} \\ \dfrac{u_0^2 - u_d^2}{p_0 u_d + p_d u_0} & \dfrac{p_d u_d + p_0 u_0}{p_0 u_d + p_d u_0} \end{bmatrix} \tag{B.9}$$

B.3 Evaluation of Material Properties

Independently on the load case adopted in the experiments for the evaluation of the TM, once its elements are known the material acoustic properties can be evaluated as follows.
Transmission Coefficient (anechoic-backed):

$$t = \frac{2e^{jkd}}{T_{11} + (T_{12}/\rho c) + \rho c T_{21} + T_{22}} \tag{B.10}$$

Normal Incidence Transmission Loss:

$$TL_n = 20 \log_{10} \left| \frac{1}{t} \right| \tag{B.11}$$

Reflection Coefficient (hard-backed):

$$R = \frac{T_{11} - \rho c T_{21}}{T_{11} + \rho c T_{21}} \tag{B.12}$$

Absorption Coefficient (hard-backed):

$$\alpha = 1 - |R|^2 \tag{B.13}$$

BIBLIOGRAPHY

[1] T. Bitzer, *Honeycomb Technology: Materials, Design, Manufacturing, Applications and Testing* (Chapman & Hall, London SE1 8HN, UK, 1997).

[2] L. J. Gibson and M. F. Ashby, *Cellular solids: Structure and Properties* (Cambridge University Press, Cambridge, 1997).

[3] M. Ranjbar, L. Boldrin, F. Scarpa, S. Neild, and S. Patsias, "Vibroacoustic optimization of anti-tetrachiral and auxetic hexagonal sandwich panels with gradient geometry", *Smart Materials and Structures* **25**, 054012 (2016).

[4] C. Droz, Z. Zergoune, R. Boukadia, O. Bareille, and M. N. Ichchou, "Vibro-acoustic optimisation of sandwich panels using the wave/finite element method", *Composite Structures* **156**, 108–114 (2016).

[5] S. Rajaram, T. Wang, and S. Nutt, "Sound transmission loss of honeycomb sandwich panels", *Noise Control Engineering Journal* **54**, 106–115 (2006).

[6] C. L. Dym and M. A. Lang, "Transmission of sound through sandwich panels", *The Journal of the Acoustical Society of America* **56**, 1523–1532 (1974).

[7] M. A. Lang and C. L. Dym, "Optimal acoustic design of sandwich panels", *The Journal of the Acoustical Society of America* **57**, 1481–1487 (1975).

[8] W. Larbi, J. Deü, and R. Ohayon, "Vibroacoustic analysis of double-wall sandwich panels with viscoelastic core", *Computers & Structures* **174**, 92–103 (2016).

[9] M. S. Mazloomi, M. Ranjbar, L. Boldrin, F. Scarpa, S. Patsias, and N. Ozada, "Vibroacoustics of 2d gradient auxetic hexagonal honeycomb sandwich panels", *Composite Structures* **187**, 593–603 (2018).

[10] R. Palumbo, D. Ivanov, C. Droz, F. Scarpa, O. Bareille, and M. Ichchou, "A multi-scale reinforced sandwich panel for vibroacoustic applications: shear transition effects", in *IX ECCOMAS Thematic Conference on Smart Structures and Materials, SMART 2019,* (2019).

[11] S. E. Moosavimehr and A. S. Phani, "Sound transmission loss characteristics of sandwich panels with a truss lattice core", *The Journal of the Acoustical Society of America* **141**, 2921–2932 (2017).

[12] D. Palumbo and J. Klos, "Quiet honeycomb panels", in *24th National Conference on Noise Control Engineering 2010 (Noise-Con 10), Baltimore,* (2010).

[13] K. F. Tee, A. Spadoni, F. Scarpa, and M. Ruzzene, "Vibroacoustics and wave propagation of novel chiral honeycombs", in *Active and Passive Smart Structures and Integrated Systems 2008,* vol. 6928 (International Society for Optics and Photonics, 2008), p. 69280J.

[14] G. Ghiringhelli, M. Terraneo, and E. Vigoni, "Improvement of structures vibroacoustics by widespread embodiment of viscoelastic materials", *Aerospace Science and Technology* **28**, 227–241 (2013).

[15] M.-A. Boucher, C. Smith, F. Scarpa, R. Rajasekaran, and K. Evans, "Effective topologies for vibration damping inserts in honeycomb structures", *Composite Structures* **106**, 1–14 (2013).

[16] O. Tanneau, J. Casimir, and P. Lamary, "Optimization of multilayered panels with poroelastic components for an acoustical transmission objective", *The Journal of the Acoustical Society of America* **120**, 1227–1238 (2006).

[17] C. Thomas and R. Gerstner, "Sandwich panel for sound absorption", (2010). US Patent 7,743,884.

[18] D. W. Lapins and R. Szymanski, "Acoustical panel", (1986). US Patent 4,630,416.

[19] E. Herup, S. Huybrechts, S. Griffin, and S. Tsai, "Method of making composite chamber-core sandwich-type structure with inherent acoustic attenuation", (2001). US Patent 6,231,710.

[20] D. Palumbo and J. Klos, "The effects of voids and recesses on the transmission loss of honeycomb sandwich panels", *Noise Control Eng. J.* **59**, 631—-640 (2011).

[21] F. Scarpa, C. W. Smith, W. Miller, K. Evans, and R. Rajasekaran, *Vibration damping structures* (US9382962B2, United States, 2016).

[22] Z. Li and M. J. Crocker, "A review on vibration damping in sandwich composite structures", *International Journal of Acoustics and Vibrations* **10**, 159–169 (2005).

[23] M. D. Rao, "Recent applications of viscoelastic damping for noise control in automobiles and commercial airplanes", *Journal of Sound and Vibration* **262**, 457–474 (2003).

[24] Z. Xue and J. W. Hutchinson, "A comparative study of impulse-resistant metal sandwich plates", *International Journal of Impact Engineering* **30**, 1283—1305 (2004).

[25] N. A. Fleck and V. S. Deshpande, "The resistance of clamped sandwich beams to shock loading", *ASME. J. Appl. Mech.* **71**, 386—-401 (2004).

[26] F. Côté, V. Deshpande, N. Fleck, and A. Evans, "The out-of-plane compressive behaviour of metallic honeycombs", *Materials Science and Engineering: A* **380**, 272–280 (2004).

[27] G. Petrone, S. Rao, S. D. Rosa, B. Mace, F. Franco, and D. Bhattacharyya, "Initial experimental investigations on natural fibre reinforced honeycomb core panels", *Composites Part B: Engineering* **55**, 400–406 (2013).

[28] A. K. Mohanty, M. Misra, and L. T. Drzal, "Sustainable bio-composites from renewable resources: Opportunities and challenges in the green materials world", *Journal of Polymers and the Environment* **10**, 19–26 (2002).

[29] A. K. Mohanty, M. Misra, and L. T. Drzal, *Natural fibers, biopolymers, and biocomposites* (CRC press, 2005).

[30] O. Faruk, A. K. Bledzki, H.-P. Fink, and M. Sain, "Biocomposites reinforced with natural fibers: 2000–2010", *Progress in Polymer Science* **37**, 1552–1596 (2012). Topical Issue on Polymeric Biomaterials.

[31] F. Scarpa, C. W. Smith, W. Miller, K. Evans, and R. Rajasekaran, *Vibration damping structures* (US9382962B2, United States, 2016).

[32] R. Rajasekaran, M.-A. Boucher, C. W. Smith, F. Scarpa, and K. E. Evans, *Vibration damping* (US9494206B2, United States, 2016).

[33] X. Zhou, D. Yu, X. Shao, S. Zhang, and S. Wang, "Research and applications of viscoelastic vibration damping materials: A review", *Composite Structures* **136**, 460–480 (2016).

[34] H. Rajoria and N. Jalili, "Passive vibration damping enhancement using carbon nanotube-epoxy reinforced composites", *Composites Science and Technology* **65**, 2079—-2093 (2005).

[35] G. Barra, L. Guadagno, L. Vertuccio, B. Simonet, B. Santos, M. Zarrelli, M. Arena, and M. Viscardi, "Different methods of dispersing carbon nanotubes in epoxy resin and initial evaluation of the obtained nanocomposite as a matrix of carbon fiber reinforced laminate in terms of vibroacoustic performance and flammability", *Materials* **12** (2019).

[36] Y. Aminanda, B. Castanié, J. J. Barrau, and P. Thevenet, "Experimental analysis and modeling of the crushing of honeycomb cores", *Applied Composite Materials* **12**, 213–227 (2005).

[37] R. Seemann and D. Krause, "Numerical modelling of nomex honeycomb sandwich cores at meso-scale level", *Composite Structures* **159**, 702–718 (2017).

[38] M. Osei-Antwi, J. de Castro, A. P. Vassilopoulos, and T. Keller, "Shear mechanical characterization of balsa wood as core material of composite sandwich panels", *Construction and Building Materials* **41**, 231–238 (2013).

[39] W. Cantwell and P. Davies, "A study of skin-core adhesion in glass fibre reinforced sandwich materials", *Applied Composite Materials* **3**, 407–420 (1996).

[40] J. L. Grenestedt and B. Bekisli, "Analyses and preliminary tests of a balsa sandwich core with improved shear properties", *International journal of mechanical sciences* **45**, 1327–1346 (2003).

[41] V. D'Alessandro, G. Petrone, F. Franco, and S. D. Rosa, "A review of the vibroacoustics of sandwich panels: Models and experiments", *Journal of Sandwich Structures & Materials* **15**, 541—582 (2013).

[42] D. I. G. Jones, *Viscoelastic vibration damping* (John Wiley & Sons Ltd, Baffins Lane, Chichester, West Sussex PO19 1UD, England, 2001).

[43] H. P. Gavin, *Dynamics of Simple Oscillators (single degree of freedom systems)* (Department of Civil and Environmental Engineering, Duke University, 2018).

[44] F. Scarpa, J. Giacomin, Y. Zhang, and P. Pastorino, "Mechanical performance of auxetic polyurethane foam for antivibration glove applications", *Cellular Polymers* **24**, 253–268 (2005).

[45] M. Bianchi and F. Scarpa, "Vibration transmissibility and damping behaviour for auxetic and conventional foams under linear and nonlinear regimes", *Smart Materials and Structures* **22**, 084010 (2013).

[46] Q. Zhang, D. Zhang, Y. Dobah, F. Scarpa, F. Fraternali, and R. E. Skelton, "Tensegrity cell mechanical metamaterial with metal rubber", *Applied Physics Letters* **113**, 031906 (2018).

[47] S. O. Oyadiji and G. R. Tomlinson, "Determination of the complex moduli of viscoelastic structural elements by resonance and non-resonance methods", *Journal of Sound and Vibration* **101**, 277–298 (1985).

[48] C. W. De Silva, *Vibration damping, control, and design* (CRC Press, 2007).

[49] G. Petrone, V. D'Alessandro, F. Franco, and S. D. Rosa, "Damping evaluation on eco-friendly sandwich panels through reverberation time (rt 60) measurements", *Journal of Vibration and Control* **21**, 3328–3338 (2015).

[50] L. Cremer, M. Heckl, and B. A. Petersson, *Structure-borne sound: structural vibrations and sound radiation at audio frequencies* (Springer Science & Business Media, 2005).

[51] A. D. Nashif, D. I. Jones, and J. P. Henderson, *Vibration damping* (John Wiley & Sons, 1985).

[52] E. J. Graesser and C. R. Wong, "The relationship of traditional damping measures for materials with high damping capacity: a review", in *M 3 D: Mechanics and Mechanisms of Material Damping,* (ASTM International, 1992).

[53] B. Bloss and M. D. Rao, "Measurement of damping in structures by the power input method", *Experimental techniques* **26**, 30–32 (2002).

[54] A. Mohanty, M. Misra, and G. Hinrichsen, "Biofibres, biodegradable polymers and biocomposites: An overview", *Macromolecular materials and Engineering* **276**, 1–24 (2000).

[55] A. Mohanty, M. Misra, and L. T. Drzal, "Surface modifications of natural fibers and performance of the resulting biocomposites: an overview", *Composite interfaces* **8**, 313–343 (2001).

[56] D. Puglia, J. Biagiotti, and J. M. Kenny, "A review on natural fibre-based composites—part ii", *Journal of Natural Fibers* **1**, 23–65 (2005).

[57] W. Brouwer, *Natural fibre composites saving weight and cost with renewable materials* (Society of Manufacturing Engineers, 2000).

[58] P. Wambua, J. Ivens, and I. Verpoest, "Natural fibres: can they replace glass in fibre reinforced plastics?" *Composites Science and Technology* **63**, 1259–1264 (2003). Eco-Composites.

[59] A. L. Leao, R. Rowell, and N. Tavares, "Applications of natural fibers in automotive industry in brazil — thermoforming process", in *Science and Technology of Polymers and Advanced Materials,* P. N. Prasad, J. E. Mark, S. H. Kandil, and Z. H. Kafafi, eds. (Springer, Boston, 1998), pp. 755–761.

[60] M. Karus and M. Kaup, "Natural fibres in the european automotive industry", *Journal of Industrial Hemp* **7**, 119–131 (2002).

[61] R. Dunne, D. Desai, R. Sadiku, and J. Jayaramudu, "A review of natural fibres, their sustainability and automotive applications", *Journal of Reinforced Plastics and Composites* **35**, 1041–1050 (2016).

[62] I. Verpoest, J. Baets, J. V. Acker, H. Lilholt, M. Hugues, and C. Baley, *Flax and Hemp fibres: a natural solution for the composite industry* (JEC Compos, 2012).

[63] P. Balakrishnan, M. John, L. Pothen, M. Sreekala, and S. Thomas, "12 - natural fibre and polymer matrix composites and their applications in aerospace engineering", in *Advanced Composite Materials for Aerospace Engineering,* S. Rana and R. Fangueiro, eds. (Woodhead Publishing, 2016), pp. 365–383.

[64] H. Deka, M. Misra, and A. Mohanty, "Renewable resource based "all green composites" from kenaf biofiber and poly(furfuryl alcohol) bioresin", *Industrial Crops and Products* **41**, 94–101 (2013).

[65] G. Toriz, R. Arvidsson, M. Westin, and P. Gatenholm, "Novel cellulose ester–poly(furfuryl alcohol)–flax fiber biocomposites", *Journal of Applied Polymer Science* **88**, 337–345 (2003).

[66] F. Duc, P. E. Bourban, C. J. G. Plummer, and J. A. E. Manson, "Damping of thermoset and thermoplastic flax fibre composites", *Composites Part A: Applied Science and Manufacturing* **64**, 115–123 (2014).

[67] V. Fiore, A. Valenza, and G. D. Bella, "Mechanical behavior of carbon/flax hybrid composites for structural applications", *Journal of Composite Materials* **46**, 2089–2096 (2011).

[68] V. Fiore and L. Calabrese, "Effect of stacking sequence and sodium bicarbonate treatment on quasi-static and dynamic mechanical properties of flax/jute epoxy-based composites", *Materials* **12**, 1363 (2019).

[69] A. W. V. Vuure, J. Baets, K. Wouters, and K. Hendrickx, "Compressive properties of natural fibre composites", *Materials Letters* **149**, 138–140 (2015).

[70] K. S. Kumar, I. Siva, P. Jeyaraj, J. W. Jappes, S. Amico, and N. Rajini, "Synergy of fiber length and content on free vibration and damping behavior of natural fiber reinforced polyester composite beams", *Materials & Design (1980-2015)* **56**, 379–386 (2014).

[71] A. Belaadi, A. Bezazi, M. Bourchak, and F. Scarpa, "Tensile static and fatigue behaviour of sisal fibres", *Materials & Design* **46**, 76–83 (2013).

[72] A. Belaadi, A. Bezazi, M. Bourchak, F. Scarpa, and C. Zhu, "Thermochemical and statistical mechanical properties of natural sisal fibres", *Composites Part B: Engineering* **67**, 481–489 (2014).

[73] Y. Dobah, M. Bourchak, A. Bezazi, A. Belaadi, and F. Scarpa, "Multi-axial mechanical characterization of jute fiber/polyester composite materials", *Composites Part B: Engineering* **90**, 450–456 (2016).

[74] L. M. G. Vieira, J. C. dos Santos, T. H. Panzera, J. C. C. Rubio, and F. Scarpa, "Novel fibre metal laminate sandwich composite structure with sisal woven core", *Industrial Crops and Products* **99**, 189–195 (2017).

[75] J. Summerscales, N. Dissanayake, A. Virk, and W. Hall, "A review of bast fibres and their composites. part 2–composites", *Composites Part A: Applied Science and Manufacturing* **41**, 1336–1344 (2010).

[76] M. Kabir, H. Wang, T. Aravinthan, F. Cardona, and K.-T. Lau, "Effects of natural fibre surface on composite properties: A review", in *Proceedings of the 1st international postgraduate conference on engineering, designing and developing the built environment for sustainable wellbeing (eddBE2011),* (Queensland University of Technology, 2011), pp. 94–99.

[77] D. U. Shah, "Natural fibre composites: Comprehensive ashby-type materials selection charts", *Materials & Design (1980-2015)* **62**, 21–31 (2014).

[78] K. L. Pickering, M. A. Efendy, and T. M. Le, "A review of recent developments in natural fibre composites and their mechanical performance", *Composites Part A: Applied Science and Manufacturing* **83**, 98–112 (2016).

[79] S. Dixit, R. Goel, A. Dubey, P. R. Shivhare, and T. Bhalavi, "Natural fibre reinforced polymer composite materials-a review", *Polymers from renewable resources* **8**, 71–78 (2017).

[80] N. Ramli, N. Mazlan, Y. Ando, Z. Leman, K. Abdan, A. A. Aziz, and N. A. Sairy, "Natural fiber for green technology in automotive industry: A brief review", *IOP Conference Series: Materials Science and Engineering* **368**, 012012 (2018).

[81] R. Ilyas, S. Sapuan, M. N. Norizan, M. Atikah, M. Huzaifah, A. Radzi, M. Ishak, E. Zainudin, S. Izwan, A. N. Azammi *et al.*, "Potential of natural fibre composites for transport industry: a review", in *Prosiding Seminar Enau Kebangsaan,* vol. 2019 (2019), pp. 2–11.

[82] K. L. Pickering, *Properties and Performance of Natural-Fibre Composites* (Woodhead Publishing, 2008).

[83] A. Hodzic and R. Shanks, *Natural Fibre Composites: Materials, Processes and Properties* (Woodhead Publishing, 2014).

[84] R. Campilho, *Natural Fiber Composites* (CRC Press, 2015).

[85] M. Fan and F. Fu, *Advanced High Strength Natural Fibre Composites in Construction* (Woodhead Publishing, 2016).

[86] R. Fangueiro and S. Rana, *Advances in Natural Fibre Composites: Raw Materials, Processing and Analysis* (Springer, 2017).

[87] S. Prabhakaran, V. Krishnaraj, M. Senthilkumar, and R. Zitoune, "Sound and vibration damping properties of flax fiber reinforced composites", *Procedia Engineering* **97**, 573–581 (2014).

[88] G. Petrone, V. D'Alessandro, F. Franco, B. Mace, and S. D. Rosa, "Modal characterisation of recyclable foam sandwich panels", *Composite Structures* **113**, 362—368 (2014).

[89] M. Z. Rahman, K. Jayaraman, and B. R. Mace, "Vibration damping of flax fibre-reinforced polypropylene composites", *Fibers and Polymers* **18**, 2187–2195 (2017).

[90] M. L. Longana, V. Ondra, H. Yu, K. D. Potter, , and I. Hamerton, "Reclaimed carbon and flax fibre composites: Manufacturing and mechanical properties", *Recycling* **3**, 52 (2018).

[91] M. L. Longana, P. Aryal, H. Yu, and K. D. Potter, "The high performance discontinuous fibre (hiperdif) method for carbon-flax hybrid composites manufacturing", in *ICCM21 21st International Conference on Composite Materials,* (2017).

[92] J. Holbery and D. Houston, "Natural-fiber-reinforced polymer composites in automotive applications", *JOM* **58**, 80–86 (2006).

[93] B. Weager, "High-performance biocomposites: novel aligned natural fibre reinforcements: Natural fibres-the future of composites?" *JEC composites* pp. 31–32 (2010).

[94] S. Mallaiah, K. V. Sharma, and M. Krishna, "Development and comparative studies of bio-based and synthetic fiber based sandwich structures", *Int J Soft Compos Eng* **2**, 332–5 (2012).

[95] S. Rao, K. Jayaraman, and D. Bhattacharyya, "Micro and macro analysis of sisal fibre composites hollow core sandwich panels", *Composites Part B: Engineering* **43**, 2738–2745 (2012).

[96] S. Rao, R. Das, and D. Bhattacharyya, "Investigation of bond strength and energy absorption capabilities in recyclable sandwich panels", *Composites Part A: Applied Science and Manufacturing* **45**, 6–13 (2013).

[97] M. Hao, Y. Hu, B. Wang, and S. Liu, "Mechanical behavior of natural fiber-based isogrid lattice cylinder", *Composite Structures* **176**, 117–123 (2017).

[98] M. Zuhri, Z. Guan, and W. Cantwell, "The mechanical properties of natural fibre based honeycomb core materials", *Composites Part B: Engineering* **58**, 1–9 (2014).

[99] A. Stocchi, L. Colabella, A. Cisilino, and V. Alvarez, "Manufacturing and testing of a sandwich panel honeycomb core reinforced with natural-fiber fabrics", *Materials & Design* **55**, 394–403 (2014).

[100] X. Zhou, D. Yu, X. Shao, S. Zhang, and S. Wang, "Research and applications of viscoelastic vibration damping materials: A review", *Composite Structures* **136**, 460–480 (2016).

[101] J. D. Ferry, *Viscoelastic properties of polymers* (John Wiley & Sons, 1980).

[102] E. M. Kerwin, "Damping of flexural waves by a constrained viscoelastic layer", *The Journal of the Acoustical society of America* **31**, 952–962 (1959).

[103] D. Ross, "Damping of plate flexural vibrations by means of viscoelastic laminae", *Structural damping* pp. 49–97 (1959).

[104] A. Lall, N. Asnani, and B. Nakra, "Damping analysis of partially covered sandwich beams", *Journal of Sound and Vibration* **123**, 247–259 (1988).

[105] S.-W. Kung and R. Singh, "Complex eigensolutions of rectangular plates with damping patches", *Journal of sound and vibration* **216**, 1–28 (1998).

[106] S.-W. Kung and R. Singh, "Development of approximate methods for the analysis of patch damping design concepts", *Journal of Sound and Vibration* **219**, 785–812 (1999).

[107] G. Tomlinson, "The use of constrained layer damping in vibration control", *International Journal of Mechanical Sciences* **32**, 233–242 (1990).

[108] B. Bhattacharya, G. R. Tomlinson, and J. R. House, "Effect of shapes of viscoelastic inserts on vibration absorption in laminated composites", in *Proc. SPIE 3672, Smart Structures and Materials 1999: Passive Damping and Isolation,* (1999).

[109] F. Agnese and F. Scarpa, "Macro-composites with star-shaped inclusions for vibration damping in wind turbine blades", *Composite Structures* **108**, 978–986 (2014).

[110] P. Aumjaud, C. W. Smith, and K. E. Evans, "A novel viscoelastic damping treatment for honeycomb sandwich structures", *Composite Structures* **119**, 322–332 (2015).

[111] R. Rajasekaran, M.-A. Boucher, C. W. Smith, F. Scarpa, and K. E. Evans, *Vibration damping* (US9494206B2, United States, 2016).

[112] S. Iijima, "Helical microtubules of graphitic carbon", *nature* **354**, 56–58 (1991).

[113] J.-P. Salvetat, J.-M. Bonard, N. Thomson, A. Kulik, L. Forro, W. Benoit, and L. Zuppiroli, "Mechanical properties of carbon nanotubes", *Applied Physics A* **69**, 255–260 (1999).

[114] P. Avouris, T. Hertel, R. Martel, T. Schmidt, H. Shea, and R. Walkup, "Carbon nanotubes: nanomechanics, manipulation, and electronic devices", *Applied Surface Science* **141**, 201–209 (1999).

[115] B. Kilbride, J. Coleman, J. Fraysse, P. Fournet, M. Cadek, A. Drury, S. Hutzler, S. Roth, and W. Blau, "Experimental observation of scaling laws for alternating current and direct current conductivity in polymer-carbon nanotube composite thin films", *Journal of applied physics* **92**, 4024–4030 (2002).

[116] M. Biercuk, M. C. Llaguno, M. Radosavljevi, J. Hyun, A. T. Johnson, and J. E. Fischer, "Carbon nanotube composites for thermal management", *Applied physics letters* **80**, 2767–2769 (2002).

[117] X. Xu, M. M. Thwe, C. Shearwood, and K. Liao, "Mechanical properties and interfacial characteristics of carbon-nanotube-reinforced epoxy thin films", *Applied physics letters* **81**, 2833–2835 (2002).

[118] A. Allaoui, S. Bai, H.-M. Cheng, and J. Bai, "Mechanical and electrical properties of a mwnt/epoxy composite", *Composites science and technology* **62**, 1993–1998 (2002).

[119] D. Li, X. Zhang, G. Sui, D. Wu, J. Liang, and X.-S. Yi, "Toughness improvement of epoxy by incorporating carbon nanotubes into the resin", *Journal of materials science letters* **22**, 791–793 (2003).

[120] J. N. Coleman, U. Khan, W. Blau, and Y. Gun'ko, "Small but strong: A review of the mechanical properties of carbon nanotube-polymer composites", *Carbon* **44**, 1624–1652 (2006).

[121] K.-T. Lau and D. Hui, "Effectiveness of using carbon nanotubes as nano-reinforcements for advanced composite structures", *Carbon (New York, NY)* **40**, 1605–1606 (2002).

[122] N. A. Koratkar, B. Wei, and P. M. Ajayan, "Multifunctional structural reinforcement featuring carbon nanotube films", *Composites Science and Technology* **63**, 1525–1531 (2003).

[123] H. Rajoria and N. Jalili, "Determination of strength and damping characteristics of carbon nanotube-epoxy composites", in *ASME 2004 International Mechanical Engineering Congress and Exposition,* (American Society of Mechanical Engineers Digital Collection, 2004), pp. 1461–1466.

[124] X. Zhou, E. Shin, K. Wang, and C. Bakis, "Interfacial damping characteristics of carbon nanotube-based composites", *Composites Science and Technology* **64**, 2425–2437 (2004). Developments in carbon nanotube and nanofibre reinforced polymers.

[125] K. P. Dharmasena, H. N. Wadley, Z. Xue, and J. W. Hutchinson, "Mechanical response of metallic honeycomb sandwich panel structures to high-intensity dynamic loading", *International Journal of Impact Engineering* **35**, 1063–1074 (2008).

[126] Z. Xue and J. W. Hutchinson, "Crush dynamics of square honeycomb sandwich cores", *International Journal for Numerical Methods in Engineering* **65**, 2221–2245 (2006).

[127] H. J. Rathbun, D. D. Radford, Z. Xue, M. Y. He, J. Yang, V. Deshpande, N. A. Fleck, J. W. Hutchinson, F. W. Zok, and A. G. Evans, "Performance of metallic honeycomb-core

sandwich beams under shock loading", *International Journal of Solids and Structures* **43**, 1746–1763 (2006).

[128] A. Hayes, A. Wang, B. Dempsey, and D. McDowell, "Mechanics of linear cellular alloys", *Mechanics of Materials* **36**, 691–713 (2004).

[129] L. Pil, F. Bensadoun, J. Pariset, and I. Verpoest, "Why are designers fascinated by flax and hemp fibre composites?" *Composites Part A: Applied Science and Manufacturing* **83**, 193–205 (2016). Special Issue on Biocomposites.

[130] H. E. Hoydonckx, M. Monti, G. Camino, P. D. Monica, and C. O'Neill, "Polyfurfuryl alcohol thermosets resins in fire resistant composite applications", in *20th International Conference on Composite Materials, ICCM20,* (2015).

[131] M. Zarrelli, A. A. Skordos, and I. K. Partridge, "Investigation of cure induced shrinkage in unreinforced epoxy resin", *Plastics, Rubber and Composites* **31**, 377–384 (2002).

[132] J. R. Davis, *Tensile testing, 2nd Edition* (ASM International, 2004).

[133] W. Chauvenet, *A Manual of Spherical and Practical Astronomy V.II* (Lippincott, Philadelphia, 1863).

[134] J. Halpin, "Effect of environmental factors on composite material design", *US Air Force Materials Laboratory, Technical Report AFML-TR 67-423* (1969).

[135] J. Halpin and J. Kardos, "The halpin-tsai equations: A review", *Polymer Engineering and Science* **16**, 344–352 (1976).

[136] E. Thostenson and T. Chou, "On the elastic properties of carbon nanotube-based composites: modelling and characterization", *Journal of Physics D: Applied Physics* **36**, 573–582 (2003).

[137] M. R. Loos, V. Abetz, and K. Schulte, "Dissolution of mwcnts by using polyoxadiazoles, and highly effective reinforcement of their composite films", *Journal of Polymer Science Part A* **48**, 5172–5179 (2010).

[138] B. T. Kelly, *Physics of graphite* (1981).

[139] E. W. Wong, P. E. Sheehan, and C. M. Lieber, "Nanobeam mechanics: elasticity, strength, and toughness of nanorods and nanotubes", *science* **277**, 1971–1975 (1997).

[140] P. Poncharal, Z. Wang, D. Ugarte, and W. A. D. Heer, "Electrostatic deflections and electromechanical resonances of carbon nanotubes", *science* **283**, 1513–1516 (1999).

[141] J.-P. Salvetat, A. J. Kulik, J.-M. Bonard, G. A. D. Briggs, T. Stöckli, K. Méténier, S. Bonnamy, F. Béguin, N. A. Burnham, and L. Forró, "Elastic modulus of ordered and disordered multiwalled carbon nanotubes", *Advanced Materials* **11**, 161–165 (1999).

[142] M.-F. Yu, O. Lourie, M. J. Dyer, K. Moloni, T. F. Kelly, and R. S. Ruoff, "Strength and breaking mechanism of multiwalled carbon nanotubes under tensile load", *Science* **287**, 637–640 (2000).

[143] M.-F. Yu, O. Lourie, M. J. Dyer, K. Moloni, T. F. Kelly, and R. S. Ruoff, "Strength and breaking mechanism of multiwalled carbon nanotubes under tensile load", *Science* **287**, 637–640 (2000).

[144] C. Zweben, W. S. Smith, and M. W. Wardle, *Test methods for fiber tensile strength, composite flexural modulus, and properties of fabric-reinforced laminates* (Composite Materials: Testing and Design (Fifth Conference), ASTM International, 1979).

[145] A. W. Coats and J. P. Redfern, "Thermogravimetric analysis: A review", *Analyst* **88**, 906––924 (1963).

[146] E. S. Watson and M. J. O'neill, *Differential microcalorimeter* (US3263484A, United States, 1962).

[147] J. D. Ferry, *Viscoelastic Properties of Polymers, 3rd Edition* (Wiley, United States, 1980).

[148] A. I. Malkin, A. Malkin, and A. Isayev, *Rheology: Concepts, Methods and Applications* (ChemTec Publishing, Toronto, 2006).

[149] S. P. Timoshenko, *History of strength of materials* (McGraw-Hill, New York, 1953).

[150] S. Timoshenko, "On the correction for shear of the differential equation for transverse vibrations of prismatic bars", *The London, Edinburgh, and Dublin Philosophical Magazine and Journal of Science* **41**, 744–746 (1921).

[151] S. Timoshenko, "X. on the transverse vibrations of bars of uniform cross-section", *The London, Edinburgh, and Dublin Philosophical Magazine and Journal of Science* **43**, 125–131 (1922).

[152] L. B. Manfredi, E. S. Rodriguez, M. Wladyka-Przybylak, and A. Vazquez, "Thermal degradation and fire resistance of unsaturated polyester, modified acrylic resins and their composites with natural fibre", *Polymer Degradation and Stability* **91**, 255–261 (2006).

[153] F. Yao, Q. Wu, Y. Lei, W. Guo, and Y. Xu, "Thermal decomposition kinetics of natural fibers: Activation energy with dynamic thermogravimetric analysis", *Polymer Degradation and Stability* **93**, 90–98 (2008).

[154] R. Kozlowskiy and M. Wladyka-Przybylak, "Flammability and fire resistance of composites reinforced by natural fibers", *Polymers for Advanced Technologies* **19**, 446—453 (2008).

[155] C. L. Burket, R. Rajagopalan, A. P. Marencic, K. Dronvajjala, and H. C. Foley, "Genesis of porosity in polyfurfuryl alcohol derived nanoporous carbon", *Carbon* **44**, 2957—2963 (2006).

[156] K. Resch-Fauster, J. Džalto, A. Anusic, and P. Mitschang, "Effect of the water absorptive capacity of reinforcing fibers on the process ability, morphology, and performance characteristics of composites produced from polyfurfuryl alcohol", *Advanced Manufacturing: Polymer & Composites Science* **4**, 13–23 (2018).

[157] *ANSYS Mechanical APDL 2019 R3* (ANSYS Inc., Canonsburg, PA 15317, 2019).

[158] F. Cote, V. S. Deshpande, and N. A. Fleck, "The shear response of metallic square honeycombs", *Journal of Mechanics of Materials and Structures* **1**, 1281–1299 (2006).

[159] R. Seeman and D. Krause, "Numerical modelling of nomex honeycomb sandwich cores at meso-scale level", *Composite Structures* **159**, 702–718 (2017).

[160] J. M. Whitney, *Structural Analysis of Laminated Anisotropic Plates* (Technomic Publishing Coompany, Inc., Lancaster, Pennsylvania 17604 (USA), 1987).

[161] F. Scarpa and G. Tomlinson, "Theoretical characteristics of the vibration of sandwich plates with in-plane negative poisson's ratio values", *Journal of Sound and Vibration* **230**, 45–67 (2000).

[162] D. P. Kroese, T. Brereton, T. Taimre, and Z. I. Botev, "Why the monte carlo method is so important today", *WIREs Computational Statistic* **6**, 386–392 (2014).

[163] M. D. McKay, R. J. Beckman, and W. J. Conover, "A comparison of three methods for selecting values of input variables in the analysis of output from a computer code", *Technometrics* **21**, 239—245 (1979).

[164] J. Zhang and M. Ashby, "The out-of-plane properties of honeycombs", *International Journal of Mechanical Sciences* **34**, 475–489 (1992).

[165] P. Montgomery, *A Block Lanczos Algorithm for Finding Dependencies over GF(2). In: Guillou L.C., Quisquater JJ. (eds) Advances in Cryptology — EUROCRYPT '95. EUROCRYPT 1995. Lecture Notes in Computer Science, vol 921.* (Springer, Berlin, Heidelberg, 1995).

[166] M. R. Hestenes and E. Stiefel, "Methods of conjugate gradients for solving linear systems", *Journal of Research of the National Bureau of Standards* **49**, 409–436 (1952).

[167] A. Savitzky and M. J. E. Golay, "Smoothing and differentiation of data by simplified least-squares procedures", *Analytical Chemistry* **36**, 1627–1639 (1964).

[168] H. N. Dhakal, Z. Y. Zhang, and M. O. W. Richardson, "Effect of water absorption on the mechanical properties of hemp fibre reinforced unsaturated polyester composites", *Composites Science and Technology* **67**, 1674–1683 (2007).

[169] A. C. Karmaker, A. Hoffmann, and G. Hinrichsen, "Influence of water uptake on the mechanical properties of jute fiber-reinforced polypropylene", *Journal of Applied Polymer Science* **54**, 1803–1807 (1994).

[170] R. Neville, A. Monti, K. Hazra, F. Scarpa, C. Remillat, and I. Farrow, "Transverse stiffness and strength of kirigami zero-ν peek honeycombs", *Composite Structures* **114**, 30–40 (2014).

[171] S. Del Broccolo, S. Laurenzi, and F. Scarpa, "Auxhex – a kirigami inspired zero poisson's ratio cellular structure", *Composite Structures* **176**, 433–441 (2017).

[172] F. Fahy and P. Gardonio, *Sound and Structural Vibration: Radiation, Transmission and Response* (Academic Press, second edition, 2007).

[173] F. Wahl and G. Schmidt, "On the significance of antiresonance frequencies in experimental structural analysis", *Journal of Sound and Vibration* **219**, 379–394 (1999).

[174] A. Monti, A. E. Mahi], Z. Jendli, and L. Guillaumat, "Experimental and finite elements analysis of the vibration behaviour of a bio-based composite sandwich beam", *Composites Part B: Engineering* **110**, 466–475 (2017).

[175] J. J. Sargianis, H.-I. Kim, E. Andres, and J. Suhr, "Sound and vibration damping characteristics in natural material based sandwich composites", *Composite Structures* **96**, 538–544 (2013).

[176] A. Ferri, "Friction Damping and Isolation Systems", *Journal of Mechanical Design* **117**, 196–206 (1995).

[177] L. Gagnon, M. Morandini, and G. L. Ghiringhelli, "A review of friction damping modeling and testing", *Arch Appl Mech* **90**, 107—-126 (2020).

[178] Z. Fan, "Transient vibration and sound radiation of a rectangular plate with viscoelastic boundary supports", *Int. J. Numer. Meth. Engng* **51**, 619–630 (2001).

[179] R. Palumbo, D. Ivanov, C. Droz, O. Bareille, M. Ichchou, and F. Scarpa, "Design of a multi-scale reinforced sandwich panel with enhanced vibroacoustics performances", in *International Conference on Noise and Vibration Engineering, ISMA 2018,* (2018).

[180] O. Baho, Z. Zergoune, M. Ichchou, B. Harras, R. Benamar, B. Troclet, and O. Bareille, “On global bending shear core transition effects for the vibroacoustics of sandwich structures: Analytical and numerical investigations”, *Composite Structures* **154**, 453–463 (2016).

[181] Z. Zergoune, M. Ichchou, O. Bareille, B.Harras, R. Benamar, and B.Troclet, “Assessments of shear core effects on sound transmission loss through sandwich panels using a two-scale approach”, *Computers & Structures* **182**, 227–237 (2017).